Improving solar-induced fluorescence retrieval from GOME-2 and TROPOMI for long-term vegetation monitoring



Juliëtte C.S. Anema

Propositions

1. Careful correction of instrumental degradation is essential to meaningful interpretation of satellite-derived solar-induced fluorescence data.
   (this thesis)
2. Solar-induced fluorescence reveals changes in vegetation activity, not in drivers of those changes.
   (this thesis)
3. The rapid evolution of data-driven methods challenges scientific analysis.
4. Understanding present-day climate change is incomplete without knowledge of paleoclimates.
5. The dominance of English in academic communication widens the gap between scientific knowledge and society.
6. Climate policy reliance on land-based interventions exceeds the demonstrated effectiveness.
7. Perspectives narrow when engagements stays within familiar circles.

Propositions belonging to the thesis, entitled

Improving solar-induced fluorescence retrieval from GOME-2 and TROPOMI for long-term vegetation monitoring

Juliëtte C.S. Anema
Wageningen, 5 June 2026

Improving solar-induced fluorescence retrieval from GOME-2 and TROPOMI for long-term vegetation monitoring

Juliëtte C.S. Anema

Thesis committee

Promotor
Prof. Dr K.F. Boersma
Professor in Meteorology and Air Quality
Wageningen University & Research
Research Scientist, R&D Satellite Observations
Royal Netherlands Meteorological Institute (KNMI), De Bilt

Other members
Prof. Dr *ir.* L. Kooistra, Wageningen University & Research
Dr *ir.* C. van der Tol, University of Twente, Enschede
Dr F. Maignan, Laboratory for Climate and Environmental Sciences, Gif sur Yvette, France
Dr J. Joiner, ASTICOU Earth Systems, Bar Harbor, USA

This research was conducted under the auspices of the Graduate School for Socio-Economic and Natural Sciences of the Environment (SENSE)

Improving solar-induced fluorescence retrieval from GOME-2 and TROPOMI for long-term vegetation monitoring

Juliëtte C.S. Anema

Thesis
submitted in fulfilment of the requirements for the degree of doctor at
at Wageningen University
by the authority of the Rector Magnificus
Prof. Dr C. Kroeze,
in the presence of the
Thesis Committee appointed by the Academic Board
to be defended in public
on Friday 5 June 2026
at 1:00 p.m. in the Omnia Auditorium.

Juliëtte C.S. Anema
Improving solar-induced fluorescence retrievals from GOME-2 and TROPOMI for long-term vegetation monitoring,
229 pages.

PhD thesis, Wageningen University, Wageningen, the Netherlands (2026)
With references, with summary in English
https://doi.org/10.18174/681681

Summary

Carbon uptake by terrestrial vegetation plays a key role in mitigating climate change by damping atmospheric CO_2 buildup. Consequently, land-based mitigation technologies (LMTs) have become central to climate strategies. LMTs are defined as deliberate human actions aimed at enhancing or maintaining the land's capacity to sequester carbon, including practices such as reforestation and agroforestry. Despite the recognised critical role of LMTs in achieving the Paris Agreement targets, the amount of carbon sequestrated and its long-term permanence remains poorly understood. Moreover, the magnitude and variability of the global land carbon sink itself remain highly uncertain. Hence, these uncertainties highlight the need for robust observational constraints on vegetation activity to improve our understanding of the land carbon sink and to support climate policy decision-making. To meet this demand, this thesis concentrates on developing and using a climate solar-induced fluorescence (SIF) data record derived from satellite retrievals to monitor vegetation dynamics and photosynthetic carbon uptake. SIF captures the faint optical signal (650–850 nm) emitted by vegetation during photosynthesis, the process through which plants assimilate CO_2. Therefore, SIF observations provide valuable and relatively direct insight into plant photosynthetic activity.

This thesis serves a dual connected aim. The first objective is to examine the use of satellite-based SIF as a robust monitoring tool for vegetation dynamics. Specifically, we focus on its use to quantify the impact of LMT implementation, as part of the *Land Use-Based Mitigation for Resilient Climate Pathways* (LANDMARC) project, funded by the European Union Horizon 2020 program. For SIF to meet its full potential as a monitoring tool, a consistent long-term record is needed. Long-term multi-decadal observations facilitate the detection of continuing LMT efforts and the capturing of climate variability. Yet, such climate records of SIF are sparse. Operational life times of individual sensors are limited (generally around 10 years). Additionally, differences in sensor characteristics complicate harmonising across sensors to create a single coherent long-term record. This challenge leads us to the next objective: constructing a climate satellite-based SIF record exhibiting spatial and temporal stability. Satellite sensors from the Global Ozone Monitoring Experiment-2 (GOME-2) series were exploited to retrieve far-red SIF data (from 734–758 nm) as part of EUMETSAT's *Atmospheric Composition Satellite Application Facility* (AC SAF).

The GOME-2 series was selected because, taken together, it provides a continuous operational record (since October 2006) spanning over 18 years (and counting). The series consists of three sensors (GOME-2A, GOME-2B, and GOME-2C) with an identical design, launched in sequence

on board the Metop satellites. The GOME-2 sensors enable SIF retrieval at almost daily global coverage, supporting continuous global monitoring. Their identical design offers high potential in constructing a harmonised, coherent across-sensor SIF record, by minimising differences introduced by varying sensor characteristics. However, data quality issues within each record limit their use for robust monitoring and for across-sensor harmonisation. In particular, GOME-2 observations are heavily affected by calibration issues, such as reflectance degradation, in which the sensor loses sensitivity to the measured light. In this thesis, we found that these effects are present from early in each record, exhibit sensor-specific patterns, and vary significantly with time, wavelength, and scan angle (Chapters 2, 3, and 5). Failing to correct these instrumental artefacts thoroughly can cause false temporal trends in SIF and introduce east-west biases in the observations. Moreover, the sensor-specific artefact effects cause observations from the different GOME-2 sensors to diverge over time, despite their identical design. Hence, it's essential to properly correct for these instrumental artefacts. The following paragraphs describe how these challenges were solved.

The retrieval of consistent SIF is first assessed by examining how the retrieval algorithm could accurately account for these internal inconsistencies. Here, we build on the methodological heritage of the Solar-Induced Fluorescence of Terrestrial Ecosystems Retrieval (SIFTER) algorithm, initially developed for GOME-2A retrieval. Chapter 2 presents the updated version, SIFTER v3, which introduces an advanced correction compensating for the observed degradation patterns. This correction explicitly models the behaviour of the reflectance degradation and its key dependencies of time (at daily time steps), wavelength, and scan angle throughout the entire record. The latter factor is previously neglected in GOME-2 SIF retrievals. Our findings highlight the need to account for the dependence of GOME-2 reflectance degradation on scan position. It introduces an east-west bias of similar magnitude to the time-dependent degradation (up to 8 % for GOME-2A), whose substantial impact on record stability is widely recognised. Additional algorithmic improvements further enhanced the retrieval robustness of SIFTER v3. The improved algorithm advances the spatiotemporal consistency of SIF and provides a stable foundation for robust vegetation monitoring. This stability was demonstrated by using SIFTER v3 to retrieve GOME-2 SIF from GOME-2A (2007–2017, Chapter 2), GOME-2B (2012–2023, Chapter 3), and GOME-2C (2019–2024, Chapter 5). The degradation correction settings were tuned for each sensor to align with the observed degradation characteristics.

Next, we assessed how well the individual GOME-2 records could function as a single coherent record, demonstrated using GOME-2A and GOME-2B SIF in Chapter 3. We found that the calibration corrections within SIFTER v3 not only resolved internal inconsistency but also served as the foundation for harmonising the two records. The retrieved GOME-2A and GOME-2B SIF records show strong coherence across various regions. However, in some areas, a slight step change is observed in the time series at the transition from GOME-2A to GOME-2B. This thesis presents a framework to detect and, when needed, correct for such step-change effects. Aside from instrumental effects, consistent sampling is shown to play a substantial role in ensuring temporal consistency. During the overlapping period of GOME-2A and GOME-2B (July 2013 to December 2017), the sensors observe SIF under different viewing geometry ranges ($-35°$ to $+35°$ versus $-54°$ to $+54°$). This sampling difference can lead to discrepancies of up to 15 % between GOME-2A and GOME-2B across regions and periods with high vegetation activity. Co-

sampling under similar viewing conditions reduces the bias between GOME-2A and GOME-2B SIF within 2 %. The robustness of the combined GOME-2A and GOME-2B SIF record, and its suitability as a single coherent dataset, is underscored by its high correlation with independent GPP data from the global FluxSat dataset. Together, these results demonstrate that the GOME-2A and GOME-2B data can be used as a single coherent long-term record through calibration and intersensor bias corrections, and consistent sampling.

Preliminary evaluation of GOME-2C, in Chapter 5, indicates that it captures similar seasonality and magnitude as GOME-2A and GOME-2B over most regions, but with noted differences over the Amazon. This discrepancy may reflect more substantial South Atlantic Anomaly (SAA) effects over GOME-2C. The SAA denotes a region over the South Atlantic and South America where elevated radiation levels can introduce noise into satellite observations. Despite this discrepancy, the GOME-2C results overall indicate the potential to combine observations from all three GOME-2 sensors into a continuous time series from 2007 to the present (and counting). Furthermore, we demonstrated the strong potential of SIFTER v3 to extend SIF retrieval beyond GOME-2 sensors. We present the first results of SIF retrievals from the TROPOspheric Monitoring Instrument (TROPOMI) using SIFTER v3. The consistent application of the retrieval algorithm across different sensors helps limit intersensor biases and enables comparisons of SIF across missions. SIF comparability across missions benefits from complementary sensor characteristics, such as different overpass times. For instance, TROPOMI offers an overpass time in the early afternoon (13:30), whereas GOME-2 observes in the late morning (09:30). We retrieved TROPOMI SIF for a single day (6 February 2024) over the Amazon (shown in Chapter 5). Minimal adaptations to SIFTER v3 were made to optimise its performance, while maintaining consistency in retrieval methodology. A comparison of our TROPOMI SIF data with the alternative TROPOSIF product indicates that SIFTER v3 performs better over this area and on this day. Notably, SIFTER v3 resulted in more than three times as many valid retrievals (62 % versus 18.6 %). This provides confidence in the algorithm's ability to retrieve robust long-term SIF from both GOME-2 and TROPOMI.

The demonstrated ability to construct long-term SIF records supports the use of satellite-based SIF for vegetation monitoring. In our 2024 study (Chapter 4), we examined how SIF could be used to quantify the impact of interventions, such as LMT implementation, on photosynthetic carbon uptake. We evaluated the effects of two distinct changes in vegetation cover: (i) eucalyptus wildfire in Australia and (ii) large-scale reforestation in China, using the then-available SIF data from TROPOMI (Caltech product) and GOME-2A. Although the GOME-2A record spanned from 2007 to 2018, only part of it was suitable for time series analysis due to instrumental artefacts that affected temporal stability. This instability motivated the development of the improved SIFTER v3 algorithm, published in 2025 (Chapter 2). Finally, the reforestation impact was assessed from 2007 to 2012, with a simple degradation correction applied to ensure temporal stability. Our results demonstrate the strength of satellite-based SIF in capturing vegetation responses to interventions, including both prompt, disruptive and slower, more gradual land-cover changes. We showed how SIF can be used in combination with supporting in situ and satellite data, for example, land use and soil moisture, to align SIF with the intervention and attribute the detected changes to their respective drivers. A framework for applying SIF in intervention monitoring is presented in Chapter 5. For SIF to serve as a reliable monitoring

tool, its spatial resolution and temporal coverage must match those of the intervention. Overall, this work shows that carefully retrieved and interpreted satellite-based SIF can provide valuable assessments of vegetation responses to land-based interventions.

The results of this thesis enhance the potential of satellite-based SIF to support improved understanding of vegetation dynamics and photosynthetic carbon uptake worldwide. We developed methodological improvements to the SIFTER algorithm that advance the robustness and consistency of SIF retrievals. Consistent GOME-2 SIF records were constructed using the improved SIFTER v3 algorithm: GOME-2A (from 2007 to 2017), GOME-2B (from 2012 to 2023), and GOME-2C (from 2019 to 2024). The SIFTER v3 algorithm is shown to serve as a building block for constructing coherent long-term SIF records from the GOME-2 series, which can be used for vegetation monitoring purposes. We also demonstrated the potential of SIFTER v3 to retrieve robust SIF from TROPOMI, thereby contributing to the standardisation of SIF time series across satellite sensors. Finally, this work demonstrates how satellite-based SIF can be used to quantify vegetation responses to interventions. A practical SIF-based monitoring framework is presented, integrating SIF with supporting in situ and remote sensing data to attribute detected changes to the intervention. These results provide a solid foundation for the future use of satellite-based SIF in global vegetation monitoring.

Samenvatting

Ecosystemen spelen een belangrijke rol bij het vastleggen van koolstofdioxide (CO_2) in de bodem en in vegetatie als koolstof. Hierbij reguleren ze de hoeveelheid CO_2 in de atmosfeer. Vanwege de centrale rol in koolstofvastlegging wordt het aanplanten of aanpassen van vegetatie steeds vaker ingezet in klimaatmitigatiestrategieën, bijvoorbeeld in de vorm van biosfeergerichte mitigatiemaatregelen (*land-based mitigation techniques*, LMT's). LMT's zijn door menselijke ingrepen gedreven maatregelen die zich richten op het verhogen of behouden van de opname- en opslagcapaciteit van koolstof door de biosfeer, bijvoorbeeld via herbebossing of bosbeheer. Hoewel LMT's van groot belang worden geacht om de doelen van het Parijs Akkoord te behalen, blijft hun daadwerkelijke koolstofvastleggingspotentieel onzeker. Daarnaast vorm de vastleggingscapaciteit van de biosfeer één van de grootste onzekerheden binnen de mondiale koolstofkringloop. Deze onzekerheden benadrukken de noodzaak van robuuste metingen die de koolstofvastleggingsactiviteit van vegetatie op aarde in kaart kunnen brengen en klimaatbeleidvorming kan ondersteunen. Dit proefschrift gaat hierop in door te onderzoeken in hoeverre satellietmetingen van zon-geïnduceerde fluorescentie (*solar-induced fluorescence*, SIF) verbeterd en gebruikt kunnen worden om de koolstofvastlegging van vegetatie te kwantificeren. SIF-metingen volgen de kleine hoeveelheid licht die planten tijdens fotosynthese uitstralen als fluorescentie (650–850 nm). Fotosynthese is een fundamenteel proces waarin planten energie uit zonlicht gebruiken om CO_2 vast te leggen en dit samen met water om te zetten in bouwstoffen en zuurstof. Omdat de hoeveelheid uitgestraalde fluorescentie gerelateerd is aan fotosynthese, en dus de CO_2-vastlegging, kan SIF dienen om deze activiteit te volgen.

Dit proefschrift stelt een tweedelig doel. In de eerste plaats onderzoeken we het gebruik van satellietmetingen van SIF voor het volgen van plantenactiviteit en CO_2-vastlegging door vegetatie. We richten ons specifiek op het gebruik van SIF-metingen voor de kwantificatie van het succes van LMT-implementaties. Deze doelstelling is onderdeel van het door de Europese Unie gefinancierde Horizon 2020 *Land Use-Based Mitigation for Resilient Climate Pathways* (LANDMARC) project. Voor optimaal gebruik van SIF-metingen is consistentie vereist en reiken de metingen over meerdere jaren tot decennia. Dergelijke langdurige SIF-reeksen maken het mogelijk om de effectiviteit van LMT-implementaties door de tijd heen te volgen en om de effecten van klimaatvariabiliteit te detecteren. Echter, de beschikbaarheid van langdurige SIF-metingen vanuit satellieten is beperkt. Ten eerste komt dit doordat individuele satellietsensoren slechts gedurende een beperkte periode operationeel zijn (meestal rond de 10 jaar). Ten tweede bemoeilijken verschillen tussen satellietsensoren het samenvoegen en harmoniseren van afzonderlijke meetreeksen. Hierdoor is het genereren van één consistente langdurige SIF-reeks uitdagend. Deze

uitdaging brengt ons bij het tweede doel van dit proefschrift. Dit doel richt zich op het genereren van een langdurige, robuuste SIF-tijdreeks op basis van satellietobservaties van de Global Ozone Monitoring Experiment-2 (GOME-2) sensorreeks. Deze inspanning valt binnen het kader van het *Atmospheric Composition Satellite Application Facility* (AC SAF) van EUMETSAT.

De GOME-2-sensorreeks is bijzonder interessant omdat zij bestaat uit drie vrijwel identieke sensoren (GOME-2A, GOME-2B en GOME-2C) met hetzelfde instrumentontwerp. De drie sensoren zijn in opeenvolgende MetOp-missies gelanceerd, met de eerste in oktober 2006, en beslaan gezamenlijk meer dan 18 jaar aan operationele metingen. Daarnaast bieden de GOME-2-sensoren bijna dagelijkse wereldwijde dekking. Het gestandaardiseerde ontwerp van de sensoren minimaliseert onderlinge verschillen, wat essentieel is voor het harmoniseren en het genereren van een consistente SIF-tijdreeks. Problemen in de meetkwaliteit van de sensoren kunnen echter de consistentie en stabiliteit van de SIF-metingen aanzienlijk belemmeren. De GOME-2-sensoren ondervinden in de loop van de missie kalibratieproblemen, waaronder degradatie van het gemeten licht en reflectantie, waarbij de sensoren gevoeligheid verliezen. In andere woorden, het gemeten licht kan in de tijd variëren, niet alleen door veranderingen aan het aardoppervlak, maar ook door veranderingen in de sensor zelf. In dit proefschrift tonen we aan dat deze problemen al vanaf het begin van de meetreeksen aanwezig zijn, per sensor verschillen en variëren afhankelijk van tijd, golflengte en de kijkhoek (hoofdstukken 2, 3 en 5). Doordat de effecten verschillen per sensor, leiden zij niet alleen tot instabiliteit in de individuele SIF-tijdreeksen, maar vergroten zij ook de onderlinge verschillen tussen de reeksen, waardoor harmonisatie wordt beperkt. Daarom is het van groot belang om voor deze instrumentele artefacten te corrigeren, zodat schijnbare trends in zowel de individuele als de gecombineerde SIF-tijdreeksen worden voorkomen. In de volgende alinea's licht ik toe hoe we deze uitdagingen hebben aangepakt.

Allereerst onderzoeken we hoe het retrievalalgoritme kan worden geoptimaliseerd om te corrigeren voor de instrumentele artefacten. Het retrievalalgoritme bepaalt op basis van het door de satelliet gemeten licht, hoeveel fluorescentie (SIF) door planten wordt uitgestraald. Daarbij bouwen we voort op de methodologische basis van het Solar-Induced Fluorescence of Terrestrial Ecosystems Retrieval (SIFTER) algoritme. Dit algoritme is oorspronkelijk ontworpen voor de bepaling van SIF vanuit GOME-2A-metingen. In hoofdstuk 2 presenteren we de verbeterde versie van het SIFTER-algoritme: SIFTER v3. SIFTER v3 introduceert een geavanceerde correctie voor de degradatie-effecten. Het modelleert daarbij expliciet de afhankelijkheden van tijd, golflengte en kijkhoek, zodat instrumentgedreven veranderingen in de reflectantie zorgvuldig worden geëlimineerd. De afhankelijkheid van de degradatie over kijkhoek wordt doorgaans genegeerd in SIF-bepalingen van GOME-2-metingen, waarin de tijdsafhankelijkheid als belangrijkste component van de degradatie wordt beschouwd. Echter, onze resultaten benadrukken het belang van de kijkhoekafhankelijkheid. Het effect van de degradatie varieert met de oost-west kijkrichting van de satelliet. Dit veroorzaakt een afwijking tot 8 % bij GOME-2A en is van dezelfde orde grootte als de tijdsafhankelijke afwijking. Naast de verbeterde degradatiecorrectie hebben we in SIFTER v3 een aantal andere punten geoptimaliseerd die de stabiliteit van de SIF-bepalingen verder verbeteren. Met behulp van het verbeterde algoritme hebben we SIF-tijdreeksen bepaald vanaf GOME-2A (over 2007 tot 2017, hoofdstuk 2), GOME-2B (over 2012 tot 2023, hoofdstuk 3) en GOME-2C (van 2019 tot 2024, hoofdstuk 5). De correctie-instellingen zijn aangepast per sensor om de sensor-specifieke degradatiepatronen te volgen.

De volgende stap is om te onderzoeken of de GOME-2 SIF-tijdreeksen gecombineerd kunnen worden tot één tijdreeks. Dit wordt beschreven in hoofdstuk 3 door SIF-metingen van GOME-2A en GOME-2B te vergelijken. De geavanceerde degradatiecorrectie in SIFTER v3 stabiliseert niet alleen de individuele SIF-reeksen in de loop der tijd, maar fungeert ook als harmonisatie en brengt beide metingen dichter bij elkaar. De GOME-2A en GOME-2B SIF-metingen kwamen sterk overeen over verschillende gebieden. Echter, we vonden in sommige gebieden een kleine abrupte verandering bij de overgang van de GOME-2A- naar de GOME-2B-tijdreeks. We presenteren we een raamwerk om dusdanige abrupte instrumentgedreven veranderingen te detecteren en, waar nodig, te corrigeren via statistische modellering. Naast het elimineren van instrumentgedreven instabiliteit in de SIF-tijdreeks benadrukken we ook het belang van consistente sampling voor het verkrijgen van een consistente en stabiele tijdreeks. Met sampling wordt de manier bedoeld waarop satellietmetingen in ruimte, tijd en onder bepaalde observatiecondities worden geselecteerd voor de uiteindelijke analyse. Tijdens de overlappende periode (van juli 2013 tot december 2017) meten GOME-2A en GOME-2B onder verschillende kijkhoeksbereiken ($-35°$ tot $+35°$ versus $-54°$ tot $+54°$). We laten zien dat dit verschil in kijkhoeksampling kan leiden tot afwijkingen tot 15 % tussen SIF-metingen van beide instrumenten tijdens perioden en gebieden met hoge vegetatieactiviteit. Wanneer GOME-2A en GOME-2B SIF-metingen op dezelfde wijze worden gesampled (zogenoemde co-sampling), verkleint de afwijking tot binnen 2 %, wat acceptabel is voor langdurige trendanalyse. Samen laten deze resultaten zien dat GOME-2A en GOME-2B SIF-metingen als één doorlopende tijdreeks gebruikt kunnen worden, mits voldoende wordt gecorrigeerd voor instrumentgedreven afwijkingen en consistente co-sampling wordt toegepast. Het succes van de harmonisatie wordt verder ondersteund door de sterke correlatie tussen de gecombineerde SIF-tijdreeks en onafhankelijke schattingen van de bruto primaire productie (*gross primary productivity*, GPP), ofwel fotosynthesische koolstofvastlegging.

Voorlopige analyses van de in hoofdstuk 5 gegenereerde GOME-2C SIF-tijdreeks tonen vergelijkbare seizoensvariatie als de tijdreeksen van GOME-2A en GOME-2B over de meeste gebieden, met uitzondering van de Amazone. De afwijkingen in de Amazone kunnen wijzen op een sterkere invloed van de Zuid-Atlantische Anomalie (ZAA) op de GOME-2C sensor. De ZAA is een gebied boven een deel van de Atlantische Oceaan en Zuid-Amerika waar een verhoogde flux van geladen deeltjes ruis in satellietmetingen veroorzaakt. Ondanks deze afwijkingen tonen de resultaten het potentieel om SIF-metingen van alle drie de GOME-2 sensoren te harmoniseren tot één lange tijdreeks van 2007 tot heden. Daarnaast laten we in dit proefschrift zien dat SIFTER v3 de potentie heeft om SIF-tijdreeksen te genereren van andere satelliet sensoren. We presenteren, eveneens in hoofdstuk 5, de eerste resultaten van SIF-metingen van TROPOspheric Monitoring Instrument (TROPOMI), bepaald met SIFTER v3. Door één retrievalalgoritme te gebruiken voor verschillende sensoren verminderen we de verschillen tussen SIF-dataproducten en creëren we mogelijkheden voor consistente vergelijking en integratie. Het integreren van SIF-metingen van verschillende satellieten biedt bovendien veel inzichten, bijvoorbeeld doordat ze op verschillende tijdstippen meten. Zo meet de GOME-2 sensor SIF aan het einde van de ochtend (09:30), terwijl TROPOMI SIF-metingen verricht aan het begin van de middag (13:30). We bepalen SIF uit TROPOMI-metingen voor één dag, op 6 februari 2024, in de Amazone. Het SIFTER v3-algoritme is minimaal aangepast om de consistentie met GOME-2-metingen te waarborgen, terwijl het tegelijkertijd wordt geoptimaliseerd voor toepassing op TROPOMI. Vergelijkingen van

onze TROPOMI SIF-metingen met het alternatieve TROPOSIF-product tonen aan dat SIFTER v3 voor dit gebied en deze dag beter presteert dan TROPOSIF. Opmerkelijk is dat het SIFTER v3 algoritme meer dan drie keer zoveel succesvolle SIF-bepalingen oplevert (62,0 % versus 18,6 %). Deze resultaten versterken het vertrouwen in SIFTER v3 voor het bepalen van robuuste, consistente en langdurige SIF-metingen, zowel voor GOME-2 als voor TROPOMI.

Deze inzichten onderbouwen het gebruik van SIF-satellietmetingen om de CO_2-vastlegging door vegetatie te volgen. We onderzoeken in een in 2024 gepubliceerde studie (hoofdstuk 4) hoe SIF ingezet kan worden om het effect van interventies, zoals LMT-implementaties, op de CO_2-vastlegging te kwantificeren. We onderzoeken dit aan de hand van twee studies: (i) een natuurbrand in een eucalyptusbos in Zuid-Oost Australië, en (ii) grootschalige, langdurige herbebossing in China. Voor de bosbrandstudie gebruikten we TROPOMI SIF-metingen van het Caltech-product, en voor de China-studie gebruikten we het toen beschikbare SIFTER v2-product van GOME-2A. Hoewel de dataset van 2007 tot 2018 liep, bleek een groot deel niet geschikt voor tijdreeksanalyse vanwege de reeds aanwezige invloed van instrumentartefacten die de stabiliteit verstoorden. Dit vormde mede de motivatie voor de ontwikkeling van het verbeterde SIFTER v3-algoritme gepubliceerd in 2025 (hoofdstuk 2). De impact van herbebossing in China werd bestudeerd met GOME-2A SIF-metingen van 2007 tot en met 2012. Om de data stabiliteit te waarborgen, is een eenvoudige degradatiecorrectie toegepast. Onze resulten benadrukken het potentieel van satellietmetingen van SIF om veranderingen in vegetatieactiviteit en CO_2-vastlegging te detecteren na een interventie, zowel bij meer geleidelijke als bij abrupte veranderingen in landgebruik. We laten zien hoe SIF-metingen in combinatie met plaatselijke metingen en andere satellietmetingen, zoals van landgebruik en bodemvocht, kan worden gebruikt voor vegetatiemonitoring en we presenteren een raamwerk in hoofdstuk 5 waarin de stappen en beperkingen worden toegelicht. Om SIF-metingen te gebruiken om het succes van LMT's te kwantificeren, moeten de ruimtelijke resolutie van de metingen aansluiten bij de omvang van de betreffende LMT. Deze resultaten laten zien dat SIF-satellietmetingen, mits zorgvuldig bepaald en geïnterpreteerd, waardevol zijn om veranderingen in CO_2-vastlegging in kaart te brengen en daarmee het begrip over LMT effectiviteit te vergroten.

De resultaten van dit proefschrift vergroten het potentieel van satellietmetingen van SIF om tot een beter inzicht in vegetatiedynamiek en CO_2-vastlegging wereldwijd te komen. We verbeterden de methodiek om SIF-metingen te bepalen met het SIFTER-retrievalalgoritme. Met het verbeterde algoritme SIFTER v3 hebben we consistente SIF-tijdreeksen gegenereerd uit de drie GOME-2 sensoren: GOME-2A (van 2007 tot 2017), GOME-2B (van 2012 tot 2023) en van GOME-2C (van 2019 tot 2024). Dankzij de expliciete correctie voor instrumentgedreven afwijkingen zijn deze tijdreeksen stabiel en onderling vergelijkbaar. Deze GOME-2 SIF-tijdreeksen kunnen gebruikt worden om CO_2-vastlegging over tijd te volgen. Bovendien laten we zien dat het SIFTER v3 algoritme ook kan worden toegepast op TROPOMI-metingen, waarmee we de basis leggen voor het standaardiseren van SIF-tijdreeksen tussen verschillende satellieten. Tot slot hebben we het potentieel van SIF-metingen aangetoond om de impact van LMT's op de CO_2-vastlegging te kwantificeren. We presenteren hiervoor een praktische handleiding waarin het gebruik van SIF-metingen gecombineerd met plaatselijke en aanvullende satelliet-metingen wordt toegelicht. Deze resultaten leggen een stevig fundament voor toekomstig gebruik van satellietmetingen van SIF in mondiale vegetatiemonitoring.

Contents

Page

Summary **vii**

Samenvatting **xiii**

Contents **xvii**

Chapter 1 Introduction **1**
1.1 The role of terrestrial vegetation into Earth's system 3
1.2 Monitoring vegetation dynamics 7
1.3 Chlorophyll *a* fluorescence: a direct proxy of photosynthesis 11
1.4 Remote sensing of solar-induced fluorescence 13
1.5 Thesis Overview 20

Chapter 2 Improved consistency in SIF retrievals from GOME-2A with the SIFTER v3 algorithm **23**
2.1 Introduction 25
2.2 GOME-2 instrument 26
2.3 In-flight degradation correction 28
2.4 SIFTER v3 retrieval algorithm 32
2.5 SIFTER v3 retrieval results 40
2.6 Conclusions 46

Chapter 3 Long-term solar-induced fluorescence data record from GOME-2A and GOME-2B (2007–2023) using the SIFTER v3 algorithm **61**
3.1 Introduction 63
3.2 GOME-2 instruments 64
3.3 Application of SIFTER v3 to GOME-2B 66
3.4 Comparison of GOME-2A and GOME-2B SIF 72
3.5 Long-term time series analysis 78
3.6 Conclusions and outlook 85

Chapter 4 Monitoring the impact of forest changes on carbon uptake with space-bases SIF measurements **115**
4.1 Introduction 117
4.2 Data 118
4.3 Forest loss following eucalyptus fire in South-East Australia 121
4.4 Reforestation in north-central China 127
4.5 Conclusions and Discussion 132

Chapter 5 General discussion, recent developments, and outlook **143**
5.1 Next steps for satellite remote sensing of SIF 144
5.2 Solar-induced fluorescence as monitoring tool 162
5.3 Conclusions and outlook 168

References **181**

Publications **201**

Acknowledgements **203**

Chapter 1

Introduction

This thesis centres on retrieving consistent satellite-based solar-induced fluorescence (SIF) records and its use for monitoring vegetation dynamics. SIF captures the faint optical signal emitted during photosynthesis. As this signal directly links to photosynthesis, SIF provides a unique vegetation proxy. Over the past 15 years, developments in satellite sensors and retrieval methods facilitated observation of SIF from space (e.g., Joiner et al., 2011; van Schaik et al., 2020). Figure 1.1 shows SIF observations during December–February and June–August from the GOME-2 instrument aboard the Metop-B satellite, illustrating SIF's ability to capture the spatial and temporal variability of vegetation dynamics at regional to global scales.

The functioning of terrestrial vegetation is fundamental to life and key processes in Earth's system. A prominent role of terrestrial vegetation is that of Earth's largest carbon sink. This carbon, in the form of CO_2, is continuously captured by plants through photosynthesis. Over the past decade, the total CO_2 captured by terrestrial vegetation equals roughly 30 % of the total anthropogenic CO_2 emissions (Friedlingstein et al., 2025). However, the sink's strength remains uncertain. A recent study suggests that the net terrestrial carbon sink might be nearly half as strong as previously thought (Randerson et al., 2025). Part of this large uncertainty stems from the lack of direct observations of vegetation carbon fluxes at the global scale. Ongoing climate change affects vegetation functioning, for example, through shifts in seasonality (Piao et al., 2019) and regional reductions in photosynthetic activity, such as over the Amazon (Brienen et al., 2015; Gatti et al., 2021), contributing to the uncertainty. To better understand the land carbon sink and its response to climate variability, there is a pressing need for more robust observations on vegetation activity and carbon uptake.

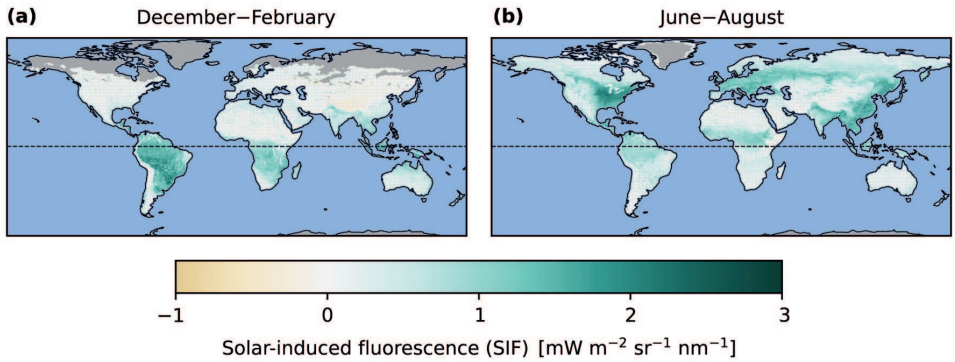


Figure 1.1: Global terrestrial vegetation activity depicted by solar-induced fluorescence (SIF) retrieved from GOME-2B in this work. Panels (a) and (b) show the averaged SIF during the December–February (DJF) and June–August (JJA) periods for 2013–2017, with the equator indicated by the dashed line. The averaged data is re-gridded at a $0.5° \times 0.5°$ resolution.

1.1 The role of terrestrial vegetation into Earth's system

1.1.1 Fundamental ecosystem functions

Terrestrial vegetation is deeply integrated into Earth's system. Through several feedback processes, terrestrial ecosystems regulate Earth's environment by influencing the physical landscape, the energy balance, atmospheric composition, the hydrological cycle, and the carbon cycle (Heimann and Reichstein, 2008). These interactions are summarised in Figure 1.2.

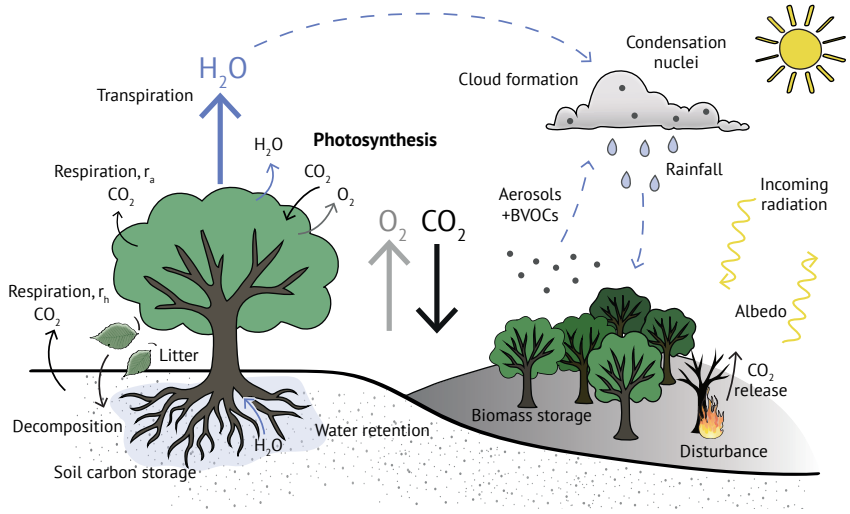


Figure 1.2: Terrestrial vegetation is connected to Earth's system in multiple ways. It influences, e.g., the atmospheric composition through the production of O_2, the carbon cycle through acting as a carbon sink, the Earth's energy budget through the drawdown of greenhouse gas CO_2, as well as albedo-warming and cooling, and the hydrological cycle by recycling atmospheric moisture and influencing cloud formation. The blue dashed arrows represent the connection between terrestrial vegetation and the hydrological cycle. The large arrows represent the net effects of the vegetation system.

Plant photosynthesis is fundamental in connecting the biosphere to Earth's system. The process of photosynthesis takes place in the leaf chloroplasts, where glucose ($C_6H_{12}O_6$) is generated from carbon dioxide (CO_2) and water (H_2O). Oxygen (O_2) is released to the atmosphere as a byproduct. These biochemical reactions are powered by sunlight (400–700 nm), which is absorbed by chlorophyll ($a + b$) within the chloroplasts, and can be summarised by:

$$6CO_2 + 6H_2O \xrightarrow{\text{light}} C_6H_{12}O_6 + 6O_2 \tag{1.1}$$

The produced glucose is an organic form of carbon that serves as an energy source for plant metabolism and a building block for biomass accumulation. The needed CO_2 molecules are diffused from the atmosphere to the chloroplasts through small pores in the leaves that regulate gas exchange between the plant and the atmosphere, which are called stomata.

The total photosynthetic carbon uptake by the Earth is known as gross primary production

(GPP), generally expressed in gC m^{-2} day^{-1}. Part of GPP is used to build and maintain biomass, whereas a slightly smaller part contributes to autotrophic respiration (Re_a), the re-release of CO_2 to the atmosphere. Re_a is the process by which plants burn the produced glucose through photosynthesis to generate energy for their metabolism. Unlike GPP, it does not depend on solar energy and occurs continuously, both during day and night. The balance between the GPP and Re_a fluxes is known as the net primary production (NPP):

$$NPP = GPP - Re_a \tag{1.2}$$

In addition to autotrophic respiration, ecosystems release CO_2 to the atmosphere through heterotrophic respiration (R_h). This is the process by which dead organic material, such as fallen leaves, is decomposed by, e.g., microorganisms. Together, R_a and R_h are represented as total respiration (Re). Finally, the total carbon loss or gain by the ecosystem, the net ecosystem production (NEP), is determined as:

$$NEP = GPP - Re \tag{1.3}$$

In the above equation, we consider NEP from the ecosystem's perspective, with negative values representing a loss of carbon to the atmosphere.

When the overall GPP term exceeds total respiration, terrestrial ecosystems function as a global net carbon sink (Friedlingstein et al., 2025). This net sink includes the NEP as well as secondary terms representing carbon release to the atmosphere through disturbances, such as fires, harvest, and land-use change. Terrestrial vegetation is a significant driver of the global carbon cycle. Its impact is evident from the well-known oscillation in the atmospheric CO_2 concentration trend in, for example, the Keeling Curve. The troughs and peaks reflect the seasonal cycle in the Northern Hemisphere, where most of the land and vegetation is located, with minima in the spring (May), and maxima in autumn (September). Satellite observations of SIF capture this seasonal cycle in photosynthesis (CO_2 uptake) as shown in Figure 1.1.

In addition to its role in the global carbon cycle, terrestrial vegetation plays a key role in the global water cycle. Plants connect soil moisture to the atmosphere through the process of transpiration. Roots reach and absorb groundwater, which is partly exchanged with the atmosphere through the stomata. Alongside evaporation, transpiration is responsible for transferring water from the land to the atmosphere. Together, these fluxes are referred to as evapotranspiration. Both fluxes together are referred to as evapotranspiration, which sustains 61 % of the annual land precipitation (Schneider et al., 2017). The dominant role of transpiration in evapotranspiration (typically accounting for over 70 % (Sutanto et al., 2014)) indicates the substantial role of vegetation in recycling atmospheric water.

Moreover, terrestrial vegetation also impacts the water cycle through influencing the formation of clouds. Studies have shown that changes in forest cover, such as ongoing deforestation, can impact cloud cover and potentially affect precipitation patterns (Leite-Filho et al., 2021; Xu et al., 2022; Meier et al., 2021; Teuling et al., 2017). These effects are partly driven by differences in albedo and surface roughness between forests and bare neighbouring land, which can drive forest-breeze circulations and subsequently impact local cloud formation (Xu et al.,

2022; Teuling et al., 2017; Bosman et al., 2019). Additionally, vegetation can influence cloud formation indirectly through the emission of biogenic volatile organic compounds (BVOCs). When oxidised, BVOCs can form secondary organic aerosols (SOAs), which can serve as cloud condensation nuclei (Zhao et al., 2017; Petäjä et al., 2022).

Besides the indirect effect of BVOCs on cloud formation, BVOCs can also impact the atmosphere in another way, namely, by contributing to air pollution. First, the SOAs formed from BVOCs significantly contribute to the concentrations of fine particulate matter ($PM_{2.5}$). Moreover, BVOCs act as the precursor of another harmful air pollutant: ground-level ozone (O_3). Ground-level O_3 can form via photochemical reactions from oxidised BVOCs, if in the presence of sufficient nitrogen oxides ($NO_x = NO + NO_2$) and sunlight (Sillman, 1999). Both pollutants, $PM_{2.5}$ and ground-based O_3, pose serious risks to human health, including cardiovascular and lung diseases (WHO, 2022; Ebi and McGregor, 2008), as well as to the ecosystem environment (Wedow et al., 2021).

1.1.2 Vegetation and climate interactions

The climate system is shaped by the complex internal interactions among the atmosphere, the ocean, ice, the land surface, and vegetation. Throughout geological time, the evolution of vegetation has significantly shaped the climate and the planet's habitability (Berry et al., 2010; Schreiber et al., 2022; Dahl and Arens, 2020). For example, massive forest expansion during the favourable climatic conditions of the Carboniferous period (∼300 Myr ago) contributed to a major decline in atmospheric CO_2. This drawdown of carbon triggered one of the largest ice ages (Beerling, 2007) and illustrates the tight two-way connection between global vegetation and climate systems.

The buried organic remains of the Carboniferous, which transformed into coal, oil, and natural gas, contribute to today's ongoing global warming. Since the Industrial Revolution, from 1750, humans have burned these "fossil fuels", releasing the Carboniferous carbon back into the atmosphere to meet increasing energy uses. Moreover, other human activities, such as land-use change, significantly add to the exchange of carbon from terrestrial ecosystems to the atmosphere. These anthropogenic activities have substantially and steadily increased the atmospheric CO_2 concentration by approximately 51 % – from 280 parts per million (ppm) preindustrial to 422.45 ppm in 2024 (Friedlingstein et al., 2025; Ruddiman, 2014).

The substantial increase in atmospheric CO_2 has distorted the Earth's energy balance by enhancing the trapping of outgoing radiation, contributing to a rise in global temperatures. The Intergovernmental Panel on Climate Change (IPCC) estimates that global surface temperatures increased by 1.15 °C over the 2013–2022 period relative to 1850–1900 (Calvin et al., 2023). As a result of global warming, weather patterns are changing, as well as the frequency and intensity of extreme events such as droughts, heavy rainfall, and wildfires (Seneviratne et al., 2023; Clarke et al., 2022). With fossil fuel emissions not expected to come to an end soon, combating them is necessary to keep the Paris Agreement goals of limiting warming to 1.5–2 °C by 2050 within reach. To address and mitigate climate change, it is essential to understand the buildup of atmospheric CO_2 and processes that affect it.

The growth in atmospheric CO_2 is not solely dependent on anthropogenic CO_2 emissions into the atmosphere. The 2024 Global Carbon Budget reports that of the anthropogenic emissions, around 48 % remained in the atmosphere over the past decade (Friedlingstein et al., 2025, see Figure 1.3a). Roughly half of the emissions were partitioned among the other two major sinks: the ocean (around 26 %) and land (around 30 %). These contributions leave a residual imbalance of approximately 4 %, which reflects the uncertainty within the estimated budget rather than a physical flux. The reported carbon budgets indicate a substantial role for terrestrial vegetation in dampening atmospheric CO_2. Figure 1.3b shows the change in carbon emissions and their partitioning among the sinks (atmosphere, ocean, and land) over time since 1850 (pre-industrial). As emissions increased over time, the terrestrial carbon sink increased accordingly. Hence, the land's carbon uptake capacity has played a pivotal role in mitigating climate change so far. Subsequently, land-based techniques to enhance or maintain the land sink are key to national climate strategies and Intergovernmental Panel on Climate Change (IPCC) climate scenarios (United Nations Environment Programme et al., 2024; Calvin et al., 2023). These land-based mitigation techniques (LMTs) include practices such as reforestation, wildfire management, and agroforestry (Karki et al., 2023).

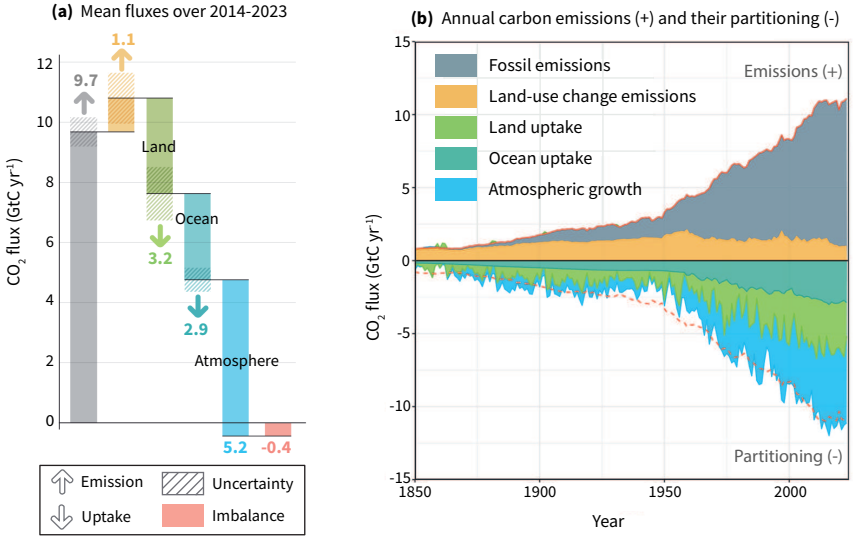


Figure 1.3: Components of the global carbon budget over (a) the past decade (2014–2023) and (b) over time since 1850. CO_2 emissions from fossil fuels and net land-use change are indicated as positive (+, ↑), and CO_2 uptake by the land, ocean, and atmosphere as negative (−, ↓). The fluxes are shown in units of GtC yr^{-1}. Hatching in (a) indicates the uncertainty in the mean carbon fluxes. The legend in panel (b) holds for both plots. The red dashed line in (b) indicates the budget imbalance between the total emitted (red line) and partitioned carbon. Figures are adapted from Friedlingstein et al. (2025).

The strong CO_2 uptake capacity of the land, however, is not guaranteed. First, the terrestrial carbon sink has the highest uncertainty in the global carbon budget (Figure 1.3). Global ter-

restrial carbon fluxes cannot be measured directly. Therefore, reported terrestrial carbon fluxes, such as shown in Figure 1.3, generally rely on dynamic global vegetation models (DGVMs). However, estimated terrestrial carbon fluxes from DGVMs vary widely and deviate (with a positive bias) from independent constraints based on satellite observations (Randerson et al., 2025) or atmospheric O_2 measurements (Friedlingstein et al., 2025). Secondly, vegetation functioning is sensitive to climate change, which can undermine the future persistence of the terrestrial carbon sink. For instance, the net terrestrial carbon flux can decrease due to enhanced tree mortality following climate-induced disturbances (e.g., droughts, wildfires, and pest outbreaks) (Anderegg et al., 2020; Xiao et al., 2021; Seidl et al., 2017), or due to higher autotrophic respiration rates (Re_a) with increased heat stress (Von Buttlar et al., 2018; Duffy et al., 2021). The uncertainty on the magnitude and variability of the terrestrial carbon sink highlights the need for comprehensive observational data. A better understanding of global vegetation dynamics is crucial for informing climate policies and mitigation strategies. Within this context, this thesis contributes to the EU's Horizon 2020 Land Use Based Mitigation for Resilient Climate Pathways (LANDMARC) project, which aims to enhance the understanding of the carbon uptake capacity of LMTs by constructing robust monitoring tools.

1.2 Monitoring vegetation dynamics

Measuring photosynthesis beyond the scale of individual leaves is limited and complex. Eddy covariance (EC) flux tower measurements are widely recognised as the standard method to quantify CO_2 exchange between vegetation and the atmosphere at the ecosystem level. These EC systems measure turbulent CO_2 fluxes by the covariance of fluctuations in wind velocity and CO_2 concentrations (Liang and Wang, 2020; Moene and van Dam, 2014). The spatial representation of the EC measurements spans around 1000 m, depending on wind and height above the canopy. Flux towers provide detailed insight into subdaily variability of ecosystem carbon fluxes, including NEP, GPP, and Re, which are typically aggregated at 30- or 60-minute intervals (Lasslop et al., 2010; Aubinet et al., 1999). Continuous records of flux towers revolutionised our understanding of vegetation dynamics across temporal scales, from diurnal to decadal. Today, observations from hundreds of sites across various biomes are integrated and standardised by regional networks, such as OzFlux (Beringer et al., 2016), used in this work in Chapter 4, or the global FLUXNET network (Baldocchi et al., 2001). Figure 1.4 illustrates the spatial distribution of FLUXNET towers, with the inset showing GPP time series over the Tumbarumba site in Australia. While flux towers provide direct constraints on terrestrial carbon fluxes, they cannot provide a complete global view of ecosystem fluxes due to the sparse and uneven spatial distribution of towers. Satellite remote sensing complements the sparse coverage of flux towers by offering continuous global observations.

1.2.1 Satellite monitoring of vegetation

Since the 1990s, rapid developments in earth observation have expanded a diverse toolbox for monitoring vegetation from space, including light detection and ranging (LiDAR), radar systems, and passive optical sensors, each offering new and complementary insights into ecosystem functioning (Schimel et al., 2019). Space-based LiDAR reveal insights into the complex vertical

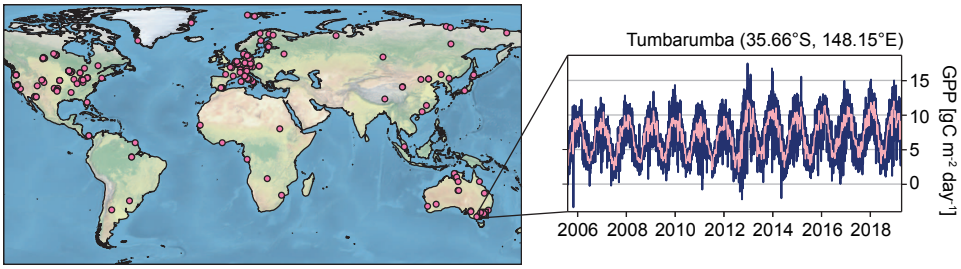


Figure 1.4: Global distribution of over 200 sites contributing to the FLUXNET2015 dataset. Observation periods vary from months to +20 years. Locations were extracted from `https://fluxnet.org`. The inset shows estimated GPP over time from the Tumbarumba Wet Eucalypt SuperSite for a subset of the more than 20-year record (Stol and Kitchen, 2022), which are also used in Chapter 4. The navy blue lines indicate GPP averaged per day, and the pink lines indicate daily GPP averaged per week.

canopy structure, canopy height, and growth dynamics (e.g., Guo et al., 2021b; Tang et al., 2019). Microwave remote sensing, such as radar, can be used to obtain insights on above-ground biomass and water content (e.g., Hu et al., 2024). Radar is insensitive to light and cloud conditions and can therefore continuously track changes in biomass, for instance, disturbances such as deforestation (Joshi et al., 2015). Observations from optical sensors can indicate photosynthetic activity and, thus, carbon uptake, and are particularly valuable due to their generally frequent and global coverage. These optical measurements are widely used to track vegetation dynamics and to upscale eddy covariance measurements using statistical or machine-learning methods, for example, the global FluxSat GPP product (Joiner et al., 2018), used in Chapters 2 to 4 (e.g., Badgley et al., 2017; Ashok et al., 2021; Joiner et al., 2018). Since this thesis centres on global vegetation activity monitoring, the remainder of this section will focus on optical remote sensing.

Principles of optical remote sensing for vegetation monitoring

Optical spectrometers measure the backscattered radiance spectrum across wavelengths. This detected signal represents the portion of solar radiation that, after interaction with the surface, is reflected and scattered back to the sensor. Interactions between sunlight and vegetation create a distinct spectral signature in backscatter radiance, which holds information on vegetation status. These interactions involve the absorption and scattering of light, which are shaped by chemical and structural traits of vegetation, such as chlorophyll and water content, cell arrangement, leaf orientation, canopy structure, and the underlying soil (Ollinger, 2011; Myneni et al., 1995). For vegetation monitoring, reflectance is typically used, which is derived by relating the backscattered radiance to the incoming solar irradiance spectrum. Vegetation reflectance spectra mainly cover three spectral regions: the visible (VIS, 400–750 nm), near-infrared (NIR, 750–1300 nm), and shortwave infrared (SWIR, 1300–2500 nm), with each carrying specific information about vegetation.

Chlorophyll molecules in leaves absorb light strongly between 400 and 700 nm in the visible range, also referred to as photosynthetically active radiation (PAR), which provides energy for

photosynthesis. Light absorption is higher in the blue and red regions than in the green region, making vegetation appear green (Govender et al., 2009). Beyond the red, in the NIR, reflectance is high due to strong scattering by the leaves and canopy and limited to no absorption. The red-edge, or transition zone, marks a substantial increase in reflectance by leaves over absorption. Leaf water content affects solar radiation through scattering and absorption, resulting in distinct absorption features in the SWIR region (Ollinger, 2011). Variations in these reflectance features can mirror changes in biochemical and morphological traits, both of which regulate photosynthetic function (Xue and Su, 2017). Figure 1.5 illustrates how changing vegetation properties impacts the vegetation reflectance. For example, increasing chlorophyll content further reduces the reflectance in the VIS, and higher water content deepens absorption features in the SWIR.

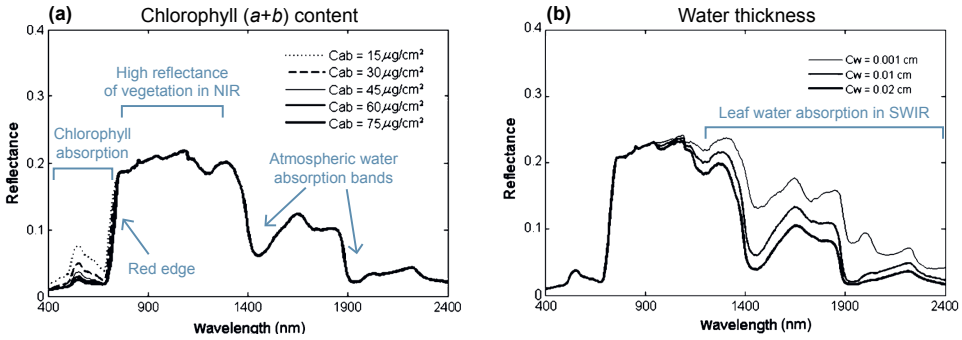


Figure 1.5: Effects of varying vegetation properties (a) chlorophyll content, and (b) water thickness on spectral reflectance simulated by the PROFLAIR model. Here, Cab, and Cw represent the total chlorophyll $a+b$ concentration and the mass of liquid water per unit leaf area, respectively. The annotations in blue indicate major spectral features within the vegetation reflectance. Figure adapted from Omari et al. (2013).

Reflectance-based vegetation proxies

Spectral vegetation reflectance is compressed into vegetation indices (VIs) by combining specific spectral regions to extract vegetation properties (Govender et al., 2009; Xue and Su, 2017). Over the past decades, numerous VIs have been developed, including the Normalised Difference Vegetation Index (NDVI) (Rouse et al., 1974), the Enhanced Vegetation Index (EVI) (Huete et al., 2002), and the more recently developed, Near-Infrared Reflectance of Vegetation (NIRv) (Badgley et al., 2017). Water-content-sensitive VIs, like the Normalised Difference Water Index (NDWI) (Gao, 1996), are widely used for drought monitoring and use the SWIR bands (Gu et al., 2007; Amalo et al., 2018). Table 1.1 summarises their simple equations and spectral band usages. Their simplicity enabled broad application across broadband sensors, such as MODIS, AVHRR, and Landsat, with global coverage at resolutions ranging from 100 m to 1 km, and long-term archives spanning up to three decades (Wen et al., 2023; Robinson et al., 2017).

Each of these VIs reflects different aspects of vegetation properties. NDVI and EVI are often

Table 1.1: Summary of the names, acronyms, equations, and represented proxies of widely used reflectance-based vegetation indices (VIs) for vegetation monitoring. The VIs use combinations of spectral regions, specifically the near-infrared R_{red}, near-infrared R_{NIR}, and the shortwave-infrared R_{SWIR}. Within the EVI equation, variables G, C1, C2, and L reflect the scaling constant, two coefficients of aerosol resistance, and a canopy background adjustment term, respectively (Huete et al., 2002).

Name	Acronym	Equation	Proxy
Normalised difference vegetation index	NDVI	$\frac{R_{NIR}-R_{red}}{R_{NIR}+R_{red}}$	Greenness of vegetation, photosynthetic capacity
Enhanced vegetation index	EVI	$\frac{G\times(R_{NIR}-R_{red})}{R_{NIR}+C1\times R_{red}-C2\times R_{blue}+L}$	Greenness of vegetation, photosynthetic capacity
Near-infrared reflectance of vegetation	NIRv	$NDVI\times R_{NIR}$	Absorbed PAR, photosynthetic activity related to canopy structure
Normalised difference water index	NDWI	$\frac{R_{NIR}-R_{SWIR}}{R_{NIR}-R_{SWIR}}$	Vegetation water content

referred to as greenness indices, due to their use of the spectral contrast between strong chlorophyll absorption in the red (R_{red}) and scattering in the NIR region, making them sensitive to leaf area and chlorophyll concentration, and indirectly linked to photosynthesis. NDVI is extensively used and is considered the most popular VI for vegetation monitoring (Huang et al., 2021; Xue and Su, 2017). Applications of NDVI include the monitoring of long-term vegetation dynamics (Pang et al., 2017; Zhang et al., 2013), land-use change (Usman et al., 2015), droughts (Nanzad et al., 2019; Wang et al., 2010), and crop productivity (Pan et al., 2015; Seo et al., 2019; Huang et al., 2014). Compared to NDVI, EVI includes the blue band, as well as several correction coefficients to mitigate the influence of soil and atmosphere, and to reduce saturation in high-biomass regions (Huete et al., 2002). Therefore, EVI has been shown to capture seasonal dynamics in productive and dense ecosystems more accurately than NDVI (Huete et al., 2002; Lara et al., 2018).

NIRv is defined as the product of NDVI and NIR reflectance, thereby isolating the vegetated-attribution of the NIR reflectance (Badgley et al., 2017). Studies demonstrated NIRv to strongly correlate with eddy-covariance flux tower GPP estimates and to accurately capture the seasonality across biomes (Wu et al., 2020; Wang et al., 2021; Badgley et al., 2019). Moreover, NIRv often outperforms traditional greenness indices NDVI and EVI in capturing vegetation responses and phenology (Wang et al., 2022c; Zhang et al., 2022a; Wang et al., 2024). The physical basis for the relation between NIRv and photosynthesis lies in its sensitivity to the canopy and leaf structure. Plants adjust their structural architecture to align absorbed sunlight with the photosynthetic capacity; this canopy-optimisation is likely represented in NIRv data products (Badgley et al., 2017).

Aside from VIs, widely used reflectance-based vegetation proxies include estimates of the fraction of absorbed photosynthetically active radiation (fAPAR) and leaf area index (LAI). Both vegetation properties are recognised as Essential Climate Variables (ECVs) by the Global Climate Observing System (GCOS) (GCOS, 2016). fAPAR represents the fraction of incoming solar radiation reaching the top of the canopy available for absorption, while LAI is a measure of total live green leaf (one-sided) area per unit ground surface. Both proxies are generally retrieved by inverting radiation transfer models, although they can also be retrieved empirically (Mota et al., 2021; Tao et al., 2016). LAI and fAPAR are widely used to monitor vegetation phenology and long-term vegetation trends (Duveiller et al., 2013; Brandt et al., 2014; Song et al., 2020).

While reflectance-based vegetation products have proven valuable as a proxy for GPP, particularly NIRv, they do not directly track GPP. Although linking to vegetation functioning by capturing morphological and biochemical traits, these products do not reflect physiological characteristics (e.g., photosynthetic efficiency). As a result, they can show lags in vegetation response when structural and biochemical changes do not coincide with physiological downregulation (Walther et al., 2016; Wang et al., 2022c). In addition, reflectance-based products remain sensitive to background contamination from soil or snow (Pierrat et al., 2022), and tend to saturate with increasing biomass (van der Meer et al., 2001). This underscores the need for a signal that more directly relates to photosynthesis.

Solar-induced fluorescence as direct vegetation proxy

Solar-induced fluorescence (SIF) observations offer promising and unique opportunities to track vegetation activity directly (Joiner et al., 2011; Frankenberg et al., 2011a; Mohammed et al., 2019). SIF is a faint light signal (650–850 nm) emitted as a by-product of photosynthesis. Unlike reflectance-based vegetation proxies, SIF is intrinsically linked to photosynthetic activity and reflects physiological dynamics (Frankenberg and Berry, 2018). Developments of the past 15 years have enabled the retrieval of SIF from space-based hyperspectral optical sensors (e.g., GOSAT, GOME-2, and TROPOMI). These sensors offer higher spectral sampling than broadband sensors (commonly used for reflectance-based vegetation proxies), which is needed to extract the subtle spectral features of SIF from vegetation reflectance. This thesis focuses on SIF retrieval from GOME-2 (Chapters 2, 3, and 5) and TROPOMI (Chapter 5), as well as their use for vegetation monitoring (Chapter 4). Before examining the SIF retrieval and its use to monitor vegetation activity, we first need to understand the physical process behind this signal: chlorophyll *a* fluorescence.

1.3 Chlorophyll *a* fluorescence: a direct proxy of photosynthesis

Plants naturally fluoresce when illuminated by photosynthetically active radiation (PAR, within the 400–700 nm range). Fluorescence represents the re-emission of a small portion of absorbed light by chlorophyll *a* at longer wavelengths (650–850 nm) due to the Stokes shift in the excited chlorophyll *a* molecules (Bittner et al., 1994; Sun et al., 2023). The chlorophyll *a* fluorescence exhibits two distinct peaks at around 680 nm and 740 nm, corresponding to the red and far-red spectral regions, respectively. Figure 1.6 shows the light absorbance of chlorophyll molecules as

well as the typical chlorophyll *a* fluorescence spectrum. For convenience, we will henceforth refer to chlorophyll *a* fluorescence simply as "fluorescence".

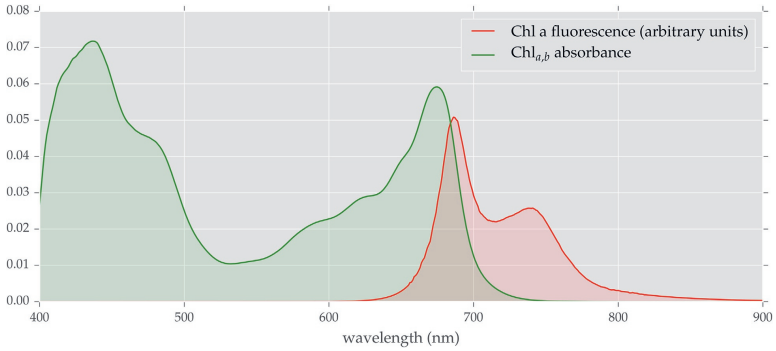


Figure 1.6: Absorbance spectrum of chlorophyll *a* and *b* (in green), and a typical fluorescence spectrum as re-emitted by chlorophyll *a* molecules, both in arbitrary units. The first, and highest, chlorophyll *a* fluorescence peak is referred to as the red-peak, and the second peak as the far-red peak. Figure from Frankenberg and Berry (2018).

The antenna complexes of the Photosystems absorb light, which raises the electronically excited states of the chlorophyll. Unavoidably, plants re-emit a small fraction of the absorbed photons as fluorescence (typically $< 5\,\%$), reflecting the imperfect efficiency of the photosystems (Porcar-Castell et al., 2014; van der Tol et al., 2014; Frankenberg and Berry, 2018). Under ideal conditions, 90 % or more of the energy is transferred to the reaction centres and converted into chemical energy (Kalaji et al., 2017; Fleming et al., 2012). This process, known as photochemical quenching (PQ), fuels the dark reactions of photosynthesis, during which atmospheric carbon is assimilated. Because fluorescence and PQ compete for the same energy, changes in photosynthetic efficiency are reflected in the fluorescence signal.

Traditionally, plant fluorescence has been measured using active fluorometry techniques. These fluorescence measurements substantially enhanced the understanding of vegetation activity. More recently, passive techniques, including satellite-based, enable the observation of fluorescence. When the fluorescence signal results from solar illumination, it is referred to as solar-induced fluorescence (SIF). SIF observations are generally obtained at the canopy level, whereas active fluorometry is observed at the leaf level. When fluorescence is measured at the canopy level, its spectral features differ slightly from those at the photosystem or leaf level.

Figure 1.7 shows how various processes affect the spectral distribution of SIF from emission to observation by the sensor. Some fluorescence photons are immediately reabsorbed by chlorophyll molecules, especially in the red region, where chlorophyll absorbs strongly. Scattering effects further modify the photon's propagation; not all fluorescence ultimately escapes the canopy. The red peak ($\sim$685 nm) is reduced relative to the far-red peak ($\sim$740 nm), resulting in a more dominant far-red peak at the canopy level (Fournier et al., 2012; Porcar-Castell et al., 2021). During its path through the atmosphere, the fluorescence signal is further attenuated by interaction with aerosols, and molecular absorption, mainly by oxygen (O_2) and water vapour

(H_2O) (Frankenberg and Berry, 2018; van Schaik et al., 2020). These interactions leave distinct gas-specific spectral absorption features, which are noted as dents in the light pink spectrum on the right of Figure 1.7.

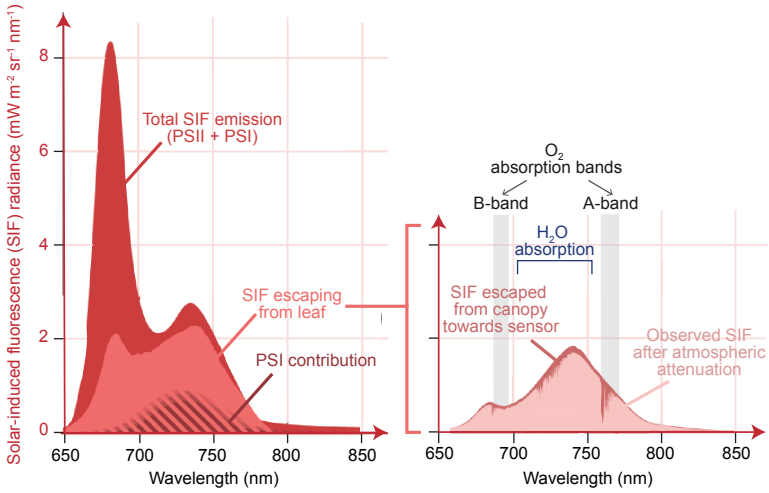


Figure 1.7: Spectral properties of the overall solar-induced fluorescence signal as observed across photosystem-, leaf-, and canopy-scale. The change in magnitude and structure of the signal over scales is due to reabsorption by chlorophyll molecules, scattering effects, and atmospheric attenuation. Figure adapted from Porcar-Castell et al. (2021).

1.4 Remote sensing of solar-induced fluorescence

Remote sensing of solar-induced fluorescence (SIF) presents new opportunities to study photosynthesis across various scales, ranging from leaf to canopy to global scales (Gamon et al., 1990; Rascher et al., 2009; Frankenberg et al., 2011b; Joiner et al., 2011). SIF can now be retrieved from towers (Pacheco-Labrador et al., 2019), aircrafts (Siegmann et al., 2019), and satellites (e.g., Khosravi et al., 2015; Joiner et al., 2013; Doughty et al., 2022; Köhler et al., 2018). This section focuses on SIF retrieved from satellite-based sensors, with a brief reference to tower- and airborne-based SIF observations for context.

Retrieving SIF from satellite-based instruments depends on its sensor specifications. In the past 15 years, SIF retrieval has proven feasible from several hyperspectral spectrometers designed for atmospheric composition retrievals (e.g., Guanter et al., 2012; Sanders et al., 2016; Köhler et al., 2018; Noël et al., 2024). Their high spectral resolution and (partial) overlap with fluorescence emissions enable the use of fine absorption features in the solar spectrum (e.g., Fraunhofer lines, discussed subsequently) to extract SIF signals from vegetation reflectance. ESA's upcoming Fluorescence Explorer (FLEX) mission, launch expected in 2026, will be the first instrument explicitly dedicated to SIF (Davidson et al., 2003; Moreno et al., 2016).

Table 1.2 summarises the main specifications of satellite sensors from which SIF has or can

be retrieved. The diversity in instrument specifications and mission timing is complementary, providing continuity and spatial and temporal detail in SIF, aspects that we examine in Chapters 3 and 5. Differences in sensor specifications, such as spectral resolution and coverage, influence the choice of retrieval methodology, which we further discuss in Sections 1.4.1 and 1.4.2.

Table 1.2: Instrument specifications of launched or scheduled sensors with the technical feasibility to retrieve SIF. The spectral specifications and spatial resolutions reported refer to the specific bands from which SIF can be retrieved. Sensor or satellite names are listed according to the most common usage in the literature. TEMPO provides continuous daytime observations from geostationary orbit over North America, rather than along a polar-orbiting swath.

Sensor/Satellite	Spectral coverage [nm]	Spectral resolution [nm]	Spatial resolution [km]	Swath [km]	Overpass time (local)	Period
SCIAMACHY	604–805 nm	0.48	30 × 60	960	10:00	2002–2012
GOSAT	758–775	0.025	10.5	N/A	13:00	From 2009
GOME-2A	593–790	0.48	40 × 80, 40×40*	1920, 960*	09:30	2006–2022
GOME-2B	593–791	0.50	40 × 80	1920	09:30	From 2012
GOME-2C	592–791	0.50	40 × 80	1920	09:30	From 2019
OCO-2	757–775	0.042	1.3 × 2.25	10	13:30	From 2014
OCO-3	757–771	0.042	1.6 × 2.2	10	13:30	From 2019
TROPOMI	665–785	0.37	3.5 × 7.5, 3.5×5.5**	2600	13:30	From 2017
TEMPO	540–740	0.6	2 × 4.75	N/A	N/A	From 2023
CO2M	747–773	0.12	2 × 2	240	11:30	2026*
TanSat-2	672–702, 747–777	0.12	2 × 2	2900	13:30	2026⋆
FLEX	500–780 nm	0.1◇, 0.5–2.0	0.3 × 0.3	150	10:00	2026⋆

* From 15 July 2013, ** From 2019, ⋆ Expected launch

◇ Resolution within O_2 bands (686–697 nm, 759–769 nm)

1.4.1 Retrieval principles

As explained in Section 1.2, the optical remote sensing instruments measure the backscatter radiation across wavelengths. This signal represents the solar radiation $E_0(\lambda)$ (in W m^{-2} nm^{-1}) that has travelled through the atmosphere, interacted with the surface, and returned towards the sensor. In the presence of vegetation, the measured radiance $I(\lambda)$ (in W m^{-2} nm^{-1} sr^{-1}) contains both the reflected signal $A_s(\lambda)$ and an additive signal of SIF $I_F(\lambda)$ (in W m^{-2} nm^{-1} sr^{-1}) emitted

by chlorophyll across the canopy. The measured radiance can be expressed as:

$$I(\lambda) = \frac{E_0(\lambda)\mu_0 A_s(\lambda)T^{\uparrow}(\lambda)T^{\downarrow}(\lambda)}{\pi} + I_F(\lambda)T^{\uparrow}(\lambda) \tag{1.4}$$

where μ_0 represents the cosine of the solar zenith angle, and $T(\lambda)$ denotes the upward ($\uparrow$) or downward ($\downarrow$) atmospheric transmission. Atmospheric transmission involves changes in light spectra as it travels through the atmosphere, caused by scattering and absorption by air molecules, aerosols and clouds. Key absorbers include H_2O and O_2, as discussed previously (Figure 1.7).

In practice, SIF retrieval is framed as an inverse problem in which a parameterised form of Equation (1.4) is fitted to the observed radiances. For satellite-based SIF retrievals, the fitting is typically based on reflectance spectra, obtained by normalising the measured radiance by the solar irradiance. The challenge in SIF retrieval is to separate the additive SIF term ($I_F(\lambda)$) from the reflectance signal. Over water, this is relatively straightforward. The strong NIR absorption by water generates a low-reflectance background against which the aquatic SIF signal from phytoplankton is relatively high and stands out (Köhler et al., 2020). Over land, however, separating the terrestrial SIF signal is more challenging due to much higher and variable surface reflectance (Meroni et al., 2009; Frankenberg and Berry, 2018). Terrestrial SIF represents only around 1–2 % of the measured reflectance signal, highlighting the sensitivity required for SIF retrieval.

To facilitate this careful separation, SIF retrievals exploit the relative infilling of narrow absorption features in the spectrum by the spectrally smooth SIF. Specifically, it uses absorption features caused by gases within the Sun's photosphere, known as solar Fraunhofer lines, or by oxygen (O_2) within the Earth's atmosphere, namely the telluric O_2 A-band and O_2 B-band. Figure 1.8a shows that numerous Fraunhofer lines are distributed across the fluorescence spectrum, while the O_2 B-band (∼690 nm) and O_2 A-band (∼760 nm) are located near the red and far-red SIF peak, respectively. As illustrated in Figure 1.8b, the fractional depth of these absorption features decreases when SIF is present, resulting in an enhanced apparent reflectance over the feature. This effect forms the foundation for the SIF retrieval.

The telluric O_2 bands are deeper and wider than the Fraunhofer lines, providing a stronger SIF signal and therefore widely used in ground-, tower-, or aircraft-based SIF retrievals (van der Tol et al., 2023; Meroni et al., 2009). However, accurate retrieval within these bands requires compensation for strong atmospheric effects (Sabater et al., 2018; Mohammed et al., 2019). For example, oxygen abundance depends on pressure, meaning that variations in surface elevation affect the depth of O_2 absorption features (Sabater et al., 2021). These complications are particularly pronounced for satellite-based observations due to the long optical path through the atmosphere. van Schaik et al. (2020) demonstrates that far-red SIF sensitivity is roughly halved when retrieved from the O_2 A-band compared to retrieval outside this region. Sensitivity to SIF was found to be largest when bands with strong O_2 or H_2O (< 740 nm) absorption are avoided. Fraunhofer lines are largely unaffected by these atmospheric effects and are therefore more robust, enabling a simpler retrieval. For this reason, all current satellite-based SIF retrievals make use of Fraunhofer lines (e.g., Sun et al., 2018; Köhler et al., 2018, 2015; van Schaik et al., 2020), including the work in this thesis.

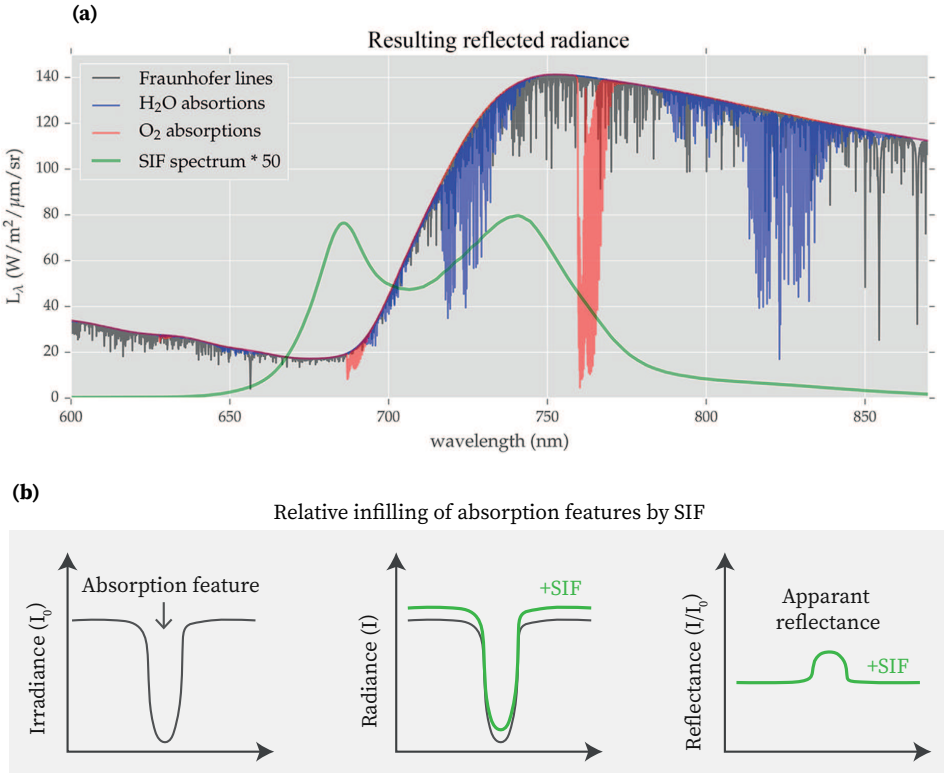


Figure 1.8: (a) Reflected radiance spectrum showing Fraunhofer lines, H_2O and O_2 features, and the chlorophyll fluorescence emission (scaled $\times 50$). (b) Conceptual illustration of the relative infilling of absorption features by SIF. Panel (a) from Frankenberg and Berry (2018), panel (b) inspired by the conceptual structure of Porcar-Castell et al. (2021).

Finally, the SIF retrieval models the components of the reflected radiance (Equation (1.4)). We can distinguish this modelling into (i) physically-based and (ii) data-driven or empirical fitting approaches (Guanter et al., 2021). Physically based models use a physical formulation of radiative transfer. This type of retrieval is used, for instance, to retrieve SIF from sensors with higher spectral resolution (< 0.2 nm), such as GOSAT (0.025 nm) and OCO-2 (0.042 nm). The fine spectral resolution of these sensors enables the use of micro-windows over isolated Fraunhofer features, limiting interference of atmospheric effects (Parazoo et al., 2019; Frankenberg et al., 2012; Sun et al., 2018). Sensors with coarser spectral resolutions ($\sim$0.5 nm), such as GOME-2 and TROPOMI used in this work, need wider windows to retrieve SIF. These wider retrieval windows increase sensitivity to atmospheric effects. Without detailed knowledge of atmospheric inputs, the use of full-physics retrievals is constrained. Therefore, retrievals from such sensors generally rely on data-driven approaches.

Data-driven approaches assume that the reflectance spectra can be represented as a linear combination of spectral basis functions plus SIF (Köhler et al., 2015, 2018, 2020; Joiner et al., 2013; van Schaik et al., 2020). These functions are statistically derived using singular value decomposition (SVD) or principal component analysis (PCA) and obtained from vegetation-free spectra to capture atmospheric transmission without SIF. The baseline albedo is typically modelled with a low-order polynomial. The PCA approach will also be used in this thesis (Chapters 2, 3, and 5). More recently, SIF retrievals using machine learning (ML) approaches have been explored, extending the data-driven approaches (Pato et al., 2025). These ML approaches use training datasets to learn non-linear statistical relationships between spectral features and SIF.

In practice, the choice of retrieval approach thus depends on the spectral information provided by the sensor and the complexity of separating fluorescence from reflectance over the specific window (e.g., Parazoo et al., 2019; Joiner et al., 2016; van der Tol et al., 2023; Morata et al., 2025). SIF is typically retrieved over a narrow spectral window covering part of the red or far-red peak. Most satellite sensors retrieve SIF only over the far-red peak due to limited spectral coverage (e.g., GOSAT, OCO-2, and OCO-3). Furthermore, uncertainties in SIF retrieval are substantially higher over the red peak (discussed subsequently). Each stage of the retrieval chain is affected by limitations and uncertainties arising from instrumental, atmospheric, and methodological factors. These sources of uncertainty are discussed in the next section.

1.4.2 Retrieval challenges

First, instrument-related uncertainties arise from sensor hardware, calibration, and long-term stability issues. Radiometric calibration errors can introduce small but systematic biases into measured radiances. In Fourier Transform Spectrometer instruments, such as GOSAT, signal non-linearity causes false infilling and deepening of solar Fraunhofer lines (Frankenberg et al., 2011b,a; Oshio et al., 2019). These effects are known as zero-level offsets and are clearly noted over barren areas where SIF is expected to be zero. Similar effects have been reported for grating spectrometers such as GOME-2, OCO-2, and SCIAMACHY, and are likely linked to various calibration issues (e.g., Sun et al., 2018; Joiner et al., 2012; van Schaik et al., 2020). Additionally, degradation of radiometric sensitivity can affect reflectance stability over time, as reported for several instruments, including GOME, GOME-2, and SCIAMACHY (Tilstra et al., 2012a,b). Such reflectance degradation affects the SIF retrieval. If left uncorrected, this instrumental artefact causes false declining trends in SIF time series (Koren et al., 2018; van Schaik et al., 2020). This sensor degradation is addressed in this thesis (specifically in Chapter 2).

Second, atmospheric absorption complicates SIF retrieval, particularly when the spectral windows overlap with strong H_2O or O_2 absorption features (van Schaik et al., 2020). As the fluorescence signal is substantially smaller than the reflectance, even minor errors in the modelling of atmospheric transmittance can distort the retrieved SIF. Retrievals from the red SIF peak are especially challenging. The red SIF signals are substantially smaller than far-red peaks ($\sim$6 times; Figure 1.7; Köhler et al., 2020). Furthermore, the peak is located in a more complex spectral region. Solar Fraunhofer lines are narrower and less deep near 680 nm (red peak) than near 740 nm (far-red peak) (Figure 1.8). In addition, O_2 absorption features overlap large

sections of the red peak (Figure 1.8; Joiner et al., 2016). Even in field and tower installations, where the path between the target and sensor is on the order of meters, the atmospheric effects were found to affect retrievals significantly (Sabater et al., 2018; van der Tol et al., 2023). The atmospheric absorption (mainly from H_2O) will be accounted for in this thesis, we discuss the approach in Chapters 3 and 5.

Finally, retrievals must balance the inclusion of enough Fraunhofer lines to ensure a sufficient signal-to-noise ratio while avoiding wavelengths affected by strong atmospheric absorption from O_2 or H_2O (van Schaik et al., 2020; Parazoo et al., 2019). Uncertainties also arise from settings in applied retrieval techniques. For instance, SIF retrieved from data-driven approaches using SVD or PCA are sensitive to the number of vectors or PCs used (van Schaik et al., 2020; Köhler et al., 2015). The use of too many PCs can, for example, lead to overfitting of the linear regression. Chapters 3 and 5 evaluate how retrieval choices affect SIF retrievals from GOME-2 and TROPOMI.

1.4.3 Applications of SIF

The rapid development of satellite-based SIF retrievals of the past 15 years has attracted considerable interest across fields, including ecology, hydrology, and biogeosciences (e.g., Green et al., 2019; Zhang et al., 2025; Liu et al., 2025). Satellite-based SIF retrievals offer a unique direct link to photosynthesis at a global scale. Consequently, applications of SIF centre around tracking photosynthetic activity, and thus GPP. Several studies found strong, often linear, relationships between satellite-based SIF and GPP across biomes (e.g., Verma et al., 2017; Mengistu et al., 2021). These empirical SIF–GPP relationships accelerated the widespread application of SIF for quantifying GPP at local, regional, and global scales. Additionally, SIF is increasingly assimilated into models to optimise photosynthetic parameters and constrain GPP estimates (MacBean et al., 2018; Bacour et al., 2019). For example, within the CORSO (CO2MVS Research on Supplementary Observations) project, TROPOMI SIF observations are assimilated into the European Centre for Medium-Range Weather Forecasts (ECMWF) Integrated Forecast System to better constrain land carbon fluxes (Garrigues et al., 2024).

A key advantage of SIF over traditional vegetation proxies (e.g., NDVI and EVI) lies in its ability to capture physiological changes in vegetation (Zhang et al., 2023a, 2022a). This mechanistic benefit of SIF enables robust monitoring of seasonality and phenology across biomes (Joiner et al., 2014; Wen et al., 2025; Magney et al., 2019). For example, Figure 1.9 shows the seasonal variability over an evergreen forest as captured by SIF, GPP, NDVI, and APAR. While NDVI and APAR show nearly flat lines over time, SIF clearly follows the strong seasonal pattern in GPP. Seasonal dynamics in evergreen systems are primarily regulated by changes in photosynthetic efficiency rather than by structural or biochemical factors (e.g., chlorophyll content) (Walther et al., 2016). Hence, the development of satellite-based SIF accelerated the potential to study these systems across spatial scales (Walther et al., 2016; Magney et al., 2019; Pierrat et al., 2022).

Another manifestation of SIF's mechanistic advantage is its demonstrated sensitivity to environmental stress and disturbances. Therefore, SIF is widely used to detect and quantify anomalies related to heat stress (Song et al., 2018; Wang et al., 2019b), droughts (Chen et al., 2021a; Li

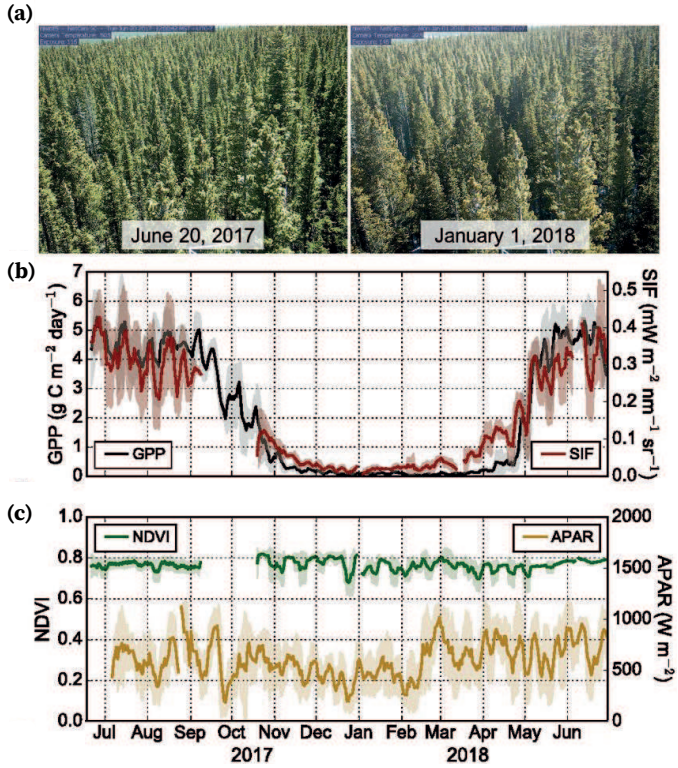


Figure 1.9: Seasonal dynamics of (b) GPP, far-red SIF, and (c) NDVI and APAR over an evergreen forest in Colorado. Seasonal variations in structural characteristics and chlorophyll content (or "greenness") are limited (a). SIF observations are tower-based and retrieved from the PhotoSpec instrument. Figure adapted from Magney et al. (2019).

et al., 2023; Wang et al., 2019b; Zhang et al., 2023d), floods (Turner et al., 2021; Yin et al., 2020), and wildfires (Guo et al., 2021a). Additionally, results from Ač et al. (2015) indicate that shifts in the ratio of far- to far-red SIF can relate to nitrogen deficiency. The strength of SIF in immediately reflecting changes in vegetation functioning has motivated its application in crop monitoring and yield estimation for agricultural purposes (e.g., Peng et al., 2020; Guan et al., 2016; Sloat et al., 2021). Furthermore, studies applied SIF to monitor vegetation dynamics with respect to land management or land-use changes. For example, Gerlein-Safdi et al. (2020) used GOME-2 SIF to assess the impact of various large-scale reforestation techniques in China.

The examples of SIF applications demonstrate the potential of satellite-based SIF retrievals to enhance our understanding of global vegetation dynamics. Robust observations supporting verification of photosynthetic carbon uptake are fundamental to reduce uncertainties in the land's carbon uptake term and informing climate mitigation strategies. In this thesis, Chapter 4, we evaluate how SIF can be used to quantify the efficiency of land mitigation techniques

(e.g., reforestation). To reach the full potential of SIF applications, consistent climate records are needed. Such long-term records can provide insights into vegetation response to climate variability. Hence, one of the aims in this thesis is to construct a consistent SIF climate record from the GOME-2 series (Chapters 2, 3, and 5).

1.5 Thesis Overview

The motivation of this thesis consists of two parts, with one facilitating the other. The first centres on how and to what extent satellite-based SIF observations can serve as a robust monitoring tool for vegetation dynamics. In particular, this thesis examines the application of SIF to quantify vegetation responses to identifiable interventions (i.e., natural disturbances or changes in land management). This ambition is part of the LANDMARC project, which aimed to develop monitoring tools to quantify LMT impact. In line with the project's timing and requirements, my research began with this application-driven focus. One essential finding of this work, published in a peer-reviewed paper in 2024 (Chapter 4), was that the then-available GOME-2A SIF (SIFTER v2) dataset exhibited temporal inconsistencies driven by instrumental artefacts. Such temporal instability hinders robust vegetation monitoring if not accounted for. This finding motivated the second focus of this thesis: improving the consistency of the GOME-2A SIF retrievals.

For SIF to perform the monitoring role effectively, records must be consistent across space and time. Data consistency is needed to confidently attribute observed changes to the underlying drivers, such as land-use change, rather than to instrumental or retrieval artefacts. In addition, building a long-term climate record is essential to advance the monitoring capabilities of SIF. Extended SIF data can capture interannual to decadal variability and long-term effects (e.g., driven by climate variability). The GOME-2 series, consisting of the sequential satellite sensors GOME-2A, GOME-2B, and GOME-2C, offers the potential to construct a decadal-scale SIF record. Hence, EUMETSAT's Atmospheric Composition Satellite Application Facility (AC SAF) aims to construct a coherent, consistent, long-term SIF record from the GOME-2 series. The development of such a harmonised GOME-2 climate record forms the second motivation of this thesis.

Chapters 2 and 3 focus on retrieving robust SIF records from sensors in the GOME-2 series, which offer long individual records spanning over ten years. Here, we build on the heritage of the Solar-Induced Fluorescence of Terrestrial Ecosystems Retrieval (SIFTER) algorithm (Sanders et al., 2016; van Schaik et al., 2020), initially developed for GOME-2A retrieval. Chapter 2 improves the SIFTER algorithm to enhance spatial and temporal consistency by addressing instrumental artefacts (e.g., reflectance degradation). The resulting SIFTER v3 algorithm is demonstrated by the retrieval of a consistent GOME-2A SIF record, spanning from 2007 to 2017. In Chapter 2 we address the following research question:

> How can the SIFTER algorithm be improved to retrieve a temporally and spatially consistent SIF record from GOME-2A observations?

Chapter 3 extends this work to GOME-2B and obtains a harmonised and consistent SIF record

that combines GOME-2A and GOME-2B, together spanning from 2007 to 2023. This chapter demonstrates how intersensor biases can be detected and corrected to enable a long-term record. In Chapter 3 we address the following research question:

> How can SIF retrievals from GOME-2A and GOME-2B be harmonised to construct a consistent multi-sensor SIF record, and how can their differences be interpreted?

In Chapter 4, we shift the focus from SIF retrieval to the application of SIF as a monitoring tool. Within the LANDMARC project, we evaluate the feasibility of using the then-available satellite-based SIF, in combination with other satellite and in-situ data, to monitor the impact of land mitigation techniques on regional carbon uptake. Using then-available SIF observations from GOME-2A (SIFTER v2) and TROPOMI (Caltech product), two contrasting case studies are analysed: abrupt forest loss following wildfire in Australia, and gradual forest regrowth in northern China. These example cases demonstrate how SIF can be used to detect and interpret changes in vegetation carbon uptake in response to disturbance and management. In Chapter 4 we adress the following research question:

> How can satellite-based SIF observations be used to quantify vegetation response to land-based disturbances and interventions?

Finally, Chapter 5 synthesises the results, reflects on the broader implications of this work, and presents my recent work on extending the SIFTER v3 algorithm to the GOME-2C and TROPOMI sensors. In Chapter 5 we address the following research question:

> How can insights gained from the GOME-2 SIF retrieval help extend the SIFTER v3 algorithm to TROPOMI?

Chapter 2

Improved consistency in SIF retrievals from GOME-2A with the SIFTER v3 algorithm

This chapter is based on:

Anema, J. C. S., Boersma, K. F., Tilstra, L. G., Tuinder, O. N. E., and Verstraeten, W. W. (2025b). Improved consistency in solar-induced fluorescence retrievals from GOME-2A with the SIFTER v3 algorithm. *Atmospheric Measurement Techniques*, 18(8):1961–1979

Abstract

Space-based observations of solar-induced fluorescence (SIF) provide valuable insights into vegetation activity over time. The GOME-2A instrument, in particular, facilitates SIF retrievals with extensive global coverage and a record extending over 10 years. SIF retrievals, however, are sensitive to calibration issues, and instrument degradation complicates the construction of temporally consistent SIF records. This study introduces the improved Sun-Induced Fluorescence of Terrestrial Ecosystems Retrieval (SIFTER) v3 algorithm, designed to obtain a more accurate and reliable long-term SIF record from GOME-2A for the 2007–2017 period, building upon the previous SIFTER v2. The SIFTER v3 algorithm uses newly reprocessed level-1b Release 3 (R3) data, which provide a more homogenous record of the reflectances by eliminating spurious trends from changes in level-0 to level-1 processing. This improved consistency supports detailed analysis and correction of the reflectance degradation across the SIF retrieval window (734–758 nm). To address the reflectance degradation accurately, SIFTER v3 incorporates an advanced in-flight degradation correction that accounts for time, wavelength, and scan angle dependencies throughout the entire record. Additionally, algorithm revisions have consistently reduced the retrieval residuals by around 10 % and reduced sensitivity to water vapour absorption by better capturing the atmospheric and instrumental effects. A revised latitude bias adjustment resolves unrealistic values of GOME-2A SIF over desert areas. The SIFTER v3 dataset demonstrates improved robustness and consistency, both spatially and temporally, throughout the 2007–2017 record, and aligns closely with NASA GOME-2A SIF data and independent GPP measurements from the global FluxSat and FLUXCOM-X products.

2.1 Introduction

During the process of photosynthesis, vegetation emits part of the absorbed light as fluorescence. The integrated signal of this phenomenon across the canopy is known as solar-induced fluorescence (SIF). Observations of SIF provide direct measurements of photosynthetic activity and offer critical insights into terrestrial vegetation dynamics. Recent advancements in SIF retrieval from satellite measurements have facilitated continuous global monitoring of photosynthetic activity. This includes the retrieval from spectrometer instruments, such as SCIAMACHY (Khosravi et al., 2015; Köhler et al., 2015), GOSAT (Frankenberg et al., 2011a; Joiner et al., 2011; Guanter et al., 2012), OCO-2 (Sun et al., 2018), OCO-3 (Doughty et al., 2022), GOME-2 (Joiner et al., 2013; van Schaik et al., 2020), TROPOMI (Köhler et al., 2018; Guanter et al., 2021); and soon, the FLEX mission (Vicent et al., 2016). With up to nearly daily global coverage, satellite-based SIF has emerged as a powerful tool for capturing vegetation dynamics across various biomes (e.g., Smith et al., 2018a; Gerlein-Safdi et al., 2020; Mengistu et al., 2021). Furthermore, SIF has been shown to outperform traditional reflectance-based vegetation indices in consistently tracking the impact of disturbances on photosynthetic carbon uptake, or gross primary productivity (GPP) (e.g., Magney et al., 2019; Wang et al., 2019a; Turner et al., 2021; Qiu et al., 2022).

SIF observations from the long-running GOME-2 instruments are particularly important for their potential to eventually construct a climate record spanning up to over 20 years. The first of the three instruments, GOME-2A, was launched on board Metop-A in late 2006. SIF retrieval from GOME-2 is serendipitous and stems from the spectral overlap of the instrument with the fluorescence range, enabling retrieval of SIF from the red (∼690 nm) and far-red (∼740 nm) fluorescence peaks (Köhler et al., 2015; Joiner et al., 2016; van Schaik et al., 2020). The additive signal emitted as SIF leads to enhanced total upwelling, which can be detected as an infilling of Fraunhofer absorption lines present in the incoming sunlight. The spectral resolution of the GOME-2 instrument, approximately 0.5 nm (shown in Table 1.2 in Chapter 1), allows for a technique that matches modelled and observed reflectance across a spectrum covering multiple Fraunhofer lines (Joiner et al., 2013; Köhler et al., 2015; van Schaik et al., 2020). SIF retrieved from GOME-2 is widely used to analyse interannual variations in vegetation growth (e.g., Koren et al., 2018; Gerlein-Safdi et al., 2020; Chen et al., 2021b; Fancourt et al., 2022; Qiu et al., 2022). We use GOME-2A SIF (SIFTER v2) for vegetation monitoring in Chapter 4. However, care should be taken to mitigate the issue that instrumental features can cause false spatial and temporal trends, impacting the consistency of the product (Parazoo et al., 2019).

Reflectances from GOME-2 instruments are subject to significant instrument degradation. The degradation trends exhibit strong wavelength and even scan angle dependencies over time (Tilstra et al., 2012a; EUMETSAT, 2022), similar to those found in its predecessor GOME (Coldewey-Egbers et al., 2008) and SCIAMACHY (Tilstra et al., 2012b). SIF is sensitive to these effects of instrument degradation, which cause false temporal trends (Gerlein-Safdi et al., 2020; van Schaik et al., 2020; Wang et al., 2022b; Zou et al., 2024). To address these issues, van Schaik et al. (2020) implemented a seasonal wavelength-dependent degradation correction to the level-1 reflectance data prior to the GOME-2A SIF retrieval. Although this approach enhanced the consistency of the Sun-Induced Fluorescence of Terrestrial Ecosystems Retrieval (SIFTER)

v2 product (van Schaik et al., 2020), persistent unrealistic trends in SIF, indicating degradation, remain (as we show in Chapter 4). Moreover, globally averaged SIF values from the SIFTER v2 product show large interannual fluctuations that do not align with other SIF or vegetation products (Wang et al., 2022b; Zou et al., 2024), further suggesting ongoing inconsistency in the previous product, especially in the later years of the GOME-2A data record.

This study aims to improve the SIF retrieval algorithm and enhance the consistency of the GOME-2A SIF long-running record, spanning from 2007 to 2017. To achieve this, we use the new reprocessed GOME-2 level-1b dataset, Release 3 (R3), which ensures consistent processing and auxiliary data throughout the record. R3's homogenous nature supports the development of degradation coefficients that accurately reflect the characteristics of degradation trends in GOME-2A reflectances. We implement an advanced daily in-flight degradation correction that corrects for significant time, wavelength and scan angle dependencies identified in the level-1b reflectance data, following the methodology of Tilstra et al. (2012b,a). This correction is applied to the level-1b R3 reflectances across 2007–2017, which then serve as input for the SIF retrieval. Additionally, we introduce improvements in the retrieval algorithm that address atmospheric effects and incorporate enhanced understanding of the instrument's behaviour. Finally, we evaluate the consistency over time of our new SIFTER v3 dataset with SIFTER v2, the previous algorithm version, alongside independent GPP data from the FluxSat and FLUXCOM-X products.

2.2 GOME-2 instrument

GOME-2 is a spectrometer that measures the earthshine radiance and solar irradiance over the wavelength range 240–790 nm in four main spectral channels. Operating with a whiskbroom scanning scheme, it uses a scan mirror to perform measurements in a nadir orbit swath with a default width of 1920 km, which allows global coverage in 1.5 days (Munro et al., 2016). For most of its orbit, the instrument scans from east to west and measures 24 forward pixels with a resolution of 80×40 km^2 (across $\times$ along track), followed by 8 larger back-scan pixels with a resolution of 240×40 km^2 for the main spectral channel data. At least once per day, GOME-2 switches to Sun mode for calibration purposes and measures the solar spectrum.

The instrument is part of the payload of the Metop satellite series (Metop-A, Metop-B, and Metop-C) that fly in a Sun-synchronous orbit with equatorial crossing at 09:30 local solar time in the descending node. GOME-2A was the first instrument to be launched, on board the Metop-A satellite, on 6 November 2006, followed by GOME-2B and GOME-2C on 17 September 2012 and 7 November 2018, respectively. The main science objective of GOME-2 is to continuously monitor ozone column densities and other atmospheric trace gases like NO_2, BrO, OCIO, HCHO, SO_2, and H_2O, over a long period of time (Munro et al., 2006). Additionally, the instrument specifics enable retrieval of SIF from the near-infrared channel, which spans from 593 to 791 nm, overlapping with the far-red fluorescence peak at 740 nm (Joiner et al., 2016; Sanders et al., 2016; van Schaik et al., 2020). This channel, band 4, has a spectral resolution of $\sim$0.5 nm (full width at half maximum) and a spectral sampling interval of $\sim$0.2 nm. In this chapter, we focus on the SIF retrieval from the GOME-2A instrument.

Since 15 July 2013, GOME-2A has operated with a reduced swath width of 960 km, resulting in ground pixels of radiance and irradiance observations measuring 40×40 km^2. This reduction changed the instrument's viewing geometry, from [−53.8°, +53.8°] (before) to [−33.6°, +33.6°] (after), requiring GOME-2A data collected before and after 15 July 2013, to be treated as if recorded by two different sensors. From its early life, GOME-2A has experienced transmission loss or radiometric degradation that shows scan angle and wavelength dependencies (EUMETSAT, 2009; Dikty and Richter, 2011; Tilstra et al., 2012a). Likely sources of the degradation have been identified as contamination on the scan mirror, along with other factors such as thin layer deposits on the detectors and degradation of the diffuser plate (Munro et al., 2016; EUMETSAT, 2022). The build-up contamination on the exposed scan mirror was expected based on the experience with predecessor GOME (Coldewey-Egbers et al., 2008). Although the source of the contaminant is unidentified, outgassing of the satellite itself is a suspected cause (Krijger et al., 2014; Hassinen et al., 2016).

To ultimately correct for the effects of instrument degradation, it is crucial to understand all drivers of the varying degradation rate. EUMETSAT performed two throughput tests in January and September 2009 to understand and act on the throughput loss. These tests, especially the second one, significantly reduced the throughput and resulted in deceleration of the degradation over time (EUMETSAT, 2022). Furthermore, they altered the scan angle dependencies of the degradation. The different degradation trends of Earth radiance and solar irradiance paths affect GOME-2A's reflectance, which represents the ratio between the two, with observed scan angle dependencies across UV and NIR ranges (Tilstra et al., 2012a). We will further discuss the characteristics of the reflectance degradation in the NIR range in Section 2.3 of this chapter. The reflectance degradation impacts the retrieval of various level-2 products, including the absorbing aerosol index (Tilstra et al., 2012a), ozone profiles (Cai et al., 2012) and SIF (van Schaik et al., 2020).

The long-term consistency of the reflectance measurements is affected not only by changes at instrument level, such as degradation, but also by variations in raw data processing to level-1b data (EUMETSAT, 2022). The level-1b data contain calibrated Earth radiance and solar irradiance measurements, as well as auxiliary information such as geolocation and cloud parameters. Processor-related variation in the level-1b data can introduce spurious trends and complicate data coherence over time, which is crucial for climate monitoring studies. Inconsistent processing over time raised concerns in previous SIF retrievals from GOME-2A, given the retrieval's sensitivity to small changes in level-1b data (van Schaik et al., 2020). To address this issue, EUMETSAT has recently reprocessed the GOME-2A level-1b dataset using the level-0 to level-1b operational processor version 6.3.3 across the entire 2007–2018 period. By eliminating processor-version-related changes in the dataset, a more homogenous dataset is achieved, facilitating the evaluation and construction of soft calibration corrections to mitigate long-term degradation of the instrument (EUMETSAT, 2022).

Figure 2.1 shows the time series of monthly averaged reflectance (at 740 nm) over the Sahara between 2007 and 2017. Although GOME-2A was in operation till 2021, we omit data beyond January 2018 due to the loss of orbit control for Metop-A, resulting in a satellite drift and constrained solar visibility of GOME-2A. The reflectance data are presented for two data sets:

(i) the reprocessed level-1b data using processor version 6.3.3 and (ii) the previous level-1b data used in SIFTER v2, which encompasses three processor versions (5.3, 6.0, and 6.1) over time. We will use the reprocessed R3 level-1b data to retrieve GOME-2A SIF.

The difference in reflectance magnitude between both datasets is small and diminishes progressively with newer processor versions in the previous level-1b dataset, as seen from Figure 2.1. Thus, the differences between successive processor versions become smaller, indicating that the data processed with v5.3 differs more from R3 data than data processed with v6.1. Overall, this suggests improved temporal consistency in reflectance due to the reprocessing. Furthermore, both datasets show similar tendencies with noted downward trends in the later period after 2014 and a strong jump after the change of the swath width in July 2013. The downward trend is the result of instrument degradation, while the jump is caused by the change in viewing zenith angles after the swath reduction, leading to decreased reflectance due to the bidirectional reflectance distribution function (BRDF) of the Earth's surface (Tilstra et al., 2021). The impact of BRDF on the retrieved SIF will be discussed in Chapter 3.

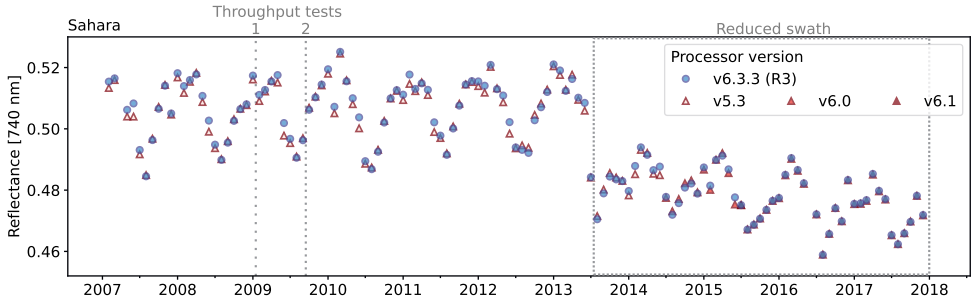


Figure 2.1: Monthly averaged reflectance measured by GOME-2A at 740 nm over the Sahara region (16–30° N, 8° W–29° E) as a function of time. Reflectances ($R(\lambda)$) are obtained by: $(\pi I(\lambda))/(I_0(\lambda)\cos(\theta_0))$, where $I(\lambda)$ is the radiance, $I_0(\lambda)$ the solar irradiance and θ_0 the solar zenith angle. Reflectances obtained from the re-processed R3 level-1b data have processor version 6.3.3 and are shown in blue bullets. Reflectances of the previous level-1b data set consists of different processor versions (v5.3, v6.0, and v6.1) and are shown in triangles with different hues of red. The reflectances from both level-1b datasets were co-sampled, and both data had to meet the criteria of cloud fraction < 0.4. Data of days that are listed as outliers, including measurements in a narrow swath, are excluded from both datasets. Events that impact the reflectance are indicated by grey dashed lines.

2.3 In-flight degradation correction

In this section, we describe a method to analyse and address the scan angle and wavelength dependency of degradation trends observed in the near-infrared GOME-2A reflectances. Adapted from the method used to correct for reflectance degradation in SCIAMACHY and GOME-2A for absorbing aerosol index (AAI) retrieval (Tilstra et al., 2012b,a), our in-flight degradation correction method examines daily global mean reflectance over time (t, per day), scan angle position (s) and wavelength (λ).

This more advanced approach improves upon the degradation correction used in SIFTER v2 (van Schaik et al., 2020), which relied on a wavelength-dependent seasonal factor with the 2007–2012 reflectance average as baseline. Furthermore, the correction was only applied to reflectances from June 2014 onward (see Table 2.2). In contrast, our method applies a continuous daily correction factor across the entire 2007–2017 record that addresses the early degradation patterns and the varying trends of degradation over time (e.g., before and after the throughput tests). Moreover, we include a scan angle dependency in the degradation correction. Findings from Tilstra et al. (2012a) and EUMETSAT (2022), which identified scan angle dependencies in GOME-2 reflectance – particularly in shorter wavelengths and in eastward-looking directions – prompted the inclusion.

We analysed the global mean reflectances at each measured wavelength between 712 and 785 nm (in total 356 detector pixels), covering the SIF retrieval window (734–758 nm) and the spectral bands used to calculate the scene albedo (van Schaik et al., 2020). Valid reflectances of GOME-2A ($R_{\lambda,s}$) are collected between 60° S and 60° N, with solar zenith angles smaller than 85°, and averaged daily. Observations containing Sun glint or cloudy conditions are not filtered out, but days corresponding to narrow swath and nadir static measurements are excluded from the analysis. For GOME-2A, the scan position parameter s runs from 1 (eastward) to 24 (westward), considering only forward pixels. The daily global reflectance at 747.1 nm for the most eastward ($s = 1$), centre ($s = 12$), and westward ($s = 24$) pixels from 2007 to 2012 is shown in Figure 2.2.

We modelled the variation in daily global mean reflectance ($R^*_{\lambda,s}$) using a Fourier series ($F^q_{\lambda,s}$), representing the seasonal variation, multiplied by a polynomial term ($P^p_{\lambda,s}$) to account for instrument degradation over time:

$$R^*_{\lambda,s}(t) = P^p_{\lambda,s}(t)[1 + F^q_{\lambda,s}(t)] \tag{2.1}$$

Here, p denotes the degree of polynomial $P_{\lambda,s}$, and q represents the order of the finite Fourier series $F_{\lambda,s}$. $P_{\lambda,s}$ is written as:

$$P^p_{\lambda,s}(t) = \sum_{m=0}^{p} u^m_{\lambda,s} t^m \tag{2.2}$$

and $F^q_{\lambda,s}$ defined as:

$$F^q_{\lambda,s}(t) = \sum_{n=1}^{q} [v^n_{\lambda,s} \cos(2\pi \mathrm{nt}) + w^n_{\lambda,s} \sin(2\pi n t)] \tag{2.3}$$

The implicit assumption is that the global averaged reflectance shows no long-term trends. Therefore, the observed trends captured by the polynomial are attributed to instrumental effects.

We analysed $R^*_{\lambda,s}$ separately for the period before and after the reduced swath on 15 July 2013. Equation (2.1) is fitted to reflectances collected (i) between January 2007 and December 2012 and (ii) between January 2007 and December 2017. In the latter fit, reflectances between 2007 and 15 July 2013, were first interpolated to match the scan angles covered by the reduced swath. Each fit covers complete years to prevent biases from seasonal variation. Here, we set $p = 2$ for the 2007–2012 fit and $p = 3$ for the 2007–2017 fit. These higher-order polynomial

degrees offer the flexibility to capture the varying behaviour of the instrument degradation over time (discussed in Section 2.2). In both fits, $q = 6$ was used for the order of the Fourier series. Table 2.1 summarises the characteristics of the 2007–2012 and 2007–2017 fits. These fits are shown in Figures 2.2 and S1.2, respectively.

The resulting 2007–2012 fits of $R^*_{\lambda,s}$ for the most eastern ($s = 1$), centre ($s = 12$), and western ($s = 24$) scan indices are shown as solid black lines in Figure 2.2. These fits accurately follow the temporal pattern of the global reflectance, with correlations of 0.99, 0.99, and 0.98, respectively, for the scan indices 1, 12, and 24. The dashed lines represent the fitted polynomial component $P^p_{\lambda,s}$, illustrating the degradation effect over time. A gradually increasing trend is noted in the 747.1 nm reflectance, particularly at the most eastward position ($s = 1$). This increase in reflectance results from the stronger decrease in measured solar irradiance (the *denominator* in R) than in measured radiance (the *numerator* in R). Furthermore, a slight reduction in increase is noted around 2010, possibly the result of the second throughput test in September 2009 (Figure 2.1) (Munro et al., 2016; EUMETSAT, 2022).

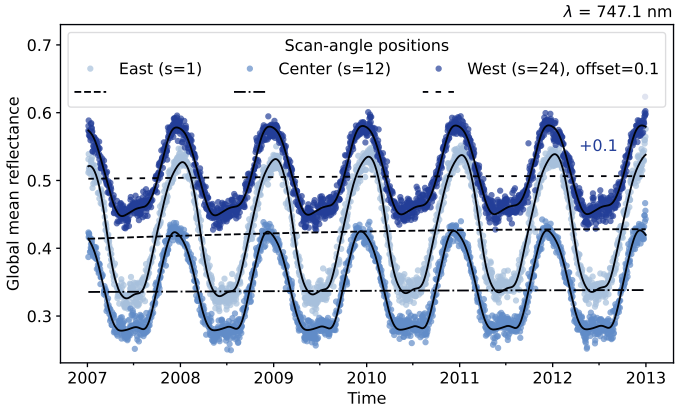


Figure 2.2: Global mean daily reflectance at 747.1 nm from GOME-2A over time, between 2007 and 2012, for the most eastward ($s = 0$), centre ($s = 12$), and most westward ($s = 24$) scan angle positions. Differences in magnitude and amplitude of the plotted reflectance time series are caused by the angular dependences of cloud and surface reflection. To separate the time series graphically, an offset of 0.1 was added only to the reflectances of the most westward scan angle position ($s = 24$) (denoted in dark blue). The solid black lines show the fitted daily global reflectance $R^*_{\lambda,s}$ and the dashed black lines illustrate the effect of instrument degradation, as described in the main text.

Finally, the correction for instrument degradation is obtained by scaling the polynomial value at each day to its value at the reference date (t_0):

$$c_{\lambda,s}(t) = P^p_{\lambda,s}(t_0)/P^p_{\lambda,s}(t) \tag{2.4}$$

The reference date for both fits, 2007–2012 and 2007–2017, is 5 January 2007. We use the polynomial from the 2007–2012 fit to derive the correction factors for January 2007 to mid July 2013, and that of the 2007–2017 fit for mid-July 2013 to December 2017 (Table 2.1). We multiply

Table 2.1: Summary of the characteristics for the fitted global mean GOME-2A reflectance over 2007–2012 and 2007–2017. Collected reflectances have latitudes between 60° S and 60° N and solar zenith angles < 85°. The scan angles reflect the instrumental mirror angle, with ranges around −45.5° to +45.4° for the 1920-km swath, and around −28.3° to +28.3° for the reduced 960-km swath (post-15 July 2013). Fitting parameters p and q represent the polynomial degree of $P_{\lambda,s}$ and the order of the finite Fourier series $F_{\lambda,s}$ in Equation (2.1). The derived correction factors are applied to reflectances at 712–785 nm and scan index 1–24 to the specified application periods.

Fit period	Scan angles	Fit parameters		Application period
		p	q	
4 Jan. 2007–31 Dec. 2012	−45.4° to +45.4°	2	6	4 Jan. 2007–5 July 2013
4 Jan. 2007 – 31 Dec. 2017	−28.3° to +28.3°	3	6	16 July 2013–31 Dec. 2017

these wavelength and scan-angle-dependent corrections by the level-1b reflectances to correct for the degradation trends.

Figure 2.3 shows the averaged correction factor at 747.1 nm, broken down per year and scan angle, for the observations (a) before and (b) after the swath reduction. In both periods, the variation in correction factors across scan angle positions is of the same order as the variation over time, reaching up to 5 %. This indicates the significance of a scan-angle-dependent degradation correction. From 2007 to 2014 the annual averaged correction factors at 747.1 nm are below 1, meaning the reflectances were higher than the baseline in January 2007. From 2015, the correction factor for most scan indices exceeds 1 and then gradually increases further to correct for the decreasing reflectances over time.

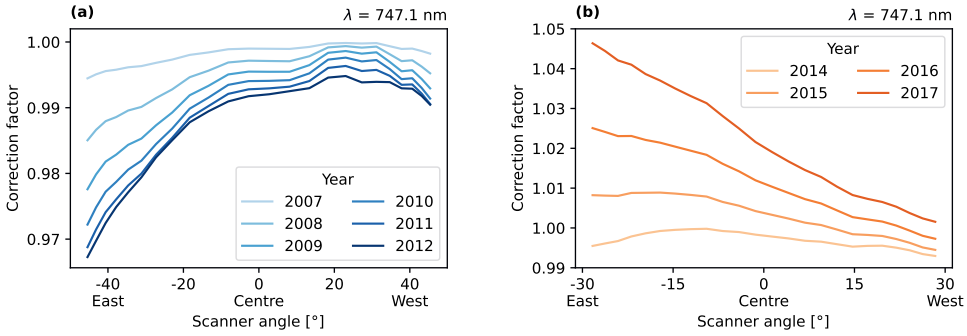


Figure 2.3: Reflectance degradation correction factors for GOME-2A at wavelength 747.1 nm, averaged annually across the 24 scan angle positions. Panels (a) and (b) show the obtained corrections over the periods before and after the swath reduction at the 15$^{\text{th}}$ of July 2013, respectively. Only full-year averages are shown, so 2013 is omitted due to the mid-year swath reduction.

The gradual shifts in the correction factors over time are also visible in Figure 2.4, which displays the factors over time and wavelength across the retrieval window range (734–758 nm) at scan angle −28.3° ($s = 1$ for post-swath reduction period). The correction factors reflect the gradual

increase of the reflectance from 2007, followed by a tipping point around 2011–2012 for most wavelengths, ultimately falling below the baseline of January 2007. This transition from lowering ($c < 1$) to increasing corrections ($c > 1$) occurs around 2014–2015, with this shift occurring earlier at shorter wavelengths.

Our analysis shows strong variations in reflectance over time, with increases around 2007–2012 followed by decreases from around 2014. These variations arise from the changing rates of throughput loss in both the Earth and solar paths, where the relative rates of throughput loss in these paths determine the observed fluctuations in reflectance. Overall, the impact of instrument degradation on the measured GOME-2 reflectance in the NIR shows a parabolic pattern with time, a stronger effect in the eastward scan positions, and a decrease with increasing wavelengths.

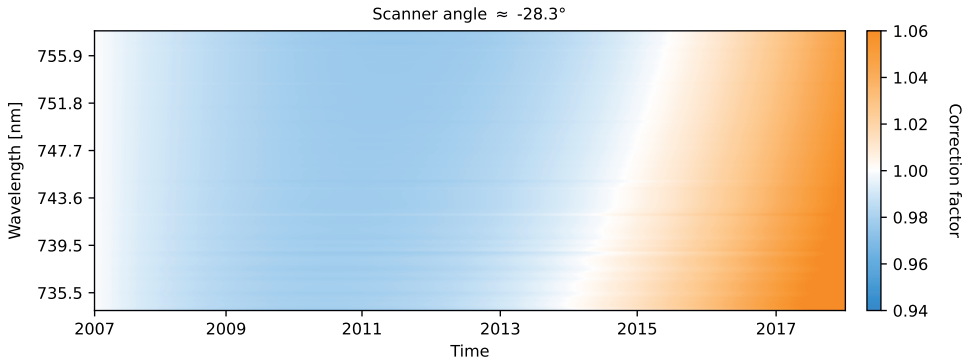


Figure 2.4: Temporal evolution of the degradation correction factors for each wavelength within the SIF retrieval window (734–758 nm, $n = 118$) at scan angle −28.3°, representing the easternmost scan position, $s = 1$, in the reduced-swath mode (similar to $s = 7$ in the 1920-km swath). The shown correction factors are derived from the 2007–2017 reflectance fits for GOME-2A SIF.

2.4 SIFTER v3 retrieval algorithm

2.4.1 SIFTER retrieval algorithm

The SIFTER retrieval algorithm relies upon the relative infilling of solar Fraunhofer absorption lines in the radiance spectra by the far-red SIF (peak at ∼740 nm) – an approach pioneered by Joiner et al. (2011), Frankenberg et al. (2011a), and Guanter et al. (2012) for SIF retrieval from space. To detect the infilling of the narrow Fraunhofer lines from GOME-2A, with a spectral resolution of 0.5 nm, a spectral window covering multiple deep Fraunhofer lines is needed (Parazoo et al., 2019). From version 2 onwards, the SIFTER algorithm has used a relatively narrow retrieval window of 734–758 nm to limit complications by absorption signatures from water vapour and the O_2 A-band (van Schaik et al., 2020). The key of the retrieval is to separate the contributions of surface-emitted SIF from those of direct reflection to the overall reflectance. This is done by matching a modelled spectrum to the measured reflectance. Using a Lambertian

model, the reflectance (R) can be written as:

$$R(\lambda,\mu,\mu_0) \approx a_s(\lambda)T^{\downarrow}(\lambda,\mu_0)T^{\uparrow}(\lambda,\mu) + \frac{\pi I_{\mathrm{SIF}}(\lambda)}{E_0(\lambda)\mu_0}T^{\uparrow}(\lambda,\mu) \tag{2.5}$$

where μ and μ_0 are the cosines of the viewing and solar zenith angles, respectively. The atmospheric molecular scattering in the near-infrared region is neglected (e.g., Joiner et al., 2013). In Equation (2.5), a_{s} is the surface albedo; $T^{\uparrow}$ and $T^{\downarrow}$ are the upward and downwelling atmospheric transmission factors, respectively; I_{SIF} is the SIF emission at the Earth's vegetated surface; and E_0 is the solar irradiance. The SIFTER algorithm uses a fourth-order polynomial to describe the spectral surface albedo a_{s}. The atmospheric transmittance ($T^{\uparrow}$, $T^{\downarrow}$) is described by 10 principal components (PCs) that are obtained over non-vegetative areas.

The 10 basic functions describing the atmospheric transmittance are obtained in three main steps. First, a large ensemble of reflectance spectra without cloud coverage (cloud fraction < 0.4) is collected over a non-vegetative reference area to represent the transmittance for a wide variety of conditions where I_{SIF} equals zero. The Sahara region (16–30° N, 8° W–29° E) is used as the reference area, and spectra are collected over the January 2007 to December 2012 period. Secondly, the contribution of the surface albedo to the spectra is eliminated by subtracting a second-order polynomial function obtained over spectral regions with negligible atmospheric absorption over no cloud conditions (described in more detail in van Schaik et al. (2020)). Finally, using the widely used iterative principal component analysis NIPALS (Nonlinear Iterative Partial Least Squares) (Esbensen et al., 2002), the first 10 principal component spectral functions ($f_{\mathrm{k}}(\lambda)$) are retrieved that explain the variance within the spectra. Note that for the retrieval of data after the swath reduction in July 2013, PCs are obtained from spectra with viewing zenith angles $< 35°$ to match the observations in reduced swath.

Following the preparatory step of obtaining the 10 PCs, the SIFTER algorithm proceeds to fit a model to each individual reflectance spectrum by minimising the differences between the observed and modelled reflectance spectra using a Levenberg-Marquardt least-squares regression (van Schaik et al., 2020). The modeled spectra (R_m), follows on Equation (2.5) and is written as

$$R_m(\lambda,\mu,\mu_0) \approx (\sum_{j=0}^{n} a_j\lambda^j)e^{-\sum_{k=1}^{m} b_k f_k(\lambda)} + \frac{\pi c I_{\mathrm{SIF}}(\lambda)}{\mu_0\overline{E_0}}e^{-\frac{\mu^{-1}}{\mu^{-1}+\mu_0^{-1}}\sum_{k=1}^{m} b_k f_k(\lambda)} \tag{2.6}$$

Here a_j represent the fitting coefficients of the surface albedo, b_k is the coefficients that match the set of the 10 PCs, $f_k(\lambda)$ describes the atmospheric transmission contribution to R, and c is the fit coefficient for I_{SIF} that characterises the strength of the fluorescence signal. In total there are 16 fitting coefficients: 5 from a_j, 10 from b_k, and 1 from c. In Equation (2.6), the solar irradiance, $\overline{E_0}(\lambda)$, is taken to be the solar irradiance reference spectrum from Chance and Kurucz (2010) convolved with the GOME-2A slit function and scaled to the Earth-Sun distance. The solar irradiance reference spectrum is used in the model to mitigate the influence of instrument degradation on the observed solar irradiance (Sanders et al., 2016).

2.4.2 Processing and improvements of SIFTER v3 retrieval

The GOME-2A SIFTER v3 product presented here is an implementation of the general approach described in Section 2.4.1 and of three proposed revisions with respect to SIFTER v2,

including the in-flight degradation correction described in Section 2.3. For the SIF retrieval process, EUMETSAT's reprocessed level-1b R3 data were used as input. The daily degradation correction factors were applied to stabilise the R3 reflectances over the entire 2007–2017 record. These degradation-corrected reflectances were then used to extract the 10 Principal Components (PCs) that describe the atmospheric transmission, and to retrieve SIF. Figure S1.1 shows a flowchart of the processing algorithm. In this section, we will discuss the proposed algorithm changes, listed in Table 2.2.

Table 2.2: Overview of the implemented changes, ordered by importance for the fit retrieval, in the SIFTER algorithm by this study: a comparison between SIFTER v3 and SIFTER v2 (van Schaik et al., 2020). The changes are placed in order of largest impact on the fit retrieval. Changes (1) and (2) are expected to significantly affect the fit quality of the retrieval, whereas alteration (3) is expected to mainly impact the consistency of SIF over time and across scan angles.

	Subject of change	SIFTER v2	SIFTER v3
1	Scaling method of level-1 reflectance reference spectra prior to PCA	Variance scaling	Standard deviation scaling
2	Interpolation across slit functions for convolution with reference solar spectrum	Fully sampled pixels ($n = 10$)	Both fully and not fully sampled pixels ($n = 765$)
3	Degradation correction	In-flight degradation correction	In-flight degradation correction
	• Time step	• Seasonally	• Daily
	• Scan angle dependent	• No	• Yes
	• Baseline	• 2007–2012	• January 5, 2007
	• Application period	• From June 2014	• 2007–2017

The first change concerns the pre-treatment of the reflectance reference spectra prior to the principal component analysis. In SIFTER v2, the collected level-1 reflectance spectra over the reference area (Sahara) underwent mean centring and scaling by the variance across wavelengths before conducting the principal component analysis (PCA). Our study explores an alternative "autoscaling method" that combines mean centring with scaling by the standard deviation, which ensures equal importance across the variables (van den Berg et al., 2006). Figure S1.4 demonstrates that the use of standard deviation scaling on the mean-centred spectra results to a more distinct pattern with tighter magnitude variations across the wavelengths as compared to variance scaling. This autoscaling approach outperforms the SIFTER v2 pretreatment method, with the 10 PCs explaining 99.95 % of the spectra variance compared to 99.85 %, as shown in Figure 2.5c. More orthogonal PCs are expected to improve the fit by capturing the variation across wavelengths more consistently, leading to a more accurate representation of the atmospheric transmission.

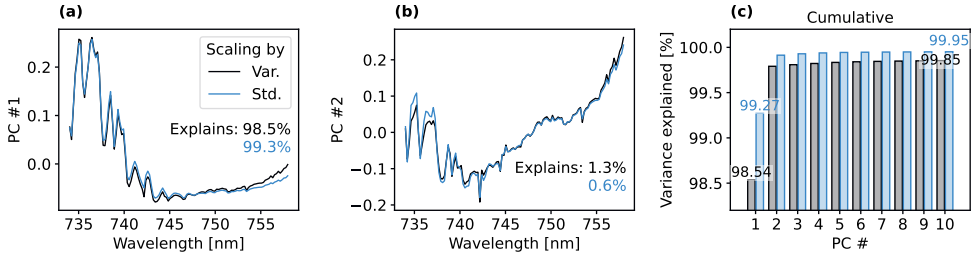


Figure 2.5: The leading principal components, (a) PC 1 and (b) PC 2, of GOME-2A reflectance spectra using scaling by the standard deviation (in black) and the variance (in blue) as pre-treatment method prior to the principal component analysis. Panel (c) shows the cumulative explained variance of PCs 1 to 10 using both pre-treatment scaling methods. The PCs are obtained from collected GOME-2 reflectance spectra over the Sahara between 2007 and 2012.

Next, we discuss the revision of the convolution of the slit function with the solar irradiance reference spectrum. In the SIFTER algorithm, the high-resolution solar irradiance reference spectrum from Chance and Kurucz (2010) is used, convolved with the GOME-2A slit function, and scaled to the Earth-Sun distance (Sanders et al., 2016; van Schaik et al., 2020). We denote this spectrum $\overline{E_0}$. Before this convolution can be done, we interpolate the slit functions across the wavelengths to match the high spectral resolution of the reference spectrum ($\Delta\lambda = 0.01$ nm). We use slit functions in the range of ∼612–770 nm. In SIFTER v2, only the slit functions from fully sampled detector pixels ($n = 10$) are used for the interpolation process, encompassing two spectral points within the retrieval window (Figure S1.6). In this work, we include all slit functions provided in the key data ($n = 765$), consisting of both fully sampled and not fully sampled pixels, which are interpolated by EUMETSAT as described in Siddans et al. (2012). Figures S1.7a–d present the slit functions and their interpolation to the 0.01 nm spectral resolution, following the methods of SIFTER v3 and SIFTER v2, respectively.

Figure 2.6 shows the reference solar spectrum convolved with the slit functions as done in SIFTER v2 and in SIFTER v3 (this work). The solar irradiance spectrum convolved using the expanded slit function dataset follows the fine features of the Fraunhofer absorption lines better, resulting in deeper Fraunhofer lines than the convolved spectrum using only the fully sampled pixels. The solar irradiance reference spectrum $\overline{E_0}$ is applied at two instances in the algorithm retrieval. Firstly, the spectrum is used for high sampling interpolation of the measured solar irradiance spectrum to match the wavelength grid of the radiance measurements for the reflectance calculation. Secondly, the $\overline{E_0}$ spectrum is used in the modeled reflectance, Equation (2.6), replacing the observed solar spectrum E_0, as discussed in Section 2.4.1.

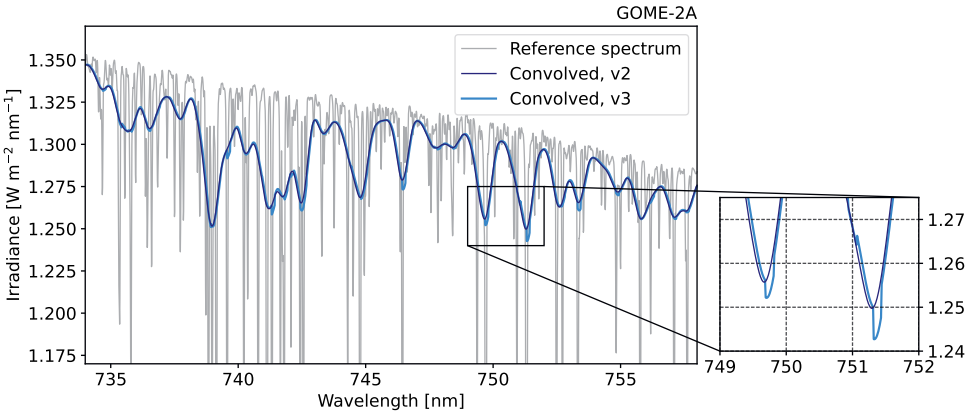


Figure 2.6: The solar irradiance reference spectrum of Chance and Kurucz (2010) convolved with the GOME-2A slit function (in grey), and the Chance and Kurucz (2010) spectrum convolved with the interpolated SIFTER v2 slit function (using fully sampled pixels) (in black), and the interpolated SIFTER v3 slit function (using fully and not fully sampled pixels) (in blue).

To understand the impact of each individual algorithm change, we examine the impact on the retrieved SIF and its fit residuals. Here, the two usages of the changed solar irradiance reference spectrum are seen as two individual changes. Figure 2.7 shows the spectral fit (on the left) and fit residuals (on the right) over a single Congo Basin pixel using the SIFTER v3 algorithm (depicted in blue) and algorithm settings where one of the subjects of change is set to SIFTER v2 (depicted in black dashed lines). The difference between the two fits illustrates the impact of the specific change made in SIFTER v3.

Figure 2.7a shows the spectral fit over a single Congo Basin pixel with PCs obtained when using (i) the variance as scaling factor as in SIFTER v2, and (ii) the standard deviation as a scaling factor. The use of the standard deviation scaling factor results in lower SIF (0.99 mW m^{-2} sr^{-1} nm^{-1}), compared to the variance scaling factor (1.07 mW^{-2} sr^{-1} nm^{-1}). Furthermore, $\mathrm{PC}_{\mathrm{std}}$ resulted in more homogenised and lower fit residual across the spectrum, as seen by the RMSE (Figure 2.7b). Notably, $\mathrm{PC}_{\mathrm{var}}$ had more difficulty to explain the 734–745 nm region of the spectrum (RMSE of 0.089 %), where water absorption features are more prominent, in comparison to the $\mathrm{PC}_{\mathrm{std}}$ (RMSE of 0.069 %) over the same spectral region. The observation of reduced fit residuals when $\mathrm{PC}_{\mathrm{std}}$ are used, specifically over 734–745 nm, holds true across a larger ensemble of pixels (Congo Basin, $n = 644$) as illustrated in Figure S1.5. This confirms that the proposed autoscaling pretreatment method results in PCs that better describe the atmospheric transmission (including the water vapour absorption), resulting in a better fit of the retrievals.

Figure 2.7c presents the fitted reflectance and the fit residual on the single Congo Basin pixel for retrievals with input reflectances that use high sampling interpolation obtained from the solar irradiance reference spectrum $\overline{E_0}$ as in (i) SIFTER v2 ($\mathrm{HSI}_{\mathrm{v2}}$) and in (ii) SIFTER v3 ($\mathrm{HSI}_{\mathrm{v3}}$). The $\mathrm{HSI}_{\mathrm{v3}}$ reflectances resulted in a reduction of SIF by 15 % in comparison to the $\mathrm{HSI}_{\mathrm{v2}}$.

Additionally, employing all key data did result in a slightly better fit as seen from the reduction in fit residuals (Figure 2.7d). This showcases the strong sensitivity of the SIF retrieval algorithm to slight changes in the reflectances.

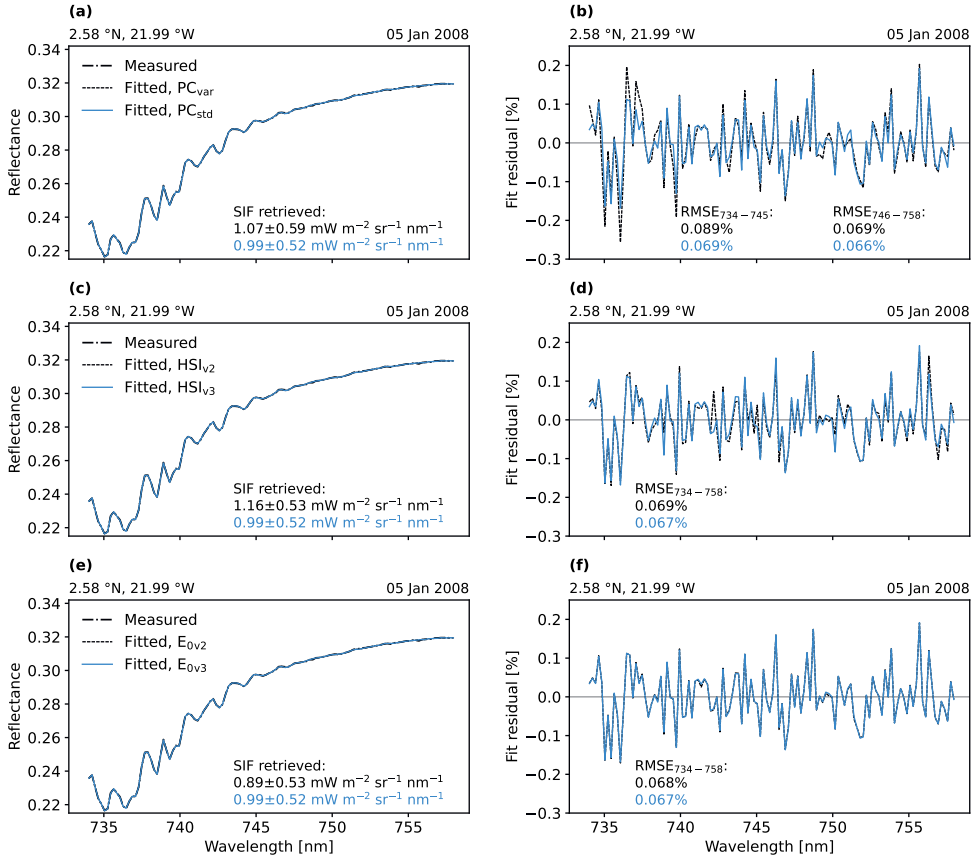


Figure 2.7: SIF retrieval from GOME-2A of a single pixel over the Congo Basin (2.58° N, 21.99° W) on 5 January 2008. The left panels show the observed reflectance and fitted reflectances, and the right panels show the fit's residuals. Plots a,b show the fitted reflectance and its residuals using PCs computed with standard deviation and variance as pretreatment scaling factors, respectively referred to as PC_{std} and PC_{var}. Plots c,d show the fitted reflectance and its residuals for retrievals from reflectances obtained using the SIFTER v3 and SIFTER v2 wavelength calibration, referred to as HSI_{v3} and HSI_{v2} respectively. Plots (e,f) show the fitted reflectance and the fit residuals for retrievals with the SIFTER v3 and SIFTER v2 convolved reference solar spectra as the solar irradiance E_0, referred to as $E_{0,v3}$ and $E_{0,v2}$ respectively. The stated SIF values reflect the values from the retrieval step and are not corrected for the latitude bias.

Figure 2.7e shows the fit results and residuals for the use of $\overline{E_0}$ as obtained in SIFTER v2, $\overline{E_{0,v2}}$, and SIFTER v3, $\overline{E_{0,v3}}$ on the single Congo Basin pixel. The retrieved SIF slightly increased from

0.89 mW m^{-2} sr^{-1} nm^{-1} to 0.99 mW m^{-2} sr^{-1} nm^{-1} when $\overline{E_{0,v3}}$ is used instead of $\overline{E_{0,v2}}$ in the modeled reflectance. This increase results from the deeper Fraunhofer absorption lines in the solar irradiance reference spectrum convolved with the slit function obtained using the SIFTER v3 method (see Figure 2.6).

Finally, to study the effects of the algorithm revisions on the retrieval performance in tandem, and for a larger ensemble of pixels, we conducted a series of four experiments in which the revisions are progressively introduced from SIFTER v2 to SIFTER v3 methodology. The first experiment is based on the SIFTER v3 algorithm approach, but with the use of (i) the variance scaling pre-treatment method (PC_{var}), and the solar irradiance reference spectrum convolved with GOME-2A slit function as done in SIFTER v2 ($\overline{E_{0,v2}}$) for (ii) the high sampling interpolation (HSI_{v2}) and (iii) computation of the modelled reflectance. The last experiment implements all revisions proposed in this chapter. Table 2.3 shows the results of the experiments over 678 pixels on 5 January 2008, over the Congo Basin (13° S–6° N, 14–31° W).

Table 2.3: Summary of experiment results on the progressive revisions from SIFTER v2 (experiment 1) to SIFTER v3 (experiment 4) settings over 678 pixels in the Congo Basin (13° S–6° N, 14–31° W) on 5 January 2008. The selected pixels of the four experiments were co-sampled and had to meet the requirements of autocorrelation < 0.2 and cloud fraction < 0.4. The scan angle-dependent degradation correction, as implemented in SIFTER v3, was used in all experiments.

	Experiment			SIF value ± uncertainty	RMSE fit residual [%]		
	PC	HSI	$\overline{E_0}$	[mW m^{-2} sr^{-1} nm^{-1}]	<746 nm	>746 nm	737–758 nm
1	PC_{var}	$\overline{E_{0,v2}}$	$\overline{E_{0,v2}}$	1.44 ± 0.58	0.075	0.061	0.068
2	PC_{std}	$\overline{E_{0,v2}}$	$\overline{E_{0,v2}}$	1.20 ± 0.57	0.070	0.061	0.065
3	PC_{std}	$\overline{E_{0,v3}}$	$\overline{E_{0,v2}}$	1.00 ± 0.54	0.067	0.059	0.063
4	PC_{std}	$\overline{E_{0,v3}}$	$\overline{E_{0,v3}}$	1.04 ± 0.54	0.066	0.059	0.063

The revision of the pre-treatment scaling method before the principal component had the most substantial impact on both the magnitude of SIF and the retrieval fit. The use of the $\overline{E_{0,v3}}$ showed the largest effect in terms of altering the reflectance in its use for the wavelength calibration of the irradiance observations to match the radiance wavelength grid. The results indicate that the discussed revisions in SIFTER v3 decreased the magnitude of SIF by 28 %, from 1.44 mW m^{-2} sr^{-1} nm^{-1} to 1.04 mW m^{-2} sr^{-1} nm^{-1}, but substantially improved the retrieval fit quality from 0.068 % to 0.063 % RMSE fit residuals. The proposed revisions decrease the sensitivity to water vapour as indicated by the reduced RMSE fit residual over the 734–746 nm, where water vapour features are present. This improvement is mainly attributed to the autoscaling method in the pre-treatment of the principal component analysis, resulting in PCs that better capture the water vapour features.

2.4.3 Zero-level offset adjustment

Our retrieval detects the presence of chlorophyll fluorescence as changes in the relative depth of the Fraunhofer lines. However, instrumental effects and artefacts can also cause infilling, or

deepening, of the Fraunhofer lines, making it indistinguishable from true fluorescence signals (e.g., Frankenberg et al., 2011a; Joiner et al., 2012; Khosravi et al., 2015). These false SIF signals are noted as so-called zero-level offsets over vegetation-free regions and may be of the same order of magnitude as SIF (Köhler et al., 2015). Previous studies have found a particularly strong latitude dependency in GOME-2A SIF over oceans (e.g., Köhler et al., 2015; Joiner et al., 2016; van Schaik et al., 2020). This latitudinal bias is possibly related to the varying width of the slit function, driven by the changing temperatures of the instrument in the descending orbit (Munro et al., 2016). Specifically, the widening of the slit function, due to a higher optical bench temperature, may cause ever shallower Fraunhofer lines along the orbit, which the SIFTER algorithm would interpret as infilling by chlorophyll fluorescence, while a narrower slit function results in deeper Fraunhofer lines, leading to retrieved negative SIF values over unvegetated regions.

Such a zero-level offset is indeed visible in the new SIFTER v3 data. The effect in SIF is visualised in Figure 2.8a (dark blue line), showing a negative trend over the Northern Hemisphere and a positive trend over the Southern Hemisphere above the Pacific Ocean, where SIF is expected to equal zero. Here we apply a *post hoc* correction to adjust for the observed bias. The applied adjustment was adapted from the method of SIFTER v2. In this method, van Schaik et al. (2020) obtained day and latitude-band specific regression coefficients between collected reflectance (at 744 nm) and SIF data per 1° latitude band over the Pacific Ocean (130–150° W). Data was collected from up to 14 days back if the minimum amount of 10 points per 1° latitude band was not met. These regression coefficients, slope a and offset b, were used to get the bias (B_{lat}) for each pixel, at day t and within latitude band *lat*, based on its reflectance at 744 nm (R), as shown in Equation (2.7).

$$B_{\text{t, lat}} = a_{\text{t,lat}} R(\lambda_{744}) + b_{\text{t,lat}} \tag{2.7}$$

Since the bias is additive due to the false infilling or false deepening, SIF is adjusted for the bias by subtracting the estimated bias, see Equation (2.8).

$$I'_{\text{SIF}} = I_{\text{SIF}} - B_{\text{t, lat}} \tag{2.8}$$

Here, we made two modifications from the adjustment method of SIFTER v2. First, we extended the non-vegetative area to obtain the regression coefficients from to cover a broader latitude range. Not only the Pacific Ocean (130–150° W), but also a box over Atlantic Ocean (12° W–2° E) is used as reference area. Secondly, we relaxed the filtering criteria to include pixels with any cloud fraction to calculate the regression coefficients, instead of the < 0.4 requirement as used in van Schaik et al. (2020). Accepting pixels over the reference area with any cloud fraction does not only significantly enhance the number of collected pixels, which resulted in better fits, but also enables representation of pixels with higher radiance values. Representativeness of higher radiance values is hypothesised to help address biases over non-vegetative desert area (Joiner et al., 2016).

The light blue line in Figure 2.8a represents SIF with the *post hoc* bias-adjustment, gridded per latitude band. The adjusted SIF portrays a realistic near zero-line across latitude over the Pacific ocean, indicating that the adjustment methods succeeds in removing the latitude-dependent bias. The effect of the adjustment is also noted when comparing unadjusted, Figure 2.8a, and adjusted

SIF, Figure 2.8b. The adjusted SIF shows values around zero over the oceans, and adjusted SIF no longer suffers from negative values over the desert areas.

Next, to evaluate the impact of the inclusion of cloudy pixels in constructing latitude bias adjustment in Equation (2.7), we constructed the latitude bias correction using SIFTER v3 SIF *with* cloud fraction requirements, as in SIFTER v2. Figure S1.8 shows that the resulting latitude bias is more negative over the Sahara area as compared to no cloud filtering. This more negative bias correction can lead to unrealistic SIF values exceeding well over zero. It indicates that including cloudy pixels in the latitude bias computation indeed provides more accurate adjusted SIF values, particularly over desert areas.

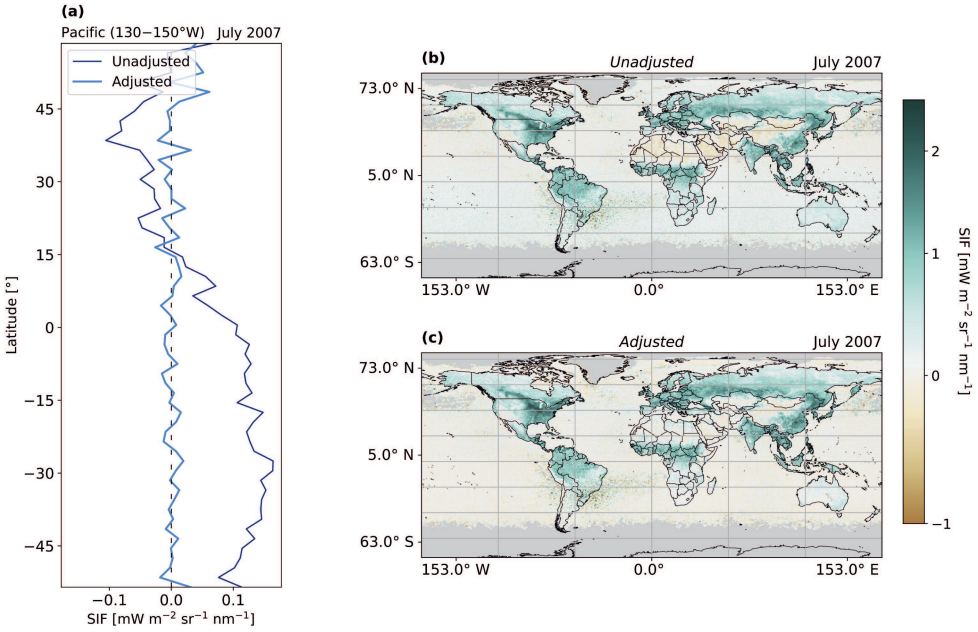


Figure 2.8: (a) Adjusted (light blue line) and unadjusted (thin dark blue line) instantaneous GOME-2A SIF over the Pacific Ocean averaged per latitude band of 2° and over July 2007, (b) level-2 SIF averaged over July 2007 without zero-level offset correction, (c) level-2 SIF averaged over July 2007 with zero-level offset correction as post-hoc correction.

2.5 SIFTER v3 retrieval results

2.5.1 Impact of in-flight degradation correction on retrieved SIF

To examine the impact of our degradation correction on the SIF retrievals, we compared time series of SIFTER v3 SIF values retrieved from corrected and uncorrected reflectances. Both SIF values, degradation corrected and uncorrected, were adjusted for the zero-level bias. Figure 2.9 shows this comparison across the Sahara (unvegetated) and five diverse vegetated areas:

Eastern Europe, United States Corn Belt, the Amazon, the Congo Basin, and Southeastern Australia.

In Eastern Europe, United States Corn Belt, the Amazon, and the Congo Basin, uncorrected SIF values (thin dark blue line) surpasses degradation-corrected SIF values (light blue line) before 2014. After 2014, uncorrected SIF falls below the corrected values. For instance, in 2010, the average degradation-corrected SIF over the United States Corn Belt was 0.67 mW m^{-2} sr^{-1} nm^{-1}, while the uncorrected SIF averaged 0.71 mW m^{-2} sr^{-1} nm^{-1}, representing a 2.8 % difference. By 2016, the corrected SIF values were 5.6 % higher than the uncorrected SIF in the same region. The largest difference between the degradation-corrected and uncorrected SIF is found over the Amazon region between 2014–2017, with a discrepancy of +11.1 %. The observed patterns indicate that degradation correction reduces SIF values in the earlier years and increases them in later years, reflecting the inverse function of the applied degradation factors. In the absence of an appropriate degradation correction, deviations from true reflectance values are, at least partly, being misattributed as SIF values by the retrieval algorithm.

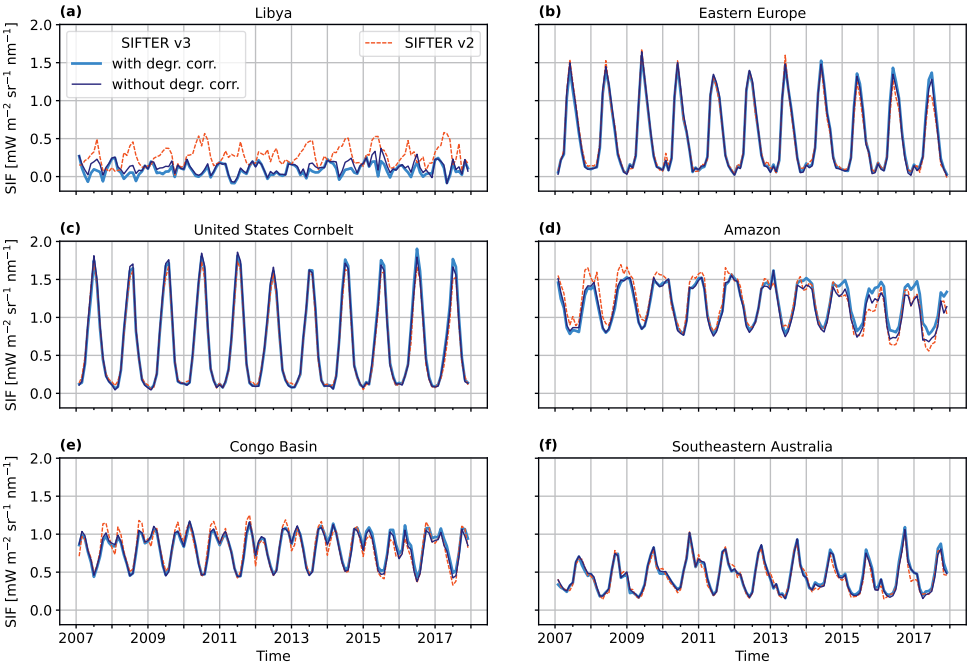


Figure 2.9: Time series of level-2 instantaneous GOME-2A SIF retrieved with the SIFTER v3 algorithm with (solid light blue line) and without the in-flight degradation correction (thin dark blue line) over the Sahara (16–30° N, 8° W–29° E) and vegetated areas: Eastern Europe (50–55° N, 24–39° E), United States Corn Belt (38–46° N, 81–96° W), Amazon (0–15° S, 55–70° W), Congo Basin (13° S–6° N, 14–31° E), and Southeastern Australia (35.5–38° S, 141.5–149.5° E). Co-sampled SIF data from SIFTER v2 is plotted in a dashed orange line.

The zero-level offset adjustment, included in the time series shown in Figure 2.9, could impact the consistency of SIF over time. To isolate the effect of degradation correction from this *post hoc* correction, we compared the time series of SIFTER v3 with and without the degradation correction for both adjusted (final product) and unadjusted values in Eastern Europe and the United States Corn Belt, as shown in Figure S1.11. We observed a clear decreasing trend in annual maximum SIF values in the uncorrected SIF values when the zero-level offset adjustment is *not* applied, but this trend disappears when the adjustment is applied. This suggests that the *post hoc* correction plays a significant role in removing the degradation trend in the uncorrected SIF. This diminishing effect of the *post hoc* correction is further emphasised by a 5.6 % and 23.3 % difference in degradation-corrected versus uncorrected SIF over the United States Corn Belt in 2016, respectively, with and without the *post hoc* zero-level offset adjustment.

Overall, the degradation correction effectively removes spurious trends over time, resulting in more consistent SIF time series. The full impact of our algorithm revisions on the SIF product will be assessed by comparing SIFTER v3 with the previous dataset, SIFTER v2, in 2.5.2.

2.5.2 Comparison of SIFTER v3 with SIFTER v2

We compared SIF from the new SIFTER v3 with our previous product, SIFTER v2 (van Schaik et al., 2020). We co-sampled the datasets to allow a fair comparison. The re-processed level-1b R3 dataset used in v3 includes a different version of FRESCO+, resulting in slight changes in effective cloud fractions compared to the previous v2 (Figure S1.9). Figure 2.9 illustrates the time series for both SIFTER products across unvegetated Sahara area and five vegetated areas. The analysis over the Sahara, where SIF is expected to remain near zero, serves as a validity check. The new product reflects this validity, with an average of 0.08 ± 0.08 mW m^{-2} sr^{-1} nm^{-1}, while the previous product fluctuates around 0.27 ± 0.13 mW m^{-2} sr^{-1} nm^{-1}. This discrepancy may be attributed to the revision in the zero-level offset adjustment calculation, as discussed in 2.4.3.

Clear seasonal patterns are observed in both products across the vegetative regions. In Eastern Europe, the Amazon and the Congo Basin, SIFTER v2 shows higher values than SIFTER v3 until around 2013, after which it drops below SIFTER v3. For example, in 2010, v2 shows values of 1.32 mW m^{-2} sr^{-1} nm^{-1} over the Amazon, compared to 1.21 mW m^{-2} sr^{-1} nm^{-1} from v3 – an 8.2 % difference. By 2016, the v2 annual average is 11.3 % lower than that of the new v3 product. This pattern aligns with trends in reflectance degradation before 2014 (see Figure 2.2). A similar trend was found when comparing degradation-corrected SIFTER v3 with the uncorrected values, as discussed in Section 2.5.1.

Table 2.4 shows SIFTER v3 and SIFTER v3 values for January and July 2008 across the vegetated areas. The year 2008 was chosen to minimise degradation-related differences. The magnitudes in SIF are similar, with a maximum difference of around -10 % over the Amazon in January. The higher SIFTER v2 values were expected following the algorithm revisions (see Table 2.3). For the analysed vegetated regions and months, v3 exhibits lower standard deviation and variability than v2. This suggests improved precision and consistency of SIFTER v3. This is supported by the lower uncertainty in the SIFTER v3 SIF values, which is approximately 13 % lower on January 8, 2008, as shown in Figure 2.10. The lower uncertainty of SIFTER v3,

around 10 %, in comparison to SIFTER v2, remains consistent in later periods when instrument degradation led to a decrease in measurement accuracy (Figure 2.10). These increased precisions result from reduced fit residuals following the revisions in the SIFTER algorithm (Table 2.3).

Overall, SIFTER v3 demonstrates enhanced consistency over space and time, and precision compared to SIFTER v2. However, to confirm whether the new version accurately captures the interannual variation of vegetation activity across the 2007–2017 record, further evaluation against independent data is necessary. This will be further analysed and discussed in Section 2.5.3 of this chapter.

Table 2.4: Monthly mean of co-sampled instantaneous GOME-2A SIF values from SIFTER v3 and SIFTER v2 for the different vegetated regions as shown in Figure 2.9 for January and July 2008. The uncertainties reflect the standard deviation. SIFTER data has been selected for autocorrelation values < 0.2 and cloud fraction < 0.4.

	January 2008		July 2008	
	SIFTER v3	SIFTER v2	SIFTER v3	SIFTER v2
	[mW m^{-2} sr^{-1} nm^{-1}]		[mW m^{-2} sr^{-1} nm^{-1}]	
Eastern Europe	0.10 ± 0.36	0.15 ± 0.38	1.20 ± 0.61	1.20 ± 0.72
US Corn Belt	0.12 ± 0.44	0.15 ± 0.47	1.61 ± 0.80	1.53 ± 0.86
Amazon	1.37 ± 0.84	1.52 ± 0.96	0.84 ± 0.78	0.90 ± 0.86
Congo Basin	0.84 ± 0.65	0.82 ± 0.77	0.45 ± 0.60	0.51 ± 0.69
SE Australia	0.48 ± 0.57	0.45 ± 0.64	0.27 ± 0.40	0.22 ± 0.43

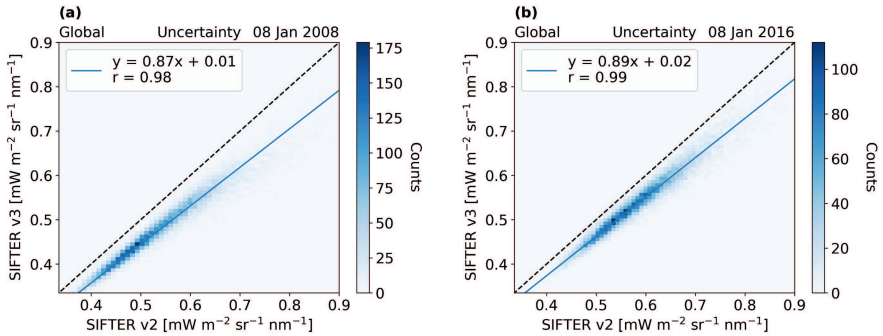


Figure 2.10: Pixel-by-pixel comparison of the uncertainty in GOME-2A SIF derived using SIFTER v3 and SIFTER v2 across all land pixels on (a) 8 January 2008 and (b) 1 July 2008. The pixels cover the global land area and are filtered for autocorrelation values < 0.2 and cloud fractions < 0.4.

2.5.3 Evaluation of SIFTER v3 with independent SIF and GPP observations

To evaluate the ability of SIFTER v3 to accurately track vegetation activity over time, we compared it with the latest version of NASA GOME-2A SIF (Joiner et al., 2023), as well as two independent datasets, namely FluxSat GPP (Joiner et al., 2018) and FLUXCOM-X (Nelson et al., 2024). Both state-of-art GPP products are widely used to track interannual variations in GPP, are known for capturing drought events (Byrne et al., 2021; Chen et al., 2021b; Lv et al., 2023), and align well with GPP estimates from independent flux towers (Joiner et al., 2018; Zhang et al., 2023b).

The NASA SIF product retrieved from GOME-2A uses the same retrieval window (734–758 nm) as SIFTER v3 and applies a similar PCA-based approach to model atmospheric transmittance (Joiner et al., 2013, 2016). The main differences between NASA SIF and SIFTER v3 lie in the absence of degradation correction and the use of a machine learning approach to address the zero-level offset (Joiner et al., 2020).

FluxSat GPP is a high-resolution, $0.05^\circ \times 0.05^\circ$, satellite-derived dataset obtained using a neural network approach and daily-scaled MODIS reflectance (MCD43) data to upscale GPP estimates from eddy-covariance flux towers (FLUXNET 2015). FLUXCOM-X similarly upscales GPP estimates from eddy-covariance data and daily-scaled MODIS reflectance data, but also incorporates meteorological data from the ERA5 reanalysis products, land surface temperature observations and land cover information (Tramontana et al., 2016; Jung et al., 2019; Nelson et al., 2024). The variations in FLUXCOM-X are driven by MODIS remote sensing data (Nelson et al., 2024). This product is obtained through a machine learning approach based on gradient boosted regression trees implemented with the XGBoost library, and it has an hourly temporal scale with a spatial resolution of $0.05^\circ \times 0.05^\circ$ (Nelson et al., 2024).

Figure 2.11 shows standardised monthly averaged time series FluxSat GPP, FLUXCOM-X GPP, SIFTER v3, SIFTER v2, and NASA SIF for the vegetative regions shown in Figure 2.9 and Table 2.4. The standardisation adjusts the dataset in a way that the values are expressed in units of standard deviation from the mean (also see the caption of Figure 2.11). This adjustment allows for direct comparison of the SIF and GPP products at the same scale. The seasonal patterns of FluxSat GPP compared well with both SIFTER products, indicating that SIFTER effectively captures the seasonal variability across different geographical regions. FLUXCOM-X GPP also closely follows both SIFTER products and FluxSat GPP, although deviations are observed in the Amazon and Congo Basin regions, which may result from known challenges in capturing carbon fluxes over the tropics (Tramontana et al., 2016).

NASA SIF captures the seasonality observed in both SIFTER and GPP products across most regions, though significant discrepancies are noted over the Amazon. A lower correlation between SIF and GPP in the Amazon compared to other regions is also observed for SIFTER v3. However, strong correlations, such as $r = 0.95$ with FluxSat (Figure S1.15) and $r = 0.85$ with FLUXCOM-X (Figure S1.16), suggest the ability of SIFTER v3 to track the seasonality in this region. In contrast, weaker correlations between NASA SIF and FluxSat GPP ($r = 0.40$) and FLUXCOM-X GPP ($r = 0.13$), suggest difficulty for NASA SIF in capturing the seasonal dynamics of the Amazon (Figure S1.17). Across other regions, NASA SIF and SIFTER v3 show strong agreement,

with correlations as high as $r = 0.99$ over Eastern Europe (Figure S1.18). Furthermore, SIFTER v3 consistently shows stronger correlations with both FluxSat and FLUXCOM-X GPP than NASA SIF.

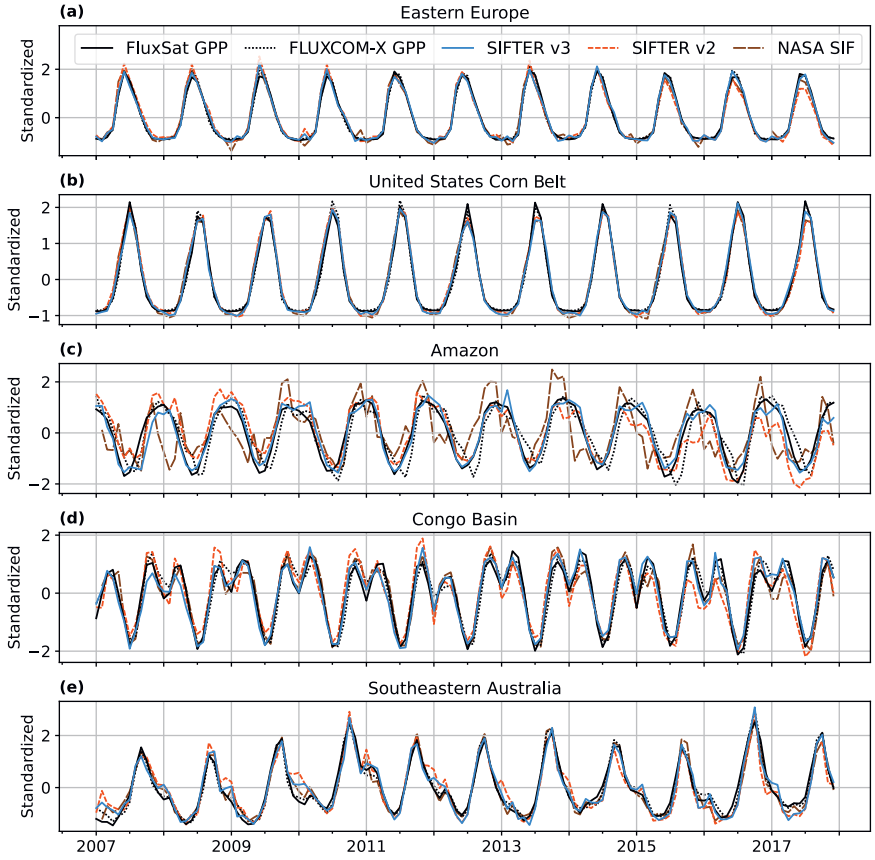


Figure 2.11: Time series of standardised FluxSat GPP (solid black line), FLUXCOM-X GPP (dashed black line), and GOME-2A SIF from SIFTER v3 (solid blue line), SIFTER v2 (dashed orange line), and NASA SIF (dashed brown line) across the five vegetative regions of Figure 2.9. GOME-2A SIF data from SIFTER v3, SIFTER v2, and the NASA product were filtered on cloud fractions < 0.4. All data are monthly averaged. The monthly data are standardised by subtracting each value (x) by the averaged value over all months (μ) and divided by the standard deviation across 2007–2017 (σ); the standardised value is calculated as $x = (x_0 - \mu)/\sigma$.

SIFTER v3 follows the seasonal peaks and troughs depicted by FluxSat GPP more accurately, compared to SIFTER v2. This is particularly evident in the Amazon region, where SIFTER v2 shows a decreasing trend between 2014 and 2017, while SIFTER v3 and FluxSat GPP remain more consistent over time. We found a consistent pattern of overestimation (before 2014) and underestimation (after 2014) by SIFTER v2 relative to FluxSat GPP. This pattern, also observed

in Figure 2.9 and discussed in Section 2.5.1 and 2.5.2 emphasise that the lack of degradation correction in SIFTER v2 from 2007 to 2013 led to an overestimation of SIF, and that the applied correction in the later years did not remove degradation effects completely.

Overall, SIFTER v3 highly correlates with FluxSat GPP (r ranges from 0.91 to 0.99, Figure S1.15) and FLUXCOM-X GPP (r ranges from 0.85 to 0.99, Figure S1.16) across all regions, indicating strong consistency, both temporally as well as across space, in capturing vegetation activity over the record. Compared to SIFTER v2, SIFTER v3 shows higher correlation with both GPP products, reflecting a more robust and consistent pattern of interannual variations in SIF over the 2007–2017 period. Moreover, SIFTER v3 data exhibits a significantly reduced spread in values, with measurements more tightly clustered together compared to SIFTER v2. This reduced variability indicates that the improvements in the SIFTER v3 algorithm have successfully minimised outliers, leading to enhanced consistency and precision in the SIF dataset.

2.6 Conclusions

We improved the Solar-Induced Fluorescence of Terrestrial Ecosystems Retrieval (SIFTER) retrieval algorithm to obtain a more consistent and accurate solar-induced fluorescence (SIF) long-term record SIF record from the GOME-2A instrument for 2007–2017. Although GOME-2A data extends to 2021, measurements beyond 2018 were excluded due to orbital control issues of Metop-A. The updated algorithm, SIFTER v3, uses the recalibrated and reprocessed GOME-2A level-1b Release 3 (R3) data as input. Additionally, it incorporates an enhanced understanding of the instrument's characteristics, leading to strong improvements in fit uncertainty, and spatial and temporal consistency.

We found that the level-1b R3 data is more consistent than previous level-1 version, but instrument degradation still affects the reflectance data. We found that the reflectance degradation strongly depends on time, wavelength, and scan angle. The reflection degradation manifests already early in the record and evolves over time, in response to throughput tests, and different trends in radiance and irradiance degradation. To address these degradation-related trends, our SIFTER v3 algorithm applies a correction that depends on time (daily time step), wavelength, and scan angle, on the observed R3 reflectances. Compared to SIFTER v2, which only corrected for degradation from June 2014 and lacked scan angle dependency, SIFTER v3 provides more consistent SIF records.

Other improvements made to the SIFTER algorithm include more orthogonal principal components (PCs), and a better representation of slit function variation across spectra. The latter resulted in more realistic solar irradiance $\overline{\mathrm{E}_0(\lambda)}$ with deeper Fraunhofer lines. These algorithm revisions led to lower magnitudes in SIF and reduced fit residuals across the retrieval window. Particularly, the new PCs improved the performance over the 734–745 nm region, where water vapour features are present, leading to a ∼14 % reduction in fit residuals. In SIFTER v3, the uncertainty in retrieved SIF decreased by approximately 10 % compared to SIFTER v2, which is the direct result of the reduced fit residuals. The improved temporal consistency of SIFTER v3 is most evident in tropical regions with higher atmospheric water vapour content, like the Amazon and the Congo Basin, highlighting its enhanced ability to capture the atmospheric effects on the

spectra, particularly the effect of water vapour absorption.

Despite these improvements, a persistent latitude bias remained, observed as a zero-level offset over non-vegetative areas. This zero-level offset bias is most likely due to varying slit functions in response to instrumental temperature warming across the orbit. To correct for this, we derived daily latitude-dependent adjustments over the Pacific and Atlantic Oceans. These adjustments are applied as a *post hoc* correction (additive). SIFTER v3 obtains the adjustments from all pixels – both cloudy and clear-sky – while SIFTER v2 solely used clear-sky pixels. Including cloudy pixels to obtain the zero-level adjustment enhanced the adjustment's representativeness in desert deserts. As a result, SIFTER v3 shows more realistic values of 0.08 mW m^{-2} sr^{-1} nm^{-1} over the Sahara area, compared SIFTER v2 with less realistic SIF values of 0.27 mW m^{-2} sr^{-1} nm^{-1}.

We evaluated the new data record against NASA GOME-2A SIF and independent FluxSat GPP data and FLUXCOM-X GPP data. SIFTER v3 is strongly correlated with FluxSat GPP across different biomes, and outperforms SIFTER v2. This improved performance is also observed when comparing FLUXCOM-X GPP with the new and previous SIFTER product. Throughout the entire 2007–2017 period, SIFTER v3 showed strong temporal consistency with both GPP products, without signs of degradation induced false trends. Additionally, SIFTER v3 exhibited substantially reduced variability across all analysed regions. Furthermore, SIFTER v3 shows strong correlations with NASA SIF, except over the Amazon region, likely due to challenges faced by NASA SIF in capturing the seasonal dynamics in this region.

In conclusion, our new SIFTER v3 product resulted in more robust and accurate SIF values, with realistic ∼0 values around the desert areas, and with a lower uncertainty of 10 %. Moreover, the new improved product showed temporal consistency for the entire 2007–2017 period across various biomes and regions. Compared to SIFTER v2 and NASA SIF, the values of SIFTER v3 follow the independent FluxSat and FLUXCOM-X GPP data more consistently over space and time, indicating that the SIFTER v3 product is a reliable proxy to track vegetation activity over the 2007–2017 period. In Chapters 3 and 5, we address the use of the SIFTER v3 algorithm to retrieve SIF from the GOME-2B and GOME-2C sensors, respectively. Both sensors suffer from similar reflectance degradation as GOME-2A.

Supplement S1

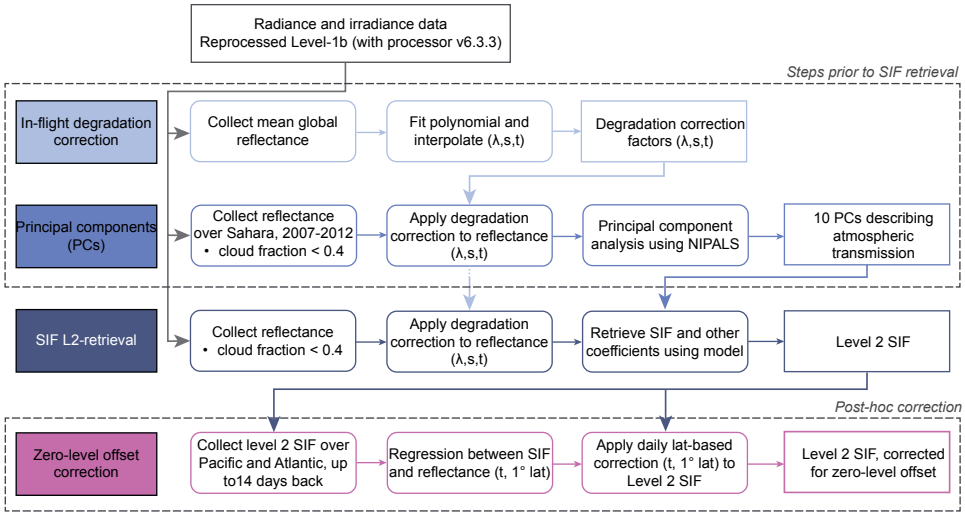


Figure S1.1: Flowchart showing the basic steps to retrieve Level-2 SIF from GOME-2A using the SIFTER v3 algorithm.

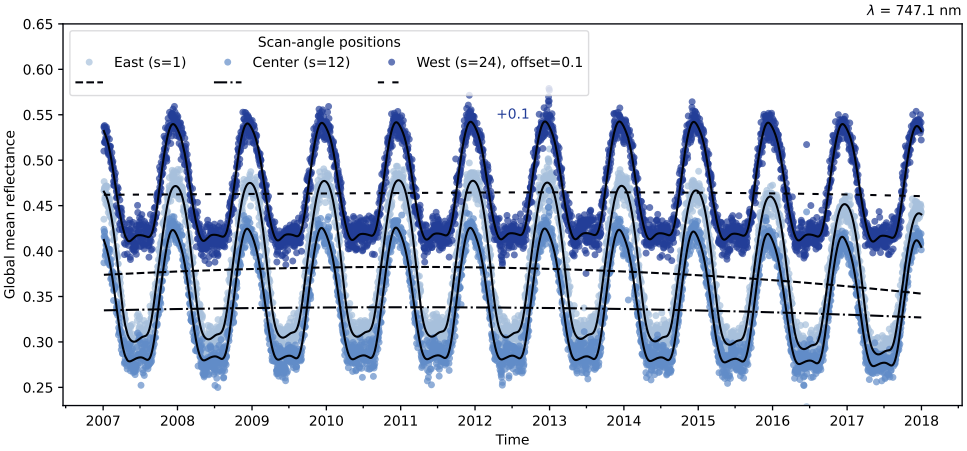


Figure S1.2: Global mean daily reflectance at 747.1 nm from GOME-2A over time, between 2007 and 2017, for the most eastward ($s = 0$), centre ($s = 12$), and most westward ($s = 24$) scan angle positions. See also the caption of Figure 2.2 in Chapter 2.

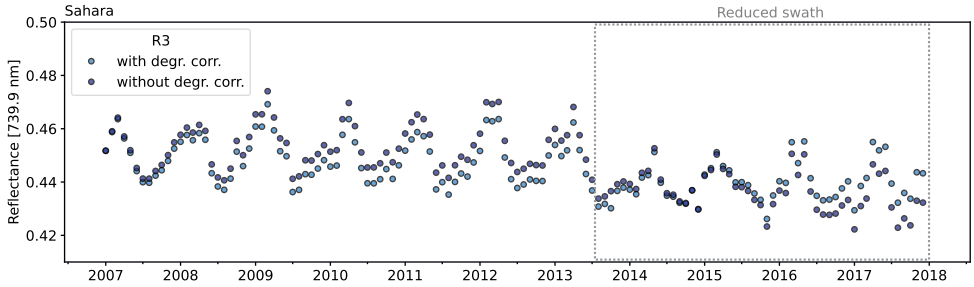


Figure S1.3: Time series of monthly averaged level-1b Release 3 (R3) reflectance data at 739.9 nm over the Sahara, including (denoted in blue) and excluding (denoted in navy) the in-flight degradation correction. The reduced swath period is indicated by the dashed box.

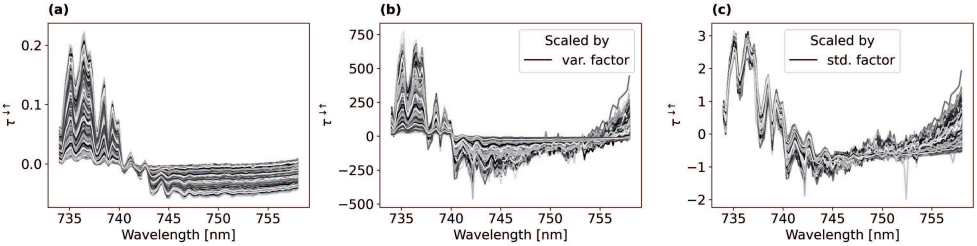


Figure S1.4: (a) Centralized two-way slant absorption optical thickness $\tau^{\uparrow\downarrow}$ spectra over the Sahara reference area between 2007 and 2012. Panels (b) and (c) show the centralised and scaled spectra, scaled by the variance and standard deviation factor, respectively.

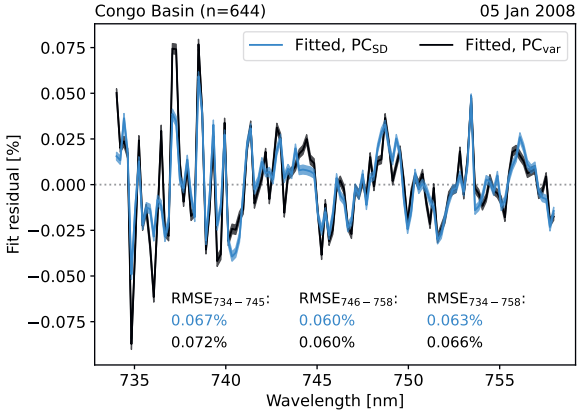


Figure S1.5: Average fit residuals of 644 pixels over the Congo Basin at 5 January 2008 obtained with PCs that used standard deviation scaling (denoted in blue) and PCs that used variance scaling (denoted in black). All other settings follow that of SIFTER v3.

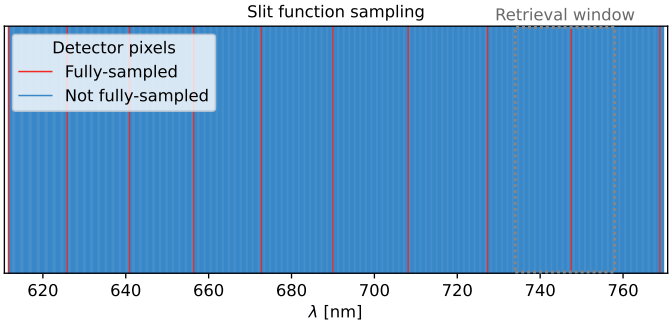


Figure S1.6: Location of all fully and not fully sampled pixels that contain slit function information. The SIF retrieval window is indicated by the grey dashed line.

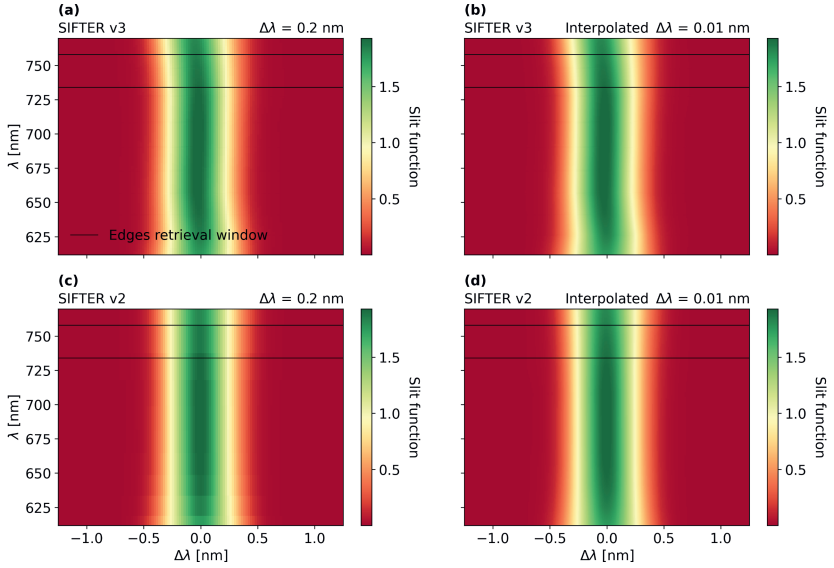


Figure S1.7: Slit functions of all (a) fully and not-fully sampled detector pixels ($n = 765$), as done in SIFTER v3, and (c) only fully sampled detector pixels ($n = 10$), as done in SIFTER v2, with the spectral resolution of 0.2 nm. The two right panels show the results of the interpolation across the slit functions to the spectral resolution of Chance and Kurucz at 0.01 nm, using (b) all pixels as input and (d) only the fully sampled pixels as input.

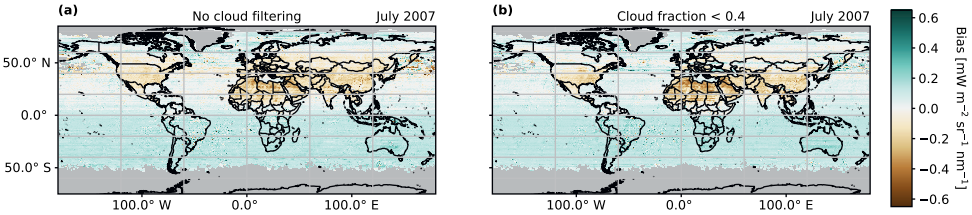


Figure S1.8: Gridded zero-level adjustment biases (0.5° × 0.5°) over July 2007 of SIFTER v3 (a) without cloud filtering and (b) with pixels that met the criteria of cloud fractions < 0.4 (as done in SIFTER v2).

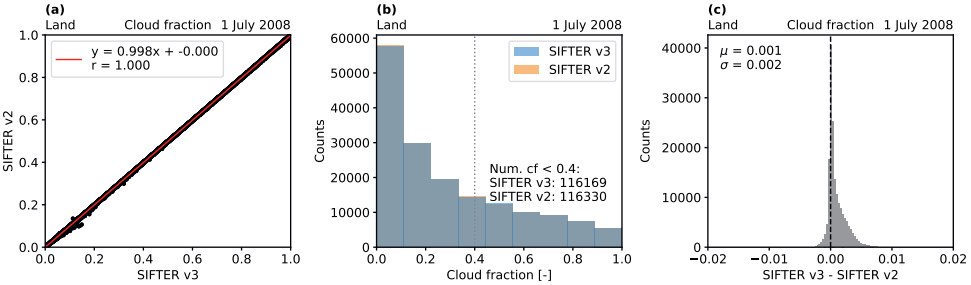


Figure S1.9: Difference in cloud fractions of SIFTER v3 and SIFTER 2, due to different versions of FRESCO+. Pixel-by-pixel comparisons of the (a) comparison of the cloud fractions in both products, (b) the histograms of both products and indicating the number of pixels that meet the criteria of < 0.4, and (c) the difference between the cloud fraction in SIFTER v3 and SIFTER v2. All shown data represent land pixels at 1 July 2008.

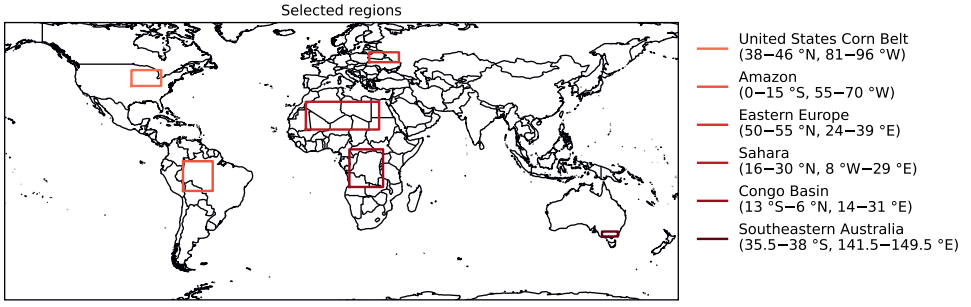


Figure S1.10: Locations of the selected regions in this study.

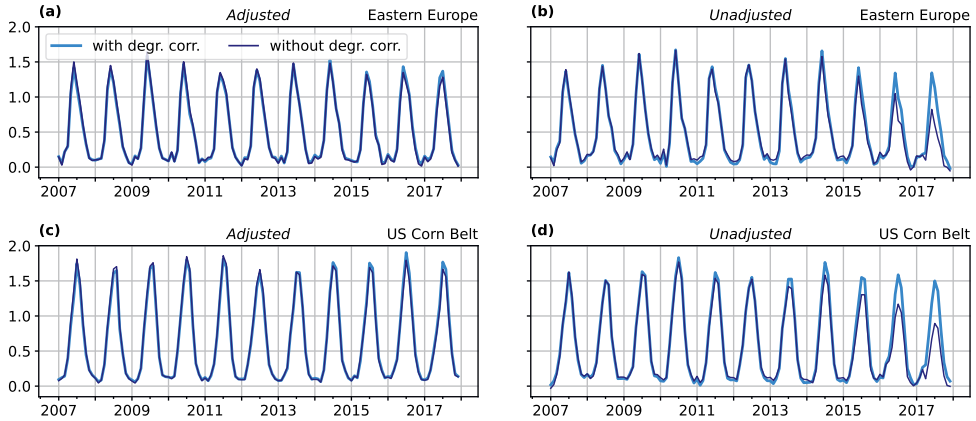


Figure S1.11: Time series of monthly averaged instantaneous SIFTER v3 values over eastern Europe (a,b) and the US Corn Belt (c,d), with (denoted in light blue) and without (denoted in dark blue) applied degradation correction. The left panels (a,c) show the values for the final product, including the zero-level adjustment; the right panels (b,d) show the values for the retrieved SIF without the zero-level adjustment.

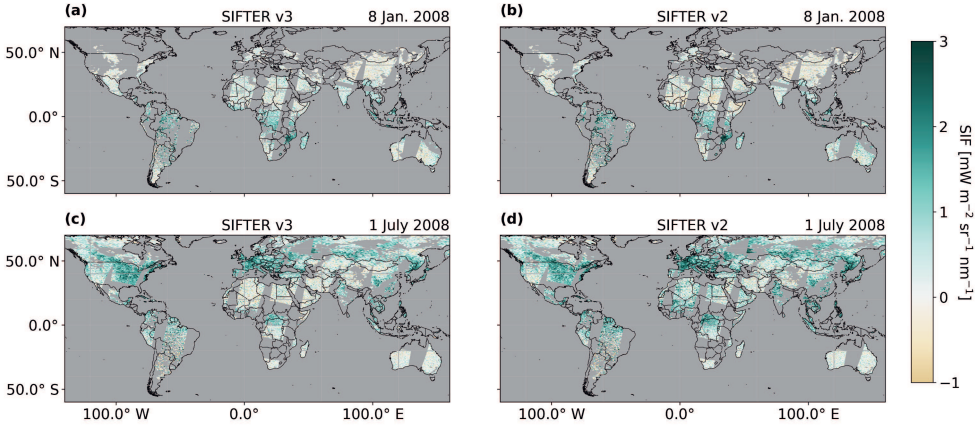


Figure S1.12: Daily instantaneous GOME-2A SIF values ($0.5° \times 0.5°$) from SIFTER v3 (a,c) and SIFTER v2 (b,d) at 8 January 2008 and 1 July 2008. SIFTER data was selected for autocorrelation values < 0.2 and cloud fractions < 0.4.

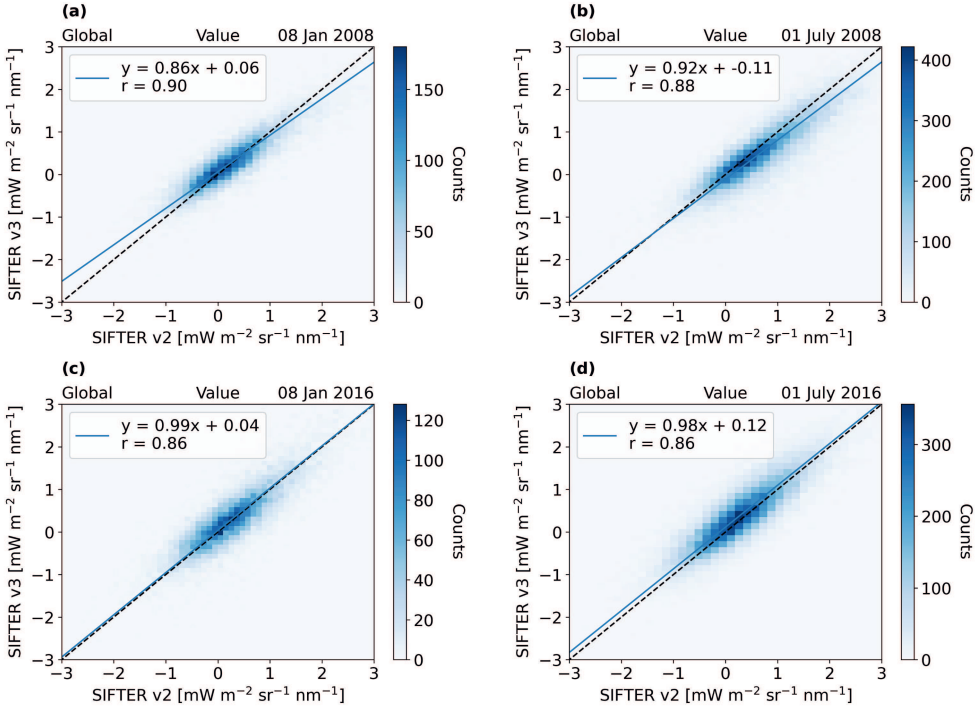


Figure S1.13: Pixel-by-pixel comparison of the instantaneous SIF values of SIFTER v3 and SIFTER v2 over all land-pixels on (a) 8 Jan 2008, (b) 1 July 2008, (c) 8 January 2016, and (d) 1 July 2016. The pixels cover the global land area and are filtered for autocorrelation values < 0.2 and cloud fractions < 0.4.

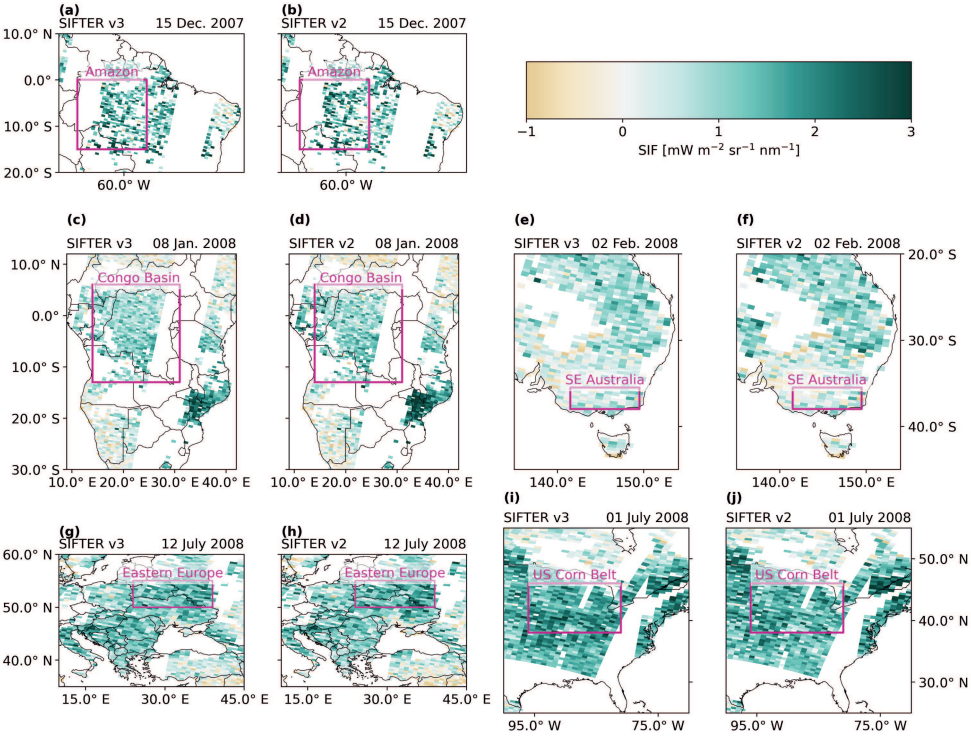


Figure S1.14: Maps across five vegetative showing the spatial variability of daily instantaneous SIF retrieved using the SIFTER v3 and SIFTER v2 algorithms. Days are selected to be within the peak season of the region, June–August for the Northern Hemisphere and December–January for the Southern Hemisphere. Regions shown are: (a,b) Amazon, (c,d) Congo Basin, (e,f) Southeastern Australia, (g,h) Eastern Europe, and (i,j) the United States Corn Belt. Regions correspond to the areas shown in Figure S1.10.

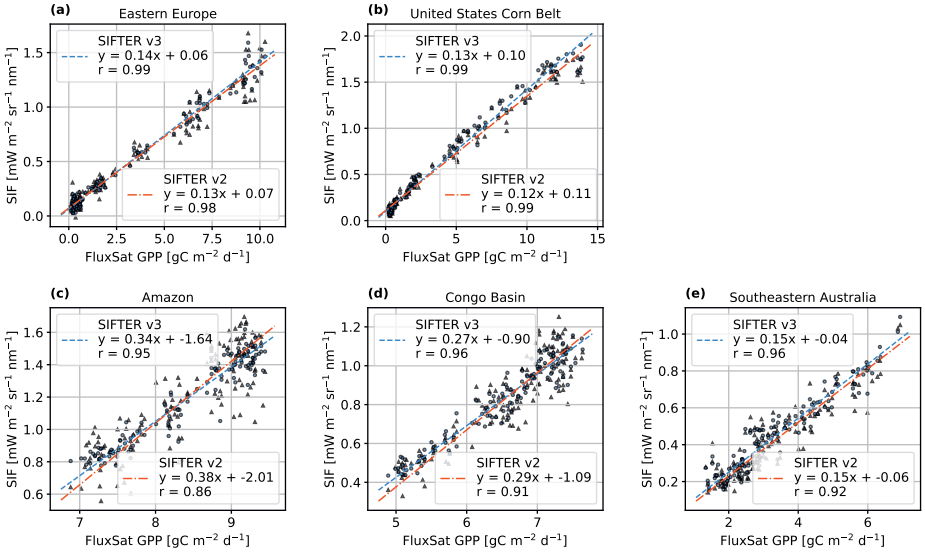


Figure S1.15: Comparison of monthly averaged FluxSat GPP with instantaneous GOME-2A SIF data from SIFTER v3 (blue bullets) and SIFTER v2 (orange triangles) across (a) eastern Europe, (b) the United States Corn Belt, (c) the Amazon, (d) the Congo Basin, and (e) southeastern Australia.

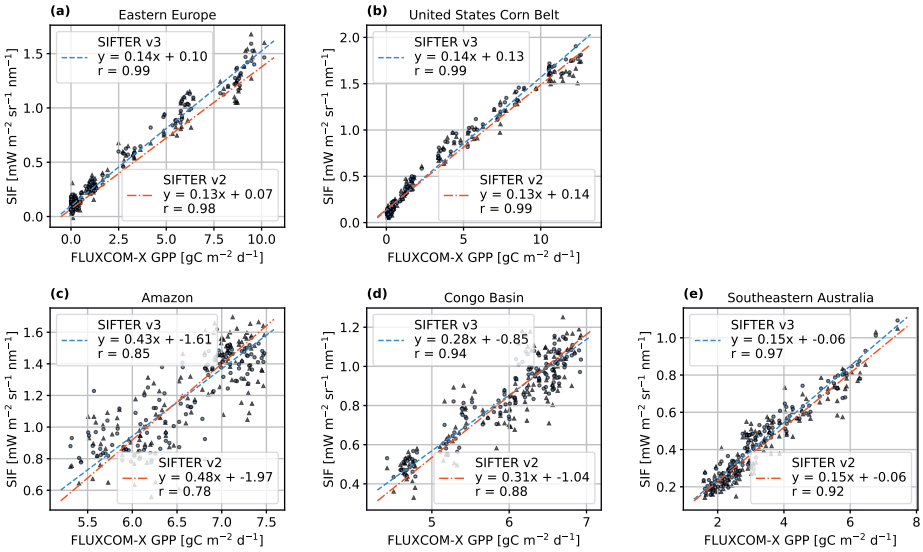


Figure S1.16: Comparison of monthly averaged FLUXCOM-X GPP with instantaneous GOME-2A SIF data from SIFTER v3 (blue bullets) and SIFTER v2 (orange triangles) across (a) eastern Europe, (b) the United States Corn Belt, (c) the Amazon, (d) the Congo Basin, and (e) southeastern Australia.

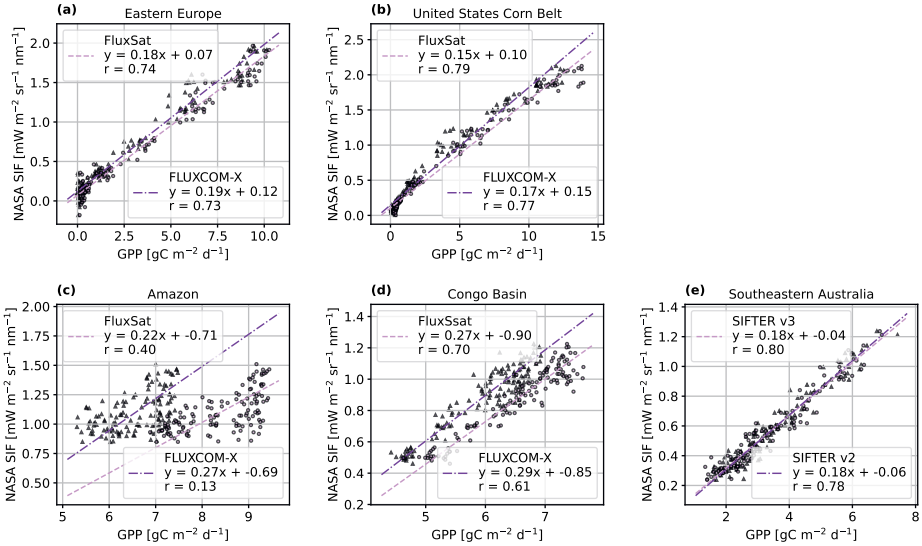


Figure S1.17: Comparison of monthly averaged FluxSat GPP (light purple bullets) and FLUXCOM-X GPP (dark purple triangles) with instantaneous SIF data from NASA GOME-2A SIF across (a) eastern Europe, (b) United States Corn Belt, (c) the Amazon, (d) the Congo Basin, and (e) southeastern Australia.

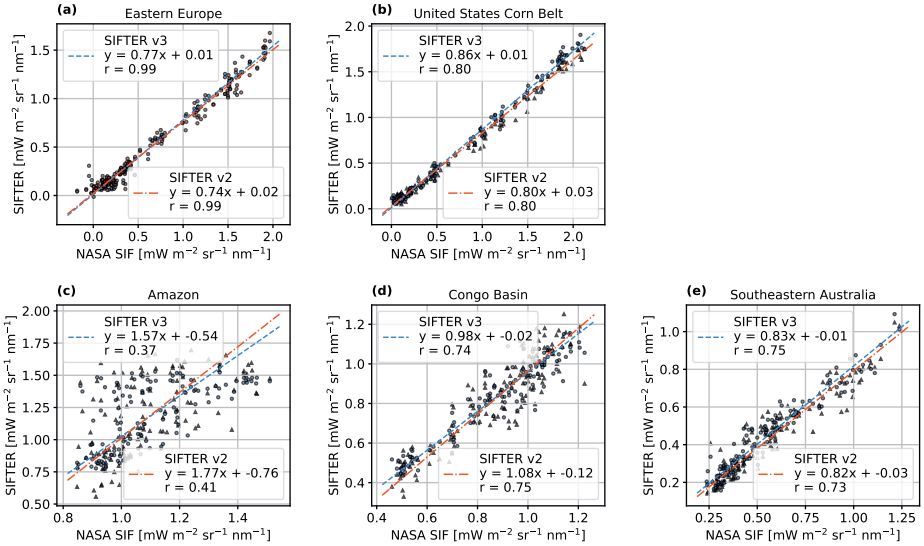


Figure S1.18: Comparison of monthly averaged instantaneous NASA GOME-2A SIF data with GOME-2A SIF data from SIFTER v3 (blue bullets) and SIFTER v2 (orange triangles) SIF across (a) eastern Europe, (b) the United States Corn Belt, (c) the Amazon, (d) the Congo Basin, and (e) southeastern Australia.

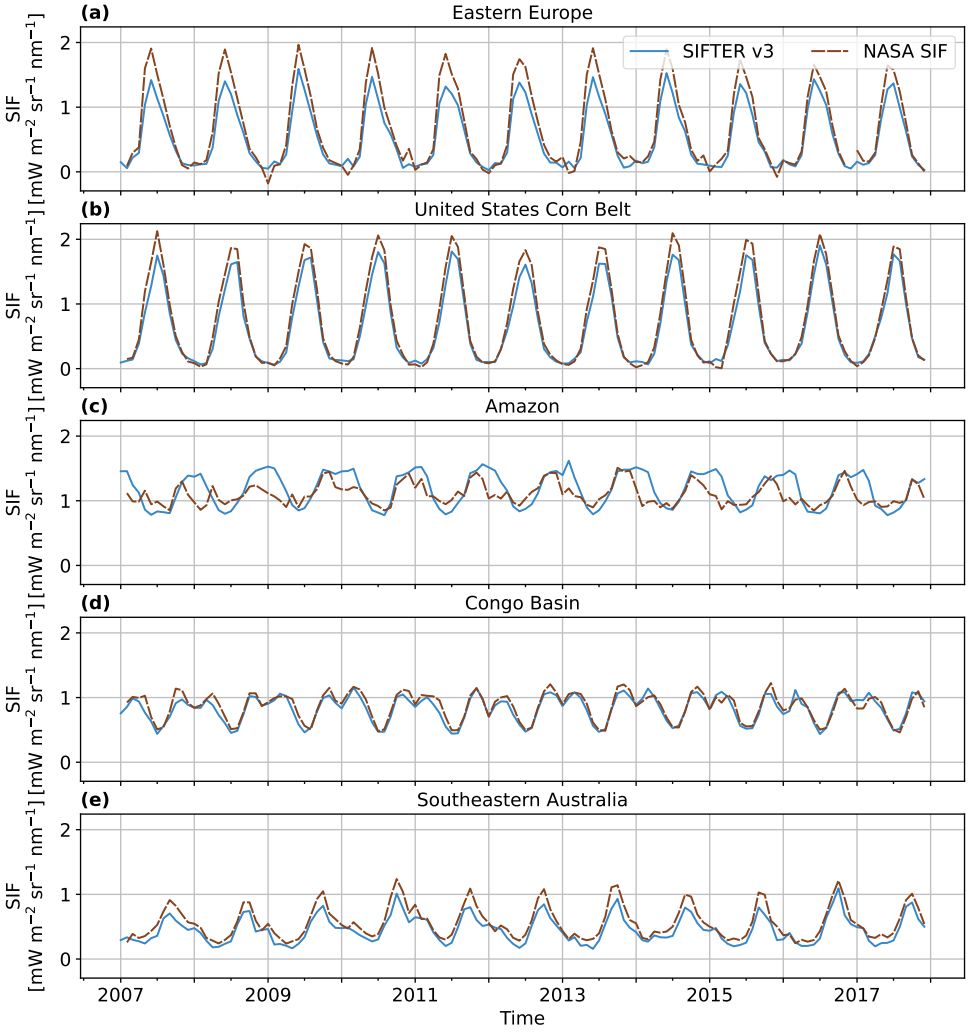


Figure S1.19: Time series of instantaneous GOME-2A SIFTER v3 (blue line) and NASA SIF (brown dashed line) across the five vegetative regions of Figure S1.10.

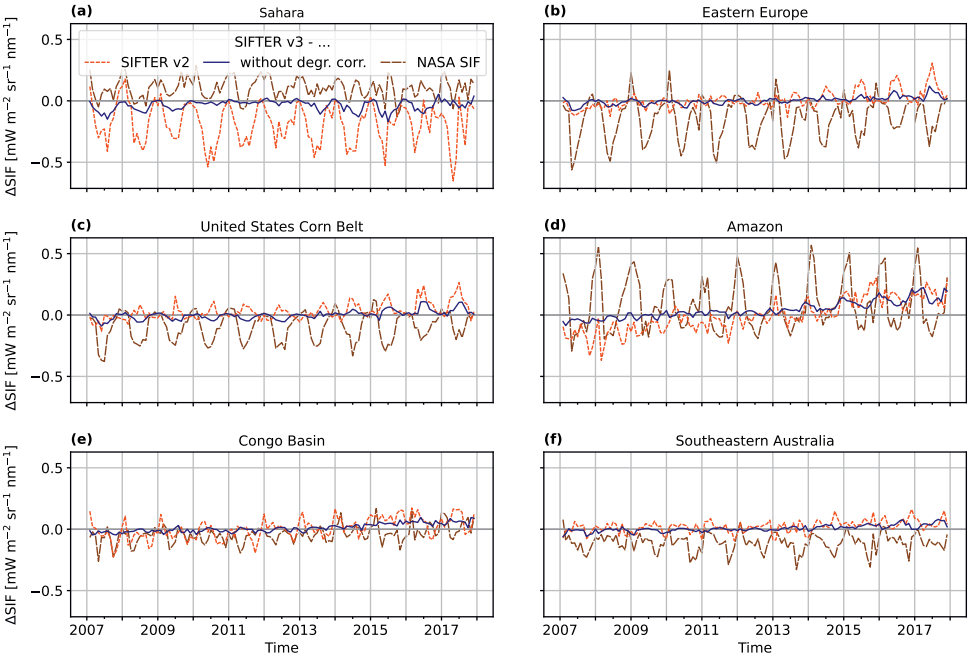


Figure S1.20: Time series of the difference between SIFTER v3 and SIFTER v2 (orange dashed line), SIFTER v3 without degradation correction (navy blue line), and NASA GOME-2A SIF (brown dashed line) across all six regions of Figure S1.10. Values above 1 indicate higher values of SIFTER v3. All SIF data shown reflects instantaneous values.

Chapter 3

Long-term solar-induced fluorescence data record from GOME-2A and GOME-2B (2007–2023) using the SIFTER v3 algorithm

This chapter is under review for Earth System Science Data (ESSD) as:

Anema, J. C. S., Boersma, K. F., Tilstra, L. G., van 't Loo, R., and Tuinder, O. N. E. (2025c). Long-term solar-induced fluorescence data record from GOME-2A and GOME-2B (2007–2023) using the SIFTER v3 algorithm

Abstract

Design differences in sensors and retrieval algorithms complicate the harmonisation of space-based solar-induced fluorescence (SIF) observations. The GOME-2 series, with its identical sensor design, offers potential for constructing a long-term coherent record. However, instrumental artefacts, such as degradation, affect the sensors differently and diverge the intersensor SIF observations. Achieving internal consistency within each record is therefore a critical first step in harmonisation. We present a combined GOME-2 SIF dataset for 2007–2023 that consists of GOME-2A (January 2007–December 2017) and GOME-2B SIF (July 2013–December 2023) data. Both individual records are retrieved using the previously developed SIFTER v3 algorithm, which applies time-, wavelength-, and scan-angle-dependent degradation corrections. Spatial agreement between GOME-2A and GOME-2B SIF during the overlapping period was strong ($r \geqslant 0.96$), although viewing geometry differences caused substantial systematic biases, specifically over high activity regions; these were reduced to within 2 % by constraining to common viewing zenith angle ranges. In terms of temporal alignment, most analysed regions showed no significant step change at the July 2013 sensor transition, from full-swath GOME-2A to GOME-2B SIF. Small offsets in Eastern China and the Amazon were corrected for using a simple additive correction, which improved the coherence and agreement with independent GPP estimations from FluxSat. Finally, the GOME-2 records align closely with FluxSat GPP and TROPOMI SIF across various biomes, and support monitoring of vegetation activity over 17 years. Our work presents a framework for detecting and, when necessary, correcting intersensor offset biases, enabling the use of GOME-2A and GOME-2B SIF as a single record. Moreover, it offers guidance for harmonising multi-sensor datasets and for other causes of potential structural breaks in long-term observation records. The GOME-2A and GOME-2B SIF (obtained in this study) datasets are available at `https://doi.org/10.21944/gome2a-sifter-v3-solar-induced-fluorescence` and `https://doi.org/10.21944/gome2b-sifter-v3-solar-induced-fluorescence`, respectively.

3.1 Introduction

Terrestrial vegetation plays a crucial role in the carbon cycle, yet it also represents one of the largest uncertainties in future climate scenarios. Understanding changes in vegetation dynamics is essential for quantifying global carbon fluxes and sustaining food production. This highlights the need for long-term, global-scale vegetation monitoring. Satellite-based retrievals of solar-induced fluorescence (SIF) constitute a powerful tool to track vegetation dynamics at local to global scales. SIF observations are directly related to photosynthetic activity and, thus, carbon uptake (Mohammed et al., 2019). Previous studies have shown SIF to be sensitive to disturbances such as droughts, wildfire impact, and land-use change and to outperform traditional greenness indices like NDVI (e.g., Chen et al., 2021a; Magney et al., 2019; Zhang et al., 2023d; Gerlein-Safdi et al., 2020; Chapter 4).

In recent years, advancements in SIF retrieval from spectrometer instruments have facilitated the growing number of SIF datasets obtained from various satellite missions, such as GOME, SCIAMACHY (Khosravi et al., 2015; Köhler et al., 2015), GOSAT, the GOME-2 series (Joiner et al., 2013; van Schaik et al., 2020; Chapter 2), TROPOMI (Köhler et al., 2018; Guanter et al., 2021), OCO-2 (Sun et al., 2018), OCO-3 (Doughty et al., 2022), and upcoming missions like FLEX (Vicent et al., 2016) and the CO2M series (Noël et al., 2024). These datasets have proven to be highly valuable for monitoring vegetation phenology and ecosystem productivity across various spatial and temporal scales (e.g., Turner et al., 2021; Wang et al., 2019a; Zhang et al., 2022a; Liu et al., 2021). However, the harmonisation of these datasets is challenging as merging is complicated by discrepancies in satellite characteristics and retrieval settings, such as local overpass time, observation geometry, spectral, spatial and temporal sampling, and the retrieval window spectral range (Parazoo et al., 2019; Sun et al., 2018).

Retrieving SIF from the GOME-2 instruments offers a unique opportunity to circumvent many of the intersensor discrepancies that limit harmonisation. Three instruments, launched in sequence as part of the Metop series, GOME-2A in 2006, GOME-2B in 2012, and GOME-2C in 2019, follow the same design and have consistent equatorial overpass times, all crossing at 09:30 AM. The instrumental similarities minimise biases between sensors, offering potential to obtain a consistent long-term SIF record. Currently, GOME-2A provides the longest individual SIF record with continuous global coverage to date and has been widely used to investigate vegetation dynamics (Gerlein-Safdi et al., 2020; Chen et al., 2021a; Fancourt et al., 2022). A robust merged GOME-2 record enhances our ability to study long-term vegetation dynamics, but would also serve as a valuable benchmark for harmonising SIF datasets, owing to its long duration and limited intersensor biases.

To our knowledge, no study has combined GOME-2 SIF into a long-term SIF record and assessed its coherence. A major challenge in obtaining a robust GOME-2 SIF record is its sensitivity to instrumental artefacts, particularly reflectance degradation, which can lead to false temporal trends in SIF (van Schaik et al., 2020; Zhang et al., 2018a; Koren et al., 2018). If not adequately corrected for, these trends make the data unsuitable for long-term vegetation analysis (Parazoo et al., 2019), and hinder harmonisation across sensors (Wen et al., 2020; Wang et al., 2022b). Our SIFTER v3 retrieval algorithm addresses this issue with an advanced degradation correc-

tion that is time, wavelength, and scan angle dependent, following the reflectance degradation characteristics closely, as shown in Chapter 2. Other GOME-2 SIF products, such as TCSIF and LT_SIFc* (Wang et al., 2022b; Zou et al., 2024), also apply time-dependent corrections, but ignore wavelength and scan angle dependencies of degradation. Notably, the scan angle dependency was found to be of similar magnitude to the temporal component, making its omission a substantial source of bias (Chapter 2). In Chapter 2, we demonstrated the algorithm's effectiveness by obtaining a 2007–2017 GOME-2A SIF record with temporal stability, internal consistency, and strong correlation with independent data. Building on this work, we apply the same approach to retrieve GOME-2B SIF over mid-2013 to 2023 and evaluate its potential to use both datasets as a single coherent combined SIF record spanning from 2007 to 2023.

Our objectives are threefold. First, we retrieve GOME-2B SIF using the SIFTER v3 algorithm and level-1b Release-3 (R3) data to ensure consistency with the existing GOME-2A SIF record generated in Chapter 2. The degradation correction parameters are tailored to the specific reflectance degradation characteristics of GOME-2B. Second, we assess the spatial intersensor consistency during their overlapping tandem phase (from July 2013), using co-sampling methods to isolate sensor-specific biases. Third, we evaluate temporal coherence and demonstrate a framework to identify and, where necessary, correct intersensor offsets, enabling a coherent long-term combined GOME-2 SIF record. Six representative vegetated regions across diverse biomes are used as case studies to examine the intersensor agreement and GOME-2 SIF performance in capturing vegetation dynamics accurately. We present the GOME-2B SIF dataset, with measurement uncertainties, which can be combined with our previous GOME-2A SIF dataset into one GOME-2 SIF data record spanning from 2007 to 2023.

3.2 GOME-2 instruments

The GOME-2 instruments are part of the payload on the Metop satellite series, which consists of three identical satellites, Metop-A, Metop-B, and Metop-C, launched sequentially to enable long-term consistent monitoring of meteorology and air quality (Klaes et al., 2007; Munro et al., 2016). The GOME-2 instruments follow an identical design, and in the following, we refer to this design as "the GOME-2 instrument". In this study, we focus on observations from the first two launched instruments: GOME-2A and GOME-2B.

GOME-2 is an optical spectrometer instrument that measures the radiance and solar irradiance from four main spectral channels, providing continuous spectral coverage between 240 and 790 nm. The instrument builds on the heritage of the Global Ozone Monitoring Experiment (GOME) instrument, continuing the monitoring of ozone and other trace gases, including NO_2, BrO, OCIO, HCHO, SO_2, and H_2O. Additionally, the covering of the near-infrared (NIR, channel 4) enables the retrieval of SIF from GOME-2 (e.g., Joiner et al., 2013; Köhler et al., 2015; van Schaik et al., 2020). Channel 4 has a spectral resolution and spectral sampling of ∼0.5 nm and ∼0.2 nm, respectively.

The GOME-2 instrument uses a scan mirror scheme that enables across-track scanning of the nominal swath with a default width of 1920 km. There are 24 forward pixels (80×40 km^2 resolution in default swath) and eight backward scan pixels. For the SIF retrieval, only the

forward scan pixels are used. For each GOME-2 ground pixel, the effective cloud fraction is retrieved using the Fast Retrieval Scheme for Clouds from the Oxygen A band (FRESCO+) (Wang and Stammes, 2008).

Following the launch of Metop-B in 2012, the GOME-2A and GOME-2B instruments operated in tandem. After its commissioning phase, Metop-B became the prime operational satellite from 16 July 2013 onwards. At that point, the swath of GOME-2A was reduced to 960 km, increasing its spatial resolution to 40×40 km^2, while the swath of GOME-2B operated under the nominal swath of 1920 km. The satellites are 174° out of phase within the same orbital plane, leading to a local time difference of 48.9 minutes between two overlapping observations (Munro et al., 2016; Grossi et al., 2015).

Table 3.1 summarises the key instrumental properties of both instruments, distinguishing the periods of GOME-2A under nominal and reduced swath configuration. The resulting coverage and overlap of both sensors are illustrated in Figure 3.1. The tandem operation ended in 2021, when Metop-A was de-orbited. However, in this study, we limit our analysis of GOME-2A to the 2007–2017 period to avoid possible effects of the orbital drift, which began in early 2018. Similarly, we restrict the analysis of GOME-2B until the end of 2023, as orbital drift started thereafter.

Table 3.1: Summary of instrumental properties of the GOME-2A and GOME-2B sensors.

	GOME-2A		GOME-2B
	Before 15-07-2013	After 15-07-2013	
Launch	October 2006		September 2012
Equator crossing time	09:30 AM L.T.		09:30 AM L.T.
Global coverage	1.5 days	3 days	1.5 days
Swath width	1920 km	960 km	1920 km
Viewing range	−52°, +52°	−35°, +35°	−52°, +52°
Spatial resolution	80 × 40 km^2	40 × 40 km^2	80 × 40 km^2
Spectral coverage, NIR	593–790 nm		593–791 nm
Spectral sampling	0.21 nm		0.20 nm
Spectral resolution	0.48 nm		0.50 nm

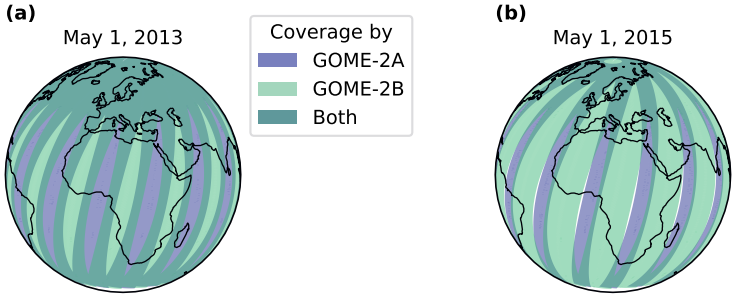


Figure 3.1: Coverage and overlap of GOME-2A (in blue) and GOME-2B (in green) when both are (a) in nominal swath mode and (b) in tandem mode with GOME-2A in reduced swath mode. The tandem operation started from 15 July 2013, when GOME-2B was fully operational (after the commissioning phase), and lasted until the de-orbiting of GOME-2A in 2021.

While orbital drift constrains the time window of reliable data analysis, instrumental artefacts impacted the GOME-2 observations more persistently. Specifically, the effects of instrument degradation on the observed reflectance represent a significant challenge for all three instruments. These effects exhibit varying patterns over time, occur early in operational life, and have sensor-specific characteristics (EUMETSAT, 2022). This degradation is thought to arise from build-up contamination on the scan mirror and is shown to be wavelength and scan angle dependent (Tilstra et al., 2012b; EUMETSAT, 2022; Chapter 2). Although the shorter wavelengths are more heavily affected, the effects in the NIR can't be neglected and are known to impact the temporal consistency of SIF retrievals (Zhang et al., 2018a; Gerlein-Safdi et al., 2020; Wang et al., 2022b; Chapter 2).

The consistency and comparability of the individual instruments' observations are also affected by their thermal stability. Temperature variations of the optical bench along the orbit lead to changes in the spectral alignment, with noted seasonal and long-term effects (Munro et al., 2016). Additionally, these temperature variations also affect the slit function width. This variation in slit function width is believed to influence retrieved SIF values, potentially causing underestimation (false negatives) or overestimation of their magnitude (Köhler et al., 2015; Khosravi et al., 2015; van Schaik et al., 2020).

3.3 Application of SIFTER v3 to GOME-2B

In this study, we retrieve SIF from the GOME-2B sensor using the SIFTER v3 retrieval algorithm. The retrieval methodology and its underlying principles are kept identical to those applied to GOME-2A, and as described in Chapter 2, to secure consistency between the two datasets. For clarity, we briefly summarise the methodology before outlining the algorithm's parameter settings tailored to GOME-2B. The SIFTER v3 retrieval consists of three main steps: degradation correction of the reflectance, the SIF retrieval, and post-hoc correction for latitude bias effects. Details about the applied corrections and their impact on the alignment of GOME-2A

and GOME-2B observations are provided in supplement S2.1.

3.3.1 Reflectance correction

The time-, wavelength-, and scan-angle-dependent degradation correction is derived from analysing daily global reflectance trends over time. First, GOME-2B reflectance data for the spectral range of 712–785 nm are collected between 60° S and 60° N, and with solar zenith angles below 85°. Scenes are not filtered on cloud conditions or sun glint, but data corresponding to static or narrow swath observations are excluded. Daily averages are then obtained for scan-index s (n = 24) and detector pixel at wavelength λ.

As an illustration, Figure 3.2 shows the daily global reflectances at $\lambda = 747.2$ nm and $s = 1$ and $s = 24$ in green. Different long-term temporal reflectance patterns are observed over the easternmost ($s = 1$) and westernmost ($s = 24$) pixel. The reflectance over the easternmost pixel shows a clear decreasing pattern over time, whereas it remains more stable over the westernmost pixel. The stronger eastward degradation is consistent with patterns observed in GOME-2A and predecessors GOME and SCIAMACHY (Chapter 2; EUMETSAT, 2022). The degree of degradation, or signal attenuation, depends on the properties of the contamination layer that develops on the scan mirrors over time and its interaction with polarised light (EUMETSAT, 2022). Eastward light is likely more affected due to the higher degree of polarisation.

Next, we model the temporal variation in global mean reflectance ($R^*_{\lambda,s}$(t)). Although described in detail in Chapter 2, specifically in Section 2.3, the method is repeated for clarity. Global mean reflectances are expected to vary seasonally due to changing geometry and scene observation. Although no long-term trends are expected, substantial long-term trends are noted (Figure 3.2). Therefore, $R^*_{\lambda,s}$(t) is represented by a combination of a polynomial $P^p_{\lambda,s}$(t) and a finite Fourier series $F^q_{\lambda,s}$(t):

$$R^*_{\lambda,s}(t) = P^p_{\lambda,s}(t)[1 + F^q_{\lambda,s}(t)] \tag{3.1}$$

$F^q_{\lambda,s}(t)$ and $P^p_{\lambda,s}$(t) capture the seasonal variation and long-term trends, respectively. For GOME-2B, the Fourier order q is set to 6, and the polynomial degree p to 5. A high polynomial degree was necessary for the fit of GOME-2B reflectances to accurately capture the abrupt drop in signal from around 2020, particularly on the eastern side, as visible in Figure 3.2.

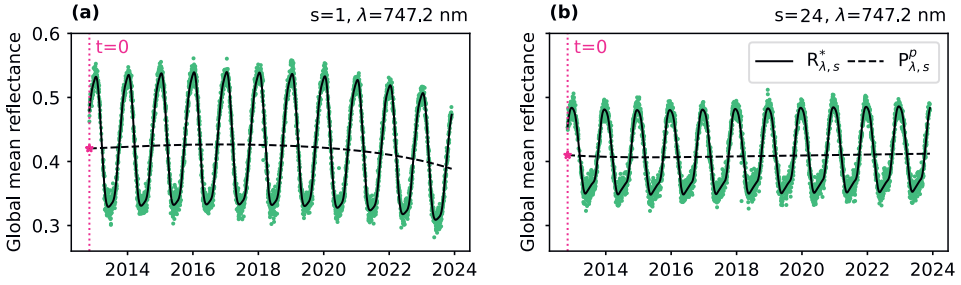


Figure 3.2: The observed (green dots) and fitted (solid black) global mean reflectance from GOME-2B at $\lambda = 747.2$ nm and scan-index (a) $s = 1$ (easternmost) and (b) $s = 24$ (westernmost). The dashed line shows the fitted polynomial, which captures the long-term change in the reflectance over time that is thought to be caused by the impact of instrument degradation. The reference day t_0, set at 1 November 2012, is indicated by the pink star.

To obtain the correction factors ($c_{\lambda,s}$(t)), Equation (3.1) is fitted to the observed reflectances using least-squares regression. The obtained coefficients of the polynomial $P^p_{\lambda,s}$ are then used to correct the long-term trends. We scale the reflectance value at day t to the value at a reference day t_0, as

$$c_{\lambda,s}(t) = P^p_{\lambda,s}(t_0)/P^p_{\lambda,s}(t) \tag{3.2}$$

With $c_{\lambda,s}$(t) as correction factor at day t, wavelength λ and scan-index s. The reference day t_0 represents a day early on in the mission, assuming no spectral degradation at that time. For GOME-2B, t_0 is selected as 1 November 2012. The resulting correction factors are applied to each observed reflectance value before the SIF retrieval to counteract the identified degradation patterns.

Figure 3.3 shows the relative change in reflectance at ∼740.1 nm across the swath for multiple years, for both GOME-2A and GOME-2B. The reflectance degradation pattern represents an inconsistency in the relative loss of throughput between the observed radiance and solar irradiance. As reflectance is defined as the ratio of radiance to solar irradiance signal, a decrease in reflectance, for instance, indicates a stronger degradation of the radiance signal. In both sensors, reflectance degradation is more pronounced on the eastern side of the swath, and an increasing east-west bias develops over time. For GOME-2A, reflectances at all scanning positions increase over the first six years, then decline and eventually drop below the reference value. For GOME-2B, an overall decreasing trend in reflectances is noted.

These results confirm that the reflectance degradation of GOME-2B, similar to GOME-2A (Chapter 2), is strongly scan angle dependent and of the same order of magnitude as the temporal dependency. Importantly, the degradation trends substantially differ between sensors. Furthermore, when GOME-2B launched in 2013, GOME-2A had already drifted significantly from its original reflectance values, amplifying intersensor divergence.

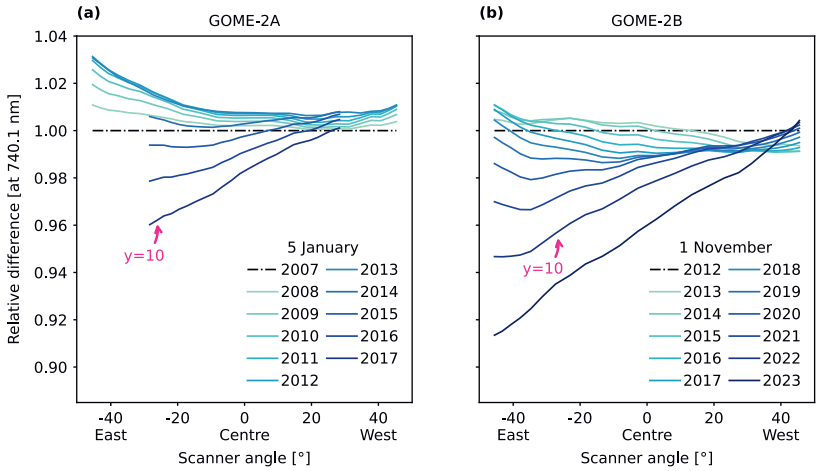


Figure 3.3: Reflectance degradation of (a) GOME-2A and (b) GOME-2B as a function of scanner angle for different moments and at $\lambda = 740.1$ nm. The dashed line indicates the selected reference day for each instrument, where it is expected that there is no impact of reflectance degradation (yet). The pink arrows indicate the 10^{th} years past the reference day.

3.3.2 SIF retrieval

The SIFTER retrieval algorithm obtains far-red SIF by making use of the relative infilling by fluorescence of solar Fraunhofer absorption lines near the 740 nm peak. A narrow retrieval window of 734 to 758 nm is used. This window represents the trade-off of minimising interference from water vapour and O_2 absorption features, while still capturing sufficient Fraunhofer lines and spectral points to ensure reliable SIF retrieval (van Schaik et al., 2020; Parazoo et al., 2019). We use the latest reprocessed level-1b dataset, Release-3 (R3), as input. The R3 dataset ensures consistent processing and auxiliary data for GOME-2A and GOME-2B up to July 2020 (EUMETSAT, 2022). From July 2020 onwards, a different processor version is used, but this is not expected to introduce significant inconsistencies in the level-1b data.

The retrieval isolates the additional vegetation fluorescence signal from atmospheric features by matching a modelled reflectance spectrum to the observed spectrum. This model is shown in Chapter 2 (Equation 2.5) and is repeated here for clarity. We model the reflectance (R) using a Lambertian surface reflectance model, as described by:

$$R(\lambda, \mu, \mu_0) \approx a_s(\lambda) T^{\downarrow}(\lambda, \mu_0) T^{\uparrow}(\lambda, \mu) + \frac{\pi I_{\text{SIF}}(\lambda)}{E_0(\lambda)\mu_0} T^{\uparrow}(\lambda, \mu) \tag{3.3}$$

where μ and μ_0 are the cosines of the viewing and solar zenith angles, respectively. The surface albedo is denoted by $a_s(\lambda)$, the SIF emissions from the vegetated surface by I_{SIF}, and the atmospheric transmission, both downwards and upwards, by $T^{\downarrow}$ and $T^{\uparrow}$. The modelled reflectance contains 16 unknowns, one of which is the SIF signal to be extracted. These unknowns are solved by minimising the difference between the modelled and observed R using a Levenberg-Marquardt

least-squares regression (van Schaik et al., 2020; Chapter 2). Among the other 15 unknowns, five coefficients come from the surface albedo, which is estimated using a fourth-order polynomial, and ten are related to the atmospheric transmittance, which is characterised by 10 principal component (PC) functions.

The atmospheric transmittance varies with each scene and atmospheric conditions. To capture its variability, we apply principal component analysis (PCA) to a large selection of spectra across the Sahara region (16–30° N, 8° W–29° E). These observations are filtered for barren areas using land classification data to ensure the absence of vegetation and, therefore, SIF emission. We select GOME-2B spectra from five complete years (2013–2018), matching the period length used for the PC calculations of GOME-2A (2007–2012). Note that degradation corrected spectra are used (Section 3.3.1) to avoid biases. Furthermore, as introduced in SIFTER v3 in Chapter 2, the spectra are mean-centred and scaled by standard deviation before the PCA.

Figure 3.4 presents the first principal component (PC) for both GOME-2A and GOME-2B, and the cumulative explained variance for each PC (10 in total) for both datasets. For both sensors, PC #1 shows a similar overall structure, but the GOME-2A pattern is more sharply defined, with more pronounced features, such as deeper troughs and higher peaks. The less defined pattern in GOME-2B may reflect its generally higher reflectance uncertainty in the NIR compared to GOME-2A. Nevertheless, the PCs capture 99.95 % of the total variance, indicating that the main spectral structures are consistently represented in both sensors.

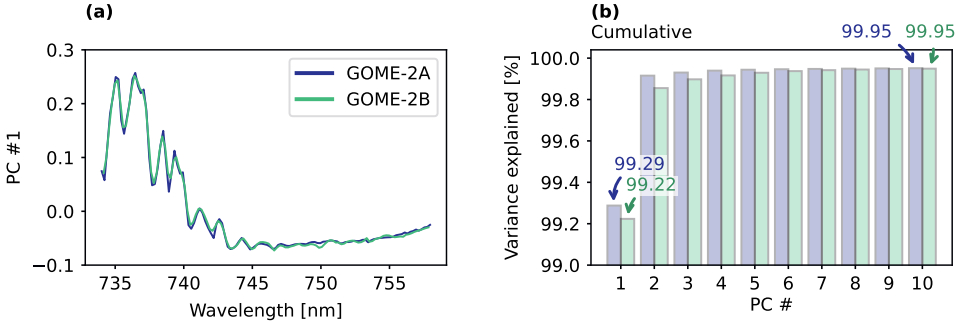


Figure 3.4: Panel (a) shows the leading principal component, PC #1, obtained for GOME-2A under nominal swath and GOME-2B. Panel (b) shows the cumulative explained variance of PCs 1 to 10 for both instruments. In both panels, GOME-2A is shown in blue, and GOME-2B is shown in green.

3.3.3 Latitude bias correction

The SIFTER retrieval algorithm detects the SIF signal as variations in the relative depth of Fraunhofer lines; however, instrumental artefacts can also cause false "infilling" or "deepening" of these lines and can therefore mimic fluorescence signals (e.g., Khosravi et al., 2015; Joiner et al., 2012; van Schaik et al., 2020). These biases are latitude-dependent and may stem from temperature-driven changes in slit function width throughout the orbit, affecting the observed depth of Fraunhofer lines. Moreover, recent work by Sanghavi et al. (2025) demonstrated that

rotational Raman scattering can induce seemingly large SIF values. Such effects are particularly evident over oceans and deserts, where fluorescence should be near zero, as a zero-level offset.

Figure 3.5 shows the zero-level offset observed in GOME-2A and GOME-2B SIF over the Pacific Ocean (130°–150° W), plotted by latitude. In GOME-2A SIF, a clear annual pattern of negative SIF values is noticeable, which shifts from north to south across latitudes. Additionally, the negative offsets intensify over time, with larger negative values observed in the later years. In GOME-2B, a different pattern is noticeable with strong positive offsets appearing early in the years ranging between 20° N–20° S. Additionally, GOME-2B shows strong variation between positive and negative offsets across latitude. Due to the differing patterns observed in both instruments, SIF values from GOME-2A and GOME-2B are not directly comparable. Consequently, it is necessary to apply a correction to account for these discrepancies, reduce intersensor biases, and ensure spatial consistency within and across the datasets.

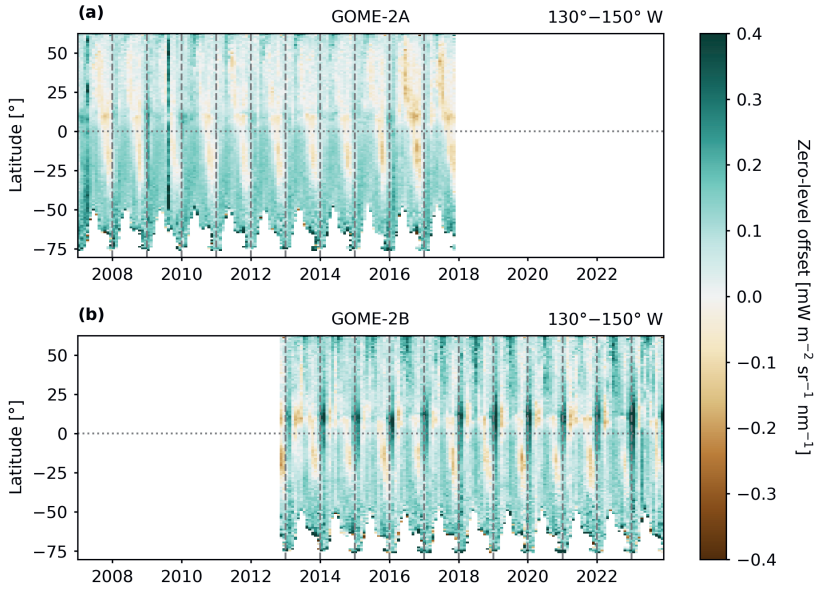


Figure 3.5: Observed zero-level offset of SIF retrieved from (a) GOME-2A and (b) GOME-2B across the Pacific ocean – where SIF is expected to be 0 – per latitude and over time. The SIF values shown are not adjusted for the latitude bias. The shown data are monthly averaged, gridded at 0.5° × 0.5° resolution, and subsequently averaged over 130°–150° W.

To address the latitude bias effects and create higher consistency between GOME-2A and GOME-2B, we apply the post-hoc correction method from SIFTER v3 described in Chapter 2. This additive correction adjusts the retrieved SIF based on daily and latitude-specific biases observed across reference areas over the Pacific and Atlantic Ocean. The latitude bias correction brings SIF values over the Pacific Ocean region, within the expected near-zero range for both GOME-2A and GOME-2B (shown in Figure S2.3). This confirms that latitude-dependent offsets

were effectively corrected for, reducing the correlated intersensor divergence.

3.4 Comparison of GOME-2A and GOME-2B SIF

3.4.1 Spatial consistency

Here, we compare the spatial distribution of SIF as retrieved from GOME-2A and GOME-2B over the period when both sensors operated in tandem. For both datasets, valid SIF data were selected and seasonally averaged over the 2013–2017 period at a $0.5^\circ \times 0.5^\circ$ spatial resolution. To avoid potential biases, we excluded the GOME-2B commissioning phase and only used complete seasons.

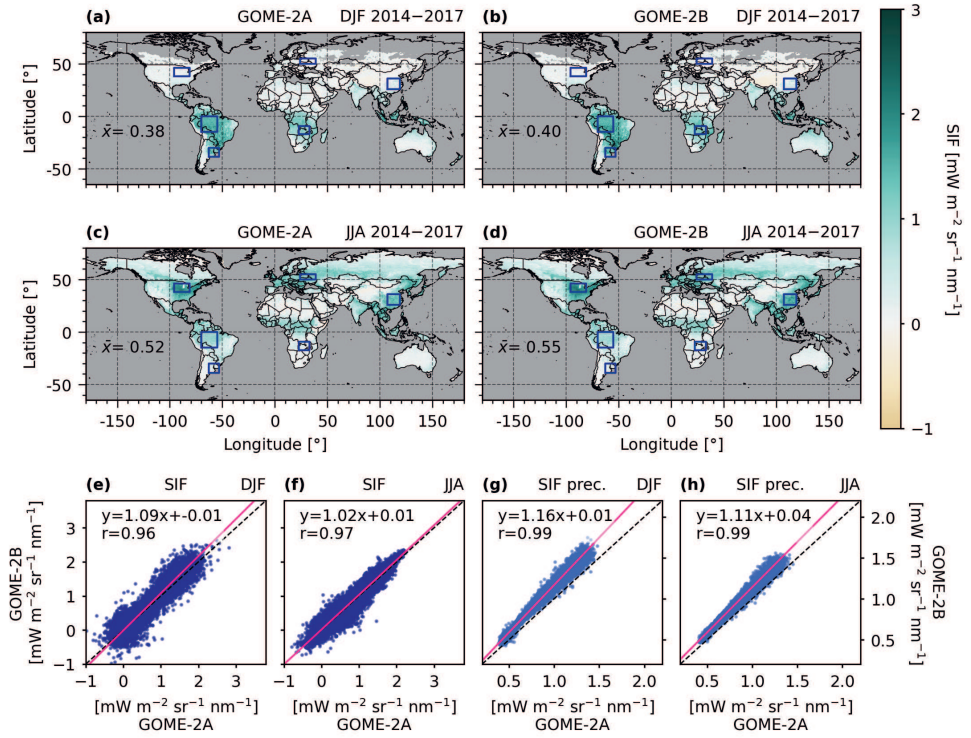


Figure 3.6: Seasonal averaged GOME-2A and GOME-2B SIF over December–February (DJF), and June–August (JJA) 2014–2017. DJF includes December of the preceding year, e.g., DJF 2014 includes December 2013. Panels (e) and (f) show the correlation between GOME-2A and GOME-2B SIF for these periods; panels (g) and (h) show the correlation between their respective uncertainty. Major axis regressions are used for the correlations (pink line). Only land pixels are shown and presented to focus on biosphere-relevant differences. SIF values are filtered for cloud fractions (cf) < 0.3 (FRESCO+ v2) and gridded at $0.5^\circ \times 0.5^\circ$. The blue rectangles mark selected study regions.

Figure 3.6 shows the mean SIF retrieved from GOME-2A and GOME-2B for the Decem-

ber—February (DJF) and June—August (JJA) seasons. Both datasets exhibit similar spatial distributions in SIF and align strongly with each other. However, slight differences are noted. GOME-2B SIF tends to be more negative over barren areas, such as Western China. Moreover, on average, GOME-2B SIF values exceed those of GOME-2A SIF by approximately 5–6 %. This positive bias appears to be most pronounced in regions with high vegetation activity, such as the Corn Belt region in JJA and the Amazon in DJF.

Aside from the differences in SIF values, GOME-2B also shows consistently higher uncertainty in SIF than GOME-2A, on the order of 17–18 %. This likely reflects a combination of larger uncertainties in the input reflectance, lower spectral resolution (Table 3.1), and the less sharply defined principal components (Figure 3.4), all of which can propagate through the retrieval and increase the final uncertainty.

Overall, GOME-2A and GOME-2B SIF values agree well with consistent spatial patterns and strong correlations ($r = 0.96$ for JJA, and $r = 0.97$ for DJF). These results indicate coherence between both datasets. Nonetheless, GOME-2B SIF values are slightly but systematically biased against GOME-2A SIF values. In the following subsections, we examine to what extent this divergence reflects true biases or results from sampling differences.

3.4.2 Impact of viewing geometry differences

During the operational tandem phase, GOME-2A and GOME-2B operated under different swath configurations. The swath reduction of GOME-2A limited the viewing zenith angle (VZA) range of the observations from $\in [-52°, +52°]$ to $[-35°, +35°]$ (Table 3.1). As a result, the GOME-2B SIF averages shown in Figure 3.6 include observations made under larger VZA angles ($|\text{VZA}| > 35°$) than GOME-2A. To understand how these discrepancies in viewing geometry might induce biases between GOME-2A and GOME-2B SIF, we first discuss the principle behind the angular dependence of SIF observations.

The SIF signal detected by the satellite sensor reflects the fraction of total emitted chlorophyll fluorescence that escaped the canopy and reached the sensor. This fraction depends on the photon scattering, leaf properties, and canopy architecture, influencing the propagation of SIF photons through the canopy (e.g., van Wittenberghe et al., 2015; Peltoniemi et al., 2005; Joiner et al., 2020; Sun et al., 2023). As a result, the SIF signal is anisotropic and therefore depends on the viewing geometry between the Sun, vegetation, and the satellite sensor (e.g., Yang and van der Tol, 2018; van Wittenberghe et al., 2015; Dechant et al., 2020).

Figure 3.7 illustrates the scan and illumination dependencies of the observed SIF by GOME-2. At nadir, the sensor mainly detects photons emitted from the top of the canopy. Toward the swath edges, at larger viewing zenith angles (VZA), the sensor observes the canopy from a slanted angle, thereby enhancing the probability of detecting photons originating deeper within the canopy. Moreover, the viewing perspective determines whether the sunlit or shaded side of the canopy is viewed, leading to higher or lower observed values, respectively. For GOME-2A observations, the western ground pixels are typically sunlit, whereas eastern ground pixels tend to be shaded.

Wide-swath instruments, such as GOME-2 and TROPOMI, also introduce across-track vari-

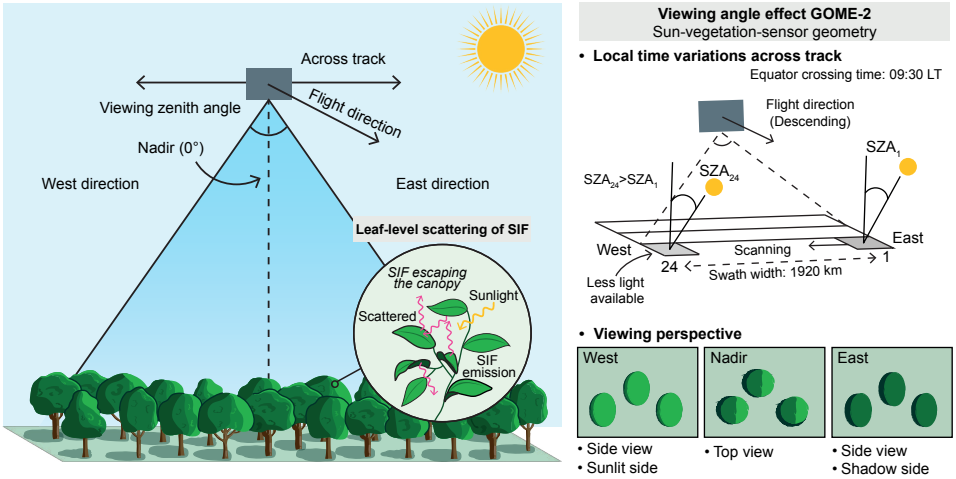


Figure 3.7: Schematic of the scan angle dependencies of GOME-2 SIF observations. The instrument scans from east (pixel 1) to west (pixel 24), with a total scanning time of around 50 minutes.

ations in incoming solar irradiance (Joiner et al., 2020). The wide swaths cover an extensive longitudinal range that spans different local solar times and thus solar zenith angles (SZA). As a result, GOME-2 observes eastern pixels later in the morning when solar illumination is typically higher (lower SZA), leading to potentially higher SIF values. Together, these viewing geometry factors can lead to systematic asymmetry in the observed SIF values across-track (Joiner et al., 2020). The geometry effects on observed SIF are well known, and SIF is generally averaged over a sufficient number of observations to mitigate these effects (e.g., Turner et al., 2021).

To assess the effect of discrepancy in viewing geometry between GOME-2A and GOME-2B, we average both datasets across scan positions. Figure 3.8 shows seasonal SIF as a function of VZA for both sensors across various geographical regions. A consistent across-track asymmetry is observed in all regions during the peak seasons, specifically JJA in the Northern Hemisphere and DJF in the Southern Hemisphere. During these high activity seasons, large SIF values near the eastern and, more prominently, the western edges of GOME-2B's 1920-km swath contribute to a higher overall average ($\overline{x_B}$), compared to GOME-2A SIF ($\overline{x_A}$). For instance, GOME-2B SIF has a bias of 13.9 % compared to GOME-2A SIF over Zambia. SIF values from both sensors align well when restricted to the shared VZA range of $[-35°, +35°]$. The largest divergence across-track emerges when the |VZA| exceeds ∼30°. Within GOME-2B's wide swath, westward pixels can exhibit up to 35 % higher SIF values than eastward pixels during peak seasons (see supplement S2.2 for more detail).

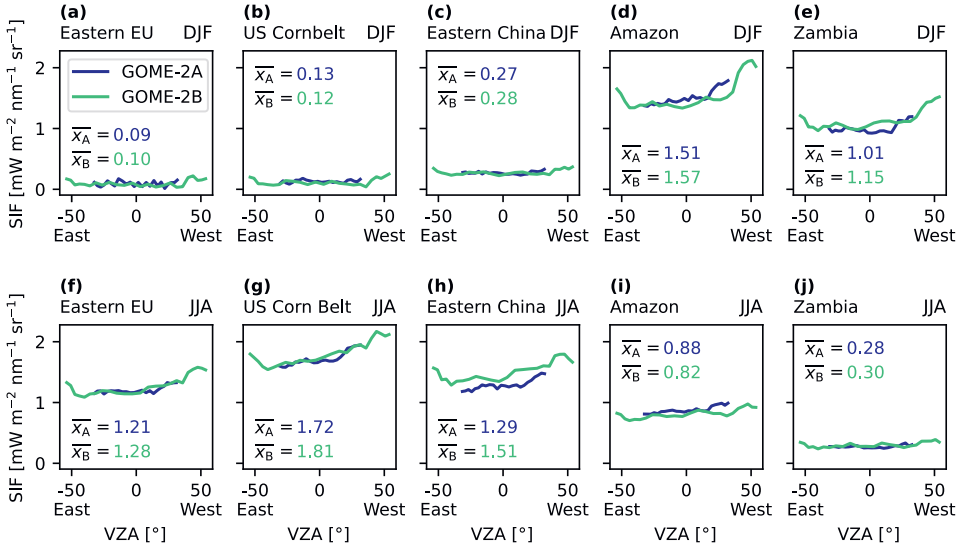


Figure 3.8: Seasonally averaged SIF from GOME-2A (blue) and GOME-2B (green) across the viewing zenith angle (in °). Showing seasonal SIF for June–August (JJA) 2014–2017 (top plots) and December–February (DJF) 2014–2017 (bottom plots), over Eastern Europe, the United States Corn Belt, Eastern China, the Amazon, and Zambia.

Figure 3.9 shows zonal averages of SIF from GOME-2A (in solid blue), GOME-2B using observations from the full VZA range (in solid green), and VZA ranges matched with GOME-2A (in dashed green). Overall, GOME-2A and GOME-2B SIF values converge when their VZA ranges match. For instance, the difference in DJF SIF between GOME-2A and GOME-2B over 0° to 40° S decreased from 13.8 % to 4.9 %. These results indicate that a significant portion of the inter-sensor differences in SIF can be attributed to variations in VZA sampling. Nonetheless, some divergence between GOME-2A and GOME-2B SIF remains. The remaining biases may result from differences in spatial and temporal sampling, as well as from differences in sensor and orbit characteristics.

3.4.3 Isolating sensor-specific differences

To further evaluate the divergence between GOME-2A and GOME-2B SIF, we perform two co-sampling experiments (see supplement S2.2). In Experiment 1, GOME-2A and GOME-2B pixels are spatially and temporally collocated. Matching pixel pairs had a maximum 50 km distance between their centres, at least 60 % spatial overlap of the smaller GOME-2A pixel with the GOME-2B pixel, and observation times less than 50 minutes apart. Experiment 2 applies the same constraints, with an additional requirement that both observations are within the same viewing geometry range of [−35°, +35°]. These constraints help to isolate instrument-specific biases from those arising from sampling mismatches. Due to the limited spatial overlap of GOME-2A and GOME-2B ground pixels, sampling in Experiment 2 is practically limited to

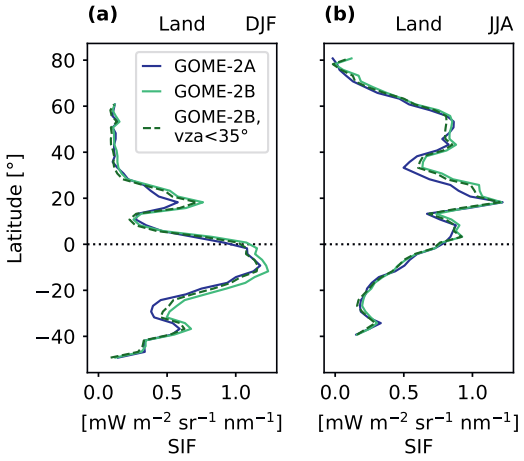


Figure 3.9: Zonal averaged SIF from GOME-2A (solid blue line), GOME-2B considering all observations (solid green line), and only those with $|\mathrm{VZA}| < 35°$ (dashed green line), for (a) DJF 2016 and (b) JJA 2016. Zonal averages reflect all land pixels. Pixels over the Sahara region (15° N–32° N, 16° W–52° E) were filtered to limit distortion of observations over desert areas and focus primarily on vegetated regions. The SIF values are plotted by latitude at 2° resolution.

the Northern latitudes.

Figure 3.10 shows GOME-2A and GOME-2B SIF data, sampled to both experiments accordingly, and averaged over JJA 2014–2017. GOME-2A and GOME-2B SIF are better aligned for Experiment 2 (1.9 % bias) than for Experiment 1 (5.6 % bias) – as expected. This is confirmed by the empirical cumulative distribution functions (ECDFs) (bottom plots in Figure 3.10). ECDFs visualise the cumulative distribution of each dataset, enabling clear detection of systematic shifts between datasets. When only spatially and temporally co-sampled, Experiment 1, GOME-2B SIF values at the 90th percentile are 7.1 % higher than the corresponding GOME-2A value. Including co-sampling of viewing angles, Experiment 2, reduces the bias of GOME-2B SIF to GOME-2A SIF to 2.1 %.

Despite the reduced structural bias in Experiment 2, the correlation between GOME-2A and GOME-2B SIF is lower ($r = 0.92$) than in Experiment 1 ($r = 0.97$) (shown in Figure S2.12). However, the SIF averages corresponding to Experiment 1 are based on nearly three times as many observations per grid cell as those in Experiment 2. This discrepancy in data density between the two experiments might reduce the comparability of their results. To enable a more balanced comparison, we constructed a reduced version of Experiment 1. The additional test involved averaging Experiment 1 data over a randomly selected subset of days from the JJA 2014–2017 period to match the data density of Experiment 2 better. The comparison between the reduced Experiment 1 and Experiment 2 was performed using only grid cells with valid and sufficient observations in both experiments. The divergence between GOME-2A and GOME-2B SIF remained similar to that of Figure 3.10, but the correlation between GOME-2A and GOME-

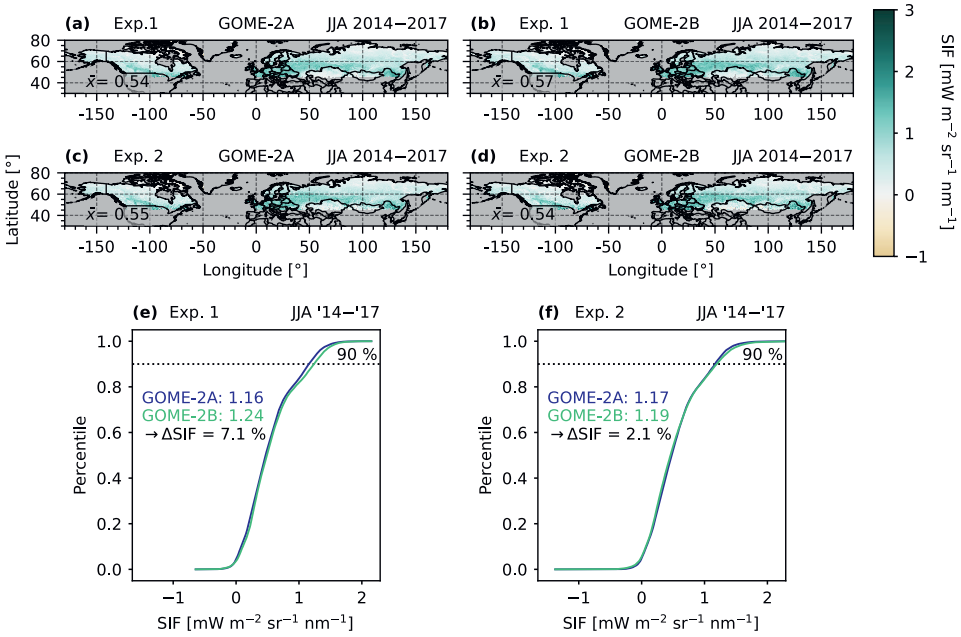


Figure 3.10: (a,c) GOME-2A and (b,d) GOME-2B sampled according to Experiments 1 and 2, averaged over June–August (JJA) from 2014 to 2017 on a 0.5° × 0.5° grid. SIF values are shown for grid cells with valid and sufficient observations (exceeding the 10th percentile of data counts) in both datasets and experiments. The mean SIF is shown as $\overline{x}$. The two bottom panels show the ECDF plots of GOME-2A and GOME-2B SIF according to (e) Experiment 1 and (f) Experiment 2. The dotted line indicates the 90th percentile, with the text indicating the corresponding SIF values.

2B SIF for Experiment 2 ($r = 0.96$) now exceeds that of Experiment 1 ($r = 0.95$) (shown in Figure S2.15). These results confirm that the co-sampling requirements as set in Experiment 2 result in the best agreement among GOME-2A and GOME-2B SIF. The details on this additional test are in the supplement S2.2.

GOME-2A and GOME-2B SIF show strong coherence in terms of spatial distribution. However, our results indicate the importance of similar sampling to reduce systematic biases between the two datasets. Particularly, discrepancies in viewing geometry sampling have been shown to distort the coherence between inter-sensor SIF datasets. When both datasets are sampled similarly, GOME-2A and GOME-2B SIF agree to within 2 %. A slight discrepancy is expected, as they are separate sensors with minor differences in instrumental characteristics (Table 3.1). These results provide confidence in the consistency of GOME-2A SIF (pre-July 2013) and GOME-2B SIF (from July 2013 onwards), when both sensors operated with the same 1920 km swath and viewing zenith angle ranges (VZA$\in [-52°, +52°]$).

3.5 Long-term time series analysis

This section evaluates the combined 2007–2023 GOME-2 SIF record over time. It uses GOME-2A data from January 2007 to June 2013 and GOME-2B data from July 2013 onwards. We focus on SIF observations from the GOME-2A instrument under its nominal swath configuration to ensure similar viewing angle ranges within both datasets, limiting the bias between GOME-2A and GOME-2B SIF and advancing their connection (as found in Section 3.4.3). The record's performance is evaluated in two ways. First, the coherence between GOME-2A and GOME-2B SIF is assessed in Section 3.5.1 using statistical tests and analysis. In Section 3.5.2, the temporal consistency of the record is evaluated using independent datasets. Both analyses use monthly-averaged SIF across six vegetative regions. The monthly and spatial averaging mitigate the effects of variation in geometry on SIF.

3.5.1 Temporal coherence of GOME-2A and GOME-2B SIF

Figure 3.11 shows the monthly regional averages of SIF from January 2007 to December 2023. For most regions, the transition from GOME-2A SIF (in blue) to GOME-2B SIF (in green) appears seamless. However, in the Amazon, a slight downward shift in GOME-2B SIF, relative to GOME-2A SIF, is noted. To test whether this shift is related to the instrument transition, we proceed with statistical and analytical tests.

To statistically investigate whether a structural break occurs at the transition month T_0, July 2013, from GOME-2A to GOME-2B SIF data, we fit a simple model to the monthly SIF time series, which includes a linear trend (αt), seasonal component (S_t), and a mean level shift term (δU_t):

$$y_t = \mu + \alpha t + S_t + \delta U_t + \varepsilon_t \tag{3.4}$$

where y_t represents the regional SIF value at month t, μ the monthly mean and ε_t the residual of the observed and fitted SIF. This equation is adapted from Weatherhead et al. (1998) and commonly used to model trends in environmental variables that include a sudden level shift (e.g., van der A et al., 2006). The seasonal component S_t represents the annual cycle of SIF as a first-order harmonic:

$$S_t = \beta_1 \sin\left(\frac{2\pi(t-\phi)}{12}\right) + \beta_2 \cos\left(\frac{2\pi(t-\phi)}{12}\right) \tag{3.5}$$

where β_1 and β_2 control the amplitude, ϕ is the phase shift, and the angular frequency corresponds to annual periodicity.

Before fitting the full model, the phase shift ϕ is fixed through a pre-optimalisation step. We estimated its value by evaluating the model with 100 evenly spaced values of ϕ, ranging from 0 to 1, and selecting the value under which the model performs best. This ensures good alignment of the modelled SIF with the real seasonal timing and avoids non-linearity in the model.

The possible offset in GOME-2 SIF related to the moment when the time series shifts from GOME-2A to GOME-2B data in July 2013, or T_0, is accounted for by the step-change indicator

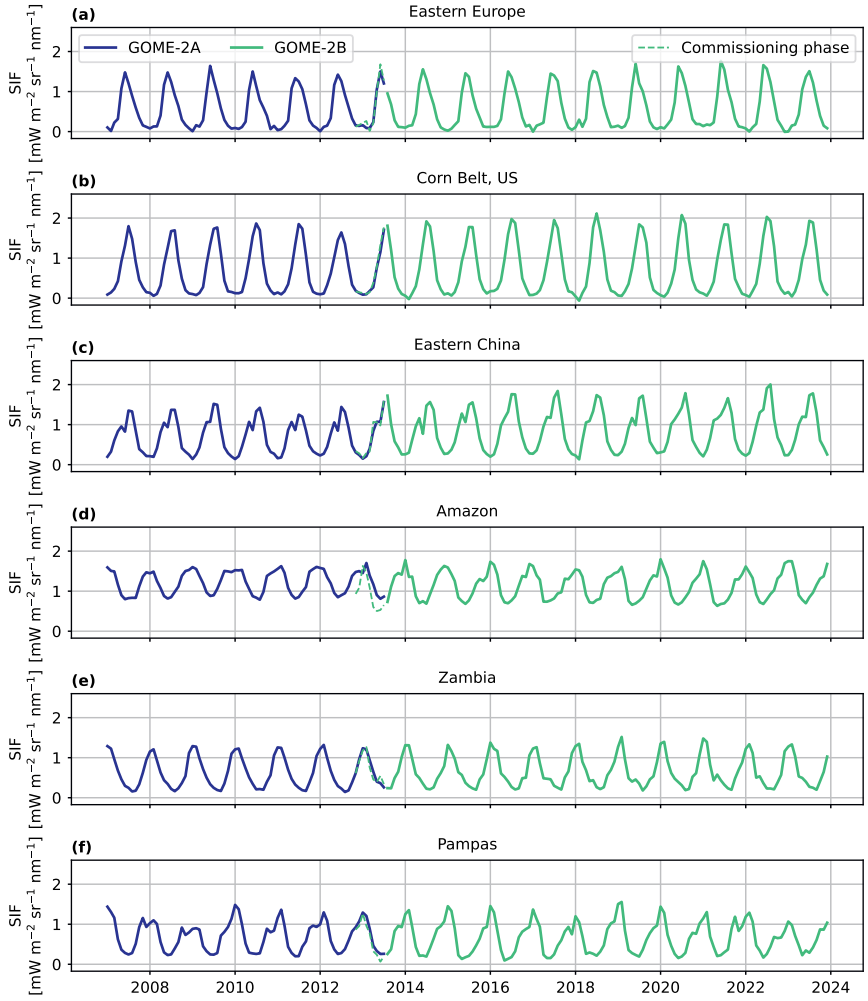


Figure 3.11: Time series of monthly averaged Level-2 SIF values retrieved from GOME-2A (in blue) and GOME-2B (in green) over (a) Eastern Europe, (b) the United States Corn Belt, (c) Eastern China, (d) the Amazon, (e) the Congo Basin, and (f) the Pampas region. GOME-2B SIF observations during the instrument's commissioning phase are indicated by the dashed green line.

U_t as:

$$U_t = \begin{cases} 0, & \text{if } t < T_0 \\ 1, & \text{if } t \geqslant T_0 \end{cases} \tag{3.6}$$

In this equation, U_t is set to 0 during the GOME-2A period (Jan. 2007–June 2013) and switches to 1 from July 2013 onwards during the GOME-2B period. Finally, Ordinary Least Squares (OLS) regression is used to fit the five remaining unknowns: μ, α, β_1, β_2, and δ.

We use the fitted coefficient δ and its p-value to evaluate the existence and magnitude of any step change at transition T_0. Additionally, we apply both the Chow and the Likelihood Ratio (LR) test to evaluate the statistical significance of the potential break. The Chow test evaluates whether regression parameters differ before and after the breakpoint. It tests if the data structure is best described with one or two regressions by fitting the same model to (i) the full GOME-2 dataset, (ii) the data before T_0 (GOME-2A), and (iii) the data after T_0 (GOME-2B). The LR test complements this by comparing the regression results from the full model (including the δU_t term) with a reduced model that excludes the step-change term. A significant p-value from the LR test indicates that including the step-change term significantly improved the fit.

Table 3.2 shows the fit and statistical test results for all cases. The modelled and observed SIF are strongly correlated ($r \geqslant 0.91$), implying that the model in Equation (S2.1) effectively captures the seasonal patterns and long-term trends necessary to detect structural breaks. In most regions, the step change coefficient δ is insignificant, indicating no jump in SIF from T_0. However, significant step changes ($p < 0.05$) are detected within the records across Eastern China and the Amazon. This bias is 0.13 ± 0.04 mW m^{-2} sr^{-1} nm^{-1} over Eastern China and -0.10 ± 0.03 mW m^{-2} sr^{-1} nm^{-1} over the Amazon region, respectively reflecting 16.6 % and 8.9 % of monthly averaged SIF over 2007–2023.

To interpret the detected offset bias δ, we evaluate its magnitude against the underlying uncertainty in SIF. Uncertainty in SIF retrieval can be distinguished into random errors and systematic errors. The first vary stochastically, arise from, for example, fit residual noise or sampling divergence, and decrease through averaging. Due to the spatial and temporal averaging applied here, random errors are small relative to the detected offsets. Systematic errors originate from algorithmic settings and persist despite averaging (Jacob et al., 2016). To obtain a first-order estimate of these systematic errors, independently of regional offsets, we performed sensitivity tests over the Congo Basin, a region previously used as a sensitivity testbed in Chapter 2. We perturbed the settings of four distinct retrieval steps: (i) the degradation correction, (ii) the PCs, (iii) the interpolation across the slit function (as discussed in detail in Chapter 2), and (iv) the latitude bias correction to assess their sensitivity. The largest sensitivity arises from the PCs used within the fitting model, particularly the number of PCs chosen to represent the atmospheric transmission. Varying the number of PCs from 10 to 6 led to a divergence of 0.47 mW m^{-2} sr^{-1} nm^{-1} for GOME-2B SIF at 14 January 2017 over the Congo Basin. Combining the uncertainties from the four perturbed retrieval settings gives an illustrative value of 0.55 mW m^{-2} sr^{-1} nm^{-1}. Retrieval sensitivities of comparable order are expected in other regions, including Eastern China and the Amazon. Details on these tests are provided in supplement S2.5.

Table 3.2: Results of the regression fit, Chow test, and Likelihood Ratio (LR) test. The given uncertainty in δ represents one standard deviation of the estimated coefficient. The column r provides the Pearson correlation between the model fit and the monthly SIF time series. Significance is indicated by "Y" (yes) when the coefficient or test is statistically significant at the 95 % confidence level with $p < 0.05$. If the p-value exceeds 0.05, "N" (no) is indicated. For clarity, "Y" is underlined. More detailed results of the regression fit are shown in Table S2.5, and the results of the Chow and LR test are summarised in Table S2.6.

Regions	Regression fit			Breakpoint significance	
	r	Coefficient δ			
		Values/bias A-B	Significant?	Chow test	Likelihood Ratio test
		[mW m-2 sr-1 nm-1]	(Y/N)	(Y/N)	(Y/N)
Eastern Europe	0.92	$9.66 \times 10^{-4} \pm 0.05$	N	N	N
Corn Belt, US	0.94	0.06 ± 0.06	N	N	N
Eastern China	0.94	0.13 ± 0.04	Y	N	Y
Amazon	0.94	-0.10 ± 0.03	Y	N	Y
Zambia	0.95	0.03 ± 0.03	N	N	N
Pampas	0.91	-0.03 ± 0.04	N	N	N

The offsets δ detected in Eastern China (+0.13) and the Amazon (−0.10) are smaller than the estimated systematic error of 0.55 mW m^{-2} sr^{-1} nm^{-1}. This indicates that the offsets lie within the range of retrieval sensitivities, but they nevertheless represent a persistent inter-sensor difference. Additionally, the LR test confirms that the addition of an offset term enhances the model fit for these two regions (Table 3.2). On the other hand, the Chow test results suggest the regression parameters remain consistent over the full GOME-2 record. These results imply that, while there is confidence in a mean-level bias at T_0, the seasonal pattern and structure did not differ significantly before and after July 2013. Therefore, we add the found δ magnitudes as a correction term to the monthly regional SIF values during the GOME-2B period (from July 2013 onward) to align the records of GOME-2A and GOME-2B and support the use of both records as one consistent record. The corrected time series for Eastern China and the Amazon are shown and evaluated in subsection 3.5.2.

Finally, we verify the impact of the correction on the record's coherence by using an independent dataset as a reference. Specifically, we use FluxSat GPP data, which overlaps with the analysed period from January 2007 to December 2020 (Joiner et al., 2018). FluxSat GPP is a satellite-derived global product that uses geometry-adjusted, daily-scaled MODIS MCD43D reflectance data and a machine learning approach to upscale eddy-covariance flux measurements from FLUXNET 2015. Assuming that FluxSat GPP correlates with SIF similarly across both sensors, it serves as a common reference to reveal intersensor biases. Each dataset – GOME-2 SIF with/without intersensor offset correction, and FluxSat GPP – is standardised over January 2007–December 2020 to enable cross-evaluation of their temporal variability. The standardisa-

tion relates the temporal variability to the data's standard deviation. We then compare the average difference between GOME-2 SIF and FluxSat GPP before and from T_0 (July 2013), using both uncorrected and GOME-2 SIF corrected for the detected intersensor offset. The period before T_0 covers January 2007 to June 2013, and the period from T_0 covers July 2013 to December 2020.

Figure 3.12 shows the improvement in temporal consistency between GOME-2 SIF and FluxSat GPP over Eastern China and the Amazon after applying the intersensor offset correction. Before the correction or the alignment of GOME-2A and GOME-2B SIF, the mean difference in SIF and GPP shifts substantially around T_0. Since the datasets are standardised, this shift in SIF–GPP directly reflects the divergence between GOME-2A ($< T_0$, January 2007–June 2013) and GOME-2B SIF ($\geqslant T_0$, July 2013–December 2020) as a fraction of the total variability over time. For example, the alignment of SIF from both sensors reduced their divergence from 27.7 % to 4.6 % of the total variability over the Amazon region – a reduction of 23.1 %. This confirms that the application of the intersensor offset correction enhanced the temporal consistency within the combined GOME-2 record. Note that remaining differences around T_0 (July 2013) may also reflect changes in the SIF–GPP relationships due to changed environmental conditions over time.

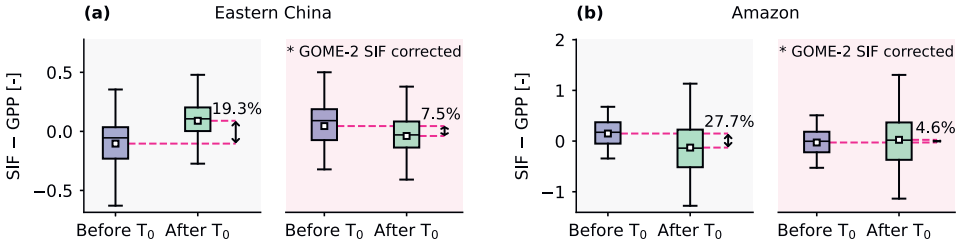


Figure 3.12: Differences in standardised FluxSat GPP and standardised GOME-2 SIF over the period before T_0 (January 2007 to June 2013) and after T_0 (July 2013 to December 2020). Each monthly averaged dataset is standardised by subtracting its mean value (μ) from each value (x_0) and dividing it by its standard deviation (σ); then $x = (x_0\text{-}\mu)/\sigma$. T_0 represents the transition of GOME-2A to GOME-2B SIF in July 2013. The box plots on the right, plotted against a pink background, show the difference between the intersensor offset corrected GOME-2 SIF and FluxSat GPP. The black arrows indicate the difference between averaged SIF–GPP before and after T_0, with the numbers indicating this difference as a percentage of total variability over the 2007–2020 period. The SIF–GPP differences are shown over (a) Eastern China and (b) the Amazon.

Overall, the presented approach to detect and correct for intersensor biases seems effective in enhancing the record's coherence. The methodology shown in this section can be used as a framework to detect, assess, and correct for potential biases between GOME-2A and GOME-2B SIF time series.

3.5.2 Evaluation of GOME-2 SIF against independent datasets

To evaluate whether the combined GOME-2 SIF records consistently track vegetation activity, we compared them to independent satellite-based proxies for photosynthesis: FluxSat GPP (Joiner et al., 2018) and TROPOMI SIF data obtained by (Köhler et al., 2018). Since TROPOMI SIF data is available from early 2018, it is explicitly used for cross-evaluation against the GOME-2B SIF period. Both datasets are widely used to track inter-annual vegetation dynamics. True validation of SIF observation is restricted due to the lack of ground truth. Direct in situ validation is limited due to the mismatch in spatial resolution and the dependence of SIF values on observation time, viewing geometry, and the instrument's spectral characteristics (Mohammed et al., 2019). Therefore, cross-comparison with established independent datasets provides the common practice (e.g., Joiner et al., 2016; Köhler et al., 2018; Köhler et al., 2015; Chapter 2). The correlations between GOME-2 SIF and independent data are shown in supplement S2.4.

Figure 3.13 shows the regional monthly time series of GOME-2 SIF, TROPOMI SIF, and FluxSat GPP, with GOME-2 SIF corrected for intersensor offsets in Eastern China and the Amazon (Section 3.5.1). All datasets were standardised to enable comparison. Across all regions, GOME-2 SIF consistently follows the seasonal cycle of FluxSat GPP with high correlations of $r \geqslant 0.98$ outside the Amazon and $r = 0.92$ over the Amazon. The application of the intersensor offset correction showed a positive impact on these correlations with an increase from $r = 0.97$ to $r = 0.98$ over Eastern China and from $r = 0.91$ to $r = 0.92$ over the Amazon (shown in Figure S2.19). Although these improvements are modest, they nonetheless suggest that applying the bias correction enhances the temporal consistency.

GOME-2 SIF also agreed strongly with TROPOMI SIF (January 2018 to December 2022), with $r = 0.86$ over the Amazon and $r \geqslant 0.95$ elsewhere. In Eastern China, GOME-2 SIF often reveals an early-season peak, which FluxSat GPP does not capture. This feature is also present in TROPOMI SIF (e.g., in 2022), suggesting that SIF is sensitive to subtle phenological features not reflected in reflectance-based GPP.

When evaluated separately, e.g., in Zambia, GOME-2A SIF generally demonstrates slightly higher correlations with FluxSat GPP ($r = 0.98$) than GOME-2B SIF ($r = 0.94$), resulting in an overall lower correlation for the combined record ($r = 0.96$). While these analyses are based on different periods and should therefore be interpreted with caution, they suggest enhanced robustness within the GOME-2A SIF record. This is consistent with larger uncertainty within GOME-2B SIF as compared to GOME-2A SIF (Figure 3.6). Nevertheless, GOME-2B SIF maintains strong correlations with both FluxSat GPP and TROPOMI SIF, indicating that the underlying signals remain sufficiently robust.

Overall, these results indicate that the combined GOME-2 SIF record does not exhibit temporal biases or inconsistencies, including false trends induced by instrumental artefacts. Together with our findings in Chapter 2, this confirms the effectiveness of the advanced degradation correction applied by SIFTER v3 to enable robust and temporally consistent SIF records from both GOME-2A and GOME-2B SIF. When small intersensor offsets are present, our framework in Section 3.5.1 has proven effective in resolving these biases and enabling GOME-2A and GOME-2B to

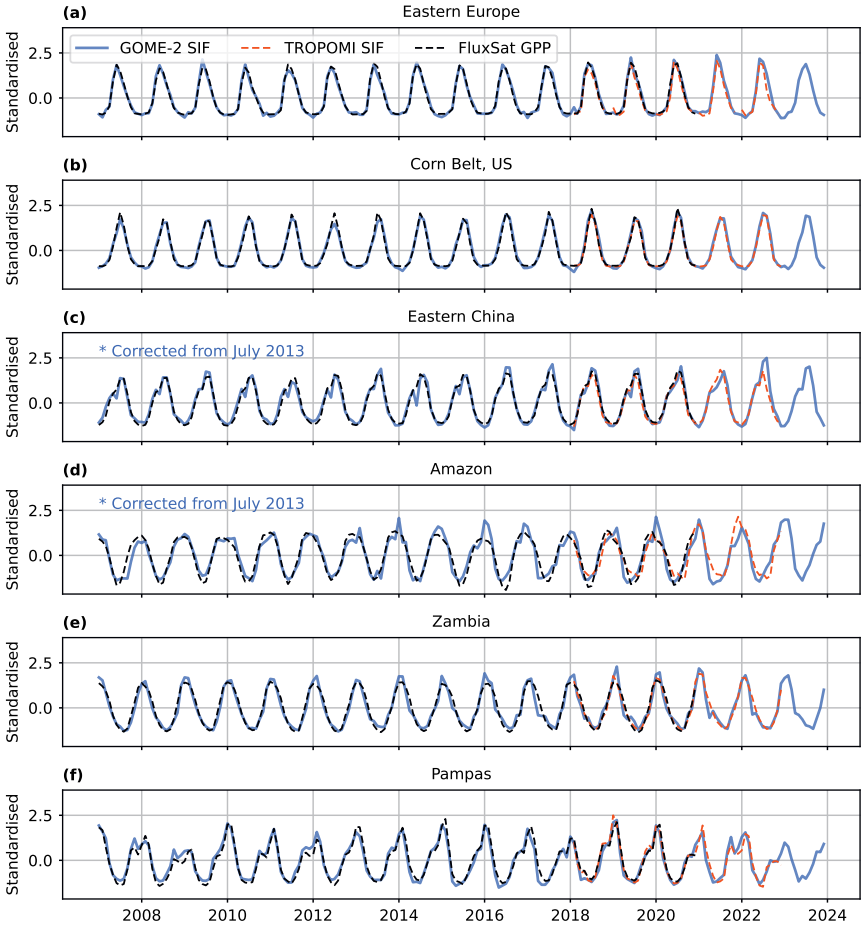


Figure 3.13: Time series of standardised SIF retrieved from GOME-2 (solid blue), FluxSat GPP (dashed black) and TROPOMI SIF (dashed orange). Since the GOME-2 dataset covers the entire FluxSat GPP period, it is standardised based on the same timespan (January 2007–December 2020). This enhances the alignment of GOME-2 SIF and FluxSat GPP.

be treated as one long-term dataset for monitoring vegetation activity.

3.6 Conclusions and outlook

We presented a combined GOME-2 SIF dataset spanning from 2007 to 2023, which combines SIF observations retrieved from both GOME-2A and GOME-2B. The GOME-2A SIF record (2007–2017) was retrieved using the SIFTER v3 retrieval algorithm in Chapter 2. Here, we extended this dataset by applying the same algorithm to GOME-2B data from 2013 to 2023. SIFTER v3 incorporates an advanced correction that addresses time, wavelength, and scan angle dependencies of reflectance degradation – resolving temporal inconsistency issues.

Although GOME-2A and GOME-2B are identical in sensor design, they are affected differently by instrumental artefacts. We showed that, if not properly corrected for, these differences can induce intersensor biases. During the overlapping tandem phase, seasonally averaged SIF values from both sensors agreed within 2.1 % when co-sampled across time, space, and viewing geometry. In contrast, failing to address differences in viewing zenith angle (VZA) sampling can introduce biases in GOME-2B SIF of up to 15 % over high SIF regions. This discrepancy mainly arises from intersensor differences in captured VZA ranges, due to the reduced swath mode of GOME-2A.

Statistical analysis revealed no significant step change at the transition from GOME-2A to GOME-2B in mid-2013 for most case studies; however, it detected small offsets in Eastern China and the Amazon. Applying an additive intersensor offset correction in these regions enhanced the temporal coherence of the GOME-2 record and increased its correlation with independent FluxSat GPP. In the Amazon, the correction reduced the absolute SIF − GPP difference across the sensor transition by more than 20 %. Finally, we demonstrated strong coherence between the GOME-2 SIF record and FluxSat GPP ($r \geqslant 0.92$), as well as between GOME-2 SIF and TROPOMI SIF ($r \geqslant 0.87$) across regions with different biomes – supporting its use for long-term monitoring of vegetation activity. Our methodology provides a framework to detect and, when necessary, correct for intersensor-related offsets, enabling the use of GOME-2A and GOME-2B SIF as a one coherent record.

Beyond the use of GOME-2 SIF for long-term monitoring, this study offers practical guidance for harmonising multi-sensor datasets. First, achieving internal consistency within each record is essential before merging. Second, differences in viewing geometry sampling can substantially bias intersensor observations and should be addressed, particularly for wide-swath instruments. Finally, the presented framework could be applied to identify and correct for structural breaks in other multi-sensor records. These insights will be valuable for extending the GOME-2 record with GOME-2C observations and for preparing to combine future SIF observations from Sentinel-5 aboard the upcoming Metop Second Generation A series (Metop-SG-A) satellites, for which SIF retrievals are expected to be technically feasible.

Supplement S2

S2.1 SIFTER v3 algorithm implementation on GOME-2A and GOME-2B

We assess the reflectance degradation characteristics of the specific GOME-2 sensors by studying the changes in globally averaged reflectance for each wavelength λ and scan index s. Figure S2.1 shows that GOME-2A reflectances ($\lambda = 740.1$ nm, $s = 1$ (most eastern)) show a spurious increase in reflectance between 2007 and 2013, followed by a decrease in reflectance between July 2013 and December 2017. The sharp drop in reflectance from July 2013 is due to the reduction of the GOME-2A swath. For GOME-2B, reflectances are more consistent, particularly between 2012 and 2019, but from 2020, a clear impact of instrument degradation occurs.

Figure S2.2 shows the corrected reflectance at $\lambda \approx 740.1$ nm and $s = 1$ for both GOME-2A (nominal swath) and GOME-2B. The corrected time series of the reflectance shows consistency over the long term and a closer connection in observed global reflectance by both sensors. The small offset (∼1.1 %) between the average of corrected GOME-2A and GOME-2B reflectances can likely be attributed to small differences in instrumental characteristics, such as the spectral resolution (see Table 3.1 in Chapter 3).

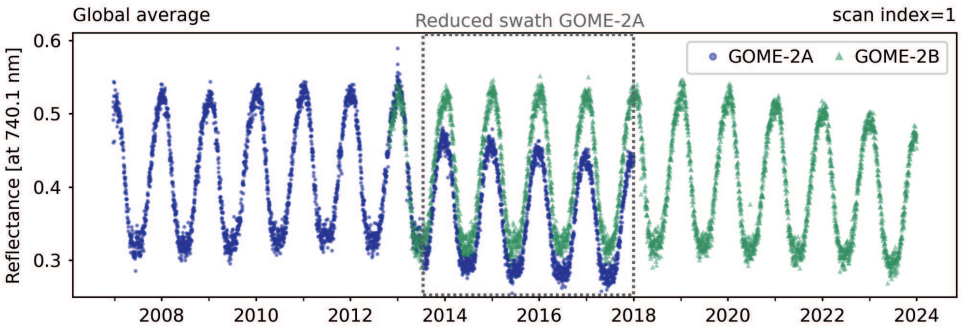


Figure S2.1: Daily averaged global reflectances (at $\lambda = 740.1$ nm) observed by GOME-2A (in blue) and GOME-2B (in green), and between December 2006–December 2017 and November 2012–December 2023, respectively. The observed reflectances are shown for scan index 1. Due to the swath reduction of GOME-2A from mid-July 2013, the subsequent GOME-2A observations are made under a smaller viewing zenith angle, resulting in decreased reflectance.

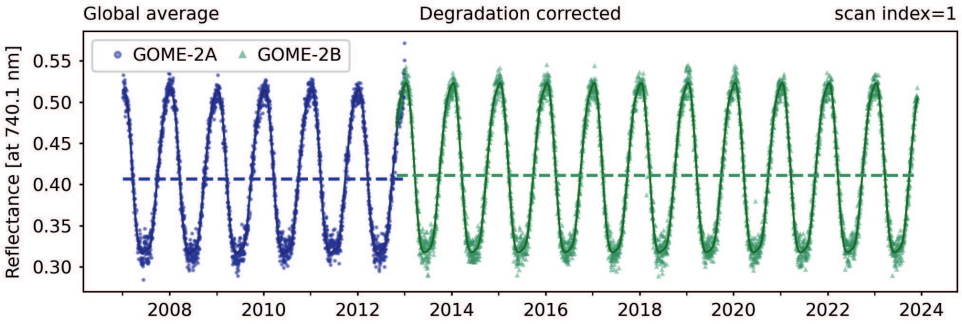


Figure S2.2: Corrected reflectance at $\lambda \approx 740.1$ nm and scan-index $s = 1$ for GOME-2A (under nominal swath, indicated in blue) and GOME-2B (indictated in green) between 2007 and 2023.

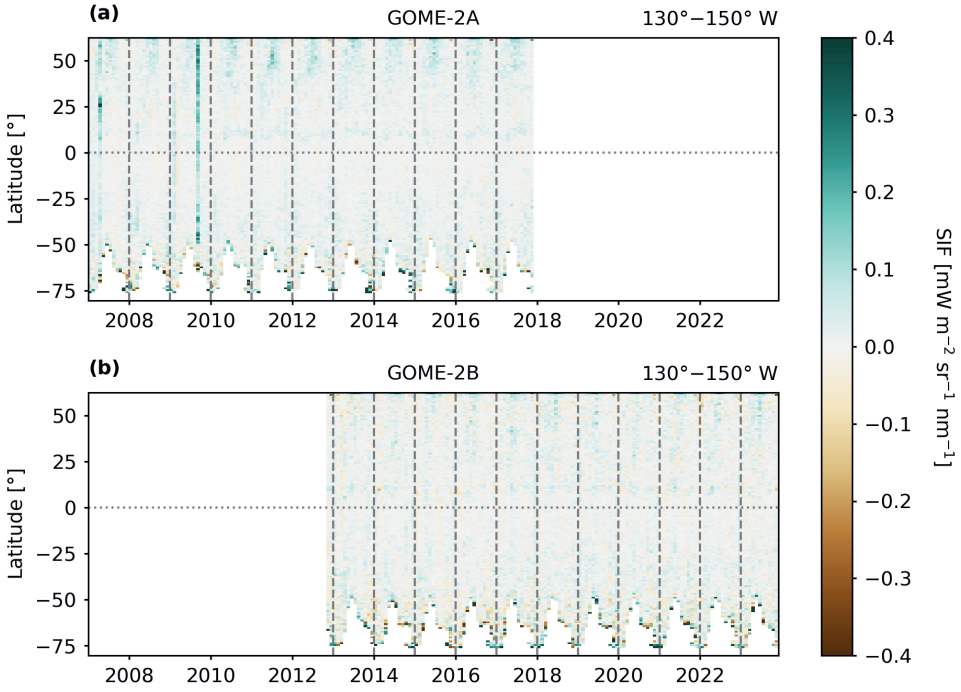


Figure S2.3: Observed SIF retrieved from (a) GOME-2A and (b) GOME-2B across the Pacific ocean, where SIF is expected to be 0, per latitude and over time. The SIF values shown *are* adjusted for the latitude bias.

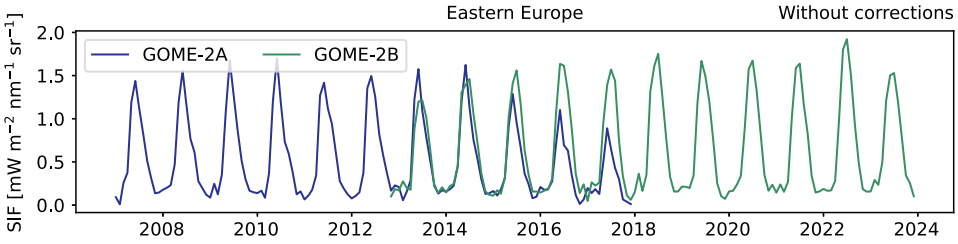


Figure S2.4: Time series of GOME-2A and GOME-2B SIF uncorrected for degradation and latitude bias correction over Eastern Europe.

Table S2.1: Shows fit parameters, analysed periods, etc. for GOME-2A and GOME-2B.

	GOME-2A		GOME-2B
	Nominal swath	Reduced swath	Nominal swath
Level-1b	Release 3 (R3)	Release 3 (R3)	Release 3 (R3)
Cloud parameters	FRESCO+ v2	FRESCO+ v2	FRESCO+ v2
Degradation correction			
- Dependencies	t (day), λ, s	t (day), λ, s	t (day), λ, s
- Reference day (t=0)	5 Jan. 2007	5 Jan. 2007 *	1 Nov. 2012
- Polynomial order, p	2	3	5
- Fourier order, q	6	6	6
- Fit period	Jan. 2007–Dec. 2012	Jan. 2007–Dec. 2017 *	Nov. 2012–Nov. 2023
- Applied period	Jan. 2007–15 July 2013	16 July 2013–Dec. 2017	Nov. 2012 –Dec. 2023
Retrieval window			
- Spectral range	734–758 nm	734–758 nm	734–758 nm
- Number of points	118	118	117
Principal components			
- Number of PCs	10	10	10
- Collected data	2007–2012	2007–2012, VZA<35°	2013–2018
- Degradation corrected	Yes	yes	yes
- Pre-treatment method	Autoscaling	Autoscaling	Autoscaling

* values measured in nominal swath interpolated to viewing angles corresponding to reduced swath

S2.2 Comparison of GOME-2A and GOME-2B SIF

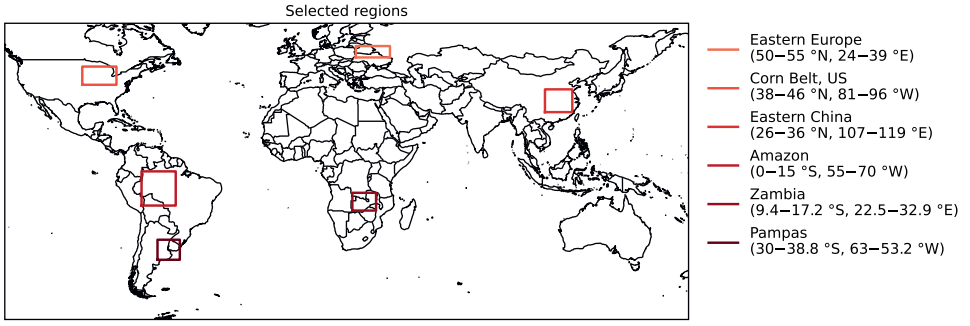


Figure S2.5: Locations of the studied regions in Chapter 3.

Spatial comparison

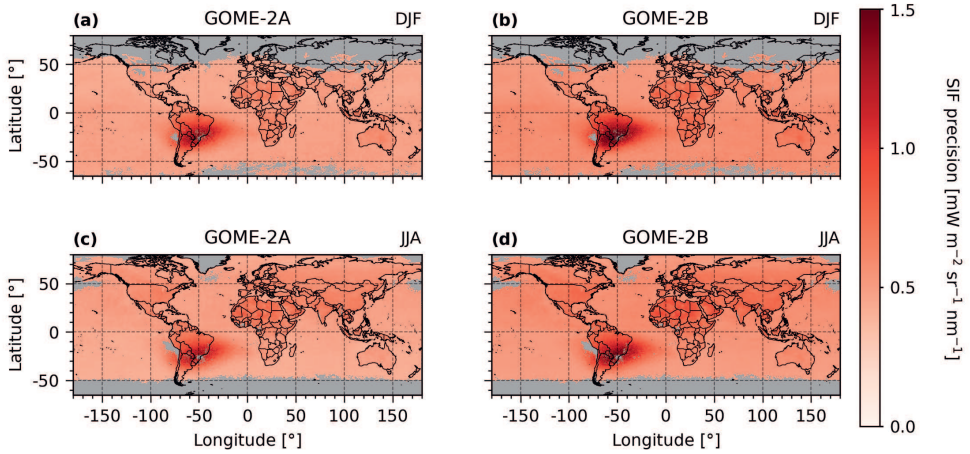


Figure S2.6: Seasonal averaged SIF precision observed by GOME-2A and GOME-2B over June–August 2016 (a,b), and December–February 2016 (c,d). Larger uncertainty in SIF retrievals is noted over areas influenced by the South Atlantic Anomaly (SAA), including the Amazon region.

Viewing geometry

Table S2.2: Seasonally (JJA and DJF 2014–2017) averaged GOME-2A and GOME-2B SIF over different regions and shown over different ranges of the viewing zenith angles. For GOME-2A, only the [−35°, +35°] range is shown, as GOME-2A operated under reduced swath in the shown period.

Region	Season 2014-2017	[−35°, +35°] GOME-2A	[−35°, +35°] GOME-2B	[−52°, +52°] GOME-2B
		[mW m^{-2} sr^{-1} nm^{-1}]		
Eastern EU	DJF	0.09	0.07	0.10
	JJA	1.21	1.22	1.28
US Cornbelt	DJF	0.13	0.10	0.12
	JJA	1.72	1.76	1.81
Eastern China	DJF	0.27	0.26	0.28
	JJA	1.29	1.46	1.51
Amazon	DJF	1.51	1.42	1.57
	JJA	0.88	0.80	0.82
Zambia	DJF	1.01	1.07	1.15
	JJA	0.28	0.29	0.30

Table S2.3: Regional averages of GOME-2B SIF observations over DJF 2014–2017 and JJA 2014–2017 for the most eastward and westward pixels. Eastward includes ground pixels with viewing zenith angles VZA < −35°, whereas westward includes ground pixels with VZA > +35°. This refers to the 6 first and 6 last across-track ground pixels, respectively.

Region	Season 2014–2017	Eastward	Westward	Difference W/E
		[mW m^{-2} sr^{-1} nm^{-1}]		[%]
Eastern EU	DJF	0.10	0.16	-
	JJA	1.18	1.51	+28
US Cornbelt	DJF	0.12	0.17	-
	JJA	1.65	2.08	+26
Eastern China	DJF	0.27	0.33	+22
	JJA	1.42	1.72	+21
Amazon	DJF	1.46	1.97	+35
	JJA	0.75	0.91	+21
Zambia	DJF	1.07	1.40	+31
	JJA	0.29	0.36	+24

Collocation

Two co-sampling experiments are performed to assess the comparability of GOME-2A and GOME-2B SIF. Figure S2.7 illustrates both experiments. Experiment 1 co-samples based on the spatial and temporal overlap, and Experiment 2 co-samples based on the spatial and temporal overlap, and on similarity in viewing geometry. Figure S2.8 demonstrates examples of accepted spatial overlap between GOME-2A and GOME-2B SIF.

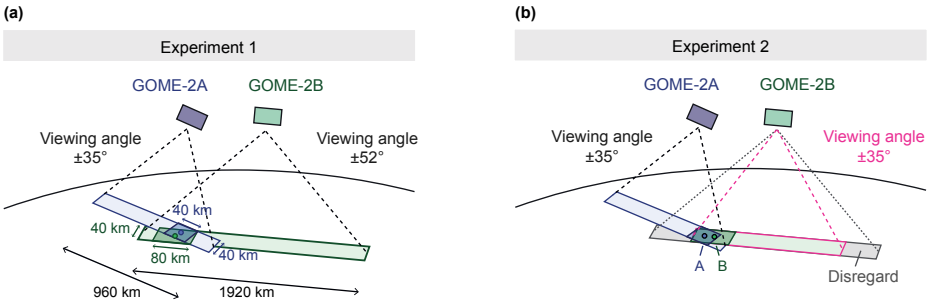


Figure S2.7: Sketch of the co-sampling of Experiments (a) 1 and (b) 2, in which ground pixels from GOME-2A and GOME-2B are spatially and temporally collocated. In addition to the spatial and temporal collocation, in Experiment 2, the viewing zenith angles of GOME-2B pixels need to align with the range of viewing geometry of GOME-2A. In these experiments, GOME-2A refers to observations done under reduced swath (after July 2013).

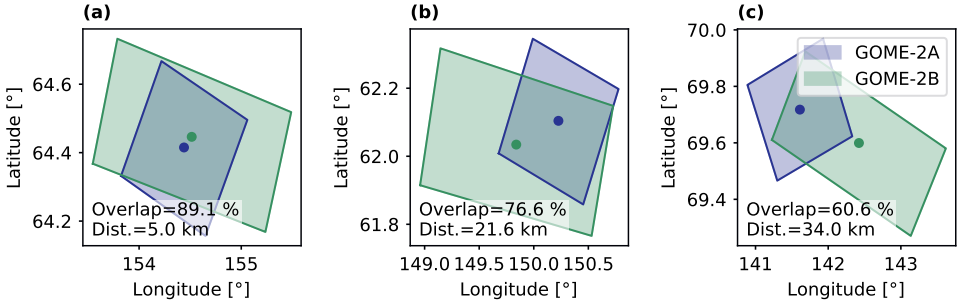


Figure S2.8: Three examples (a–c) of accepted ground pixels of GOME-2A (in blue) and GOME-2B (in green) when applying collocation. All shown ground pixels are observed over land on 15 June 2014.

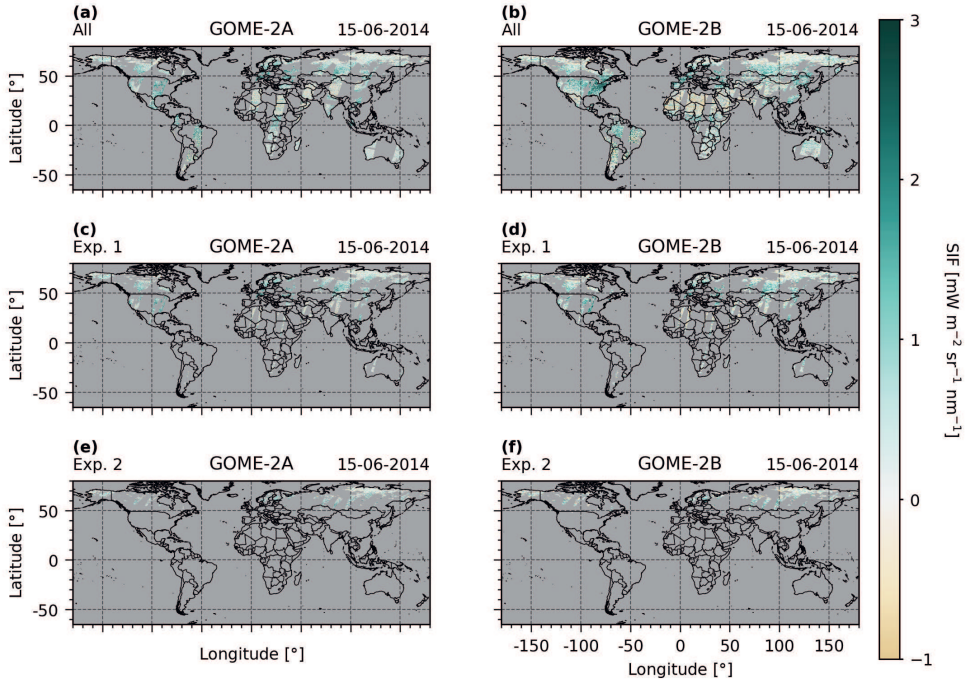


Figure S2.9: Maps of GOME-2A (on the left) and GOME-2B (on the right) showing the selected ground pixels according to each sampling setting of all data (a,b), Experiment 1 (c,d) and Experiment 2 (e,f). All pixels shown are observed over the land on 15 June 2014.

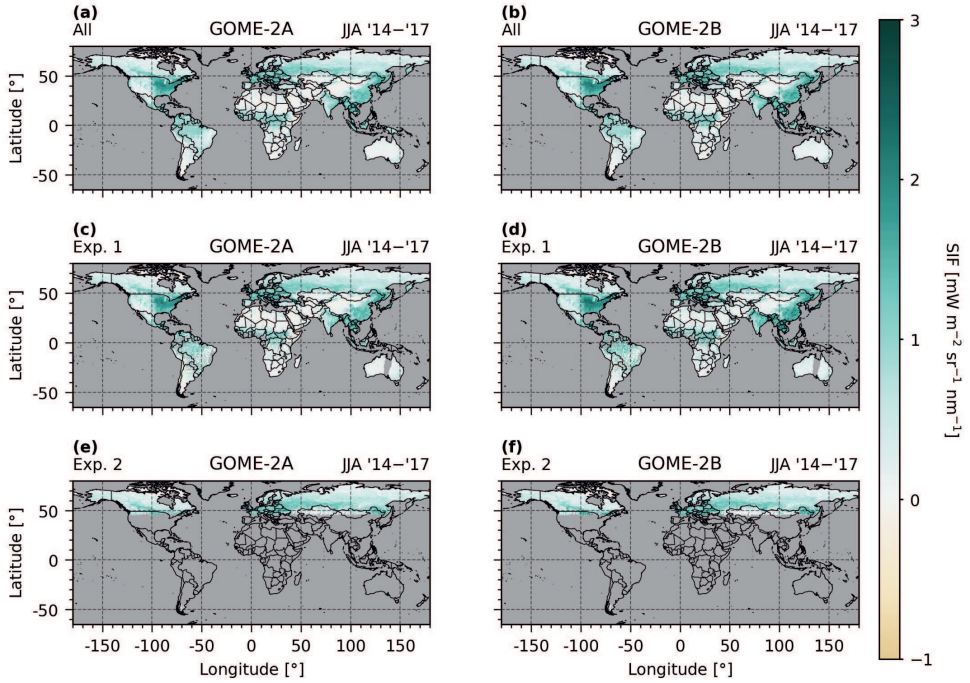


Figure S2.10: Maps show SIF from GOME-2A (left) and GOME-2B (right), averaged over June–August 2014–2017 and gridded on a $0.5^\circ \times 0.5^\circ$ resolution, using all available data (a,b), data selected according to sampling in Experiment 1 (c,d), and data selected according to sampling in Experiment 2 (e,f), for each experiment. All grid cells that contain valid data are shown. No filtering on counts per grid cell was applied.

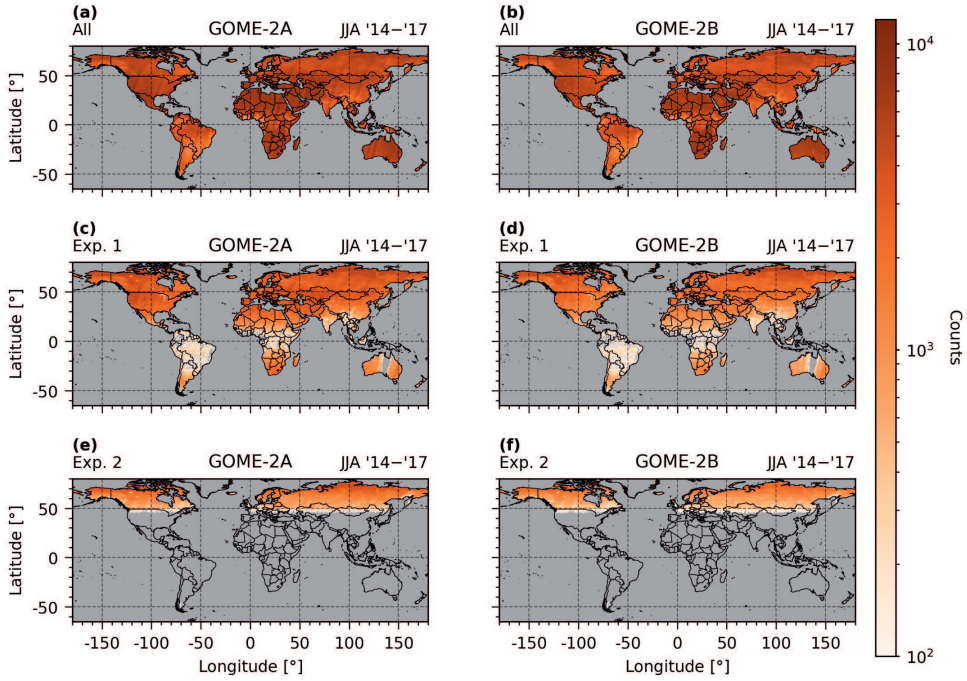


Figure S2.11: Maps show the counts per grid cell of averaged SIF from GOME-2A (left) and GOME-2B (right) over the JJA 2014–2017, using all available data (a,b), data selected according to sampling in Experiment 1 (c,d), and data selected according to sampling in Experiment 2 (e,f), for each experiment. During the gridding process, each ground pixel was divided into 16 ground pixel segments, whereafter each segment was attributed to a grid cell. The counts represent the number of ground pixel segments within each grid cell.

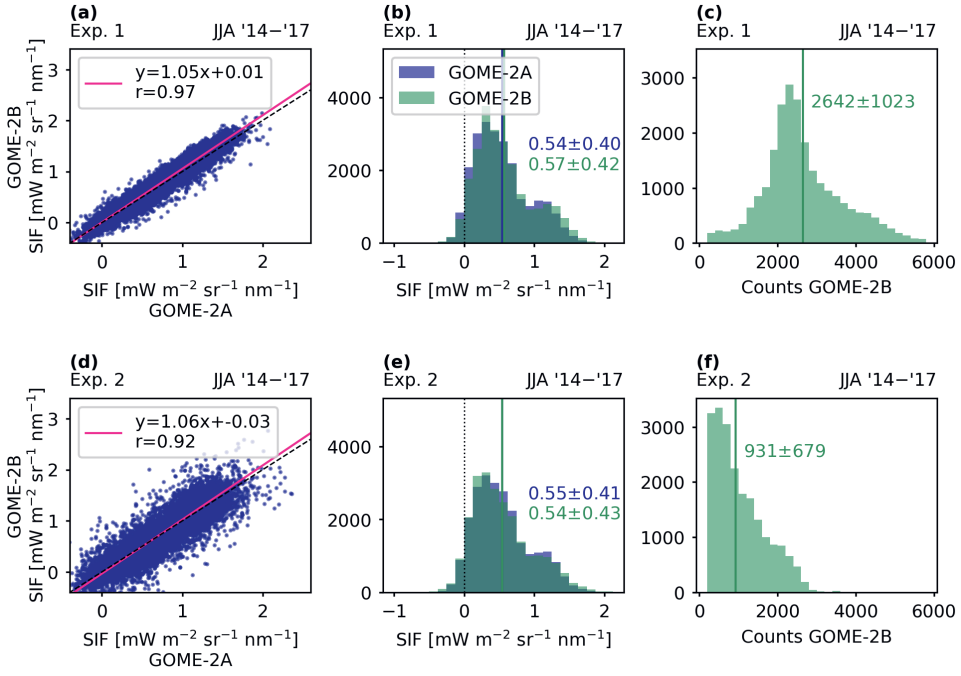


Figure S2.12: Comparison plots between GOME-2A and GOME-2B SIF observations, following the sampling selection according to Experiment 1 (upper plots) and Experiment 2 (lower plots), using all data (*full*). Subplots (a,d) show the correlation between GOME-2A and GOME-2B SIF using reduced major axis (RMA) regression, and r represents the Pearson correlation. Subplots (b,e) show the histogram plots of GOME-2A and GOME-2B SIF, and subplots (c,f) show the histograms of the ground pixel segments counts per grid cell.

Reduced version of Experiment 1

The lower correlation in Experiment 2 may be attributed to the substantially lower number of observations within each grid cell, approximately a 0.35:1 ratio compared to Experiment 1 (Figure S2.11). To enable a more balanced statistical comparison between the experiments, we subsampled Experiment 1's observation days to better match the number of observations per grid cell. In this *reduced* setup, Experiment 1 was run using 128 randomly selected days from the JJA 2014–2017 period. The 128 days reflect the approximate 0.35:1 ratio in the average number of GOME-2B pixel segments per grid cell between Experiment 2 and 1 (Figure S2.12c,f). Experiment 2 was run using data from all 366 days, but only grid cells with valid observations in both experiments were included in the comparison. Additionally, a stricter requirement for the minimum number of pixel segments per grid cell was set at $\mu - \sigma$, where μ and σ represent the mean and standard deviation of GOME-2B pixel segment counts in the *reduced* Experiment 1.

Table S2.4 summarises the comparison results between GOME-2A and GOME-2B SIF for the *full*

and *reduced* setups in Experiments 1 and 2. The Pearson correlations of 0.95 (Experiment 1) and 0.96 (Experiment 2) indicate strong coherence between the datasets, even without accounting for differences in VZA range. Furthermore, the metrics show a bias of higher GOME-2B SIF values, particularly for larger SIF values. However, the comparisons between Experiments 1 and 2 indicate that this bias is largely driven by the inclusion of larger viewing angles in GOME-2B observations. When GOME-2A and GOME-2B SIF observations were matched in VZA range, the bias was reduced to ∼2 %. Our results increase our confidence in the consistency between GOME-2A SIF observations prior to July 2013 and GOME-2B SIF observations (post-July 2013), when both sensors operated with the same 1920 km swath and ground pixel configuration. Note that this reduced experiment has been repeated five times (not shown), yielding similar results.

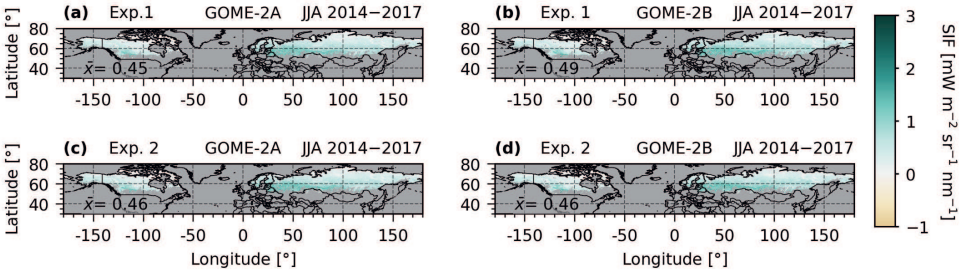


Figure S2.13: GOME-2A (left subplots) and GOME-2B (right subplots) sampled according to Experiments 1 and 2 and averaged over the June–August (JJA) period between 2014 and 2017 on a $0.5° \times 0.5°$ spatial grid. Grid cells are shown when SIF values were available in both datasets and experiments. Furthermore, the number of pixel segments must exceed the $\mu - \sigma$ threshold. With μ and σ representing the average and standard deviation of the average pixel segment counts per grid cell of GOME-2B Experiment 1 data. The mean for each SIF dataset and experiment is shown as $\overline{x}$. The data represents all available data in Experiment 2, but a subsample in Experiment to match the number of ground pixel segment counts in both Experiments.

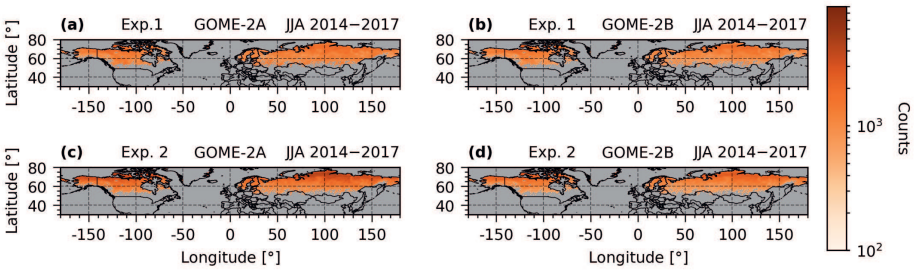


Figure S2.14: Maps show the counts per grid cell of averaged SIF from GOME-2A (left) and GOME-2B (right) over the JJA 2014–2017, according to sampling in Experiment 1 (a,b), and data selected according to sampling in Experiment 2 (c,d). Experiment 1 uses a subset of the available data (128/366 days) to equalise the counts between both experiments and to allow for a fairer comparison between the two. During the gridding process, each ground pixel was divided into 16 ground pixel segments, whereafter each segment was attributed to a grid cell. The counts represent the number of ground pixel segments within each grid cell.

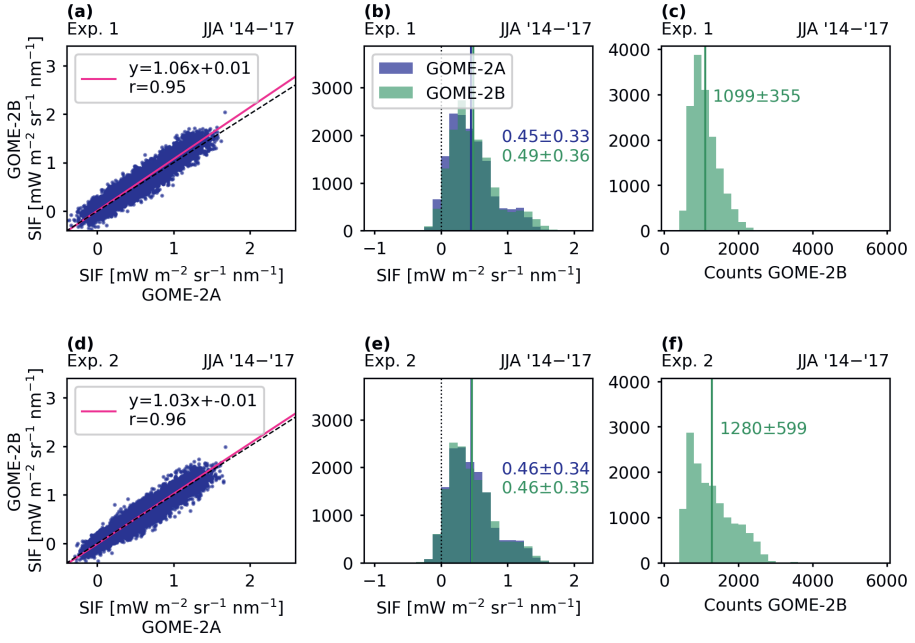


Figure S2.15: Comparison plots between GOME-2A and GOME-2B SIF observations, following the sampling selection according to Experiment 1 (upper plots) and Experiment 2 (lower plots), using a subset of the data for Experiment 1 to enable an equitable statistical comparison (*reduced*). Subplots (a,d) show the correlation between GOME-2A and GOME-2B SIF using reduced major axis (RMA) regression, and r represents the Pearson correlation. Subplots (b,e) show the histogram plots of GOME-2A and GOME-2B SIF, and subplots (c,f) show the histograms of the ground pixel segments counts per grid cell.

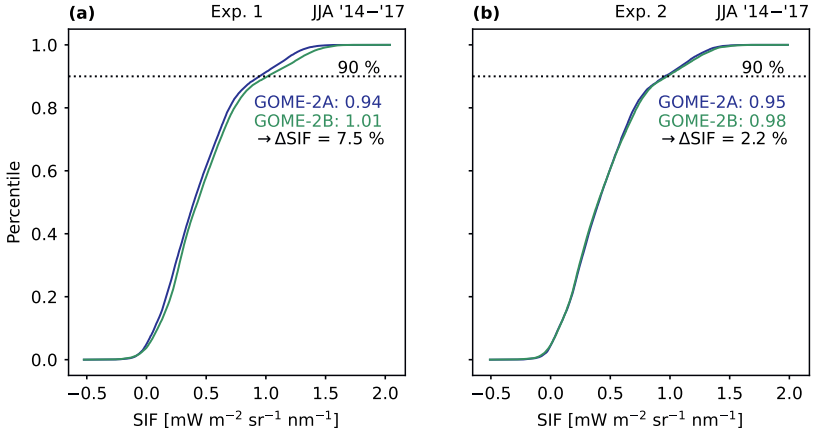


Figure S2.16: ECDF plots of GOME-2A SIF (in blue) and GOME-2B SIF (in green) in (a) Experiment 1 and (b) Experiment 2. SIF observations are averaged over the JJA 2014–2017 period and cover approximately 50° N to 80° N. The dashed black line indicates the 90th percentile line. The value at the 90th percentile for GOME-2A and GOME-2B SIF is shown, as well as the differences between them (in percentages). The data shown here refers to the *reduced* setup, where a selected subset of data is used in Experiment 1 to equalise the pixel counts per grid cell between both Experiments.

Table S2.4: Comparison of statistical and distributional metrics between GOME-2A and GOME-2B SIF observations averaged over the JJA 2014–2017 period, across two collocation experiments using all available observations within the period (*full*) and a *reduced* data sensitivity test. The sensitivity test aimed to equalise the number of pixels per grid cell between the two experiments. Observations cover the Northern latitudes between approximately 40° N and 80° N. Data and analysis of the *reduced* sensitivity test are visualised in Figs. S2.13–S2.16.

	Full		*Reduced*	
Metric	Exp. 1	Exp. 2	Exp. 1	Exp. 2
GOME-2A SIF mean	0.54 mW m^{-2} sr^{-1} nm^{-1}	0.55	0.45 mW m^{-2} sr^{-1} nm^{-1}	0.46
GOME-2B SIF mean	0.57 mW m^{-2} sr^{-1} nm^{-1}	0.54	0.49 mW m^{-2} sr^{-1} nm^{-1}	0.46
$\text{Correlation}_{\text{A,B}}$	0.97	0.92	0.95	0.96
Slope	1.05	1.06	1.06	1.03
Intercept	0.01	−0.03	0.01	−0.01
$\Delta\text{SIF}_{\text{90th perc., A,B}}$	6.9%	1.7%	7.5%	2.2%
$\text{Mean N per point}_{\text{B}}$	2642	931	1099	1280
Days JJA '14–'17	366	366	128	366

S2.3 Consistency tests of GOME-2A and GOME-2B SIF

Here, we provide the full regression results and statistical tests underlying the analysis in Section 3.5.1 in Chapter 3. For clarity, the regression equations used in the analysis are repeated here:

$$y_t = \mu + \alpha t + S_t + \delta U_t + \varepsilon_t \tag{S2.1}$$

where y_t represents the regional SIF value at month t, μ the monthly mean, αt the linear trend over time, S_t the seasonal component, δU_t the mean level shift term, and ϵ_t the residual of the observed and fitted SIF.

The seasonal component represents the annual cycle of SIF as a first-order harmonic:

$$S_t = \beta_1 \sin\left(\frac{2\pi(t-\phi)}{12}\right) + \beta_2 \cos\left(\frac{2\pi(t-\phi)}{12}\right) \tag{S2.2}$$

where β_1 and β_2 control the amplitude, and ϕ represents the phase shift.

Table S2.5 shows the regression results of the model fit in Equation S2.1 for all studied regions. Although the coefficient α is found to be insignificant across all regions, excluding this term substantially affected the step-change coefficient δ, suggesting that an underlying trend is otherwise confounded by δ. Note that the model does not account for interannual variation, limiting detailed analysis of phenological changes or other complex year-to-year dynamics. However, the strong correlation ($R^2 \geqslant 0.83$) between the modelled and observed SIF indicates a reliable fit for detecting and estimating the step-change coefficient δ. Figure S2.17 shows the fitted (in pink) and observed SIF (in blue dots) across all six regions.

Table S2.5 shows the results of the Chow and Likelihood Ratio (LR) tests for all studied regions. Regions with significant p-values are indicated with a star, * for $p < 0.1$ and ** for $p < 0.05$.

Table S2.5: Regression results of the model fit (Equation S2.1 in Chapter 3) for all studied regions. Although the coefficient α is found to be insignificant across all regions, excluding this term substantially affected the step-change coefficient δ, suggesting that an underlying trend is otherwise confounded by δ.

Regression results	Eastern Europe	Corn Belt US	Eastern China	Amazon	Zambia	Pampas
R^2	0.85	0.88	0.89	0.88	0.90	0.83
$R^2_{\text{adj.}}$	0.85	0.88	0.88	0.88	0.89	0.83
RMSE [mW m^{-2} sr^{-1} nm^{-1}]	0.20	0.22	0.16	0.11	0.12	0.16
ϕ	0.02	0.02	0.60	0.97	0.60	0.60
μ [mW m^{-2} sr^{-1} nm^{-1}]	0.53**	0.67**	0.68**	1.22**	0.63**	0.70**
α [mW m^{-2} sr^{-1} nm^{-1} month^{-1}]	3.15e-4	−2.84e-5	4.06e-4	2.02e-4	−4.16e-5	−2.18e-5
β_1	0.10**	−0.07**	0.24**	−0.30**	3.20e-4	−0.25**
β_2	−0.66**	−0.85**	−0.59**	0.30**	0.52**	0.43**
δ [mW m^{-2} sr^{-1} nm^{-1}]	9.66e-4	0.06	0.13**	−0.10**	0.03	−0.03

*$p < 0.1$, **$p < 0.005$

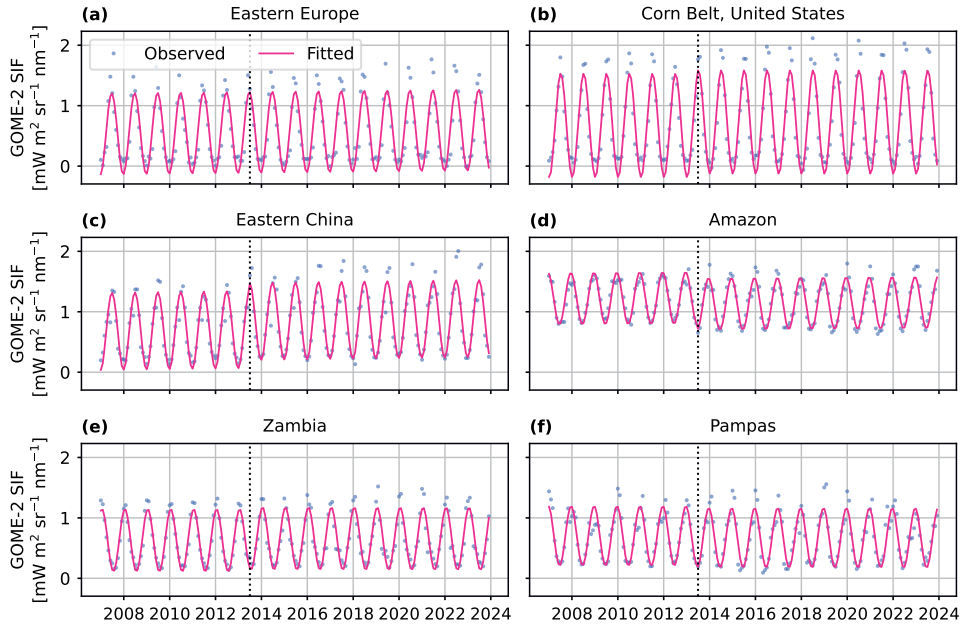


Figure S2.17: Observed monthly averaged GOME-2 SIF (in blue) and the fitted monthly averaged SIF (in pink).

Table S2.6: Results of the Chow and Likelihood Ratio (LR) tests for all studied regions.

	Eastern Europe	Corn Belt	Eastern China	Amazon	Zambia	Pampas
F-test, Chow	0.12	0.37	0.31	1.44	0.17	1.11
p, Chow	0.99	0.90	0.93	0.20	0.98	0.36
Likelihood Ratio (LR)	1.40	3.14	51.48	26.76	2.57	2.04
p, LR	0.24	7.63e-2*	7.23e-13**	2.30e-7**	0.11	0.15
$R^2_{\text{adj.}}$ (full model)	0.849	0.881	0.893	0.888	0.894	0.830
$R^2_{\text{adj.}}$ (reduced model)	0.849	0.880	0.863	0.873	0.893	0.829

*$p < 0.1$, **$p < 0.05$

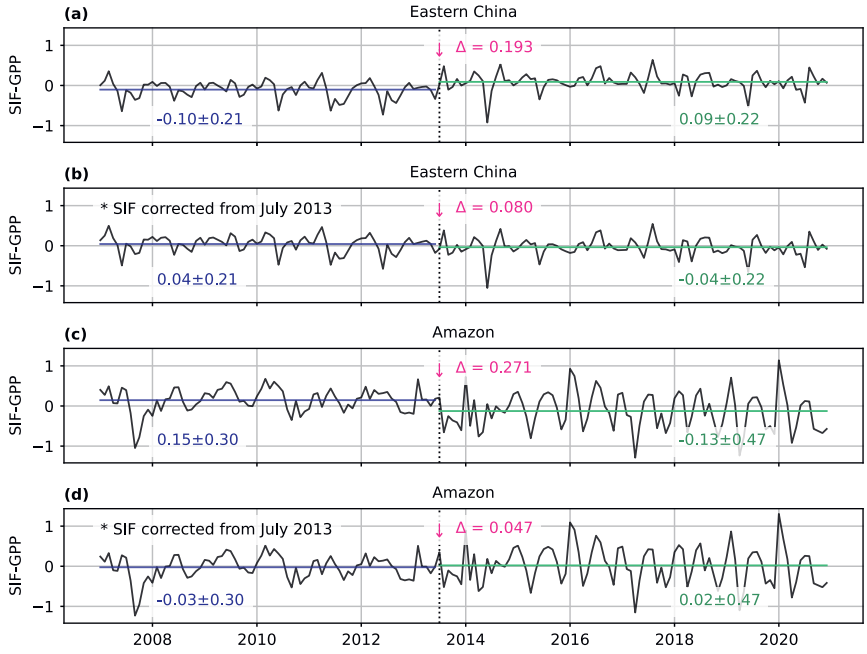


Figure S2.18: Difference between standardised GOME-2 SIF and standardised FluxSat GPP.

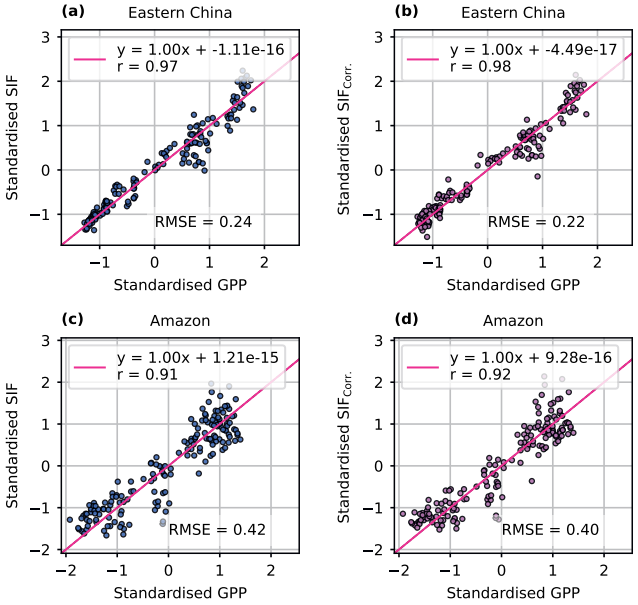


Figure S2.19: Correlations between standardised GOME-2 SIF and standardised GPP over January 2007–December 2020 for both intersensor offset uncorrected (in blue, plots on the left) and corrected GOME-2 SIF (in pink, plots on the right). Correlations are shown over Easter China (upper plots) and the Amazon region (bottom plots).

S2.4 Evaluation of GOME-2 SIF with independent SIF and GPP data

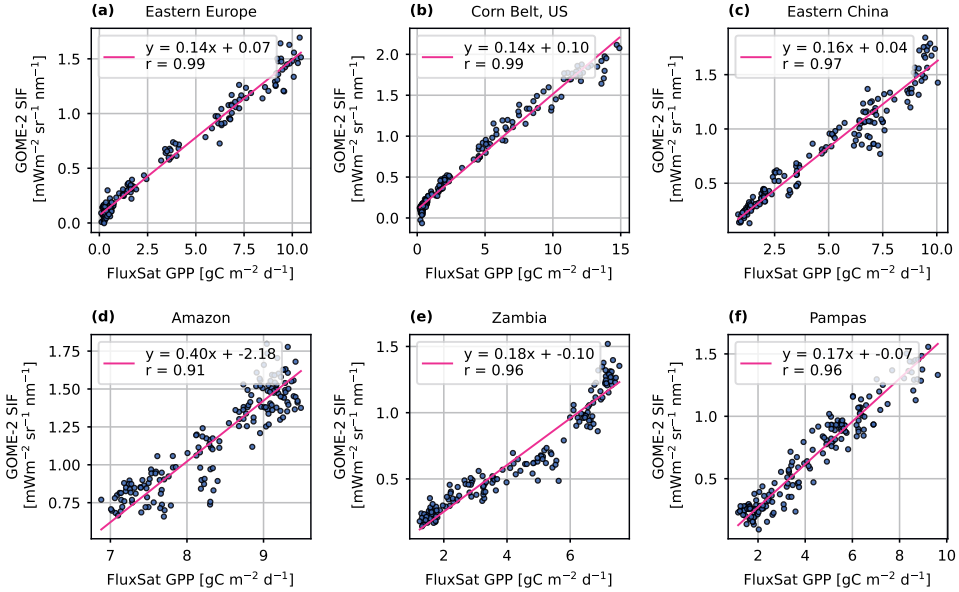


Figure S2.20: Scatterplots of FluxSat GPP values versus GOME-2 SIF across (a) Eastern Europe, (b) the US Corn Belt, (c) Eastern China, (d) Amazon, (e) Zambia, and (f) Southeastern Australia. Data reflects monthly averages ranging from January 2007 to December 2020. The GOME-2 averages between Jan. 2007 and June 2013 reflect GOME-2A data (under nominal swath configuration), and thereafter reflect the GOME-2B data (also under nominal swath configuration). The regression fit is indicated by the blue dashed line and was obtained using reduced major axis regression. The shown correlation (r) represents the Pearson correlation.

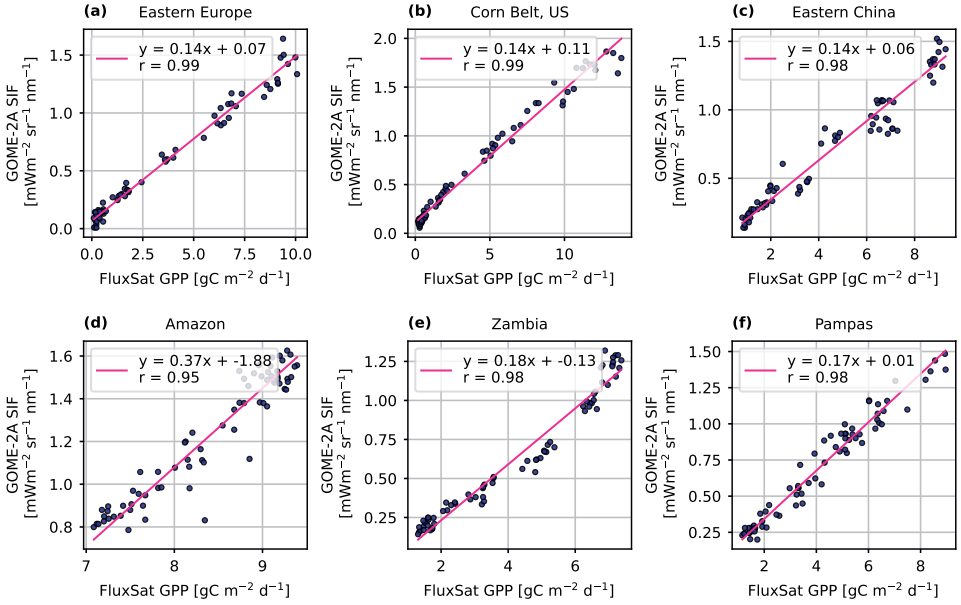


Figure S2.21: Scatterplots of FluxSat GPP values versus GOME-2A SIF across (a) Eastern Europe, (b) the US Corn Belt, (c) Eastern China, (d) Amazon, (e) Zambia, and (f) Southeastern Australia. Data reflects monthly averages ranging from January 2007 to December 2012. During this period, GOME-2A operated in nominal swath (1920 km) configuration. The regression fit is indicated by the blue dashed line and was obtained using reduced major axis regression. The shown correlation (r) represents the Pearson correlation.

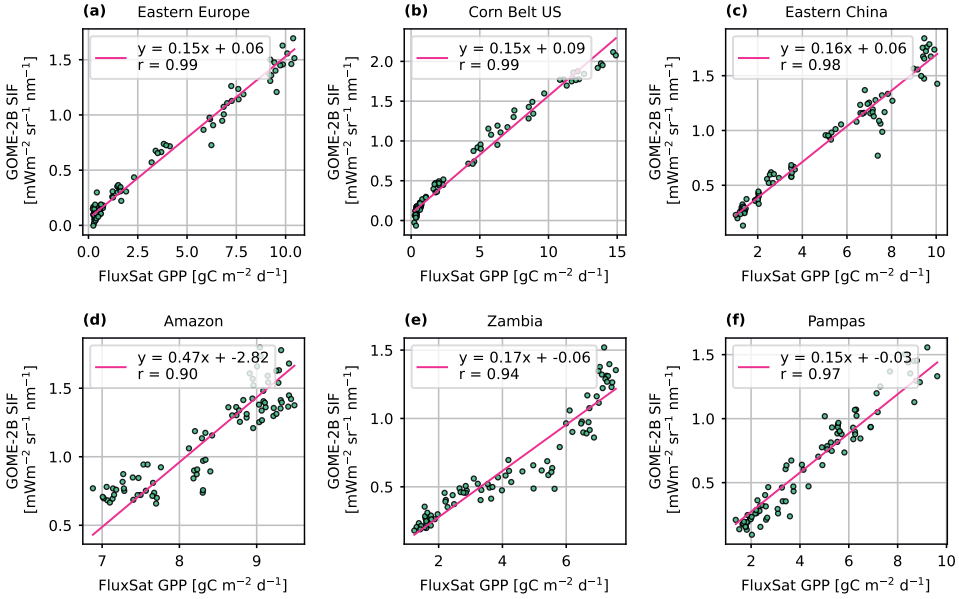


Figure S2.22: Scatterplots of FluxSat GPP values versus GOME-2B SIF across (a) Eastern Europe, (b) the US Corn Belt, (c) Eastern China, (d) Amazon, (e) Zambia, and (f) Southeastern Australia. Data reflects monthly averages ranging from January 2014 to December 2020. The regression fit is indicated by the blue dashed line and was obtained using reduced major axis regression. The shown correlation (r) represents the Pearson correlation.

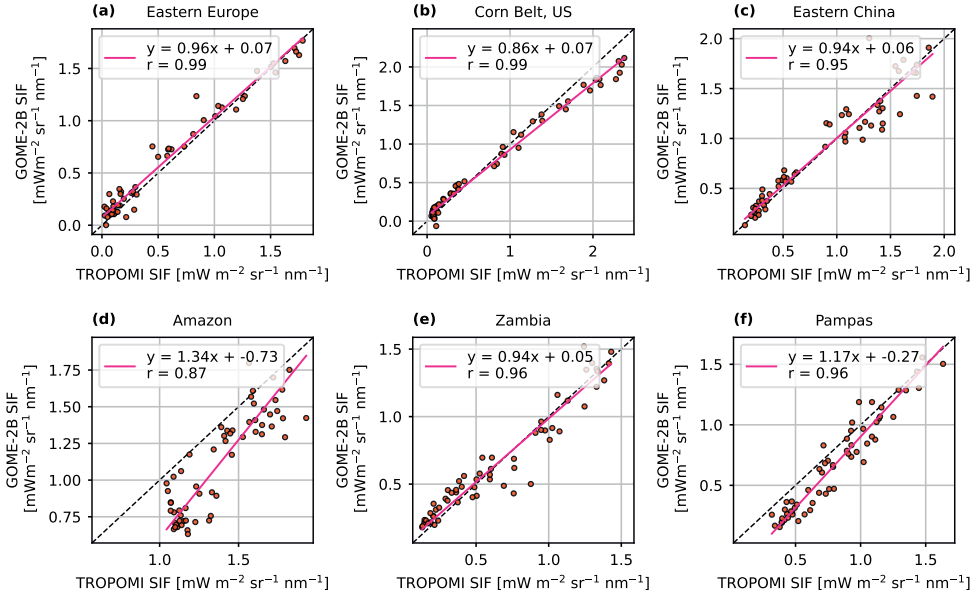


Figure S2.23: Scatterplots of TROPOMI SIF values versus GOME-2B SIF across (a) Eastern Europe, (b) the US Corn Belt, (c) Eastern China, (d) Amazon, (e) Zambia, and (f) Southeastern Australia. Data reflects monthly averages ranging from February 2018 to December 2022. The regression fit is indicated by the blue dashed line and was obtained using reduced major axis regression. The shown correlation (r) represents the Pearson correlation.

Table S2.7: Summary of obtained correlations between FluxSat GPP and GOME-2 records (GOME-2A, GOME-2B, combined GOME-2) across all six studied regions. The correlations are obtained from standardised data.

Regions	FluxSat GPP vs GOME-2 SIF		
	GOME-2A SIF	GOME-2B SIF	GOME-2A,B SIF
	Jan. 2007–Dec. 2012	Jan. 2014–Dec. 2020	Jan. 2007–Dec. 2020
Eastern Europe	$y = 1.00\,x + 2.16\text{e}{-17}$	$y = 1.02\,x + 7.34\text{e}{-19}$	$y = 1.00\,x + 1.48\text{e}{-16}$
	$r = 0.99$	$r = 0.99$	$r = 0.99$
Corn Belt, US	$y = 1.00\,x - 2.16\text{e}{-17}$	$y = 1.02\,x + 1.23\text{e}{-16}$	$y = 1.00\,x + 6.34\text{e}{-17}$
	$r = 0.99$	$r = 0.99$	$r = 0.99$
Eastern China	$y = 1.00\,x - 3.08\text{e}{-17}$	$y = 0.99\,x + 3.50\text{e}{-16}$	$y = 1.00\,x - 5.82\text{e}{-17}$
	$r = 0.98$	$r = 0.98$	$r = 0.97$
Amazon	$y = 1.00\,x - 6.46\text{e}{-16}$	$y = 1.13\,x + 7.00\text{e}{-16}$	$y = 1.00\,x + 1.59\text{e}{-15}$
	$r = 0.95$	$r = 0.90$	$r = 0.91$
Zambia	$y = 1.00\,x - 1.83\text{e}{-16}$	$y = 0.97\,x - 1.66\text{e}{-16}$	$y = 1.00\,x - 7.14\text{e}{-17}$
	$r = 0.98$	$r = 0.94$	$r = 0.96$
Pampas	$y = 1.00\,x + 1.14\text{e}{-16}$	$y = 0.86\,x + 3.48\text{e}{-16}$	$y = 1.00\,x - 2.22\text{e}{-16}$
	$r = 0.98$	$r = 0.97$	$r = 0.96$

S2.5 Sensitivity tests of GOME-2 SIF

To obtain a first-order estimate of the systematic errors within the GOME-2 SIF retrieval, we perturbed several distinct retrieval steps: (i) the degradation correction applied to the reflectance data, (ii) the obtained principal components (PCs) to model the atmospheric transmission, (iii) the interpolation across the slit function, and (iv) the latitude bias correction. For each step, settings were altered within realistic ranges, and the resulting divergence in SIF was evaluated over the Congo Basin area (13° S–6° N, 14–31° W). The maximum difference in average SIF between default (SIFTER v3) and perturbed settings was used as a proxy for the systematic uncertainty contribution of the specific retrieval step. For steps (i), (ii), and (iv), results are shown for GOME-2B SIF on 14 January 2017. For step (iii), slit function interpolation, sensitivity results are shown for GOME-2A SIF on 5 January 2008 and were obtained by Anema et al. (2025a).

Degradation correction

In SIFTER v3, GOME-2 reflectances are corrected for degradation trends by fitting a combination of a polynomial and a Fourier series to global reflectance over time (Equation 3.1 in Chapter 3). The default settings for GOME-2B use a polynomial order $p = 5$ and Fourier order $q = 6$. For the sensitivity test, we reduced the polynomial order to 2, as used for GOME-2A over January 2007–December 2012 (Anema et al., 2025a). The lower polynomial order is expected

to underfit the strong decrease GOME-2B reflectance from around 2020. This change increased averaged SIF by 0.06 mW m^{-2} sr^{-1} nm^{-1}, shown in Table S2.8.

Table S2.8: Summary of sensitivity tests on the degradation correction, comparing polynomial order $p = 5$ (default in SIFTER v3), and $p = 2$. Results are shown for 615 pixels in the Congo Basin (13° S–6° N, 14–31° W) on 14 January 2017, retrieved from GOME-2B observations. Pixels of both tests were co-sampled and had to meet the requirements of autocorrelation < 0.2 and cloud fraction < 0.3. All other retrieval settings were kept at the default setting for GOME-2B. The zero-level offset correction is not applied to these results.

Tests	SIF value	SIF uncertainty
Degr. correction settings	[mW m^{-2} sr^{-1} nm^{-1}]	[mW m^{-2} sr^{-1} nm^{-1}]
$q = 6$, $p = 5$	1.24 ± 0.68	0.69 ± 0.08
$q = 6$, $p = 2$	1.30 ± 0.67	0.68 ± 0.08
Max(ΔSIF value) = 0.06 mW m^{-2} sr^{-1} nm^{-1}		

Principal components (PCs)

The SIFTER v3 retrieval fits a modelled reflectance to the observed reflectance (Equation 3.3 in Chapter 3). To model the reflectance, a set of 10 principal components (PCs) is used to represent the atmospheric transmission. These 10 PCs are obtained from a large collection of spectra over the Sahara Desert. We tested two perturbations: the pre-processing of the collected spectra and the number of PCs used. Using variance scaling (as in SIFTER v2) instead of standard deviation scaling (as in SIFTER v3), increased the averaged SIF by 0.04 mW m^{-2} sr^{-1} nm^{-1} and increased the SIF uncertainty by 0.06 mW m^{-2} sr^{-1} nm^{-1} (Table S2.9), consistent with earlier GOME-2A results obtained by Anema et al. (2025a).

The number of PCs used in the fit retrieval is a known source of uncertainty (van Schaik et al., 2020; Köhler et al., 2015). Too many PCs could result in overfitting, while too few PCs may fail to capture all spectral information. SIFTER v1 originally used 35 PCs, which were reduced to 10 PCs in SIFTER v2 (van Schaik et al., 2020). The number of PCs in comparable SIF retrievals also varies; for example, Köhler et al. (2015) uses 5 PCs for GOME-2 and SCIAMACHY SIF, whereas Guanter et al. (2021) uses 4 or 8 PCs to retrieve TROPOMI SIF, depending on the retrieval window. We therefore progressively reduced the number of PCs from 10 (baseline in SIFTER v3) to 4 and repeated the retrieval (results in Table S2.9). Average SIF was highest with 10 PCs and lowest with 6 PCs, giving a maximum difference of 0.47 mW m^{-2} sr^{-1} nm^{-1}. In absolute terms, the reported SIF uncertainty values were lower for nine or fewer PCs than for 10 PCs; however, the relative uncertainty was lowest for 10 PCs. Nonetheless, these results suggest that using fewer PCs than 10 could potentially enhance the retrieval fit, and reducing the number of PCs should be explored further in future studies.

Taken together, changes in PC pre-processing and the number of PCs showed a maximum spread of 0.51 mW m^{-2} sr^{-1} nm^{-1}, with the number of PCs being the dominant contributor. In Chapter 5, we further assess the impact of the number of PCs on GOME-2 SIF retrieval.

Table S2.9: Summary of sensitivity tests on the PCs, comparing different pre-processing settings and numbers of PCs. The SIFTER v3 default setting is standard deviation (SD) scaling and the use of 10 PCs. Results are shown over 587 pixels in the Congo Basin (13° S–6° N, 14–31° W) on 14 January 2017, retrieved from GOME-2B observations. Pixels of each test were co-sampled and had to meet the requirements of autocorrelation < 0.2 and cloud fraction < 0.3. All other retrieval settings, such as the degradation correction, were kept at the default setting for GOME-2B. The zero-level offset correction is not applied to these results.

Tests		SIF value	SIF uncertainty
Num. of PCs	PC scaling	[mW m^{-2} sr^{-1} nm^{-1}]	[mW m^{-2} sr^{-1} nm^{-1}]
10	PC_{var}	1.27 ± 0.70	0.75 ± 0.08
10	PC_{SD}	1.23 ± 0.67	0.69 ± 0.08
9	PC_{SD}	1.00 ± 0.59	0.57 ± 0.06
8	PC_{SD}	0.91 ± 0.61	0.53 ± 0.06
7	PC_{SD}	0.88 ± 0.63	0.52 ± 0.06
6	PC_{SD}	0.76 ± 0.59	0.53 ± 0.06
5	PC_{SD}	0.79 ± 0.59	0.54 ± 0.07
4	PC_{SD}	0.80 ± 0.62	0.54 ± 0.08

Max(ΔSIF value) = 0.51 mW m^{-2} sr^{-1} nm^{-1}

Latitude bias correction

This post hoc adjustment accounts for observed biases in SIF, which are most likely caused by varying slit functions across latitude. To correct for this bias, regression coefficients between reflectance (at 744 nm) and SIF are obtained from collected data over ocean regions, up to 14 days back within each 1° latitude band (van Schaik et al., 2020; Anema et al., 2025a). In SIFTER v3, two changes were introduced compared to v2: the cloud fraction filter (< 0.4) was removed, allowing data to be used, and the correction was based on subsets of both the Pacific and Atlantic Oceans, as described in Chapter 2.

For the sensitivity test, we applied the latitude bias correction using both the SIFTER v2 and SIFTER v3 settings. The averaged SIF over the Congo Basin differed by 0.05 mW m^{-2} sr^{-1} nm^{-1} between the two tests (Table S2.10).

Table S2.10: Summary of sensitivity tests on the latitude bias correction, comparing settings as done in SIFTER v3 and SIFTER v2. Results are shown over 624 pixels in the Congo Basin (13° S–6° N, 14–31° W) on 14 January 2017, retrieved from GOME-2B observations. Pixels of both tests were co-sampled and had to meet the requirements of autocorrelation < 0.2 and cloud fraction < 0.3. All other retrieval settings were kept at the default setting for GOME-2B.

Tests	SIF value	SIF uncertainty
Lat. bias correction settings	[mW m^{-2} sr^{-1} nm^{-1}]	[mW m^{-2} sr^{-1} nm^{-1}]
SIFTER v3	0.88 ± 0.69	0.70 ± 0.08
SIFTER v2	0.93 ± 0.69	0.70 ± 0.08
Max(ΔSIF value) = 0.05 mW m^{-2} sr^{-1} nm^{-1}		

Slit function interpolation

One of the algorithm improvements in SIFTER v3 was the enhanced interpolation of the slit function. The slit functions are used in the range of around 612 nm to 770 nm. In SIFTER v2, only slit functions from fully sampled detector pixels ($n = 10$) were used, whereas in SIFTER v3, all slit functions from the key data are used ($n = 765$), including both fully and not fully sampled pixels, interpolated by EUMETSAT (Anema et al., 2025a). These slit functions are convolved with the solar irradiance reference spectrum of Chance and Kurucz (2010), which is then used both for high sampling interpolation of the measured solar irradiance spectrum to the radiance wavelength grid of the radiance and for modeling the reflectance in the SIF retrieval ($\overline{E_0}$ in Equation 2.6 from Chapter 2).

For our sensitivity study, we use the GOME-2A results reported in Chapter 2 for the Congo Basin on 5 January 2008. Average SIF decreased from 1.25 to 1.07 mW m^{-2} sr^{-1} nm^{-1} when using the slit functions as in v2 and v3, respectively, a difference of 0.18 mW m^{-2} sr^{-1} nm^{-1} (Table S2.11).

Table S2.11: Summary of sensitivity tests on the slit function interpolation, comparing the used slit functions as done in SIFTER v2 and v3. Results shown over 633 pixels in the Congo Basin (13° S–6° N, 14–31° W) on 5 January 2008, retrieved from GOME-2A observations. Pixels of both tests were co-sampled and had to meet the requirements of autocorrelation < 0.2 and cloud fraction < 0.3. All other retrieval settings were kept at the default setting for GOME-2B. The zero-level offset correction is not applied to these results. The results from this sensitivity test were run by Anema et al. (2025a).

Tests	SIF value	SIF uncertainty
Slit function interpolation	[mW m^{-2} sr^{-1} nm^{-1}]	[mW m^{-2} sr^{-1} nm^{-1}]
SIFTER v3	1.07 ± 0.62	0.54 ± 0.07
SIFTER v2	1.25 ± 0.63	0.57 ± 0.08
Max(ΔSIF value) = 0.18 mW m^{-2} sr^{-1} nm^{-1}		

Error propagation

Across all sensitivity tests, the PC settings contributed to the largest systematic difference of 0.51 mW m^{-2} sr^{-1} nm^{-1}, followed by the slit function interpolation of 0.18 mW m^{-2} sr^{-1} nm^{-1}, while degradation and latitude bias corrections contributed less than 0.1 mW m^{-2} sr^{-1} nm^{-1}. The PCs used to model the atmospheric transmission represent the dominant source of systematic uncertainty in the SIFTER retrieval. Assuming the contributions from the four retrieval steps are independent, we add them in quadrature:

$$\sigma = \sqrt{\sigma^2_{\text{degr. corr.}} + \sigma^2_{\text{PCs}} + \sigma^2_{\text{lat. bias corr.}} + \sigma^2_{\text{slit function}}} \tag{S2.3}$$

This gives a combined systematic uncertainty of 0.55 mW m^{-2} sr^{-1} nm^{-1}.

These results are illustrative but provide a valuable indication of the order of magnitude of systematic errors in the SIF retrieval. In addition to quantifying systematic errors, properly accounting for spatiotemporal error correlations is crucial for accurate uncertainty quantification (Glissenaar et al., 2025; Woolliams et al., 2018). This is especially important in harmonisation efforts, as errors within products retrieved from similar sensors and algorithms are likely correlated (Giering et al., 2019). Robust error quantification prevents misinterpretation of instrumental artefacts or intersensor divergence as real trends; it could also help unravel the origin of noted intersensor offsets in certain regions.

Chapter 4

Monitoring the impact of forest changes on carbon uptake with space-based SIF measurements

This chapter is based on:

Anema, J. C. S., Boersma, K. F., Stammes, P., Koren, G., Woodgate, W., Köhler, P., Frankenberg, C., and Stol, J. (2024). Monitoring the impact of forest changes on carbon uptake with solar-induced fluorescence measurements from GOME-2A and TROPOMI for an Australian and Chinese case study. *Biogeosciences*, 21(9):2297–2311

Abstract

Reliable and robust monitoring tools are crucial to assess the effectiveness of land mitigation techniques (LMTs) in enhancing carbon uptake, enabling informed decision making by policymakers. This study, addressing one of the scientific goals of the EU Horizon 2020 Land Use Based Mitigation for Resilient Climate Pathways (LANDMARC) project, examines the feasibility of using satellite solar-induced fluorescence (SIF) in combination with other satellite data as a monitoring proxy to evaluate the effects of LMTs on carbon uptake. Two distinct cases are explored: (1) instantaneous vegetation destruction caused by a 2019 eucalyptus wildfire in southeast Australia and (2) gradual forest gain resulting from reforestation efforts in northern China in 2007–2012. The cases are monitored using SIF from the TROPOspheric Monitoring Instrument (TROPOMI) and Global Ozone Monitoring Experiment-2A (GOME-2A), respectively. Comparing the temporal variability in SIF across the affected areas and nearby reference areas reveals that vegetation dynamics changed as a consequence of the land-use changes in both cases. Specifically, in the Australia case, TROPOMI demonstrated an immediate reduction in the SIF signal of 0.6 mW m^{-2} sr^{-1} nm^{-1} (−72%) over the eucalypt forest right after the fire. Exploiting the strong correspondence between TROPOMI SIF and gross primary productivity (GPP) at the nearby representative eddy covariance Tumbarumba site and through the FluxSat product, we estimate that the Australian fire led to a loss in GPP of 130–200 GgC in the first 8 months after the fire. Over the northern Chinese provinces of Gansu, Shaanxi, Sichuan, Chongqing, and Shanxi, we report an increase in GOME-2A summertime SIF of 0.1 to 0.2 mW m^{-2} sr^{-1} nm^{-1} coinciding with reforestation efforts between 2007 and 2012. This increase in the SIF signal is likely driven by a combination of increasingly favourable natural conditions and by the reforestation effort itself. A multivariate model that takes into account growth factors such as water availability and maximum temperature, as well as satellite-derived forest-cover data, explains the observed variability in GOME-2A SIF in the Chinese case reasonably well ($R^2 = 0.72$). The model suggests that increases in both forest cover and soil moisture have led, in step, to the observed increase in vegetation activity over northern China. In that region, for every 100 km^2 of additional forest cover, SIF increases by 0.1 mW m^{-2} sr^{-1} nm^{-1} between 2007 and 2012. Our study highlights that the combined use of satellite-based SIF, together with supporting in situ, modelled and satellite data, allows us to monitor the impact of LMT implementation on regional carbon uptake as long as the scale of the LMT is of sufficient spatial extent.

4.1 Introduction

Photosynthetic carbon uptake by the terrestrial biosphere plays a crucial part in the carbon cycle and is the largest flux that contributes to the carbon sink. Over the last 60 years, the terrestrial biosphere captured an amount of carbon equivalent to approximately 32 % of the total anthropogenic emissions in that period (Friedlingstein et al., 2020). However, the ongoing efficacy of this photosynthetic carbon flux, or gross primary productivity (GPP), is not assured due to feedback mechanisms driven by climate change and human activity (e.g., Brook et al., 2013; Huntzinger et al., 2017). Preserving the terrestrial biosphere's pivotal role in dampening the rise in atmospheric CO_2 concentrations is crucial to address the current climate crisis. In response to this urgency, land mitigation techniques (LMTs) play a key role as negative carbon technology in national climate strategies (United Nations, 2016) and in the climate pathways of the Intergovernmental Panel on Climate Change (Rogelj et al., 2018). These techniques include a variety of practices, such as reforestation and fire management, aimed at enhancing the land's carbon assimilation and preventing carbon stock loss.

The potential of large-scale LMT implementation is exemplified by observed greening trends over actively reforested areas across central to northern China (Chu et al., 2019; Gerlein-Safdi et al., 2020). However, persisting uncertainty regarding the LMTs' effectiveness in enhancing GPP and carbon sequestration in the long term limits their widespread implementation (e.g., Harper et al., 2018). The need for robust quantification of changing GPP following land-cover change is further emphasised by the uncertain impacts of rising atmospheric CO_2 concentrations and climate change itself on the terrestrial biosphere (Schimel et al., 2015; Smith et al., 2020; Duffy et al., 2021; Schurgers et al., 2018). Understanding the efficiency and applicability of LMTs is essential for effective climate action. Therefore, the Horizon 2020 LANDMARC (Land Use Based Mitigation for Resilient Climate Pathways) project (`https://www.landmarc2020.eu/`) has developed monitoring tools, including satellite-based remote sensing, to study the feasibility of negative emission monitoring using multiple LMT cases worldwide as test cases.

The recent development of satellite-based measurements of solar-induced chlorophyll fluorescence (SIF) from atmospheric sensors has opened up promising opportunities to monitor the GPP dynamics (Frankenberg et al., 2011a; Joiner et al., 2011). Chlorophyll fluorescence (650–850 nm) is the re-emission of the absorbed photosynthetically active radiation (APAR) by the leaf chlorophyll during photosynthesis (Frankenberg and Berry, 2018). The emission of fluorescence dissipates part of the excitation energy from APAR that is not transported to and used by the photochemical reactions in the plant – making both fluorescence and GPP dependent on APAR (Porcar-Castell et al., 2014). SIF measurements depict the captured chlorophyll photons integrated over the canopy within the field of view and thus directly follow the dynamics of photosynthetic activity. Therefore, SIF follows GPP more consistently than traditional greenness parameter observations such as NDVI (e.g., Magney et al., 2019; Gerlein-Safdi et al., 2020).

As part of one of the research objectives of the LANDMARC project, the main goal of this study is to assess the feasibility of satellite-based SIF in combination with other satellite data to monitor the effect of land mitigation techniques (LMTs) on carbon uptake. Monitoring tools could potentially benefit from the ability of SIF to track GPP dynamics consistently across

various biomes and scales (Zhang and Schwärzel, 2017; Verma et al., 2017; Dechant et al., 2020) and from its demonstrated sensitivity to climate stress (Song et al., 2018; Ač et al., 2015). Previous studies indicated the ability of SIF to evaluate changes in land cover (Gerlein-Safdi et al., 2020; Guo et al., 2021a). However, to our knowledge, the use of SIF aligned with supporting satellite data to quantify the isolated effect of land-use change on GPP has not been assessed.

Here, we use TROPOMI and GOME-2A SIF to monitor two cases of forest-cover change. First, we use monthly TROPOMI SIF to track the aftermath of a 2019 wildfire in southeast Australia, impacting around 210 km^2 of eucalypt forest. Next, we use summertime GOME-2A SIF to monitor multi-year reforestation efforts in northern China from 2007–2012. The Australian case acts as a proof of concept due to its immediate and distinct single-cause land-cover change, while the Chinese case tests how SIF can be used to monitor the combined effect of gradual forest-cover change and variability in growth conditions (water and radiation availability) (Gao et al., 2019; Lin et al., 2020; Wang et al., 2022a). Satellite-based data, including MODIS burned-area data and Landsat-derived annual land-cover data, are used to evaluate the spatial and temporal extent of the changed forest cover in both cases. Subsequently, a comparative analysis between the impacted and reference areas was conducted.

Our study addresses the following research questions. (1) Is it possible to monitor changes in vegetation dynamics that are linked to instantaneous or gradual land-cover changes over scales that can be resolved by the TROPOMI and GOME-2A sensors? (2) How can we quantify the impact of instantaneous land-use change on carbon uptake? (3) How can we use remotely sensed metrics to improve our understanding of climate variability and forest-cover change on interannual SIF?

4.2 Data

4.2.1 Space-based SIF observations

Satellite measurements of SIF are powerful proxies for vegetation growth, and they have been used in many studies to monitor the changes in GPP. Retrieval of SIF from satellite measurements, e.g., from GOME-2A and TROPOMI that offer near-daily global coverage, relies on the relative filling in of solar Fraunhofer lines in the Earth's radiance spectra. The apparent depth of the Fraunhofer lines is not affected by scattering or reflection from clouds or by the Earth's surface. However, if vegetation is present on the surface, the addition of solar-induced fluorescence (SIF) as a spectrally continuous surface light source dampens the relative depth of the lines, and this (relative) filling in of the Fraunhofer lines is a measure of the strength of fluorescence (Joiner et al., 2011; Frankenberg et al., 2011a). The spectral-fitting window is made wide enough to cover multiple strong Fraunhofer lines and sufficiently narrow as to limit the presence of atmospheric absorption features. Spectral-basis functions derived from observations over vegetation-free non-fluorescent areas are used to describe the impact of atmospheric interaction and possible instrumental artefacts – the reference set. Accordingly, the SIF signal is computed by fitting the satellite-observed spectrum with a modelled reflectance spectrum assembled from the spectral-basis functions. Uncertainty in the SIF data emerges from measurement noise, the

presence of optically thick clouds in the satellite field of view, and the fitting procedure, the latter depending on the quality and representativeness of the spectral-basis functions. To mitigate uncertainty, SIF observations with cloud cover fractions below 0.2 are used.

SIF retrieved from TROPOMI

In this study, we use level-2 SIF (740 nm) data retrieved from the TROPOspheric Monitoring Instrument (TROPOMI) by Caltech (Köhler et al., 2018). TROPOMI is an atmospheric spectrometer on board the Sentinel-5 Precursor that performs in a wide spectral range from the ultraviolet to the shortwave-infrared. The instrument was launched on 13 Oc- October 2017 and flies in a low-Earth polar sun-synchronous orbit with equatorial crossing at 13:30 local solar time (LST) and with a repeat cycle of 17 days (Veefkind et al., 2012). The 2600 km wide swath enables almost daily global coverage. TROPOMI SIF, with a spatial resolution of 7×3.5 km^2 at nadir, is retrieved from a subset of the NIR band with a selected window ranging from 743 to 758 nm. TROPOMI SIF has a single-pixel 1-σ uncertainty in the range of 0.3 to 0.5 mW m^{-2} sr^{-1} nm^{-1} (Köhler et al., 2018).

TROPOMI SIF has been previously used to track photosynthetic activity following extreme precipitation events in the US (Turner et al., 2021), during the dry season in the Amazon forest (Doughty et al., 2019), and over evergreen forests (Magney et al., 2019). Furthermore, it is extensively validated with GPP from multiple eddy covariance towers and with Orbiting Carbon Observatory-2 (OCO-2) SIF (Li and Xiao, 2022; Köhler et al., 2018). Until ESA's FLEX mission with a spatial resolution of 300 m (Drusch et al., 2016) is launched (in 2026), TROPOMI SIF is arguably the most appropriate data product to track photosynthetic activity from vegetation on a continuous global scale from space. The main limiters in detecting the impact of LMTs on vegetation activity are the spatial scale of a TROPOMI pixel. The main limiters for detecting the impact of LMTs on vegetation activity are the spatial scale of a TROPOMI pixel ($\pm$ 20 km^2) and the data not being available before April 2018.

SIF retrieved from GOME-2A

We also use clear-sky, gridded (level-3) SIF data from the Royal Netherlands Meteorological Institute (KNMI) Sun-Induced Fluorescence of Terrestrial Ecosystems Retrieval (SIFTER) v2 product(Kooreman et al., 2020; van Schaik et al., 2020) retrieved from the Global Ozone Monitoring Experiment-2A (GOME-2A) sensor. The data have a spatial resolution of $0.5° \times 0.5°$. GOME-2A was launched on 6 November 2006 aboard the Meteorological Operational (Metop-A) satellite and flies in a sun-synchronous orbit with equatorial crossing at 09:30 LST. The GOME-2A swath covers 1920 km, resulting in the spatial resolution of 80×40 km^2 at nadir. Due to a swath reduction on 15 July 2013, the spectral resolution thereafter was 40×40 km^2. Despite the 160-times-coarser resolution of GOME-2A in comparison to TROPOMI, the GOME-2A SIF data are of relevance due to the long temporal record, starting from 2007. The GOME-2A SIF product is retrieved from a subset of band 4 with a selected window ranging from 734 to 758nm, and the SIFTER retrieval principle is similar to that of TROPOMI SIF. GOME-2A SIF has a single-pixel uncertainty on the order of 0.6 mW m^{-2} sr^{-1} nm^{-1} (van Schaik et al., 2020). The retrieval is considered most reliable in the period before the sensor switch in July 2013 (van

Schaik et al., 2020). After the July 2013 switch, degradation of the GOME-2A sensor and subsequent calibration updates in different level-1 data versions have posed difficulties in deriving a consistent, bias-free data record. Post hoc degradation corrections introduced in van Schaik et al. (2020) have (at least partly) improved the consistency of the GOME-2A SIF data record in the post-2013 years.

We exclusively use the GOME-2A data from the years 2007–2012 for two main reasons. Firstly, this enables a constant satellite viewing geometry throughout the analysed time series. Secondly, we limit level-1 calibration issues associated with strong instrument degradation and unresolved differences in level-1 calibration post-processing within the dataset (van Schaik et al., 2020; Gerlein-Safdi et al., 2020). Additionally, we applied a year-specific multiplicative correction to the SIF data, addressing the effect of instrument degradation on SIF. The corrections are determined over China's Gobi Desert, where vegetation is mostly absent, and a constant near-zero SIF signal is expected. Supplement S3.1 describes the correction procedure in detail, and we note here that the (multiplicative) correction factors have values between 0.85 and 1.12 and that their application improves the correspondence between GOME-2A SIF and FluxSat GPP over northern China (Figure S3.3). The noted impact of instrumental artefacts within the GOME-2A SIFTER v2 product, motivated the improvement of the SIFTER algorithm (in Chapter 2) to correct for these effects accurately.

Various applications have shown the data to be of good use for detecting the effects of heatwaves on GPP in Europe (Wang et al., 2020), quantifying GPP over Africa (Mengistu et al., 2021), and mapping the impact of El Niño on forest productivity in the Amazon (Fancourt et al., 2022). GOME-2A SIF has been validated with GPP from various eddy covariance flux towers in Africa (Mengistu et al., 2021).

4.2.2 Gross primary productivity (GPP) data

GPP from Tumbarumba flux tower

This study uses estimated GPP data from the Tumbarumba OzFlux eddy covariance flux tower site as a ground reference to the TROPOMI SIF observations (AU-TUM: 35.66° N, 148.15° E) (Stol and Kitchen, 2022). The Tumbarumba site is located in the Bago State Forest and is predominantly covered by eucalyptus forest. GPP is not directly measured but is calculated using partitioning methods by the extraction of modelled respiration from the measured net ecosystem exchange (NEE) of CO_2. NEE at the site is quantified using the eddy covariance method, which involves simultaneously measuring vertical wind speed and CO_2 concentration (Moene and van Dam, 2014).

For our analysis, we use the quality-checked and gap-filled daily GPP (in gC m^2 day^{-1}) from the level-6 data. The Tumbarumba data are processed following the standard tool developed by OzFlux, which is described in more detail in Isaac et al. (2017). To match the recording time of TROPOMI SIF and account for the impact of the Dunn's Road fire that affected the OzFlux site in December 2020, GPP data between February 2018 and November 2020 are used.

FluxSat GPP product

The modelled global FluxSat GPP product is used as independent GPP data to compare against SIF and the OzFlux GPP data for the Australia case study. The dataset contains daily averaged GPP estimates (gC m^{-2} day^{-1}) at a spatial resolution of $0.05° \times 0.05°$ over the period March 2000 to August 2020. The FluxSat GPP product was found to agree well with GPP from flux towers (Joiner et al., 2018), and TROPOMI-inferred GPP (Turner et al., 2021) and has previously been used to quantify changes in carbon uptake (e.g., Byrne et al., 2021; Bacour et al., 2019).

The global FluxSat GPP (Joiner et al., 2018) product is derived from the evaluation and training of satellite-data-driven models that are based on the light use efficiency concept (Monteith, 1972), which states that there is a linear relationship between GPP and the absorbed photosynthetically active radiation. The product's objective is to estimate GPP accurately at a high temporal (daily) and spatial resolution. MODIS reflectance (MCD43) data serve as vegetation index inputs for the model. Furthermore, the models are trained and calibrated using a subset of eddy covariance flux data that contains data across various plant types. In addition, GOME-2A SIF (v27) (Joiner et al., 2013, 2016), a different SIF product from NASA, is used in the FluxSat calibration procedure to delineate highly productive regions that are not well fitted and are underestimated using the global regression model. Guanter et al. (2014) found that high GPP values from cropland deviated from the linear relationship. Therefore, highly productive regions were trained and calibrated separately using an eddy covariance GPP subset that met the high SIF and GPP criteria (Joiner et al., 2018). As GOME-2A SIF is merely used to identify productive areas, FluxSat GPP estimates remain largely independent from SIF.

4.3 Forest loss following eucalyptus fire in South-East Australia

We first investigate the case of a 2019 eucalyptus wildfire in southeastern Australia to evaluate the ability of SIF to capture the fire-induced change in vegetation dynamics. Lightning strikes on 16 January 2019 ignited multiple fires across remote forested areas in Victoria, southeast Australia. Strong northwesterly winds propagated and coalesced several individual fires into a clustered eucalyptus fire, which is locally known as the Nunnett–Timbarra River fire due to its extent between the Nunnett State Forest and the Timbarra River. Burning for nearly 4 weeks, the wildfire impacted around 210 km^2 of eucalyptus forest spanning from 148.0–148.2° E and 37.35–37.2° S. The impacted area had not previously been affected by wildfires within the 25 years prior to the event (Lindenmayer and Taylor, 2020). The fire has been documented to have caused a sharp reduction in leaf biomass in January 2019 but left eucalypt tree stems and branches mostly intact, according to witness reports by the Australian Forestry Service.

Figure 4.1 shows the location of the area impacted by the Nunnett–Timbarra River fire in the context of the wider biogeography of southeast Australia. Notably, Figures 4.1c and d show that prior to the fire, the area enclosed by the solid line (which would burn down in early 2019) as well as the surrounding area bound by the dashed line (which was spared from the fire) had high levels of SIF and GPP, indicating vigorous growth conditions in both areas under normal circumstances.

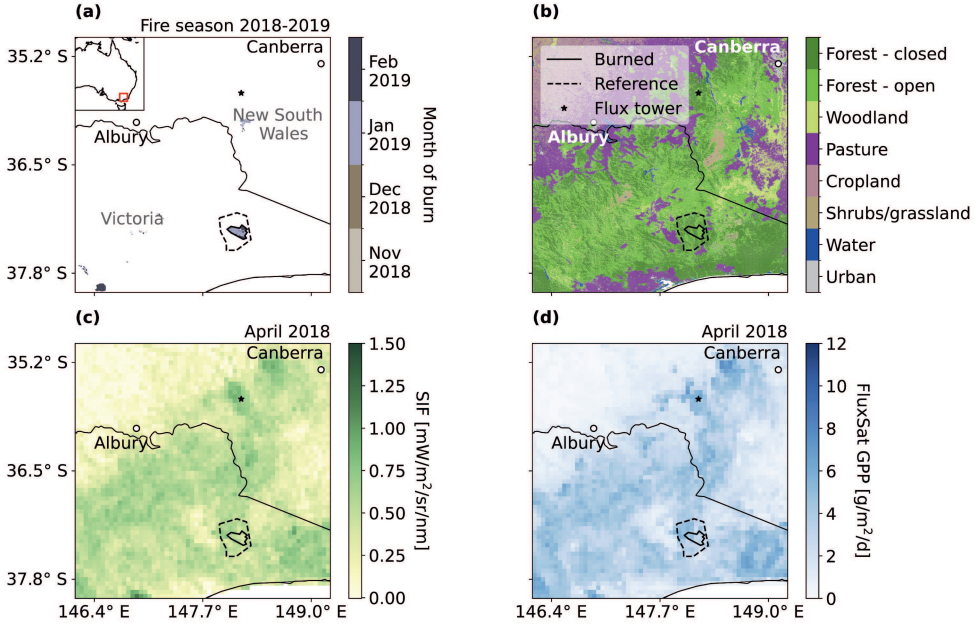


Figure 4.1: Location and extent of the Nunnett-Timbarra River Fire and selected reference area. Maps of (a) the burned area per month of burn from the MODIS MCD64A1 Burned Area product (Giglio et al., 2015), (b) dominant land cover over the area with classification based on the 2015 Land Cover Dataset (Lymburner et al., 2015), (c) monthly mean TROPOMI SIF ($0.05^\circ \times 0.05^\circ$), and (d) monthly mean of FluxSat GPP ($0.05^\circ \times 0.05^\circ$) over April 2018. The outline of the burned (approximately 210 km^2) and reference area (approximately 975 km^2) are indicated by the solid and dashed line, respectively. Location of the Tumbarumba OzFlux site (AU-TUM) used in this study is shown as a black star.

4.3.1 Reduction in SIF following the eucalyptus forest fire

We evaluate the spatial and temporal trends in TROPOMI SIF over the burned area from February 2018 until November 2020. The monitoring period ends in November 2020 to avoid potential interference from subsequent wildfire events that occurred in December 2020 and affected the studied region (Bowman et al., 2021). The extent of the eucalyptus fire is identified using the MODIS MCD64A1 Burned Area monthly product (Giglio et al., 2015) (Figure 4.2a), and the impacted burned area is defined as the region encompassing the MODIS burned pixels, indicated by the solid lines in Figure 4.1 and 4.2a and b. Next, for comparison, we carefully selected a reference area surrounding the burned area that remained unaffected by the fire. This reference area was chosen to closely match the biogeography of the impacted area, consisting of a mixture of open and closed eucalyptus forest (Figure 4.1b). SIF observations over the reference area are assumed to represent the forest dynamics over the burned area as if the fire had not taken place.

To evaluate temporal trends in SIF over both areas, we categorised TROPOMI level-2 pixels as either "burned" or "reference" based on their spatial overlap with each respective area. Criteria

were implemented for each group to ensure pixel exclusivity and minimise interference. Pixels were labelled as burned if the burned-area fraction exceeded 50 %. Pixels were labelled as reference if they comprised less than 30 % of burned area. Subsequently, within each group, the SIF values were averaged on a monthly basis. Note that throughout the reporting of the results, all uncertainty values are stated in standard error (SE).

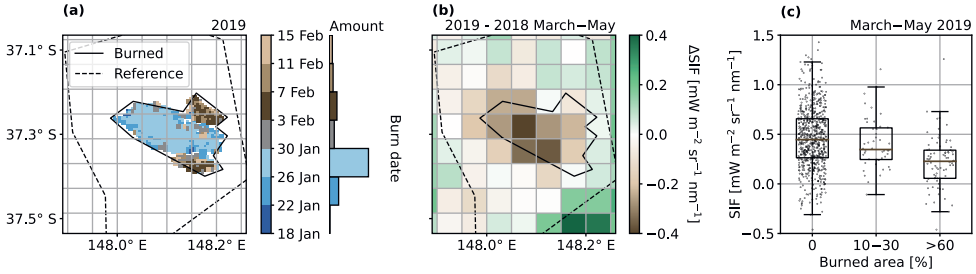


Figure 4.2: Impact of the 2019 eucalyptus fire on TROPOMI SIF over time and in comparison to the unburned reference area and pre-fire conditions. Map of (a) the burned areas and their specific burn data at 1 km scale from the MODIS MCD64A1 Burned Area product, and (b) the difference in SIF between post (2019) and pre-fire (2018) conditions over March–May (Autumn). Brown indicates higher SIF in 2018 (pre-fire), green indicates higher SIF in 2019 (post-fire). (c) Correlation between SIF over March–May 2019 (post-fire) and the coverage of the 500-m burned area pixels by the SIF pixels, in percentage.

Figure 4.2b shows the difference in SIF between autumn 2019 (post-fire) and 2018 (pre-fire). Over the area that burned down, autumnal SIF values in 2019 decreased significantly compared those in to 2018. In contrast, SIF at the reference area remained consistent across both years. Furthermore, the lowest SIF values (0.25 mW m^{-2} sr^{-1} nm^{-1}) coincide with pixels with burned-area fractions higher than 60 %, whereas SIF is much higher (0.45 mW m^{-2} sr^{-1} nm^{-1}) in pixels that had not burned, as illustrated in Figure 4.2c. We conclude that TROPOMI SIF is capable of capturing the strong reduction in vegetation activity over the burned area relative to the unburned reference area, noting that the affected area extends over some 200 km^2, equivalent to eight individual TROPOMI pixels.

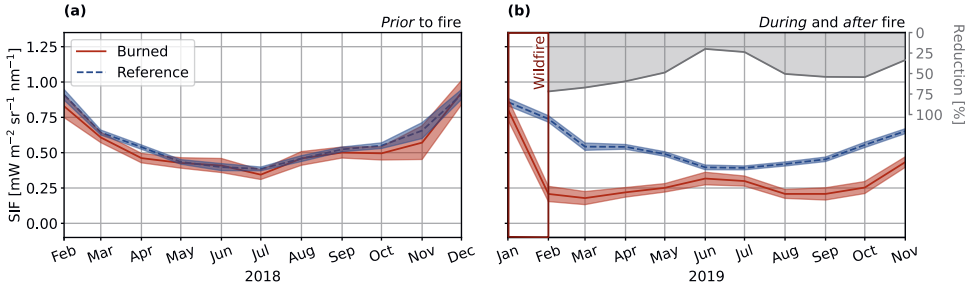


Figure 4.3: Time series of SIF over the burned and reference area (a) prior to the fire in 2018 and (b) during and after the fire in 2019. The shaded red and blue area represents the standard error (SE) in monthly SIF over the burned and reference area, respectively. The right y-axis of plot (e) shows the reduction in SIF (in %) over the burned area (F_{B}) as compared to SIF over the reference area (F_{R}), which is calculated as $1 - \frac{F_{\mathrm{R}} - F_{\mathrm{B}}}{F_{\mathrm{R}}}$. Prior to monthly averaging, SIF pixels beyond $\pm 2\sigma$ from their respective seasonal group mean were removed.

Figure 4.3a shows the seasonal cycle in 2018 (pre-fire) inferred from TROPOMI SIF over the to-be-burned and reference areas. Prior to the fire event, the observed SIF values indicate consistency and strong agreement between the two areas ($r = 0.98$, Figure S3.4a). However, shortly after the fire, a substantial reduction in SIF over the burned area becomes evident (Figure 4.3b). This immediate fire-induced impact is highlighted by a striking 72 % decrease in February SIF values compared to those of the reference area. In the subsequent months, the vegetation activity over the burned area remained low but non-zero, with an averaged SIF of 0.26 ± 0.01 mW m^{-2} sr^{-1} nm^{-1} between February and August 2019. During springtime (September–November), vegetation recovery was noticeable, with SIF values reaching 0.43 ± 0.04 mW m^{-2} sr^{-1} nm^{-1} by November. In fact, SIF grew faster in springtime over the burned area than over the reference area, with respective increases of 208 % and 144 %, hinting at accelerated regrowth in a moderately burned area, a trend which has also been reported in Zambia and Alaska (Chungu et al., 2020; Madani et al., 2021).

4.3.2 Quantifying the fire-induced reduction in GPP

Next, based on the observed reduction in SIF, we quantify the fire-induced reduction in GPP. Previous studies found space-based SIF observations to be proportional to GPP at the canopy scale. This proportionality is defined by biome-specific linear relationships that are widely used to scale SIF to GPP (e.g., Turner et al., 2020; Liu et al., 2017; Sun et al., 2018). Building upon this recognised relationship between SIF and GPP, we assume that the relative reduction in SIF (Section 4.3.1) represents the loss in GPP ($\Delta\mathrm{SIF} \propto \Delta\mathrm{GPP}$). Consequently, we express the fire-induced change in GPP over the burned area, $\Delta M_{\mathrm{B}}(t)$ (in gC m^{-2} day^{-1}) over month t as the product of the relative change in SIF ($\Delta F_{\mathrm{B}}(t)$) and "baseline" GPP (M_{R} (t)) over the reference area (as if no fire had occurred):

$$\Delta M_{\mathrm{B}}(t) = \Delta F_{\mathrm{B}}(t) M_{\mathrm{R}}(t) \tag{4.1}$$

To compute the SIF-based GPP over the reference area ($M_{\mathrm{R}}\ (t)$), we first characterise the SIF–GPP relationship using GPP data from a representative eddy-covariance site (see Supplement S3.2). Specifically, GPP data from the nearby Tumbarumba (AU-TUM) site (Stol and Kitchen, 2022) is used to compare against TROPOMI SIF. We obtain the SIF-based GPP over the reference area as:

$$M_{\mathrm{R}}(t) = F_{\mathrm{R}}(t)\frac{M_{\mathrm{TUM}}}{F_{\mathrm{TUM}}} \tag{4.2}$$

where $F_{\mathrm{R}}\ (t)$ represents the SIF evolution over the reference area, and $\frac{M_{\mathrm{TUM}}}{F_{\mathrm{TUM}}}$ is the local SIF–GPP relationship over the Tumbarumba flux site. We hold the empirical SIF–GPP relationship over Tumbarumba to be applicable to our study area. This is supported by (i) the similar biogeography of lowland eucalyptus Forest in both areas (Figure 4.1b), (ii) the strong spatiotemporal correlation between TROPOMI SIF over Tumbarumba and over the reference area in the year prior to the fire ($r = 0.92$) (Figure S3.4b) and (iii) by the good correlation between FluxSat GPP estimates over Tumbarumba and over the reference area in the year prior to the fire ($r = 0.79$) (Figure S3.4c). Moreover, the discrepancy between SIF–$\mathrm{GPP}_{\mathrm{FluxSat}}$ over Tumbarumba versus the Nunnett-Timbarra river area is small and on the order of 4 % (Supplement S3.2)

As an alternative, we also compute SIF–GPP relationships over Tumbarumba using TROPOMI SIF and modelled FluxSat GPP. The temporal dynamics of TROPOMI SIF exhibit strong consistency with both the GPP estimated from eddy covariance flux tower data ($r = 0.91$) as well as the modelled (FluxSat) GPP ($r = 0.94$), providing some confidence in both estimates. However, the SIF–GPP relationship based on the flux tower GPP measurements is 1.6 times stronger than the relationship based on the FluxSat GPP data (Table S3.1, Figure S3.5a). This discrepancy likely arises from higher GPP estimates from the eddy covariance flux tower – nearly twice that of the estimates from FluxSat (Figure S3.5b) – and inherited uncertainties and biases in the estimates of the FluxSat GPP product. Our findings are consistent with Joiner et al. (2018), who also observed magnitude differences up to a factor of 2 between FluxSat GPP and independent FLUXNET 2015 GPP data at some sites. Despite differing footprint sizes between the Tumbarumba tower and FluxSat model, this is not expected to significantly impact the uncertainty, given the extensive land cover around the tower.

Finally, we estimate the reduction in GPP employing SIF–GPP relationships that use (1) the eddy covariance GPP data and (2) FluxSat GPP data over Tumbarumba – hereon referred to as $\mathrm{GPP}_{\mathrm{SIF,\ ec}}$ and $\mathrm{GPP}_{\mathrm{SIF,\ FluxSat}}$, respectively. Additionally, we compute the reduction in GPP (3) from the FluxSat GPP data directly over the burned and reference area, referred to as $\mathrm{GPP}_{\mathrm{FluxSat}}$. Figure S3.6 shows an overview of the three approaches to compute ΔGPP.

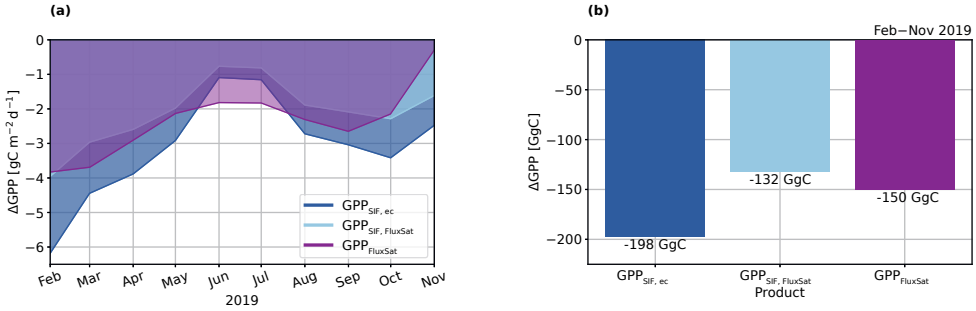


Figure 4.4: Reduction in GPP following from the eucalyptus wildfire over the first eight months post-fire (Feb–Nov 2019). (a) Time series of reduced GPP and (b) barplot of total reduction as obtained from SIF-based GPP using data from the Tumbarumba eddy-covariance site ($GPP_{SIF,\ ec}$), SIF-based GPP using FluxSat GPP ($GPP_{SIF,\ FluxSat}$) over Tumbarumba, and FluxSat GPP ($GPP_{FluxSat}$), shown in dark blue, light blue and purple, respectively.

Figure 4.4a shows the estimated fire-induced reductions in GPP over time. The SIF-based approaches, $GPP_{SIF,\ ec}$ and $GPP_{SIF,\ FluxSat}$, show a sharp reduction in GPP immediately after the fire. This is followed by smaller GPP deficits in winter, when vegetation activity is low. The FluxSat data ($GPP_{FluxSat}$) also shows a direct local impact of the wildfire on GPP. However, the FluxSat data suggest almost complete recovery in November in contrast to our SIF-based results.

When integrated over the period from February to November 2019 and across the burned area, we find SIF-based GPP losses $\Delta GPP_{SIF,\ ec}$ and $\Delta GPP_{SIF,\ FluxSat}$ of 198 and 132 GgC, respectively. The SIF-based GPP losses reflect a reduction of 48 % with respect to GPP over the same period in the reference area. Thus, the estimated SIF-based losses in the range of 130–200 GgC over the initial 8 months post-fire. For comparison, $\Delta GPP_{FluxSat}$ indicates a fire-induced loss of 150 GgC over the burned area between February–November compared to the reference area. The total $GPP_{FluxSat}$ over the burned area during this period is 58 % less than over the same period and area in 2018 (pre-fire conditions).

An uncertainty propagation analysis, described in Supplement S3.2, indicates a total uncertainty of approximately 60 % in the estimated SIF-based GPP losses. This total uncertainty is primarily driven by the use of the SIF–GPP relationship at Tumbarumba, where no fire occurred, to derive our GPP-loss estimate via Equation (4.2) over the Nunnett-Timbarra River area that burned down – introducing an estimated uncertainty of 50 %. This uncertainty was determined by comparing SIF and FluxSat GPP relationships under pre-fire and post-fire conditions (see point 2 of the uncertainty analysis in Supplement S3.2). We conclude that estimating changes in GPP based on land-cover changes is possible with TROPOMI SIF in combination with empirical SIF–GPP relationships, at least when such land-cover changes occur over a spatial scale of a few hundred km^2.

4.4 Reforestation in north-central China

We now turn to examining how GOME-2A can be used to monitor the impact of reforestation on carbon uptake in parts of northern China. Our study area includes Shaanxi province, southwestern Shanxi, eastern Gansu, and part of northern Sichuan and Chongqing. This region spans approximately 31° to 38° N and 105.0° to 111.5° W (Figure 4.5a). Over the past 15 years, the area has undergone various greening campaigns like Grain for Green, the Natural Forest Conservation Program, and the Three-North Shelterbelt Program (Delang and Yuan, 2015; Kong et al., 2021). These efforts have led to observable positive trends in vegetation activity (Gerlein-Safdi et al., 2020; Lin et al., 2020; Li et al., 2015; Sun et al., 2015; Cao et al., 2009).

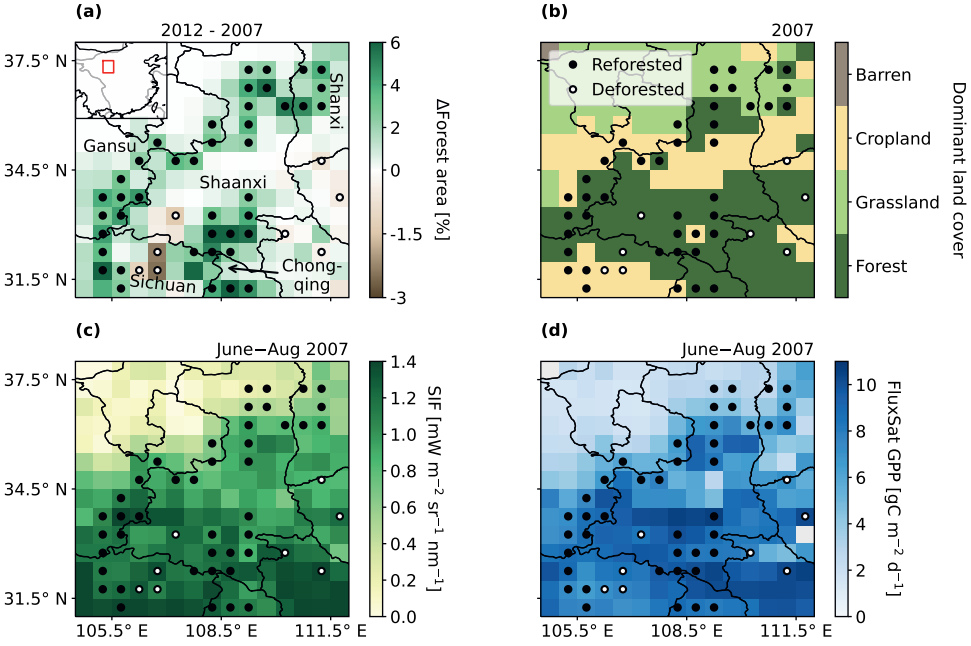


Figure 4.5: Location and extent of the reforestation efforts between 2007 and 2012 over the study region in northern China. Maps of (a) changed forest cover in 2012 with respect to 2007 (in % of cell area) obtained from the China land cover dataset (CLCD) (Yang and Huang, 2021), with green indicating higher forest coverage in 2012 (reforestation) and brown indicating larger forest coverage in 2007 (deforestation), and (b) dominant land cover in 2007 with classification based on the CLCD, aggregated over the $0.5° \times 0.5°$ GOME-2A SIF grid. Croplands are shown in yellow, grasslands in light green and forests in dark green. Maps of (c) GOME-2A SIF (van Schaik et al., 2020) and (d) FluxSat GPP (Joiner et al., 2018), averaged over summertime (June–Aug) 2007. Selected reforested cells and deforested cells are indicated by black and white-faced bullets, respectively.

Figures 4.5a and b show that most of the forest gain occurred within and at the borders of Shaanxi province, predominantly over areas dominated by forest or cropland cover. Concurrently, Figures 4.5c and d show that high SIF and FluxSat GPP values generally occur in the vegetated

southern part of the domain, including the regions where reforestation has taken place, with lower average SIF and GPP values observed in the drier northern part of the region.

4.4.1 Coinciding increase in forest cover and SIF

We first examine the 2007–2012 variability in summertime (June–August) GOME-2A SIF, when vegetation productivity is at a maximum. To evaluate the changes in SIF, we used the first Landsat-derived annual China land-cover dataset (CLCD) (Yang and Huang, 2021). These satellite-based data categorise nine major land types, such as cropland, forest, and grassland, at a spatial resolution of 30 m. Specifically, we extracted forest-coverage data for each year between 2007 and 2012, aggregated over the $0.5^\circ \times 0.5^\circ$ GOME-2A SIF grid. The conversion to forest, from any type of land cover, was determined by quantifying the change in forest cover relative to the 2007 baseline. We then compared changes in summer-time SIF between 2007 and 2012 over two contrasting groups of cells: reforested ($n = 42$) and deforested ($n = 8$). We classify cells as "reforested" if they gained more than 2 % of their area in forest coverage (approximately 50 km^2), and as "deforested" ($n = 8$) if they lost forest coverage during this period as shown in Figure 4.6a. Cells in both groups consistently gained or lost forest coverage annually with every passing year from 2007 to 2012.

The majority of reforested cells showed an increase in average summertime SIF, whereas most deforested cells experienced a decrease (Figure 4.6b). Figure 4.6c shows the clear contrast in SIF trends across cells that gained forest coverage compared to those that lost forest coverage. Reforested cells exhibited significant increase in SIF with 0.17 ± 0.03 mW m^{-2} sr^{-1} nm^{-1}, while SIF decreased with 0.09 ± 0.07 mW m^{-2} sr^{-1} nm^{-1} over the deforested cells between 2007 and 2012. The contrasting trends in vegetation activity indicated by GOME-2A SIF over the reforested and deforested cells are confirmed by co-sampled independent data from the near-infrared reflectance of vegetation (NIRv) and FluxSat GPP (Figure 4.7a and b).

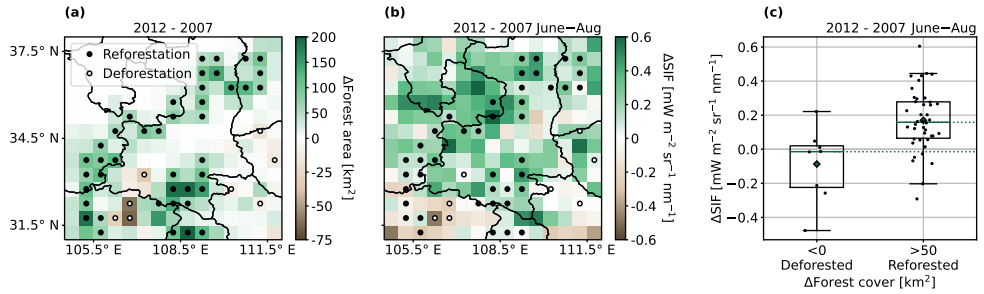


Figure 4.6: Impact of increased forest coverage in northern China between 2007 and 2012. Maps of changed (a) forest coverage (in km^2) calculated from the China land cover dataset (Yang and Huang, 2021) and (b) summertime GOME-2A SIF over the six years. Green indicates higher forest coverage/SIF in 2012 and brown indicates higher forest coverage/SIF in 2007. (c) Contrast in GOME-2A SIF trend between 2007 and 2012 over the deforested and reforested cells. The reforested and deforested cells are indicated by black and white-faced bullets in (a) and (b). The SIF data is obtained from the GOME-2A SIFTER v2 dataset by van Schaik et al. (2020)

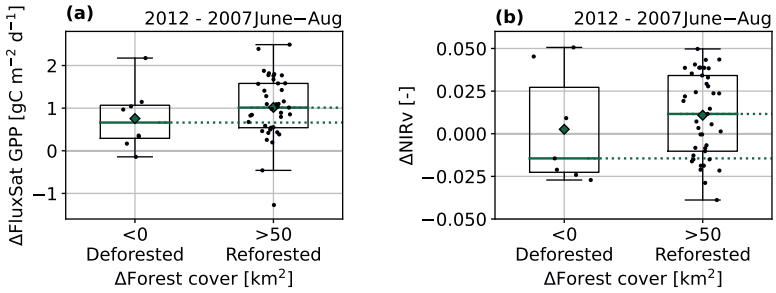


Figure 4.7: Contrast between deforested and reforested cells in changed vegetation activity between 2012 and 2007, shown using (a) FluxSat GPP, and (b) the near-infrared reflectance of vegetation (NIRv) retrieved from MODIS.

Temporal SIF variability across northern China is driven not only by reforestation alone but also by co-occurring changes in local climate factors that influence plant growth, such as water availability, heat, and the presence of photosynthetically active radiation (Zhang and Ye, 2021; Gao et al., 2019; Lin et al., 2020). To examine the co-occurring impact of climate variability and changes in forest cover, we use satellite-based soil moisture and maximum temperature. Soil moisture data were obtained from the Surface Soil Moisture (Active) product (Dorigo et al., 2019), and the daily maximum temperature was derived from hourly 2 m temperature from ERA5-Land data (Copernicus Climate Change Service, 2019). Both were aggregated to the $0.5° \times 0.5°$ GOME-2A SIF grid. The summers of 2007 to 2012 in Shaanxi and surrounding provinces are characterized by soil moisture values (50–55 %, Figure S3.7b) that are generally good for plant growth, showed a slight increase over time (1 % yr^{-1}), and had relatively stable (average) maximum temperatures (Figure S3.7a). The summer of 2010 was somewhat of an exception, with a maximum temperature more than 1 °C below the multi-annual mean, which we interpret as indicating lower radiation levels. Overall, we expect that interannual variability in climate factors favoured forest growth between 2007 and 2012 in both the reforested and deforested areas, in line with previous studies (e.g., Zhang et al., 2022b). Overall conditions for vegetation growth appear more favourable in cells where reforestation occurred, as maximum temperatures were more moderate (23 °C) and soil moisture was higher (53 %) in the cells with reforestation than in cells with deforestation.

4.4.2 Interpretation of temporal variability in SIF

We constructed a simple model that expresses the local year- to-year variability in summertime SIF as a linear combina- tion of soil moisture (S; in %), maximum temperature (T; in °C), averaged over spring to summertime (March–August), and the total forest coverage (A; in km^2) – Equation (4.3). This model serves to explore the impact of different climatic drivers on observed SIF, representing vegetation activity, alongside the effect of change in vegetation. The selection of this model is motivated by three factors: (i) soil moisture promotes the thriving of vegetation by enhancing the water availability, (ii) increasing temperature stimulates vegetation activity un- til an optimal temperature is reached (Gao et al., 2019), and is a proxy for photosynthetic

active radiation, and (iii) total photosynthetic carbon uptake increases with increasing vegetation cover. Note that the climate parameters are averaged over the spring and summer period (March–Aug) to account for the concurrent and lagging effects on the vegetation activity over summer (e.g., Sun et al. (2021)).

We use a multivariate-least-squares regression to optimise the combined fit coefficients that best explain the observed SIF over the reforested and deforested cells. Modelled SIF as a function of the year (between 2007 and 2012), F_{mod} (t), is expressed as:

$$F_{\mathrm{mod}}(t) = \alpha S(t) + \beta T(t) + \gamma A(t) + \delta \tag{4.3}$$

where α, β, γ and δ represent the coefficients that minimize the discrepancies (ϵ) between F_{mod} (t) and the observed GOME-2A time series F_{obs} (t). The predictors soil moisture, maximum temperature and forest cover are indicated by $S(t)$, $T(t)$ and $A(t)$, respectively, over year t. To ensure sufficient statistics, we pooled the time series of SIF ($n = 6$) from all 50 selected cells, resulting in a single, cell-ensemble fit. Overall, the modelled variability in SIF matches the measured variability reasonably well ($R^2 = 0.57$; $n = 300$). Figure 4.8a shows the correlation between the observed (F_{obs}) and modelled SIF (F_{mod}) over all cells.

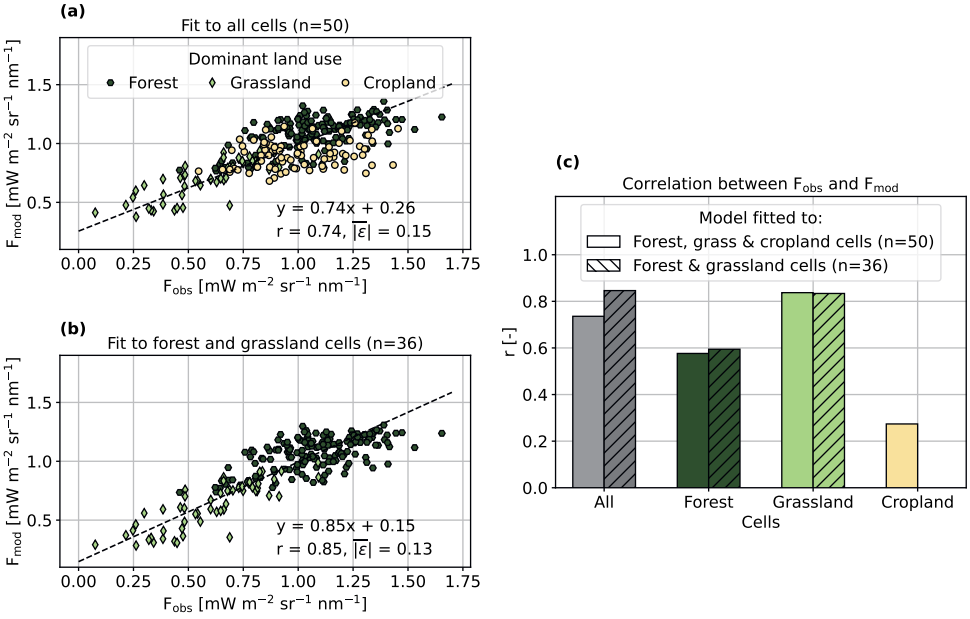


Figure 4.8: Results from the regression model in Equation (4.3) fitted to (a) all cells ($n = 50$) and (b) exclusively to forest and grassland cells ($n = 36$). (c) Shows the correlation between observed (F_{obs}) and modelled (F_{mod}) SIF for each dominant land type and for both fits.

However, the model's performance varied by land-use type across the region (Figure 4.8c). Notably, it demonstrated good agreement between observed and modelled values for cells dominated

by grassland ($r = 0.84$) or forest cover ($r = 0.58$), but struggled to represent the dynamics in cropland cells ($r = 0.27$). This suggests distinct differences in the underlying dynamics and complexities in converting cropland areas into forest. Previous studies reported that croplands were often located in drier areas with less forest cover to begin with, reducing the vigour with which vegetation increases in response to reforestation (Qu et al., 2020).

We therefore exclusively fitted our final model to data from the 36 cells dominated by grassland or forest cover ($n = 216$) (Figure 4.8b and c). By excluding cropland cells, the fit significantly improved, evident from the higher R^2 of 0.72. The improved correlation between the observed and modelled SIF suggests that the model better captures the underlying dynamics. Note that the impact of different factors on the long-term vegetation dynamics is ecosystem-specific; therefore, our model is unique to the fitted area and period. Next, to evaluate the explanatory power of including forest coverage in our model, we constructed an alternative model that solely fits the first two terms on the right-hand side of Equation (4.3), i.e., the climate parameters to the observed summertime SIF. Doing so allows us to compute the R^2 adjusted of our model (Equation (4.3)) and the alternate model to enable fair comparison between the models containing three and two predictors, respectively. The alternate model had an adjusted R^2 of 0.66. With the inclusion of forest cover data, the model's performance improved, achieving an adjusted R^2 adjusted of 0.71 – suggesting the added value of including changed forest coverage in conjunction to climate variability in the model.

Table 4.1: Regression results of model fitted to GOME-2A summertime SIF temporal variability over reforested and deforested cells with as dominant land use of grassland or forest ($n = 36$). The model was fitted to data spanning between 2007 and 2012. Uncertainty is given in standard error (SE).

Predictor		Fit coefficients		Average *	Average change *
		Value $\times 10^{-3}$	Scaled value	2007	2007-2012
Soil moisture	α	18.65 ± 2.3 mW m^{-2} sr^{-1} nm^{-1} %$^{-1}$	0.55 ± 0.06	51.5 ± 1.5 %	$+4.8 \pm 0.6$ %
Max. temp.	β	35.98 ± 6.86 mW m^{-2} sr^{-1} nm^{-1} °C^{-1}	0.21 ± 0.04	23.0 ± 0.3 °C	-0.4 ± 0.1 °C
Forest cover	γ	0.15 ± 0.02 mW m^{-2} sr^{-1} nm^{-1} km^{-2}	0.38 ± 0.06	1290.7 ± 129.8 km^2	$+96.9 \pm 6.9$ km^2

$R^2 = 0.72$

* Over reforested cells ($n = 31$)

The model's fit coefficients presented in Table 4.1 demonstrate, as hypothesised, that increases in the predictors positively influence SIF. Soil moisture and forest-cover variability explain most of the variability in GOME-2A SIF, as indicated by the scaled values of the fit coefficients (which consider predictor standard deviations). This is also expected, given the relatively strong increases in soil moisture (+5%) and in forest cover (+97 km^2) compared to the modest changes in maximum temperature over the provinces from 2007 to 2012. The effect of changes in soil

moisture cannot be disentangled from the effect of changes in forest cover on vegetation activity. However, our results show a positive impact of the forest-cover increase on vegetation activity. This is likely occurring in tandem with the changes in soil moisture because soils in regions with increased tree cover tend to hold on to their soil moisture better. We also tested a model including an additional (fourth) interaction term between soil moisture and reforestation, but this did not lead to an improved R^2 adjusted between modelled and observed SIF. We conclude that vegetation activity following reforestation efforts increases most over the temperate areas in northern China classified as grassland and forest, with already relatively high soil moisture. On average, these areas show high covariance between changes in soil moisture and changes in forest cover, indicating that both factors explain the increase in summertime SIF.

4.5 Conclusions and Discussion

Satellite-based solar-induced fluorescence (SIF) observations, a measure of plant photosynthesis, emerge as a promising tool to track changes in carbon uptake in response to land-use change. In this study we demonstrated that TROPOMI SIF captures sharp local reductions in vegetation activity – and thus carbon uptake in the aftermath of a large forest fire in southeastern Australia, the Nunnett– Timbarra River fire, in 2019 – and also that TROPOMI SIF tracks rapid recovery of vegetation activity in the affected area. By careful cross-evaluation of TROPOMI SIF with coinciding tower- and model-based estimates of global primary productivity (GPP), we estimate that the Nunnett-Timbarra River fire caused a reduction of SIF by, on average, 0.2 mW m^{-2} sr^{-1} nm^{-1} corresponding to 130–200 GgC that would otherwise have been stored by the 210 km^2 eucalypt forest if no fire had occurred in the first 8 post-fire months. This shows that TROPOMI SIF is well-capable of monitoring sudden changes in vegetation activity at a scale of some 20×10 km^2, and this predicts excellent potential for the Fluorescence Explorer (FLEX, to be launched in 2026) to monitor changes in carbon uptake from land management techniques which often occur at much smaller spatial scales than the Nunnett-Timbarra River fire.

We also found increases in GOME-2A SIF of 0.1 to 0.2 mW m^{-2} sr^{-1} nm^{-1} over the provinces of Shaanxi, Gansu, Sichuan, and Chonqing in northern China in the period 2007–2012, when China effectuated a large-scale reforestation program aimed at reversing desertification. In contrast, in areas where deforestation occurred, GOME-2A SIF showed a reduction in SIF of 0.1 m^{-2} sr^{-1} nm^{-1} over the same period. The possibility of tracking reforestation (and deforestation) with GOME-2A SIF is supported by independent and co-sampled measurements from MODIS NIRv and by the FluxSat model product over the same areas, also indicating increased (and decreased) vegetation activity. The relatively coarse-scale GOME-2A SIF measurements (40×80 km^2) indicate that vegetation activity increased the most in regions with relatively high soil moisture content and substantial reforestation as diagnosed by the China land-cover dataset. This suggests that reforestation is effective in enhancing carbon storage in the relatively wet and temperate regions of northern China but less so in the subtropical parts of the provinces, which are drier and hotter. Interpreting the observed temporal variability in GOME-2A SIF from 2007 to 2012 with a simple model that accounts for simultaneous spatiotemporal changes in soil moisture, in maximum temperature, and in forest cover, we found that the observed SIF changes in northern China can be explained well ($R^2 = 0.72$) over areas with forests and grasslands that

underwent reforestation. Reforestation efforts, in step with soil moisture increases, appear to be driving the observed increase in SIF. This implies that the impact of reforestation on increases in SIF should be interpreted in the context of simultaneous increases in soil moisture.

Satellite-based SIF observations emerge as a promising method to facilitate the tracking of carbon uptake in response to land-use change. Through the analysis of two distinct cases of forest-cover change, we demonstrated the applicability of SIF as a monitoring tool in combination with satellite data that map the land-use change. The supporting data facilitate the pinpointing of SIF cells aligned with land-cover changes. Our comparative approach revealed distinct changes in SIF dynamics related to shifts in forest coverage. This underscores the capability of SIF to capture the impact of land-cover change, whether driven by distinct abrupt events or gradual transitions, on regional vegetation activity.

Our work underscores the fact that satellite measurements of SIF are useful to monitor changes in carbon uptake following land-use change as long as the spatial and temporal scales at which these occur are sharply demarcated. In this study, the availability of high-resolution MODIS burned-area data (pixel size 1×1 km^2) and TROPOMI SIF (pixel size 7×3.5 km^2) made it possible to detect sharp changes in vegetation activity following a devastating fire over a relatively large area. It is also possible to attribute observed increases in GOME-2A SIF to changes that occur much more slowly and on an even larger spatial scale, such as the reforestation efforts in northern China, but this requires the careful selection and co-sampling of explanatory biogeographical data such as soil moisture, temperature, and forest cover.

Supplement S3

S3.1 Trend correction GOME-2A SIF over northern China

To assess the stability of GOME-2A SIF (SIFTER v2) over north-central China, we used SIF time series over the nearby Gobi Desert (95.5–105.5° E, 40.5–44° N). Figure S3.1 shows the monthly GOME-2A SIF over the Gobi Desert from 2007 to 2018. The colours indicate the respective level-1 processor version over time. Over the early period, 2007–2013, a gradual trend is noticed from around 2011. The striking positive shift in baseline SIF levels from July 2013 relates to the smaller range in viewing zenith angle ($< 35°$) following the swath reduction on 15 July 2013. From June 2014, the higher baseline trend appears to be broken for a period of 5-6 months. Figure S3.2 shows a similar structural break occurring over Sahara and 30–40° N ocean SIF pixels. The timing of the sudden drop in SIF signal coincides with the change of level-1 processor version 5.3 to 6.0 (18 May 2014) (Figure S3.1), and thus suggests a significant influence of these changes on SIF. For our analysis, we solely use the GOME-2A data from the pre-2013 period to control the record's stability. Reprocessing the SIFTER v2 SIF data using level-1 data based on the recent processor version 6.3 that covers the entire data record will eliminate the uncertainty related to level-1 processor changes throughout the data record.

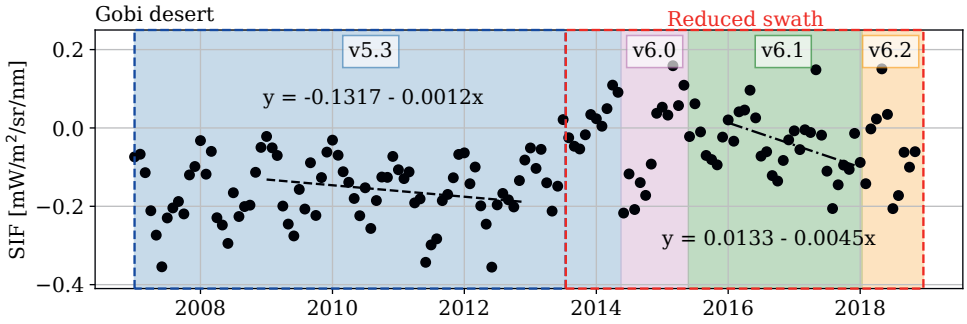


Figure S3.1: Monthly SIF retrieved from GOME-2A measurements as a function of time over the Gobi Desert (95.5–105.5 °E, 40.5–44 °N). The colored blocks indicate the used level-1 processor version (v5.3, v6.0, v6.1 and v6.2) over time. The record can be seen as coming from two different sensors, with the early and late period differentiated by the timing of the swath reduction at 15-06-2013. The early period and late period are, respectively, indicated by the blue and red dotted blocks.

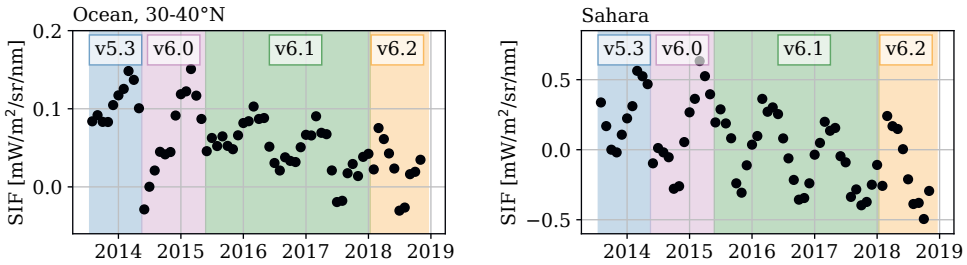


Figure S3.2: Monthly SIF retrieved from GOME-2A measurements as a function of time over the ocean (30 to 40° N) and the Sahara Desert (-8° W to 29° E, 15 to 30° N) over the late sensor period after the swath reduction at 15-06-2013. The colored blocks indicate the used level-1 processor version (v5.3, v6.0, v6.1, and v6.2) over time.

To correct for the noticed gradual trend over the early period, a multiplicative correction factor is applied. Gerlein-Safdi et al. (2020) used latitudinal average SIF to obtain multiplicative correction factors to correct for GOME-2A SIF over northern China (30–40° N). However, the SIF dynamics over the 30–40° N latitudinal band differ strongly over longitude: with higher SIF values over the west and lower over the east (e.g., north-central China). Furthermore, SIF cells that cover vegetational areas could represent the imprint of climatic variation and thus cause biases within the correction factor. The average of SIF over the Gobi desert (free of vegetation) area is expected to stay stable over time and not to be influenced by factors such as climatic fluctuation.

The year-specific correction factor is determined over the Gobi Desert area and corrects for the deviation in yearly SIF at year t with respect to the yearly SIF average over 2007 to 2012 the period of the reference spectra used in the SIFTER v2 retrieval. Therefore, the corrected SIF, $F_{(\mathrm{C,i})}\ (t)$, over cell i and year t is calculated as:

$$F_{\mathrm{C,i}}(\mathrm{t}) = F_{\mathrm{i}}(t)\frac{\overline{F_{\mathrm{Gobi}}}}{F_{\mathrm{Gobi\ ('07\text{-}'12)}}(t)} \tag{S3.1}$$

where $\overline{F_{\mathrm{Gobi('07\text{-}'12)}}}$ represents the 2007-2012 average of SIF over the Gobi Desert and F_{Gobi} (t) the averaged SIF over the Gobi Desert in year t. Yearly SIF over the Gobi Desert is used to determine the correction to limit the uncertainty coming from the low signal levels over the area. Correction values deviate between 0.85 and 1.12. Figure S3.3 shows the correlation between FluxSat GPP with uncorrected and corrected GOME-2A SIF over our study region in China.

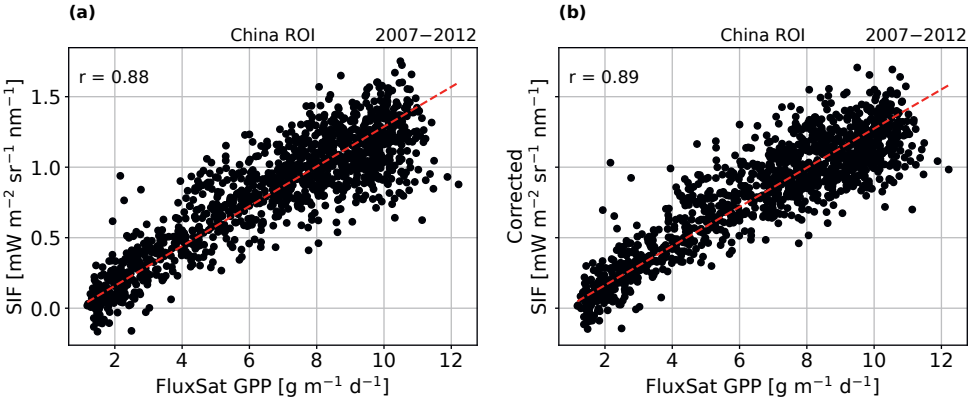


Figure S3.3: (a) Correlation between FluxSat GPP and GOME-2A SIF and (b) correlation between FluxSat GPP and corrected SIF over the China ROI area (104.5°–112° E, 31°–38° N). The data points present SIF and GPP between 2007 and 2012 and over the summer period (June–August).

S3.2 Relationships between TROPOMI SIF and GPP over eucalyptus forest

The SIF–GPP relationship over eucalyptus forest was obtained using TROPOMI SIF observations and GPP estimates from the eddy-covariance flux site in Tumbarumba (AU-TUM: 35.66° N, 148.15° E). We also used FluxSat GPP to infer an alternative SIF–GPP relationship over the eucalyptus forest at Tumbarumba. To account for the smaller footprint of the eddy-covariance measurements, typically in the range of 100–1000 m, we selected TROPOMI SIF observations within a distance of 7 km of their centre from the Tumbarumba site. The $0.05° \times 0.05°$ FluxSat GPP cells, 8 in total, were selected to match the coverage of the selected TROPOMI SIF observations covering the flux tower.

SIF and the FluxSat GPP data have been co-sampled such that observations correspond to the same dates. The temporal co-sampling of SIF and GPP is of importance due to the (mostly) clear-sky bias of SIF observations from satellites, while GPP is measured under various conditions. Previous studies (e.g., Yang et al., 2015) have shown different correlations between SIF and GPP under direct and diffuse light conditions. Therefore, it should be noted that the obtained relationship between SIF and GPP is specific for mostly clear-sky (direct light) conditions.

We inferred the empirical relationships from fitting instantaneous (TROPOMI overpass-time) SIF and daily-aggregated GPP data. In contrast to strategies using daily-corrected SIF for the analysis (Zhang et al., 2018b; Turner et al., 2021), we chose here to use instantaneous SIF because the SIF signal in our region of interest is of low magnitude, and the daily correction would decrease the magnitude even further. Furthermore, the use of instantaneous SIF observations avoids simplified assumptions regarding the scaling of SIF with the amount of sunlight available for photosynthesis.

Reduced major axis regression (RMA) was used to obtain the empirical relationships between SIF and GPP. The RMA regression accounts for uncertainty in both the SIF observations and

GPP data. The use of a linear regression is reasonable following the implied linear relation of SIF–GPP during most daily conditions (Porcar-Castell et al., 2014) as well as the enforced linearity due to integration over the canopy (Magney et al., 2020). The regression analysis of SIF vs GPP clearly indicates the presence of an intercept for the best fit (Figure S3.5). Furthermore, the top-of-canopy SIF depends on the escape ratio of the photons from the canopy and theoretically, space-based SIF could approach zero even if GPP is not 0.

Table S3.1: SIF–GPP relations using instantaneous TROPOMI SIF and daily GPP from the OzFlux dataset and FluxSat over the Tumbarumba flux tower. The OzFlux data represent the GPP estimates from the Tumbarumba tower. SIF is in units of mW m^{-2} sr^{-1} nm^{-1} and GPP in gC m^{-2} day^{-1}.

GPP source	SIF–GPP		SIF–GPP, no intercept
OzFlux	$r = 0.91$	$\mathrm{GPP} = 11.10\,\mathrm{SIF} + 0.81$	$\mathrm{GPP} = 12.19\,\mathrm{SIF}$
FluxSat	$r = 0.94$	$\mathrm{GPP} = 5.56\,\mathrm{SIF} + 1.37$	$\mathrm{GPP} = 7.40\,\mathrm{SIF}$

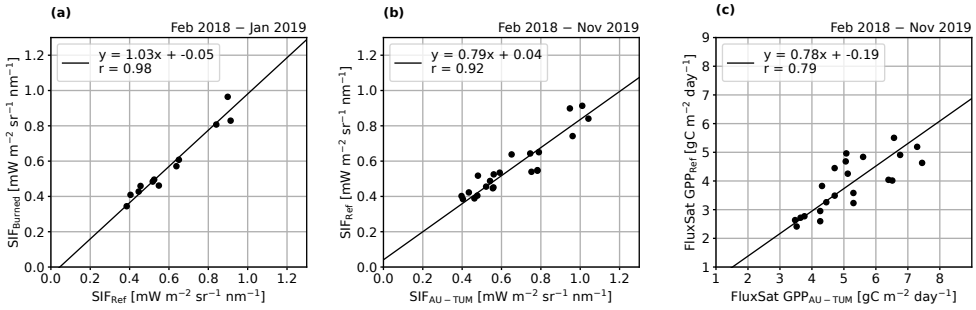


Figure S3.4: Correlation in the period February 2018 – January 2019 between (a) TROPOMI SIF over the reference area and area that would later burn down, and correlation in the period February 2018 – November 2019 between (b) TROPOMI SIF over the Tumbarumba flux tower site (AU-TUM) and TROPOMI SIF over the reference area. Subplot (c) shows the correlation between FluxSat GPP over the Tumbarumba site and the reference area.

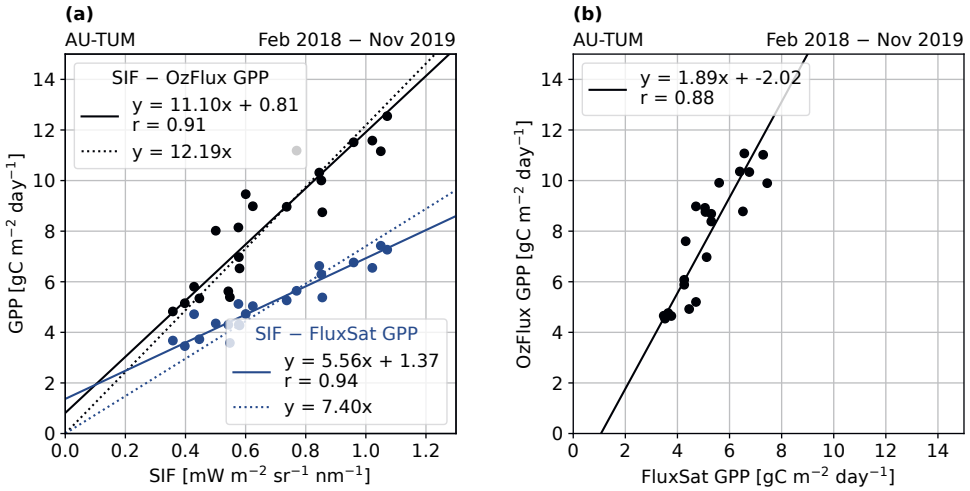


Figure S3.5: Correlation between (a) the TROPOMI SIF and daily GPP with flux tower and FluxSat GPP in black and blue, respectively, at the Tumbarumba Flux tower site (AU-TUM) and (b) monthly aggregated daily GPP versus the monthly averaged GPP where accounted days match SIF observations (collocated) at AU-TUM.

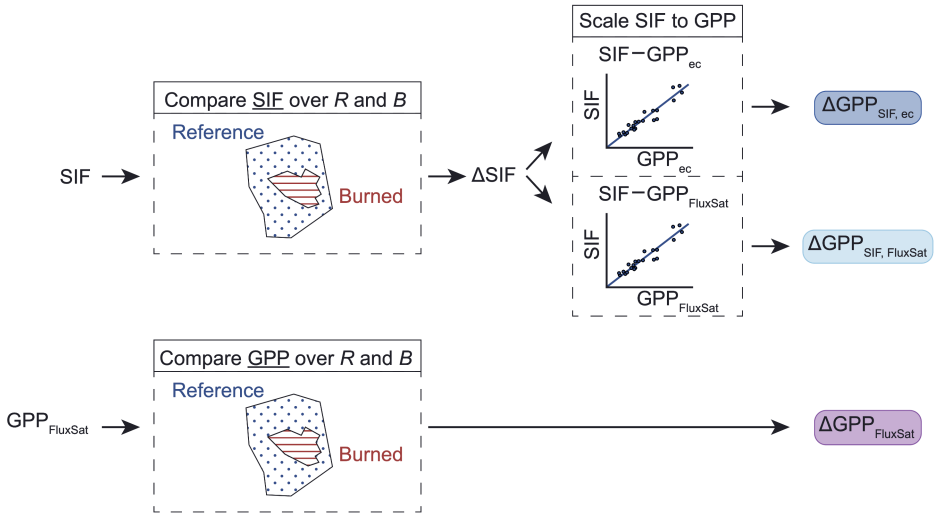


Figure S3.6: Outline of the derivation of the loss in GPP over the burned area: SIF-based GPPs, inferred from SIF–GPP relationship using eddy covariance data from the Tumbarumba OzFlux site and FluxSat GPP, and GPP directly from FluxSat GPP.

Uncertainty Analysis

We address uncertainties in the SIF-based estimated GPP loss via uncertainty propagation following equation 4.1. Factors considered include (1) SIF–GPP representativeness to Nunnett-Timbarra, (2) SIF–GPP representativeness to the post-fire period, and (3) detection of changes in TROPOMI SIF (ΔSIF). For the $\Delta GPP_{SIF,\,ec}$ estimation, we address the uncertainty in (4) footprint differences between SIF observations and GPP estimates from the eddy-covariance flux tower.

1. Comparison of the ratio between FluxSat GPP and TROPOMI SIF obtained over the Tumbarumba tower and the Nunnett-Timbarra area show the similarity of both regions, namely 7.44 ± 1.00 and 7.72 ± 1.25 (gC m^{-2} day^{-1})/(mW m^{-2} sr^{-1} nm^{-1}). The ratios were computed from monthly SIF and GPP data over Feb. 2018 to Nov. 2019. The uncertainty within the SIF–GPP relationship itself is on the order of 10–15 %.

2. To assess the uncertainty in ΔSIF detection, we examine monthly averaged TROPOMI SIF over the burned (B) and reference (R) area. Monthly averaged SIF_B and SIF_R are 0.522 and 0.264 mW m^{-2} sr^{-1} nm^{-1}, over Feb. 2019–Nov. 2019, respectively. Considering TROPOMI's single-measurement precision error of 0.4 mW m^{-2} sr^{-1} nm^{-1} (Köhler et al., 2018) and monthly pixel counts of 185 and 32 pixels over the reference and burned area, respectively, the error estimation is 30 %.

3. We compare the FluxSat GPP to TROPOMI SIF ratio over the burned area during Feb.–Nov. in 2018 (pre-fire) and 2019 (post-fire) to assess the uncertainty in applying the SIF–GPP relationship to post-fire conditions. The ratio was 7.23 ± 0.97 (gC m^{-2} day^{-1})/(mW m^{-2} sr^{-1} nm^{-1}) for pre-fire and 6.34 ± 3.02 (gC m^{-2} day^{-1})/(mW m^{-2} sr^{-1} nm^{-1}) for post-fire conditions, with the uncertainty in the post-fire ratio being approximately 50 %. Note that this analysis is limited due to the brief period between the Nunnett-Timbarra fire and a subsequent wildfire impacting the study area.

4. MODIS NDVI data (500 m resolution) indicates negligible uncertainty in footprint size differences, probably due to the extensive and uniform land cover around the Tumbarumba tower. Using MODIS pixels from 2009–2019 within (i) a 1 km and (ii) a 9 km radius from the tower, representing the eddy covariance footprint size and selected TROPOMI SIF pixels/FluxSat GPP grid cells, NDVI values were 0.77 ± 0.05 and 0.77 ± 0.04, respectively.

Adding these terms in quadrature, we estimate our estimates of SIF-based ΔGPP are associated with a relative uncertainty of 60 %.

S3.3 Climate variability in Northern China

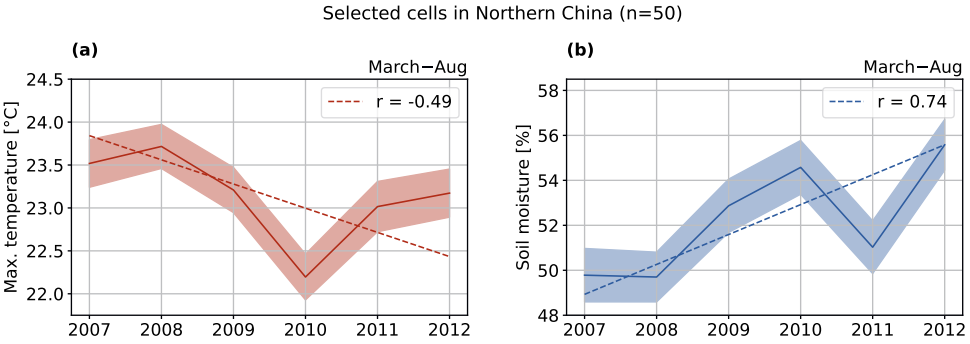


Figure S3.7: Temporal variability of climate variables (a) maximum temperature and (b) soil moisture, averaged over March–August and over all 50 selected (reforested and deforested) cells in the Northern China case study. The maximum temperature and soil moisture data are obtained from Copernicus Climate Change Service (2019) and Dorigo et al. (2019), respectively, and were aggregated to a 0.5°×0.5° grid.

Chapter 5

General discussion, recent developments, and outlook

This chapter contains parts based on results from student internship reports under my supervision and from LANDMARC deliverable reports to which I contributed as a co-author.

The mechanistic advantage of SIF makes it a promising proxy for more robust and direct tracking of photosynthetic activity. Literature often states that to interpret SIF meaningfully, one must have a sufficient understanding of the biological processes underlying the signal (e.g., Porcar-Castell et al., 2021). In parallel, interpreting satellite-derived SIF also requires awareness of the principles and challenges underlying the retrieval. This thesis overarches both the subject of retrieval and the use of satellite-based far-red SIF for vegetation monitoring. Hence, it provides a combined perspective on constructing consistent climate GOME-2 SIF records (Chapters 2 and 3) and on using SIF within a monitoring framework (Chapter 4). In this chapter, I integrate these findings, present additional analysis that builds on the work, and discuss the implications for satellite remote sensing of SIF (Section 5.1) and its use for vegetation monitoring (Section 5.2). Finally, in Section 5.3, I revisit the central research questions of this work, synthesise the main conclusions, and outline the direction for further research.

5.1 Next steps for satellite remote sensing of SIF

One of the main goals of this thesis was to construct a reliable climate SIF record. We developed and applied the SIFTER v3 algorithm to retrieve consistent and coherent SIF records from GOME-2A (2007–2017) and GOME-2B (2012–2023). Achieving SIF records suitable for long-term vegetation analysis requires careful consideration of instrumental behaviour, retrieval assumptions, and sampling strategies, as these factors can affect the stability and interpretability of the SIF observations. In the following subsections, I present additional analysis and discuss relevant aspects for constructing consistent SIF datasets that support robust vegetation monitoring.

5.1.1 GOME-2C SIF

The GOME-2 series consists of three identically designed sensors, launched in sequence, with a combined coverage expected to extend for over 20 years. Chapter 3 focused on harmonising observations from GOME-2A and GOME-2B into one coherent long-term SIF record. The combined record showed strong coherence and aligned closely with independent FluxSat GPP data. The next step is to extend this record further by incorporating observations from GOME-2C.

The GOME-2C sensor, onboard Metop-C, was launched on 7 November 2018 and is currently in full operation. Instrumental characteristics are similar and close to identical to those of GOME-2A and GOME-2B (Table 1.2). Here, I present my recent work on retrieving a SIF record from GOME-2C using the SIFTER v3 algorithm. All retrieval steps were kept equal to those applied to GOME-2A (Chapter 2) and GOME-2B (Chapter 3), with the reflectance degradation correction explicitly tailored to GOME-2C (see Section S4.1). This new record spans from January 2019 to November 2024 and, to our knowledge, is the first SIF record retrieved from GOME-2C.

GOME-2C SIF shows similar spatial distributions to GOME-2B SIF, but with slightly lower SIF values over highly active areas. Figure 5.1 shows the SIF timeseries from all three GOME-2 sensors over the six vegetative regions studied in Chapter 3. For the majority of the regions, GOME-2C closely follows the seasonality captured by GOME-2A and GOME-2B, but with slightly lower peaks over the Corn Belt, Eastern China, and Zambia. Over the Amazon region,

however, GOME-2C fails to capture the expected seasonality. The Amazon is known as a challenging region for SIF retrieval due to its high cloud coverage and water vapour content. In addition, this region is affected by the South Atlantic Anomaly (SAA).

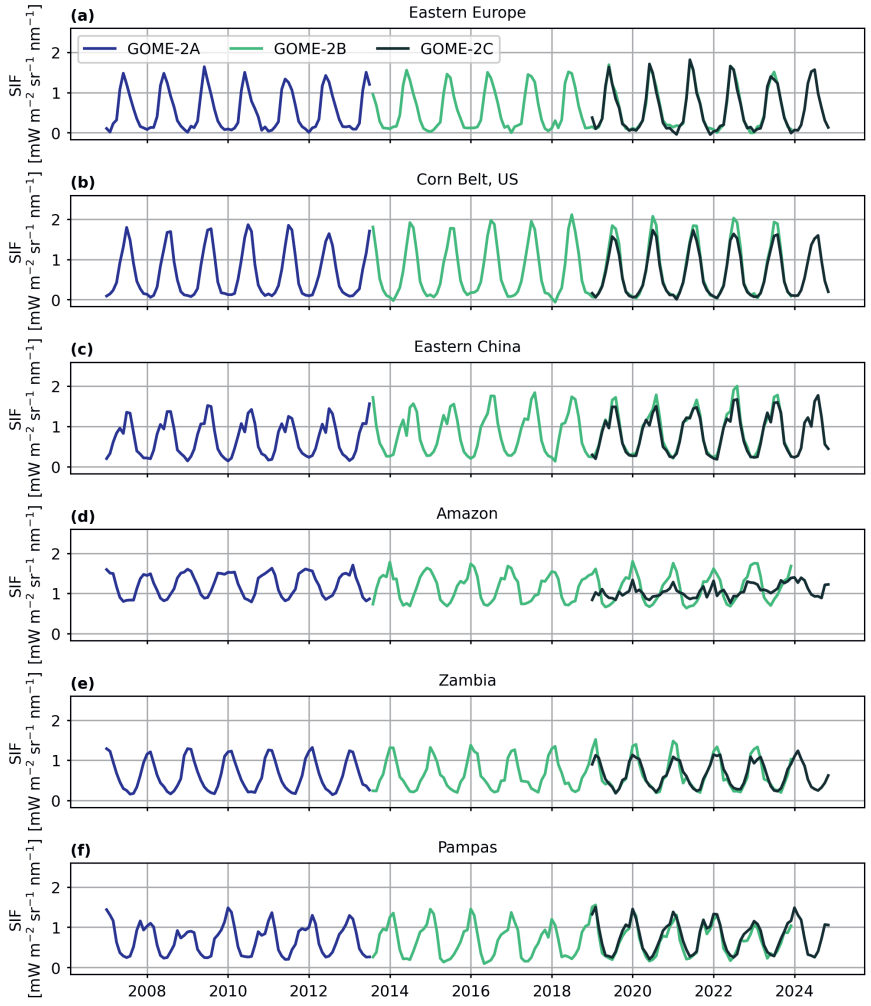


Figure 5.1: Time series of monthly averaged Level-2 SIF values retrieved from GOME-2A (in blue), GOME-2B (in green), and GOME-2C (in dark teal) over (a) Eastern Europe, (b) the United States Corn Belt, (c) Eastern China, (d) the Amazon, (e) Zambia, and (f) the Pampas region.

The SAA is a region, covering parts of the South Atlantic and South America, where the geomagnetic field is weaker. As a result, charged particles in solar radiation are less shielded, causing a peak in radiation exposure. The increased radiation can affect space-based observations, such as

GOME-2, by raising the noise in level-1 reflectances (Parazoo et al., 2019). This leads to greater uncertainty in SIF over the SAA region, as shown in Figure S2.6 (in the Supplement to Chapter 3), due to increased uncertainty in measured reflectance and reduced spectral fitting accuracy. A more substantial SAA effect on GOME-2C may explain the difficulty in capturing Amazon seasonality. This is evidenced by the pronounced reduction in valid GOME-2C SIF retrievals over the Amazon compared to globally, shown in Figures 5.2a and b. Although a reduction in valid observations is also observed for GOME-2A and GOME-2B over the Amazon, it is substantially stronger for GOME-2C. This indicates a higher rate of poor spectral fits for GOME-2C, consistent with reduced fit stability due to more substantial SAA-induced noise. Although the SAA is known to impact GOME-2 SIF retrievals (Joiner et al., 2016; Parazoo et al., 2019), its precise effect on each sensor remains understudied. This knowledge gap partly reflects the limited calibration analysis on GOME-2's band 4. Therefore, the extent of SAA-induced noise and its impact on NIR retrieval stability is insufficiently characterised.

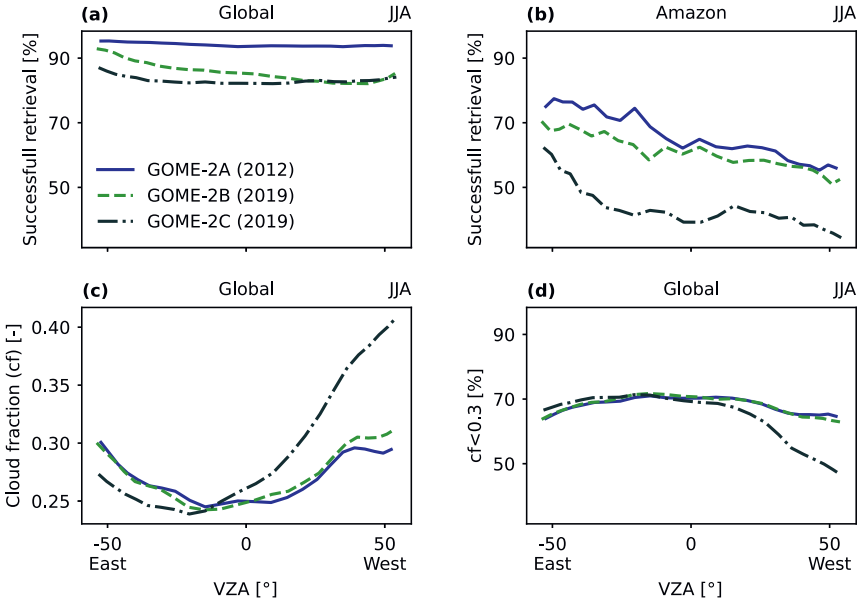


Figure 5.2: Percentage of GOME-2A (solid blue), GOME-2B (dashed green), and GOME-2C (dashed-dotted dark teal) pixels with successful retrievals over the (a) Global and (b) the Amazon region. Here, a retrieval is successful when the autocorrelation is < 0.2. The percentages reflect successful retrieval among pixels with cloud fractions < 0.3. (c) Average global FRESCO+ cloud fraction across the viewing zenith angle (VZA). (d) Percentage of global pixels meeting the cloud fraction requirement of < 0.3. Graphs reflect global data over the June–August period. All data was filtered for SZA $< 80°$ $|\text{lat}| < 60°$.

In addition, the accuracy of cloud screening may contribute to the discrepancy between GOME-2C and the GOME-2A and GOME-2B sensors. We examine the cloud fractions retrieved from

GOME-2 reflectances (around 760 nm) using FRESCO+, which is used to filter GOME-2 SIF. Figure 5.2c shows that the FRESCO+ cloud fraction product exhibits a different east-west global pattern for GOME-2C than for GOME-2A and GOME-2B. GOME-2C appears to underestimate cloud fractions for eastern pixels and overestimate them near nadir and on the western side of the swath. This asymmetry likely results in an overrepresentation of eastern pixels in the valid retrievals, as more nadir and western pixels are flagged as cloudy. The FRESCO+ discrepancies might come from calibration artefacts in GOME-2C that plague its retrieval. Future work should therefore examine the performance of the FRESCO+ GOME-2C cloud product and test alternative, GOME-2-independent cloud masks, e.g., AVHRR, to reduce such across-sensor biases. Moreover, the cloud effect is amplified by the scan angle dependency in retrieval success, which favours eastern pixels (Figure 5.2a and b). While this bias is minor in global averages, almost zero for GOME-2A, it becomes substantial over the Amazon. In JJA 2019, 44.7 % of the valid GOME-2C retrievals over the Amazon were east pixels, whereas only 25.6 % were from the west (Figure 5.3a to c). This skew introduces a larger share of partly cloudy scenes, which can affect the accuracy of SIF.

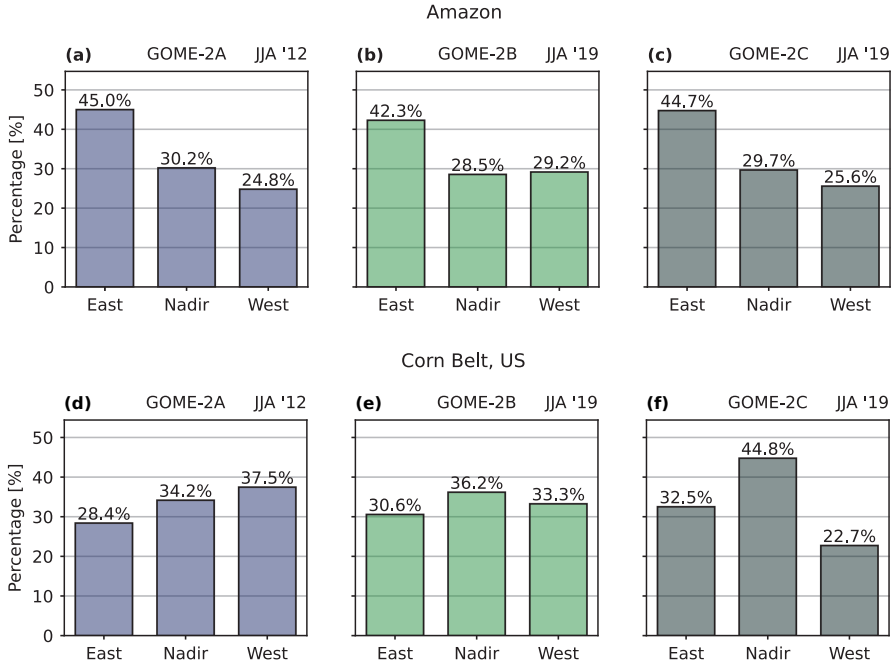


Figure 5.3: Contribution of East, Nadir, and West pixels to GOME-2 SIF averages over the Corn Belt region, United States, in the June–August period. Distributions are shown for (a) GOME-2A (in 2012), (b) GOME-2B (in 2019), and (c) GOME-2C (in 2019). SIF data is filtered on FRESCO+ cloud fraction < 0.3 and autocorrelation of < 0.2 to secure accurate retrieval fit.

Similar sampling biases may also explain slight divergences between GOME-2C and GOME-2B in other regions. Over the Corn Belt region, for instance, GOME-2C consistently underestimates

the summer SIF peak (Figure 5.1b). Figure 5.3d to f shows the distribution of east, nadir, and west pixels during June–August for all three GOME-2 sensors. For GOME-2C, 44.8 % of the accepted pixels are nadir, and only 22.7 % are west pixels. A more equal distribution is found for GOME-2B, with 36.2 % and 33.3 % of nadir and west pixels, respectively. As shown in Chapter 3, west pixels exhibit higher values due to BRDF effects than other parts of the swath, particularly over highly productive regions. Hence, the underrepresentation of west pixels in GOME-2C can (at least partly) explain the across-sensor mismatch during the peak season.

These findings align with Chapter 3 and further demonstrate that variations in the distribution of sampled viewing geometries significantly impact the spatio-temporally averaged SIF value. A potential mitigation would be to apply sampling weights when averaging, where each weight indicates the representativeness of a viewing-geometry group within the collected pixels. However, this method biases the averaging towards less frequently observed geometries, thereby increasing noise due to a reduced number of contributing observations. Nevertheless, it can help reduce apparent shifts in SIF caused by changes in sampling rather than from true physiological variability. I further discuss the treatment of scan angle dependency within SIF observations in Section 5.1.4.

Furthermore, the scan angle dependency in retrieval success introduces sampling biases. The accuracy of the spectral fitting generally decreases from the eastern to the more sunlit western pixels, with noted differences in intensity across sensors and scenes. This pattern in fit success could stem from calibration artefacts such as polarisation sensitivity or nonlinear detector response. Moreover, it may also suggest that the current retrieval setup, in which the PCs used to model the atmospheric transmittance are independent of viewing geometry, does not fully capture the scan angle variability. It is, however, crucial to identify the dominant cause before adapting the retrieval design, whether this variability is physical or instrumental.

5.1.2 TROPOMI SIF

The SIFTER algorithm was initially designed for the GOME-2A sensor. Here, I discuss our recent work on adapting and optimising the SIFTER v3 algorithm for TROPOMI. The application of the SIFTER v3 algorithm to multiple instruments supports the construction of harmonised SIF records across sensors. Consistency in the retrieval algorithm limits across sensor biases. A harmonised SIF record containing observations from the GOME-2 sensors (A, B, and C) and TROPOMI is particularly exciting due to the potential of sub-daily retrievals. GOME-2 has a late-morning overpass at 09:30 local time, while TROPOMI has an afternoon overpass at 13:30 local time. Moreover, sub-daily SIF observations can reduce the uncertainty in SIF-based GPP estimates by better constraining the diurnal variability of photosynthetic activity.

The TROPOMI sensor, onboard Sentinel-5 Precursor, was launched on October 13, 2017, and is currently operational. TROPOMI is a push-broom imaging spectrometer, measuring 448 ground pixels (in the NIR band) simultaneously across a 2600 km swath. This monitoring scheme enables daily global coverage at nadir footprints of 7×3.5 km^2 (or 5.5×3.5 km^2 after 6 August 2019). The fine spatial resolution, compared to GOME-2, advances vegetation monitoring. Moreover, increased precision is expected from the spectral resolution of 0.37 nm in the far-red SIF range, with respect to GOME-2 (e.g., 0.48 nm for GOME-2A).

Application of SIFTER v3 to TROPOMI

TROPOMI's sensor design enables direct application of the SIFTER v3 algorithm. Here, we describe how the algorithm was adapted for application to the TROPOMI sensor, accounting for its sensor-specific characteristics. The degradation correction described in Chapter 2 is not needed for retrievals from TROPOMI. Its instrumental design makes it less susceptible to degradation effects. Furthermore, degradation and other calibration issues are already accounted for in the level-1b data (Ludewig et al., 2020). The stable solar irradiance observations further allow their direct use in the retrieval model, replacing the reference spectrum used for GOME-2. Finally, a separate set of PCs is obtained for each row of TROPOMI's 2-dimensional detector array to account for variations in spectral and radiometric characteristics across-track. The 448 sets of PCs are obtained following the same procedure as for the GOME-2 instruments (Chapters 2 and 3). The Caltech TROPOMI SIF algorithm also calculates a set of PCs for each specific row (Köhler et al., 2018). For each ground pixel, spectra are collected over the Sahara region, spanning a sufficient number of years to represent a wide range of conditions. Specifically, we used spectra from the years 2019 and 2023, representing the early and later years of operation, respectively. Tests with five years of data (2019–2023) showed negligible differences in the computed PCs. Therefore, the two-year subset was used for computational efficiency.

The SIFTER v3 algorithm implemented for GOME-2 uses a fixed number of 10 PCs in the fit model. We evaluate the suitability of this configuration for TROPOMI SIF by examining how the number of PCs affects the retrieval results. The selected number of PCs is somewhat arbitrary, but substantially affects the retrieval performance (Sanders et al., 2016; Köhler et al., 2015; Chapter 3). In Chapter 3, we showed that the GOME-2 SIF retrieval is most sensitive to the number of PCs used in the model fit. Selecting the number of PCs requires careful consideration of how many are needed to sufficiently capture the true spectral variability, while avoiding overfitting.

To examine this sensitivity on TROPOMI SIFTER, we performed retrievals using different numbers of PCs, ranging from 4 to 10. Our analysis is based on retrievals over the Amazon region on 6 February 2024. All retrievals were filtered following the standard SIFTER fit quality criteria and co-sampled to ensure that each dataset represents the same observations. We applied a more relaxed cloud filter (cloud fraction < 0.4) to increase the number of valid retrievals. Figure 5.4 illustrates the changing SIF retrieval precisions with varying numbers of PCs. The median precisions decrease from 0.34 for $\mathrm{PC}_{n=4}$ to 0.31 mW m^{-2} sr^{-1} nm^{-1} for $\mathrm{PC}_{\mathrm{n=6}}$, after which it gradually rises with added PCs. The precision is largest (thus worst) for 10 PCs, with a median value of 0.42 mW m^{-2} sr^{-1} nm^{-1}. When 6 PCs are used, 94.2 % of the observations have a precision of 0.5 mW m^{-2} sr^{-1} nm^{-1} or less, compared to only 74.3 % for 10 PCs (Table 5.1).

However, a high retrieval precision alone does not warrant an accurate representation of SIF. In practice, an underfitted model can yield small statistical uncertainty. This can lead to an overconfident precision estimate. To obtain confidence in the model's performance, the physical representation of the spectral fit must be evaluated. We evaluate the quality of fit using the reduced chi-squared statistic (χ^2_{red}), which quantifies the discrepancy between the observed data and the model's predictions. Ideally, a $\chi^2_{\mathrm{red}} \approx 1$ indicates that the model captures the full

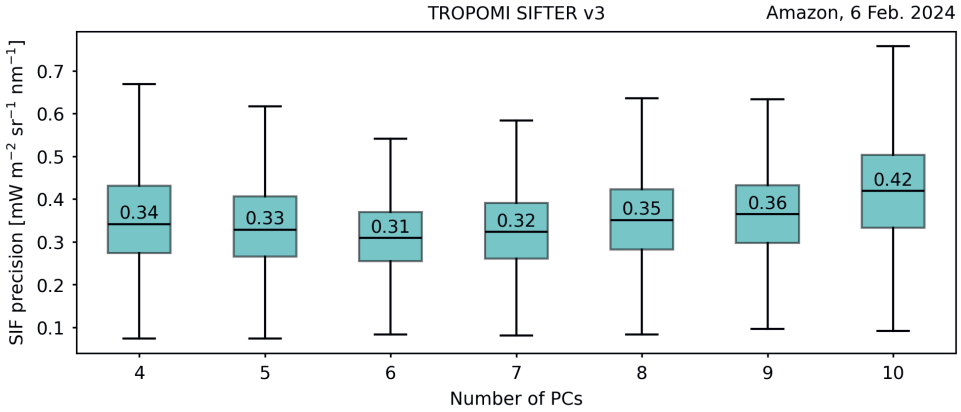


Figure 5.4: Distribution of TROPOMI SIF retrieval precision as a function of the number of PCs used in the SIFTER v3 retrievals. SIF was retrieved for a subset of a TROPOMI orbit covering the Amazon region on 6 February 2024. The precision was calculated from the fit covariance matrix and scaled by the reduced χ^2_{red}. The median value of each retrieved set is shown in text. All data were filtered based on the quality flag (> 0.6), autocorrelation (< 0.2), and cloud fraction (< 0.4). To enable fair comparison, all data were co-sampled such that each box represents the same observations. Analysis performed based on the approach of Hajaldaw (2025).

variance in the spectrum within the expected measurement noise. Values of $\chi^2_{\text{red}} < 1$ and > 1 indicate overfitting and underfitting, respectively.

Reducing the number of PCs negatively affects the fit residual (Table 5.1). The average χ^2_{red} value decreases steadily with increasing number of PCs, from 2.59 for $\text{PC}_{n=4}$ to 1.44 for $\text{PC}_{n=10}$. Between $\text{PC}_{n=6}$ and $\text{PC}_{n=7}$, the fit improvement appears to level off and shows a clear knee in the trend (indicated in Figure S4.11). The alignment of the χ^2_{red} knee with the best precision obtained for $\text{PC}_{n=6}$ suggests that the use of six PCs provides an effective compromise between the fit accuracy and model precision. Although the average χ^2_{red} for $\text{PC}_{n=6}$ (1.87) exceeds the upper threshold of 1.5 used in the Caltech TROPOMI SIF product (Köhler et al., 2018), the resulting SIF values proved to be most robust for this configuration, supporting the use of $\text{PC}_{n=6}$. Using six instead of 10 PCs leads to a tighter distribution of retrieved SIF values across the Amazon, indicated by the lower coefficient of variation (CV=$\sigma_x/\overline{x}$) of 1.0 compared to 1.28. Overall, these results suggest that the TROPOMI SIF retrieval performs best with six PCs. Therefore, we adopt the use of $\text{PC}_{n=6}$ for the final TROPOMI SIFTER configuration.

Table 5.1: Summary of retrieval results over the Amazon on 6 February 2024 from TROPOMI SIFTER v3 using four to 10 PCs. Data selection and filtering follow the details described in the caption of Figure 5.4. The relative uncertainty reflects the ratio of the averaged measurement precision to the averaged measured value. The retrieval success for each set was determined individually, without co-sampling.

SIF retrieval	Number of PCs used						
[mW m^{-2} sr^{-1} nm^{-1}]	4	5	6	7	8	9	10
Mean value	0.90	0.79	0.76	0.72	0.70	0.68	0.65
SD value	0.81	0.77	0.76	0.82	0.88	0.86	0.83
Mean precision	0.36	0.34	0.31	0.33	0.35	0.36	0.41
SD precision	0.15	0.13	0.11	0.12	0.13	0.13	0.15
Relative uncertainty	40.0 %	43.0 %	40.8 %	45.8 %	50.0 %	52.9 %	63.0 %
Retrieval success	62.6 %	74.7 %	70.5 %	70.2 %	68.4 %	71.2 %	72.5 %
χ^2_{red}	2.59	2.26	1.87	1.70	1.56	1.49	1.44

TROPOMI SIF results

We evaluate the retrieval performance of the application of SIFTER v3 to TROPOMI. Figure 5.5 shows the spatial distribution of the retrieved TROPOMI SIF and its precision over the Amazon on 6 February 2024. The map reveals detailed spatial structures, with high SIF over the Amazon land surface, and expected low (≈0) values over the Atlantic Ocean and along the contours of the upper Amazon river. We note higher uncertainty in SIF towards the swath edges, consistent with earlier findings for TROPOMI retrievals (Köhler et al., 2018; Guanter et al., 2021). The lower uncertainty at the edges results from TROPOMI's instrumental design, specifically the modified detector binning scheme. Each ground pixel reflects the binned average of several detector pixels to reduce the signal-to-noise ratio (Veefkind et al., 2012). However, toward the edges, fewer pixels are binned, which leads to higher noise (Köhler et al., 2018).

Next, we compare the TROPOMI SIFTER retrievals against the official TROPOSIF product (Guanter et al., 2021). The TROPOSIF product retrieves SIF for two different window settings: 735–758 nm and 743–758 nm. We use the SIF retrieved from the latter, narrower window, as it's more comparable to the retrieval window applied in SIFTER. Overall, TROPOSIF applied a similar retrieval algorithm, using 7 PCs, but without the ground-pixel PC approach. To allow a fair comparison, we co-sample the pixels of TROPOSIF and SIFTER, requiring valid retrievals in both products following the respective quality criteria of each dataset. Figure 5.6 shows that both products show similar spatial patterns ($r = 0.77$, Figure S4.13). SIFTER shows significantly higher SIF values, with an average almost three times greater than TROPOSIF.

Particularly striking is the difference in valid observations between the two products, which is considerably lower for TROPOSIF. To understand this discrepancy, we used the same filtering criteria as Guanter et al. in SIFTER. This filtering approach combines thresholds based on the TOA radiance, observation conditions (SZA and VZA), the retrieved SIF value, and the χ^2_{red} value ($\in [0.6, 2]$) (Guanter et al., 2021). Over the tested region, the majority of TROPOSIF

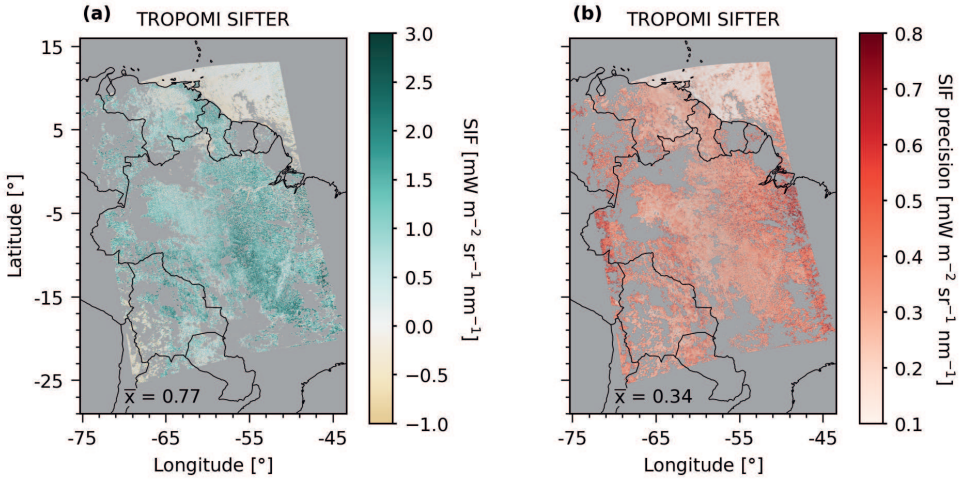


Figure 5.5: Spatial distribution of (a) TROPOMI SIF values and (b) its precision retrieved using the SIFTER v3 algorithm over a subset of a TROPOMI orbit covering the Amazon region on 6 February 2024. Data were filtered for cloud fraction < 0.4 and standard SIFTER fit quality criteria: autocorrelation < 0.2 and quality flags > 0.6. The mean ($\overline{x}$) of each variable is shown in text.

pixels are discarded due to their inadequate fits that do not meet the χ^2_{red} requirement. After applying the cloud fraction, radiance, SZA, VZA, and SIF filters, 62 % of the SIFTER retrievals meet the χ^2_{red} requirements, whereas only 18.6 % of TROPOSIF retrievals do (Figure S4.15). Interestingly, the "bad-fit" TROPOSIF pixels exhibit SIF values of reasonable ranges, but display a clear striping pattern across-track (Figure S4.14). The issue of striping is also recognised by Guanter et al.. This pattern, together with the large number of invalid retrievals, could likely stem from the non-ground-pixel-specific PCs used in the TROPOSIF algorithm. However, this should be further analysed. Overall, the results of this comparison suggest that the developed TROPOMI SIFTER algorithm enables more robust retrievals than TROPOSIF, at least for the studied area and time.

We conclude that the first SIFTER v3 retrievals for TROPOMI demonstrate the successful application of this algorithm to the TROPOMI sensor. The test retrieval over the Amazon shows promising performance in terms of precision and robustness. These results highlight the potential of our SIFTER algorithm to retrieve consistent SIF records across sensors and beyond the GOME-2 series. Applying the SIFTER framework to observations from the upcoming FLEX mission would extend the methodological harmonisation across sensors, reflecting different spatial scales. This could offer new insights into SIF variability at sub-pixel scales, strengthening the interpretation of coarser-resolution SIF retrievals.

Sensitivity tests on GOME-2 SIF

Building on the conclusion of optimisation of TROPOMI SIFTER for $\text{PC}_{n=6}$, we performed a similar analysis to examine the impact of PC numbers on GOME-2 retrieval. I selected the

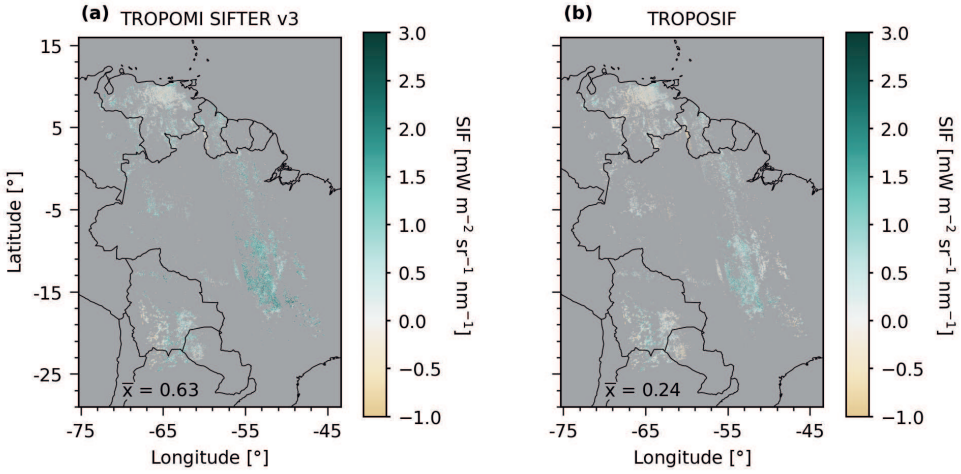


Figure 5.6: Spatial distribution of co-sampled TROPOMI SIF values from (a) SIFTER v3 and (b) the TROPOSIF product (Guanter et al., 2021). Pixels are co-sampled after filtering each dataset according to the respective quality criteria defined for each product. Data presents observations made over the Amazon region on 6 February 2024.

Congo Basin (13° S–6° N, 14–31° W) as a test region to complement the sensitivity analysis in Chapter 2, which used the same region. Moreover, I used GOME-2B data (generated in Chapter 3) from 14 January 2017. As reported in Chapter 3, over this time and region, we found a spread of 0.51 mW m^{-2} sr^{-1} nm^{-1} in mean SIF (reflecting approximately 41.5 % of SIF for $PC_{n=10}$) when varying the number of PCs used from four to 10. Figure 5.7 illustrates the distribution in GOME-2B SIF precision for $PC_{n=4}$ to $PC_{n=10}$. The precision remains relatively stable between $PC_{n=4}$ and $PC_{n=8}$ with median values around 0.52–0.54 mW m^{-2} sr^{-1} nm^{-1}, but is lowest for $PC_{n=7}$. The precision for $PC_{n=10}$ is substantially higher (0.68 mW m^{-2} sr^{-1} nm^{-1}), indicating enhanced uncertainty and overfitting when 10 PCs are used to model the atmospheric transmittance. Table 5.2 shows less variation in averaged χ^2_{red} across the number of PCs used for GOME-2B retrievals, compared to TROPOMI. This suggests that the fit quality for GOME-2B SIF depends less on the number of PCs used. For all numbers of PCs, the retrieval success exceeds 90 %, but is lowest for $PC_{n=10}$ (91.2 %).

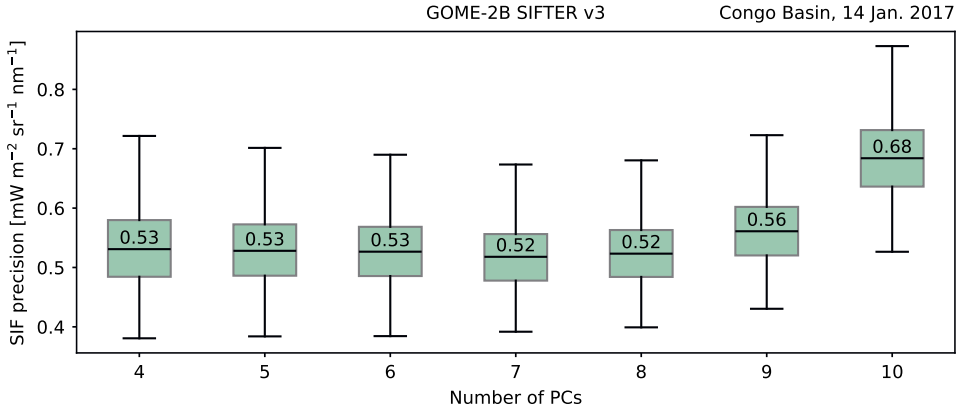


Figure 5.7: Caption as in Figure 5.4, but for GOME-2B SIF retrievals over the Congo Basin (13° S–6° N, 14–31° W) on 14 January 2017.

Despite the suggested increase in SIF uncertainty for $PC_{n=10}$, the relative uncertainty with respect to the SIF value is lowest for this configuration. This follows from the higher mean SIF retrieved when using 10 PCs. Furthermore, $PC_{n=10}$ exhibits the least spatial variability in retrieved SIF, with a coefficient of variation (CV) of 0.54, compared with 0.71 for $PC_{n=7}$. Taken together, these results indicate that 10 PCs perform favourably for GOME-2B in terms of relative uncertainty. By contrast, configurations with fewer PCs, such as $PC_{n=7}$, result in better absolute precision. Further dedicated analysis is needed to evaluate the trade-off between absolute precision and relative uncertainty when selecting the PC configuration for GOME-2 SIF retrievals.

The results from the sensitivity analysis on both TROPOMI and GOME-2B SIF indicate that the optimal numbers of PCs may differ between sensors. Sensor differences, such as noise levels and spectral resolution, may cause such a difference. While $PC_{n=6}$ appears optimal for TROPOMI, the GOME-2B analysis suggests that both $PC_{n=7}$ and $PC_{n=10}$ perform well depending on which uncertainty metric is prioritised. The TROPOMI and GOME-2B sensitivity tests were performed over different regions and dates, which may also influence the results. Therefore, it remains unresolved whether a common PC configuration, for example, of $PC_{n=6}$, can be used across both sensors. Further analysis is needed to evaluate which configuration of PCs is most favourable in retrieving robust SIF across a broader range of regions and conditions.

Table 5.2: Summary of retrieval results from GOME-2B SIFTER v3 using four to 10 PCs. Data selection and filtering follow the details described in the captions of Figure 5.7. The relative uncertainty reflects the ratio of the average measurement precision to the average measured value. The retrieval success for each set was determined individually, without co-sampling.

SIF retrieval	Number of PCs used						
[mW m^{-2} sr^{-1} nm^{-1}]	4	5	6	7	8	9	10
Mean value	0.80	0.79	0.76	0.88	0.91	1.00	1.23
SD value	0.62	0.59	0.59	0.62	0.61	0.59	0.67
Mean precision	0.54	0.54	0.53	0.52	0.53	0.57	0.69
SD precision	0.08	0.07	0.06	0.06	0.06	0.06	0.08
Relative uncertainty	67.5 %	68.4 %	69.7 %	59.0 %	58.2 %	57.0 %	56.1 %
Retrieval success	94.2 %	94.9 %	95.9 %	95.3 %	95.2 %	95.7 %	91.2 %
χ^2_{red}	1.39	1.35	1.33	1.27	1.29	1.30	1.33

5.1.3 Impacts of atmospheric absorption and scattering

Accurately accounting for the impact of atmospheric absorption is considered the most uncertain step in SIF retrieval. In Chapters 2 and 3, we showed that the retrieval is highly sensitive to the modelling of atmospheric transmission, as represented by the constructed PCs. Uncertainty arising from atmospheric absorption is evident in the fit residuals, which increase over the 734–740 nm region where water vapour absorption features are present. This behaviour is observed for both GOME-2 (Figures 2.7 and S4.16) and TROPOMI SIF retrievals (Figure S4.10).

To mitigate uncertainty from water vapour absorption, Köhler et al. (2018) used a narrower retrieval window (742–758 nm) for TROPOMI SIF retrieval than used in SIFTER v3 (734–758 nm). However, the benefit of such a reduction is not straightforward. Parazoo et al. (2019) evaluated the two window ranges for GOME-2A retrieval. They found a decreased bias in GOME-2A SIF versus TROPOMI SIF for the narrow 742–758 nm window, but at the cost of correlation and noise due to fewer spectral points. Hence, there is a clear trade-off between reducing systematic uncertainty related to atmospheric absorption and maintaining sufficient signal-to-noise to assure robust retrievals. This is particularly important for GOME-2, which has a relatively coarse spectral resolution (0.48 nm for GOME-2A) compared to newer sensors such as TROPOMI (0.37 nm). Maintaining retrieval robustness is essential in ensuring consistency across time and sensors. Future studies should further explore the optimal balance between reducing absorption uncertainty and maintaining sufficient signal-to-noise for robust SIF retrieval.

Aside from the retrieval window selection, the ability of the PCs to accurately capture atmospheric transmission affects the uncertainty arising from atmospheric absorption in the retrieval. Chapter 2 showed that improved pre-treatment of the reflectance spectra leads to PCs that better represent transmission variability. Moreover, Section 5.1.2 discussed the importance of careful selection of the number of PCs to prevent overfitting. Currently, SIFTER v3 derives PCs from spectra collected over the Sahara, which is a common reference area (Joiner et al., 2013, 2016).

However, this region may not, on its own, be representative of atmospheric conditions across all regions (van Schaik et al., 2020). Future SIFTER developments could explore more diverse fluorescence-free reference scenes to obtain PCs from. This might improve the fit performance in areas with conditions distinct from those in the Sahara, for example, at higher elevation (affecting surface pressure) or with higher water vapour content.

Another atmospheric effect affecting retrieval uncertainty is atmospheric scattering. SIF retrievals generally assume that Fraunhofer absorption signatures of the solar spectrum are retained in the measured radiance spectrum, neglecting inelastic scattering effects (Frankenberg et al., 2011a). This allows the radiance signal to be simply separated into a Fraunhofer line component and a fluorescence infilling component. However, recent work by Sanghavi et al. (2025) shows that inelastic scattering has a non-negligible impact on the Fraunhofer lines. These effects can substantially bias SIF retrievals and cause systematic biases in SIF retrieval over vegetation-free regions (up to 0.35 mW m^{-2} sr^{-1} nm^{-1}), possibly contributing to the zero-level offsets observed in SIF retrievals, including our GOME-2 retrievals (Chapter 2). Sanghavi et al. (2025) introduced a lookup table based on physical simulations to subtract the inelastic scattering effect, improving the SIF retrieval accuracy (shown for OCO-2). Future studies should investigate the applicability of this approach to SIF retrievals from other sensors, including GOME-2 and TROPOMI.

5.1.4 Scan angle dependency

Solar-induced fluorescence is a function of viewing zenith angle (VZA), meaning its value depends on the geometry between the sun, the sensor, and the vegetation. The resulting bias in SIF is particularly important for wide-swath sensors, such as GOME-2 and TROPOMI, as they measure over a wide range of VZA. The viewing geometry dependency in SIF is of physical origin, as discussed in Chapter 3. However, instrumental and retrieval challenges can alter the east-west bias. Instrumental and retrieval-induced biases in east-west SIF complicate the interpretation of SIF and limit the product's spatial and temporal consistency.

The effect of reflectance degradation on the long-term stability of SIF from instruments such as GOME-2 is widely recognised. Yet, its impact on the coherence of SIF data, by affecting the east-west bias, has received less attention. Chapters 2 and 3 highlighted the importance of accounting for scan angle dependent reflectance degradation to ensure coherent SIF retrievals, both within and across sensors. To our knowledge, SIFTER v3 is the first SIF retrieval algorithm to correct for this degradation-induced scan angle dependency. Figure 5.8 illustrates the impact of the reflectance correction on the east-west bias in GOME-2A SIF over the Amazon. The applied scan angle-dependent degradation correction reduced the east-west bias by a factor of about two, demonstrating the importance of accounting for cross-track degradation effects in SIF retrievals.

Beyond correcting instrumental artefacts, the retrieval should adequately account for the anisotropic behaviour of surface reflectance to limit false across-track biases. The surface reflectance is strongly dependent on the viewing geometry, particularly over vegetated areas (Tilstra et al., 2021). If not properly captured in the fit model, residual reflectance anisotropy could leak into the retrieved SIF term. In the SIFTER algorithm, the surface albedo is simulta-

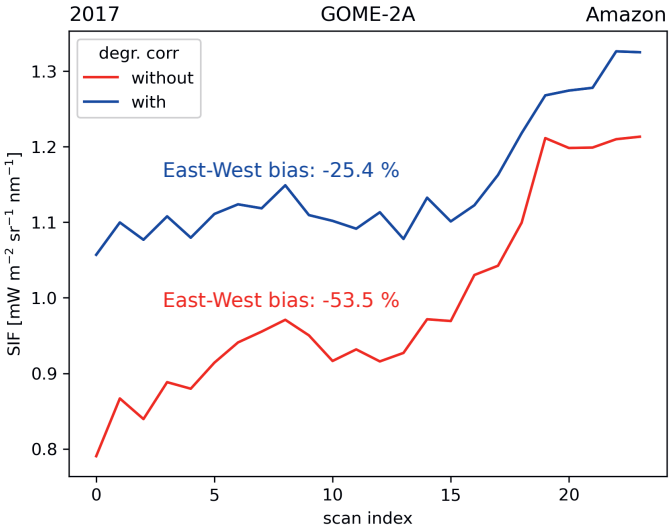


Figure 5.8: Averaged GOME-2A SIF data, both corrected (in blue) and uncorrected (in red) for reflectance degradation, as a function of scan index from east ($s = 0$) to west ($s = 23$) over the Amazon in 2017. The bias is expressed as the relative difference between the average of the eight easternmost (0–7) and eight westernmost (16–23) pixels. The viewing zenith angle ranges from around $-35°$ to $+35°$ due to the reduced swath configuration of GOME-2A.

neously fitted as a fourth-order polynomial along SIF. To evaluate this approach, we compared our fitted albedo with the climatological DLER product (Directionally dependent Lambertian-equivalent reflectivity; Tilstra et al. (2021)). DLER is a multi-year climatology derived from level-1 GOME-2 data using a radiative-transfer model, providing a global database of surface reflectance with dependence on the satellite viewing geometry. Figure 5.9 shows close agreement between the fitted and DLER albedo over different vegetative regions, although larger discrepancies towards the western edge are noted. Overall, these results provide confidence that SIFTER captures the surface reflectance anisotropy, limiting potential east-west biases leaking into the SIF signal.

SIF is often averaged over space or time to cancel out the natural directional effects. However, as shown in Chapter 3, variations in the distribution of viewing geometry sampling significantly influence the mean SIF despite such averaging. This bias arises because SIF values depend on the viewing angle at which they are observed. We found that sampling not only varies across sensors due to differences in swath configuration, but also in individual records over space and time (as shown in Section 5.1.1). Therefore, the value of the averaged SIF should be analysed with respect to its sampling distribution of viewing geometry. Inconsistent sampling and representation of viewing geometry can introduce apparent changes in SIF unrelated to vegetation dynamics. Ensuring consistent sampling over space and time is thus essential for accurately monitoring vegetational trends. This can be achieved by weighting observation so that all viewing angles contribute proportionally to the mean, as discussed in Section 5.1.1.

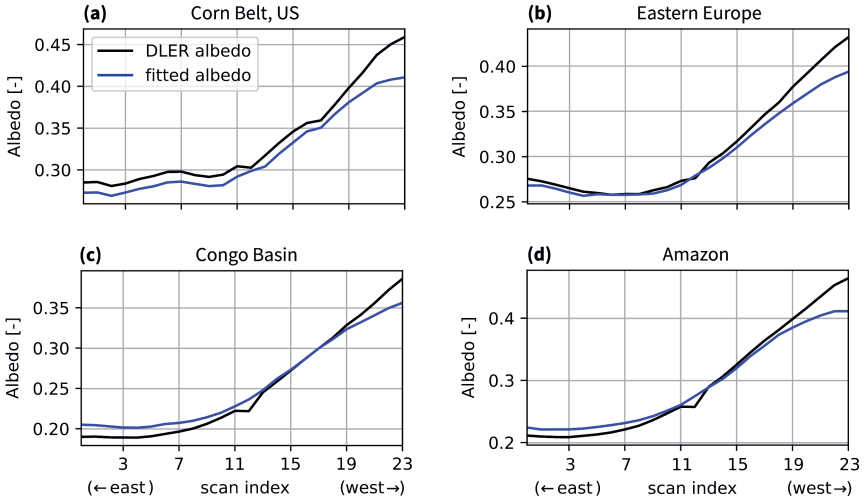


Figure 5.9: Comparison of albedo (λ = 758 nm) fitted within the SIFTER v3 algorithm (in blue) and from the DLER (in black) over the scan index over (a) the United States Corn Belt, (b) Eastern Europe, (c) the Congo Basin, and (d) the Amazon region. The graphs show data from GOME-2A. Figure adapted from van 't Loo (2024).

Another approach is to correct instantaneous SIF values for the directional effects, decoupling the canopy structural and physiological regulation on SIF. This would also advance the direct use of (daily) Level-2 observations, allowing analysis of SIF at finer spatial and temporal scales than level-3. Several approaches have been proposed to correct for these directional effects, such as the scaling of observed SIF to nadir (SIF_{nadir}) or total SIF (SIF_{total}) (Zhang and Zhang, 2023; Hao et al., 2022; Zhang et al., 2020a). Normalisation methods scaling SIF to a single geometry, e.g., nadir, often rely on using reflectance-based parameters, such as NIRv or Redv (Hao et al., 2022, 2021). Such approaches make use of the apparent similarity in directional effects on vegetation reflectance and far-red SIF (Liu et al., 2016). However, this assumption can break down in the presence of soil background, low vegetation density, or structural heterogeneity, which cause reflectance and SIF to respond differently to viewing geometry (Yang and van der Tol, 2018).

Alternatively, SIF_{nadir} could be obtained using an empirically derived correction from the long-term SIF record itself. The extensive temporal record of GOME-2 SIF obtained in this thesis, containing GOME-2A, GOME-2B, and GOME-2C, provides the opportunity to construct a climatological dataset of SIF as a function of solar zenith angle, viewing zenith angle, relative azimuth angle, and vegetation type. This climatology can be stored as a look-up table (LUT) for biome-, season-, and latitude-dependent geometry corrections. This approach provides instrument-specific, e.g., GOME-2, directional corrections independent of assumptions about vegetation structural parameters. However, this method will rely on the representation of the biome or vegetation type. This could potentially be done using an auxiliary land cover

dataset to stratify the LUT, or by constructing an LUT for each region of interest.

5.1.5 Impacts of clouds

SIF retrievals from Fraunhofer lines are less sensitive to atmospheric scattering by clouds and aerosols than reflectance-based vegetation indices (Guanter et al., 2015). This is because scattering of clouds and aerosols does not affect the depth of Fraunhofer lines (Köhler et al., 2018). Therefore, thin to moderate cloud optical depth has little impact on the SIF retrievals (Frankenberg et al., 2012). However, thick clouds do significantly impact retrievals (Guanter et al., 2015). Moreover, clouds impact SIF in ways other than affecting retrieval quality. First, clouds alter the incoming solar radiation available for photosynthesis, and thus the SIF emission itself (Zhang et al., 2020b). The effect of clouds on vegetation activity can be counteractive, as they can both shield incoming radiation and increase diffuse radiation (Zhang et al., 2020b). The latter is known to increase photosynthetic efficiency and penetrate deeper into the lower, more shaded, canopy (Yang et al., 2021). The second way clouds affect SIF retrievals is by shielding the photons from reaching the sensor (Joiner et al., 2012; Frankenberg et al., 2014). Both cloud effects likely impact the relationship between SIF and GPP (Yang et al., 2021). Therefore, the cloud filtering should be carefully considered for vegetation analysis with SIF.

Figure 5.10 shows the averaged SIF sampled under various cloud fraction (cf) bounds (with 0.1 intervals) across different vegetative regions. Here, the cloud fraction refers to the effective cloud fractions estimated by FRESCO+, which represent a simplified measure of cloudiness within the observed pixel. Specifically, FRESCO uses a Lambertian cloud model with an assumed cloud albedo of 0.8 (Wang and Stammes, 2008). It estimates the cloud fraction as the fractional coverage of such a cloud that would match the observed radiance at the top of the atmosphere. Hence, FRESCO provides a proxy for the radiation effect rather than a geometric description of the cloud cover.

Across the regions, SIF gradually decreases with cloud fraction (cf), exhibiting the shielding effect. Over the Amazon region, SIF decreases rapidly with 42.1 % from the maximum cloud fraction of 0.1 to 0.4, while over Eastern China, SIF decreases with 21.8 % across the same cf sampling. The increase in retrieval uncertainties is less steep than the decreasing SIF value over all regions (Figure S4.7). However, as the SIF value rapidly decreases due to the shielding effect, the relative uncertainty increases strongly. Moreover, the cloud shielding shows different effects depending on viewing geometry. Over the Corn Belt region, eastern pixels decrease with 32.1 % between $cf \in (0.0, 0.1]$ and $cf \in (0.3, 0.4]$, a more rapid decrease than nadir (23.4 %) and western observations (20.3 %). This implies that the presence of clouds can alter the SIF pattern across the scan angles, impacting the east-west biases.

The difference in SIF value across cloud fraction per region is likely due to different cloud characteristics. Because FRESCO+ uses an effective Lambertian cloud model, a cloud fraction of, for instance, 0.3 does not necessarily reflect the same shielding effect in all situations. Future studies should further investigate the impact of clouds on SIF (both shielding and physiologically) in terms of cloud characteristics, e.g., type and height. A better understanding of cloud effects on SIF will advance the interpretation of SIF under cloud conditions and lead to more consensus on the threshold for cloud filtering.

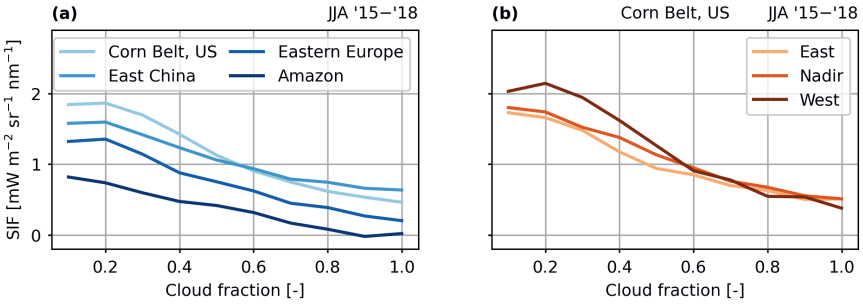


Figure 5.10: Subplot (a) shows the average regional GOME-2B SIF as a function of cloud fraction. SIF values are grouped in cloud fraction bins with 0.1 intervals (e.g., 0–0.1, 0.1–0.2, up to 0.9–1.0). The cloud fraction value shown on the x-axis represents the upper bound of each bin. Subplot (b) shows the average GOME-2B SIF over the Corn Belt region for each cloud fraction bin, shown separately for East, Nadir, and West viewing ground pixels.

A variety of cloud fraction (cf) filtering is generally used for application of SIF, for instance $cf < 0.1$, $cf < 0.3$, or $cf < 0.5$. At first glance, a clear-sky requirement seems ideal in minimising a potential shielding effect on SIF. The relatively coarse spatial resolution of GOME-2 (60×80 km^2), however, does not capture individual clouds. Therefore, most pixels are either fully or partially contaminated by clouds. A strict cloud filtering will substantially reduce the number of observations, especially over tropical regions. Moreover, it will introduce a clear-sky bias. These clear-sky observations might not accurately represent the GPP conditions over time and space. Relaxing the cloud thresholds, on the other hand, will allow a larger number of observations and be more representative of a broader range of cloud conditions, but at the cost of increased uncertainty. Additionally, lenient sampling of cloud conditions might obscure the interpretation of temporal variations. Similar to sampling bias in viewing geometry, as discussed in Section 5.1.4, varying sampling of cloud conditions can affect the average SIF value over time. Inconsistency in sampling may lead to misinterpretation of changes in SIF as physiological responses of vegetation.

To sustain the temporal consistency in SIF, it's advised to constrain the sampling range of cloud conditions. Based on Figure 5.10, a cloud fraction maximum of 0.3 seems appropriate in limiting the variation in SIF, reducing changes in the east-west bias, and preventing a doubling, or more, of relative uncertainty in SIF. However, the ideal cloud filtering bounds may vary depending on the specific application, conditions of interest, and the studied region. Importantly, SIF values, both averaged and instantaneous, need to be interpreted in the context of their sampling characteristics, including the sampling of cloud fraction.

5.1.6 Validation of SIF

Robust validation is needed to assess the accuracy of satellite-based SIF observations and enhance consistency across sensors (Parazoo et al., 2019). Validation is vital to quantify biases in SIF-based GPP estimates at regional to global scales. However, true validation is challenged by

the lack of ground-based SIF observations and mismatches across global and temporal scales. Over the last 10 years, the development of several high-spectral instruments enabling SIF observations from field, tower, and airborne platforms has proved promising in supporting the validation and interpretation of satellite-based SIF (Mohammed et al., 2019; Rascher et al., 2015; Grossmann et al., 2018). Ground-based SIF observations from the ChinaSpec network showed good correlations with OCO-2 and TROPOMI SIF (Zhang et al., 2021). Moreover, the airborne Chlorophyll Fluorescence Imaging Spectrometer (CFIS), developed by the OCO-2 team, supported the validation of OCO-2 SIF (Sun et al., 2017; Frankenberg et al., 2018).

Building on these developments, HyPlant represents another state-of-the-art sensor designed to obtain airborne-based SIF observations. The HyPlant instrument, intended for the preparation of the FLEX mission, is the first airborne-based instrument to enable both red and far-red SIF retrievals (Rascher et al., 2015). Several studies using the HyPlant sensor have contributed to an enhanced understanding of the SIF signal in relation to plant functioning at small ecosystem scales across several biomes (Jonard et al., 2020; Bandopadhyay et al., 2019; Colombo et al., 2018). The fine spatial resolution of the airborne observations, on the order of meters, makes them an essential tool for understanding sub-pixel variability within satellite pixels. Moreover, they can help bridge across spatial scales, from point observations to the km scale.

In August 2023, a HyPlant campaign was planned to fly over the Netherlands, targeting the Loobos (evergreen coniferous forest) and Cabauw (grassland site) atmospheric reference stations. We intended to compare the airborne SIF observations from this dedicated campaign with TROPOMI SIF observations. Unfortunately, due to poor weather forecasts, the campaign was postponed, and the data could not be processed within the timeframe of this thesis. Ultimately, the campaign took place on 28 August 2024. Aside from airborne and satellite-based observations, SIF was also obtained from a UAV platform using Fluorspec and from a ground-based sensor, FloX, in Cabauw.

The data gathered during this campaign provide an exciting opportunity for future studies to enhance the understanding of SIF signals across spatial scales. To our knowledge, this will be the first time that simultaneously collected airborne, UAV, ground-based, and satellite-based SIF observations are intercompared. This multi-platform intercomparison of SIF is valuable for examining the aggregation of fine-scale variability into the TROPOMI satellite-pixel scale. In particular, the Loobos forest site offers an interesting case study. The Loobos site consists of a spatially homogeneous cover of tall pine trees with a grass understory (Dolman et al., 2002). This moderately open canopy creates vertical and spatial variability of illumination conditions, with sun-lit and shaded patches. By resolving this heterogeneity at the meter scale, the combined UAV and airborne data can advance the disentanglement of illumination and canopy-structure impacts on TROPOMI SIF retrievals.

While this intercomparison holds great potential, it will be methodologically challenging. The differences in footprint and viewing geometry across the sensors must be carefully addressed. Although Sun et al. (2017) successfully compared airborne CSIF data against satellite-based SIF data from the OCO-2 sensor, the larger spatial footprint and noise of TROPOMI SIF introduce an additional obstacle. Addressing these challenges will provide valuable insights and strategies for validating not only TROPOMI SIF but also observations from other satellite missions with

coarser resolutions.

5.2 Solar-induced fluorescence as monitoring tool

In this thesis, we evaluated the use of satellite-based SIF as a monitoring tool. In particular, we focused on quantifying the impact of LMT implementation on land carbon uptake within the LANDMARC project. Chapter 4 used GOME-2A and TROPOMI SIF to evaluate vegetation response to both natural disturbances and human interventions. In this section, I report on our insights obtained from the LANDMARC project and place them within the broader perspectives of monitoring land-based mitigation. Building on the project results and our findings from Chapter 4, I outline how SIF could be integrated into vegetation monitoring frameworks and combined with supporting data (e.g., in situ and remote sensing). Furthermore, I reflect on the limitations and challenges in attributing changes in carbon uptake to specific interventions.

5.2.1 Motivation

In recent years, human land-based interventions, such as LMTs, have been considered a critical tool for mitigating climate change. While these land-based techniques are seen as essential to meeting the Paris Agreement, there is debate over their potential and effectiveness. Hence, accurate worldwide monitoring of LMT impact is critical to support policy and stakeholder decision-making. Satellite-based SIF observations are promising for monitoring vegetation dynamics with respect to LMT implementation. An effective monitoring tool should enable robust tracking of photosynthetic carbon uptake across biomes and regions. In addition, it should be sensitive to vegetation response to climate variability. SIF's mechanistic advantages meet both needs (Jiang et al., 2025; Li and Xiao, 2020; Wen et al., 2025). Furthermore, this thesis, in Chapters 2 and 3, demonstrated the construction of climate SIF records across sensors. Such long-term consistent records enable seasonal, interannual and decadal monitoring, providing insights into the long-term effects of LMTs.

The potential of SIF is evident, for instance, in dryland systems (Gerlein-Safdi et al., 2020). Drylands are increasingly targeted for land-based mitigation intervention, due to their wide extent (around 40 % of Earth's land surface) and strong impact on the global CO_2 sink (Biederman et al., 2017). The monitoring of these regions, however, is known to be challenging with reflectance-based traditional vegetation proxies such as NDVI. Drylands are characterised by a heterogeneous mixture of bare soils and diverse vegetation and are highly exposed to climate variability, including frequent droughts and high temperatures (Wen et al., 2025; Smith et al., 2019). As discussed in Section 1.2, reflectance-based proxies are sensitive to soil background contamination. Furthermore, they can't reflect physiological regulation, thereby limiting their ability to capture vegetation's response to climate variability. SIF, on the other hand, has been shown to robustly track the interannual, seasonal, and intra-seasonal variations in the complex dryland systems (Wen et al., 2025; Wang et al., 2019a; Smith et al., 2018b; Wang et al., 2022c). The insensitivity of SIF to soil also highlights its strength to, for instance, monitor reforestation from early stages.

5.2.2 Monitoring framework

Chapter 4 demonstrated SIF's use in examining vegetation response after an Australian wildfire and large-scale reforestation in China. The monitoring approach of both cases shared the same underlying structure. Here, I propose a SIF-based framework to quantify land-use impacts on vegetation activity. This framework builds on the methods used in Chapter 4 and in the LANDMARC project for broader applications. The framework's main steps are illustrated in Figure 5.11. In brief, the framework carefully selects SIF data to represent the defined intervention extent and a chosen reference baseline. The selected baseline, together with data reflecting co-occurring drivers (e.g., precipitation), is used to estimate the isolated impact of the intervention on SIF changes.

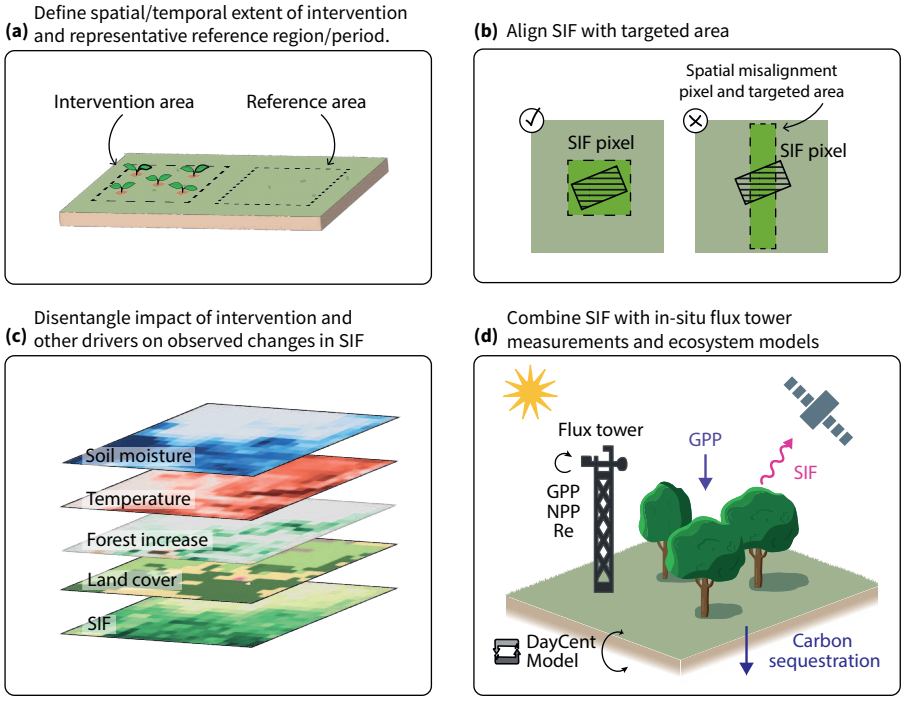


Figure 5.11: Overview of the monitoring framework to use SIF as a tool to quantify the impact of an intervention (e.g., natural or management-based) on the land's regional carbon uptake.

Before describing each step in detail, I first outline the different levels of information that the framework can provide. At its most direct level, the framework quantifies the LMT impact in relative (in %) or absolute terms of SIF (ΔSIF, in mW m^{-2} sr^{-1} nm^{-1}), referenced against a set baseline (demonstrated for the China case in Chapter 4). This first level reflects regional changes in photosynthetic activity but does not directly enable interregional comparison. Figure 5.11d illustrates how the framework can extend beyond the first level when data linking vegetation activity to carbon fluxes are available. In level-2, ΔSIF is converted to SIF-based ΔGPP (in gC),

enabling intercomparison in carbon units. SIF-based ΔGPP can be obtained through application of an empirical SIF–GPP relationship, derived from representative flux tower GPP (e.g., Tumbarumba in the Australian case) and satellite SIF over the tower footprint. If appropriate flux tower data are unavailable, GPP data from global GPP products such as FluxSat could be used. Level 3 integrates SIF-based ΔGPP with ecosystem models, such as DayCent, to estimate ultimate carbon sequestration. The practical implementation of this step is discussed in Section 5.2.4. Considering these output levels, I now describe the core components of the framework: steps (a) to (c) in Figure 5.11.

Define the intervention and reference area

The first step is to define the spatial and temporal extent of the intervention as well as a representative reference baseline, shown in Figure 5.11a. Supporting satellite products, such as land-cover maps, can help identify and characterise the intervention when details are incomplete or absent. For example, MODIS burned-area maps were used in the Australian case (Chapter 4) to define the affected area. A reference or baseline is selected to represent the vegetation dynamics in absence of the intervention. Ideally, the reference area reflects the pre-LMT landcover and undergoes the same or similar environmental and climatological conditions as the LMT area during the analysed period. In wide geographic regions with strong spatial heterogeneity, such as the China case in Chapter 4, a reference period (e.g., before LMT implementation) may be more appropriate than selecting a reference area. Subsequently, the impact of the LMTs can be extracted by comparing SIF over the intervention and baseline areas or periods.

Alignment of SIF with target area

Next, SIF observations are aligned with the defined intervention and reference. To enhance the detectability of LMT impact, selected SIF pixels should predominantly represent the designated area as shown in Figure 5.11b. Hence, the LMT or reference area should be larger than a single SIF pixel. Careful pixel selection avoids the interference from neighbouring land cover. This ensures that the observed ΔSIF signal can be accurately attributed to the intervention rather than surrounding changes.

Attribution of ΔSIF to the intervention

Changes in SIF (ΔSIF) reflect not only the intervention-driven responses but also variability in environmental and climatic drivers. Disentangling these influences is particularly important for gradual transitions or for long monitoring periods. Additional supporting biogeographical datasets, such as precipitation or temperature records, can be incorporated to describe the co-occurring drivers, as illustrated in Figure 5.11c. The intervention itself can be represented as a quantitative variable. For example, in the China reforestation case, the increase in forest area per $0.5^\circ \times 0.5^\circ$ cell. This enables the use of statistical models to assess how much of the ΔSIF is attributable to the intervention versus other drivers (demonstrated in Chapter 4). Because vegetation-climate interactions vary across biomes and regions, selecting relevant drivers requires an understanding of the regional characteristics.

Finally, after the observed changes in SIF are attributed to the intervention, the obtained ΔSIF can be translated into changes in carbon fluxes as discussed earlier in this section.

5.2.3 Monitoring constraints and uncertainties

Several factors influence the effectiveness of satellite-based SIF as a monitoring tool. Here, I distinguish limitations arising from (i) practical origins affecting the framework's applicability, (ii) uncertainties related to data quality and accuracy, and (iii) conceptual considerations in interpreting SIF.

Practical constraints

As mentioned earlier, the scale of the intervention area relative to the satellite pixel is key for successful monitoring (Figure 5.11b). The intervention area must be sufficiently large to enable precise alignment of SIF to the specific area. Small or fragmented LMT regions reduce the number of aligned SIF pixels, limiting the averaging out of random noise. For example, the coarse spatial resolution of GOME-2 at 40×80 km^2 hinders monitoring of LMT at local scales. Sensors such as OCO-2 offer finer spatial resolution (1.3×2.25 km^2), but at the cost of sparse temporal sampling resulting from their narrow swath (Table 1.2). The upcoming FLEX mission, with a spatial resolution of 300 m, will substantially advance the applicability of SIF for monitoring at finer scales.

Beyond the spatial representativeness, the intervention must also be accurately captured in time. Effective monitoring of LMTs requires sufficient overlap of the satellite record with the intervention period. Moreover, the record should exhibit temporal and spatial consistency. This links directly to the other main subject of this thesis: constructing long-term consistent SIF records. As discussed in Chapters 2 and 3, long-term consistency is essential to accurately attribute observed trends to vegetation dynamics rather than instrumental effects. The limitations of inconsistent records were evident in Chapter 4, where only the first 6 years of the GOME-2A record SIFTER v2 could be used due to substantial temporal inconsistencies. These issues were later resolved in the subsequent algorithm version presented in this thesis: SIFTER v3 (Chapter 3).

Data and model uncertainty

As mentioned in the previous paragraph, inconsistent records can introduce uncertainties in attributing ΔSIF to the intervention. Ensuring temporal consistency in the SIF time series has two components. The first comes from retrieving a stable, coherent record at the retrieval step. The second comes from consistent sampling of the SIF pixels. Variations in conditions, such as viewing geometry and cloud scenes, can introduce fluctuating SIF values that might be mistaken for changes in vegetation activity. This effect was demonstrated in Chapter 3 and further discussed in Section 5.1.

Careful selection of SIF pixels is also essential when constructing a SIF–GPP relationship to translate ΔSIF to ΔGPP. To derive this relationship, SIF pixels are sampled over the flux tower area to represent the vegetation dynamics captured in the GPP estimations. However, the footprint of the satellite pixels (e.g., $\sim$9 km for TROPOMI) substantially extends beyond that of the tower (typically $\sim$1000 m). Hence, the ability to construct a representative SIF–GPP relationship depends on the heterogeneity of the land cover surrounding the tower. Additional uncertainties inherited from the SIF–GPP relationship are discussed further in the paragraph

on SIF interpretation.

A further source of uncertainty arises from the imprecise definition of the intervention itself. The spatial and temporal extent of the LMT should be accurately defined to prevent misconceptions in the management monitoring (Karki et al., 2023). In practice, information on the implementation is often limited (Karki et al., 2023; Gerlein-Safdi et al., 2020). In Chapter 4, the level of reforestation in China is defined through changes in annual land cover maps. Increases in forest cover, however, reflect the result of reforestation (and other drivers) rather than actual reforestation efforts themselves (e.g., the number of planted seeds). Ideally, information on the effort is used to quantify the LMT efficiency and its success rate.

Considerations for SIF interpretation

The framework assumes that satellite-based SIF accurately tracks GPP. This assumption is supported by strong empirical linear relationships between SIF and GPP across various biomes (e.g., Verma et al., 2017, Mengistu et al., 2021, Chapters 2–4). However, fully interpreting satellite-based SIF as photosynthetic carbon uptake is more complex than the linear correlations might suggest. For instance, the observed linearity at canopy-scale stands in contrast to the complex nonlinear relations observed at finer scales, such as the leaf-level (Magney et al., 2020; Damm et al., 2015; Porcar-Castell et al., 2014). Understanding the mechanistic processes underlying the relationship between SIF and photosynthesis across different scales and environmental conditions remains a primary focus of current SIF research (e.g., Magney et al., 2020; Yang and van der Tol, 2018; Porcar-Castell et al., 2021). Here, I focus on the implications of these complexities for using SIF within monitoring frameworks.

A key point for monitoring is that the biome-specific SIF–GPP relationship at the canopy scale can change over time and may not be constant. These constraints are mainly driven by variations in canopy structure or physiological functioning. Structural changes, such as seasonal growth or harvest, alter the fraction of emitted fluorescence escaping the canopy and therefore affect the observed SIF (Figure 1.7). The variation in observed SIF does not necessarily reflect changes in emitted SIF or GPP. Moreover, changes in photosynthetic efficiency or physiological changes can also affect the relationship. Seasonal downregulation, as observed in evergreen forest (Pierrat et al., 2022), or substantial environmental stress can weaken or change the SIF–GPP relationship (Martini et al., 2022; Han et al., 2022; Marrs et al., 2020). Overall, this means that the observed satellite-based SIF–GPP relationship can vary when vegetation structure or functioning is substantially altered.

To improve the robustness of the SIF–GPP relationship, additional information reflecting canopy structure or stress conditions could help constrain its variability. For instance, Shi et al. (2025) demonstrated that integrating canopy structural parameters derived from LiDAR measurements improved the SIF-based GPP estimates. Similarly, indicators of stress, such as isoprene emissions, land surface temperature, the photochemical reflectance index (PRI), or the change in the red-to-far-red SIF ratio, could help identify conditions under which the relationship between SIF and GPP is altered by stress.

In Chapter 4, we used the Tumbarumba SIF–GPP relationship to translate fire-induced ΔSIF into ΔGPP for the Australian case. This relationship was assumed to remain constant before and

after the eucalyptus wildfire. At the time, data to evaluate this assumption were not available. A recent study, Woodgate et al. (2025), demonstrated a substantial change in SIF–GPP following a 2020 eucalyptus wildfire at the Tumbarumba flux tower site. SIF was found to recover faster than GPP. This suggests that our estimated fire-induced loss in GPP may be underestimated if the studied wildfire affected eucalyptus dynamics in a similar way to that of the 2020 Tumbarumba fire. Improving our understanding of changing SIF and GPP dynamics under such disturbance is essential to strengthen the robustness of SIF-based GPP estimates within monitoring frameworks.

5.2.4 From vegetation activity to carbon sequestration

The total carbon land sink does not solely depend on photosynthetic carbon uptake, but also on respiration, disturbances, and the allocation of carbon to above- and below-ground carbon pools, as discussed in Chapter 1. In this sense, SIF, as an indicator of GPP, reflects the short-term component of carbon uptake. The long-term effectiveness of LMTs, however, ultimately depends on the sequestration of the photosynthetically fixed carbon in biomass and soil. Below-ground carbon pools are not remotely sensed. Hence, assessing the long-term sequestration potential of LMTs requires ecosystem models that simulate long-term carbon dynamics, including coupling above- and below-ground carbon processes. A widely used example of such a model is the biogeochemical DAYCENT model, which models the ecosystem response to climate, land-use, and management practices (Zhang et al., 2017; Lemma et al., 2021).

As mentioned earlier in Section 5.2.2, we extend on the first two output levels of the framework by exploring the integration of SIF with the DAYCENT model (Figure 5.11d). In the LANDMARC project, this integration was tested using the Australian wildfire case from Chapter 4. To simulate the impact of fire on carbon processes, accurate input data were required, including land-use history, vegetation and soil properties, and fire-specific details, such as the degree of burning. Insight into the latter was obtained from fire severity data from Department of Energy, Environment and Climate Action (2023), based on aerial photograph interpretation of the wildfire. The data show that the eucalyptus wildfire mainly caused scorching (burning of leaves), with limited canopy burning ($< 10\%$, Figure S4.17). This aligns with the observed substantial drop and fast recovery of SIF in Chapter 4.

However, this type of burning could not be reproduced by DAYCENT because of how the model formulates NPP. DAYCENT simulates NPP from an internally calculated LAI that accounts for tree biomass, but disregards the influence of leaves (and thus the scorching effect). Consequently, the model produced unrealistically high post-fire productivity and failed to capture the observed vegetation response. The model's output in NPP (rather than GPP) further restricted direct comparison with SIF-based GPP. Additional information on autotrophic respiration (Re_a), for instance from flux towers, is needed to link GPP, NPP (Equation (1.2)), and ultimately carbon sequestration.

This example highlights the challenge of integrating satellite-derived vegetation activity with ecosystem models. The overall performance depends heavily on detailed input data, appropriate case-specific model calibration, and availability of in-situ observations at the specific site (such as Re_a). In many cases, including the Australian case, these requirements are not fulfilled. More

generally, analysing well-defined cases that meet these requirements can enhance our understanding of carbon dynamics and help refine model calibration. For example, recent flux tower observations of the 2020 wildfire at the Tumbarumba site provide a valuable opportunity to examine post-fire carbon dynamics in greater depth in eucalyptus ecosystems, as demonstrated in Woodgate et al. (2025), discussed earlier.

5.3 Conclusions and outlook

This thesis investigated two closely connected aspects of satellite-based solar-induced fluorescence (SIF): the retrieval and construction of stable long-term SIF data records, and the application of satellite-based SIF to monitor vegetation responses following land-based climate mitigation. In terms of SIF retrieval, we addressed the following research questions:

- How can the SIFTER algorithm be improved to retrieve a temporally and spatially consistent SIF record from GOME-2A observations?
- How can SIF retrievals from GOME-2A and GOME-2B be harmonised to construct a consistent multi-sensor SIF record, and how can their differences be interpreted?
- How can insights gained from the GOME-2 SIF retrieval help extend the SIFTER v3 algorithm to TROPOMI?

Chapter 2 presented the improved SIFTER v3 retrieval algorithm, featuring an advanced degradation correction accounting for time, wavelength, and scan angle dependencies to address the effects accurately. Using SIFTER v3, temporally and spatially consistent SIF records were retrieved from GOME-2A (2007–2017, Chapter 2), GOME-2B (2012–2023, Chapter 3), and GOME-2C (2019–2024, Chapter 5). The corrections within SIFTER v3 formed the basis for harmonising GOME-2A and GOME-2B SIF as one coherent record (Chapter 3). Moreover, we demonstrate SIF's sensitivity to viewing geometry sampling (e.g., VZA). Inconsistent sampling over time can cause temporal variability that does not necessarily reflect changes in vegetation activity. Therefore, accounting for this dependence is essential for constructing stable time series to perform meaningful vegetation monitoring. Building on insights gained from the GOME-2 retrieval, SIFTER v3 was expanded to TROPOMI (Chapter 5). For a one-day test case, SIFTER v3 outperformed the TROPOSIF product, retrieving more than three times as many valid observations over the Amazon.

To examine the application of SIF as a monitoring tool, we addressed the research question:

- How can satellite-based SIF observations be used to quantify vegetation response to land-based disturbances and interventions?

Chapter 4 demonstrated the sensitivity of satellite-based SIF to detect both abrupt and gradual vegetation changes related to disturbances and anthropogenic interventions, i.e. reforestation. As SIF reflects the collective impact of multiple environmental and climatic drivers, it is not an explicit indicator of a single stressor. By combining SIF with supporting in situ and remote sensing data, this work illustrated how observed vegetation changes can be placed in context and carefully interpreted. Such interpretation relies on the availability of temporally stable long-term

SIF records, as retrieved in this work.

Looking forward, further progress in satellite-based SIF as a monitoring tool requires advances on both the retrieval and application sides. This includes robust multi-mission harmonisation to enable long-term monitoring across spatial and temporal scales. It also concerns further improvements in interpreting SIF changes by integrating in situ and remote sensing observations, along with information on environmental stress and interventions.

Supplement S4

S4.1 GOME-2C SIF

Retrieval settings

Consistent with findings from Chapter 2, on GOME-2A, and Chapter 3, on GOME-2B, GOME-2C showed distinct and unique reflectance degradation characteristics with time, wavelength, and scan-angle dependencies. To capture these degradation patterns, we used a polynomial order $p = 2$ and a Fourier order $q = 6$. To obtain the degradation corrections 29 January 2019 was used as the reference date.

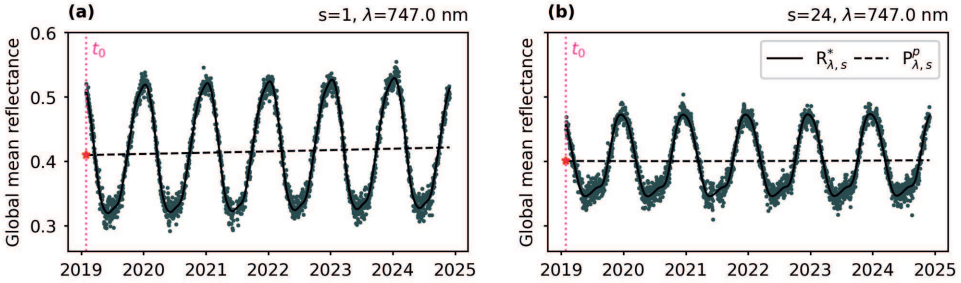


Figure S4.1: The observed (teal dots) and fitted (solid black) global mean reflectance from GOME-2C at $\lambda = 740.0$ nm and scan-index (a) $s = 1$ (easternmost) and (b) $s = 24$ (westernmost). The dashed line shows the fitted polynomial, which captures the long-term change in the reflectance over time that is thought to be caused by the impact of instrument degradation. The reference day t_0, set at 29 January 2019, is indicated by the pink star.

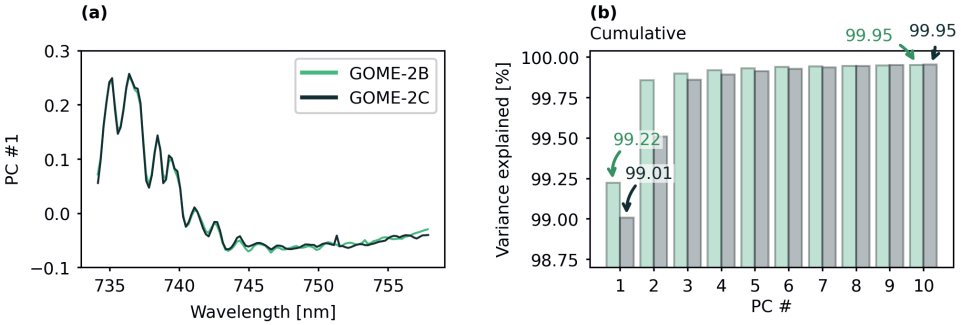


Figure S4.2: Panel (a) shows the leading principal component, PC #1, obtained from GOME-2B (in green) and GOME-2C (in dark teal). Panel (b) shows the cumulative variance of PCs 1 to 10 for both instruments.

Retrieval results

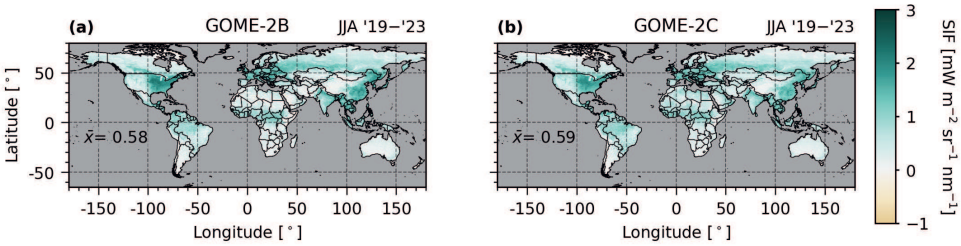


Figure S4.3: Seasonal averaged (a) GOME-2B and (b) GOME-2C over June–August (JJA) 2019–2023. SIF values are filtered for cloud fractions < 0.3 using FRESCO+ and gridded at $0.5° \times 0.5°$. Only land pixels are shown to focus on biosphere-relevant differences.

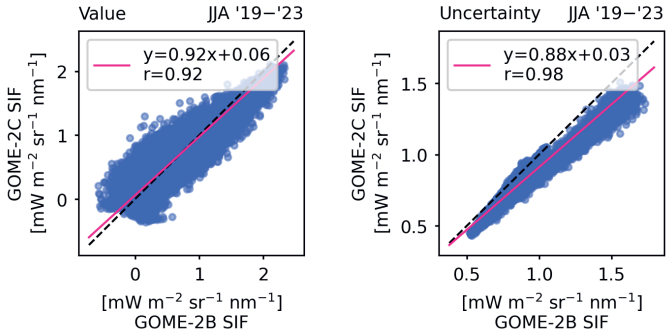


Figure S4.4: Correlation between seasonal averaged GOME-2B and GOME-2C (a) SIF values and (b) SIF uncertainty over June–August (JJA) 2019–2023. Major axis regressions are used for the correlations (pink line). On global average, GOME-2B and GOME-2C SIF uncertainty are 0.77 and 0.72 mW m^{-2} sr^{-1} nm^{-1}, respectively.

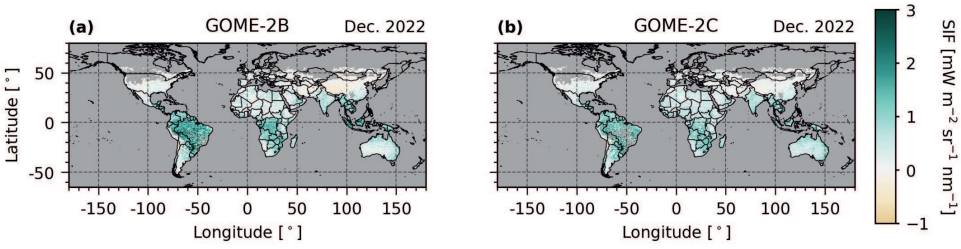


Figure S4.5: Monthly averages of (a) GOME-2B and (b) GOME-2C SIF over December 2022. SIF values are filtered for cloud fractions < 0.3 using FRESCO+ and gridded at $0.5° \times 0.5°$. Only land pixels are shown to focus on biosphere-relevant differences.

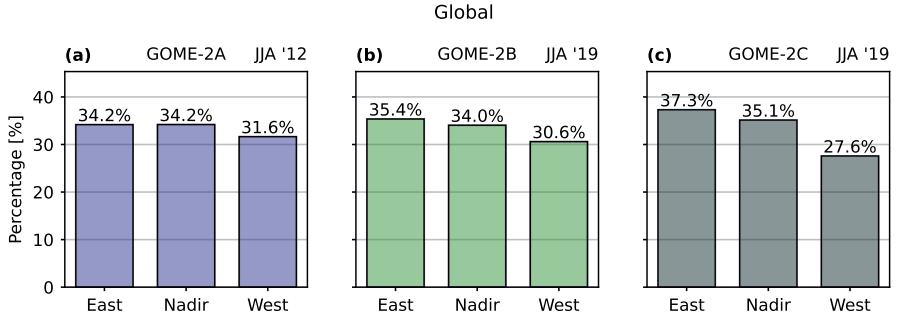


Figure S4.6: Contribution of East, Nadir, and West pixels to global GOME-2 SIF averages in the June–August period. Distributions are shown for (a) GOME-2A (in 2012), (b) GOME-2B (in 2019), and (c) GOME-2C (in 2019). SIF data is filtered on FRESCO+ cloud fraction < 0.3 and autocorrelation of < 0.2 to secure an accurate retrieval fit. Only land pixels are used.

S4.2 Cloud filtering

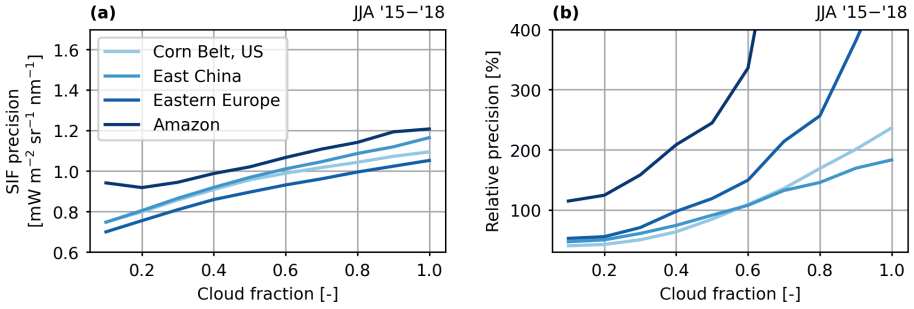


Figure S4.7: Subplot (a) shows the average regional precision in GOME-2B SIF as a function of cloud fraction. SIF values are grouped in cloud fraction (bins with 0.1 intervals (e.g., 0–0.1, 0.1–0.2, up to 0.9–1.0). The cloud fraction value shown on the x-axis represents the upper bound of each bin. Subplot (b) shows the average relative uncertainty in GOME-2B SIF. The relative uncertainty is obtained as the ratio between the precision (subplot a) and the value of SIF (Figure 5.10a).

S4.3 TROPOMI SIF

Retrieval settings and results of TROPOMI

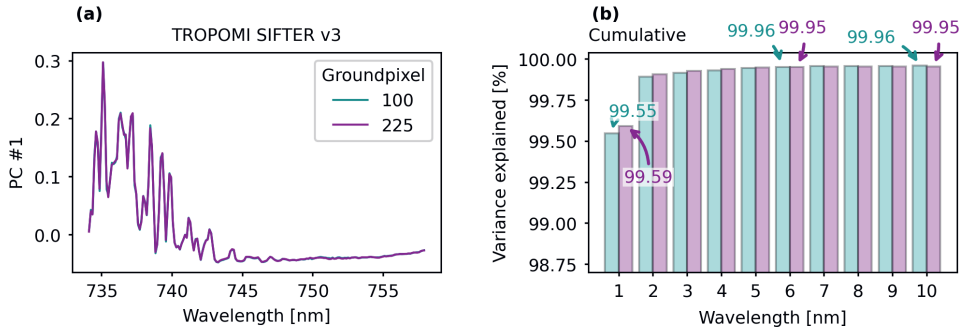


Figure S4.8: Panel (a) shows the leading principal component, PC #1, obtained from TROPOMI for ground pixel 100 (in cyan) and ground pixel 225 (in purple). Panel (b) shows the cumulative variance of PCs 1 to 10 for both ground pixels.

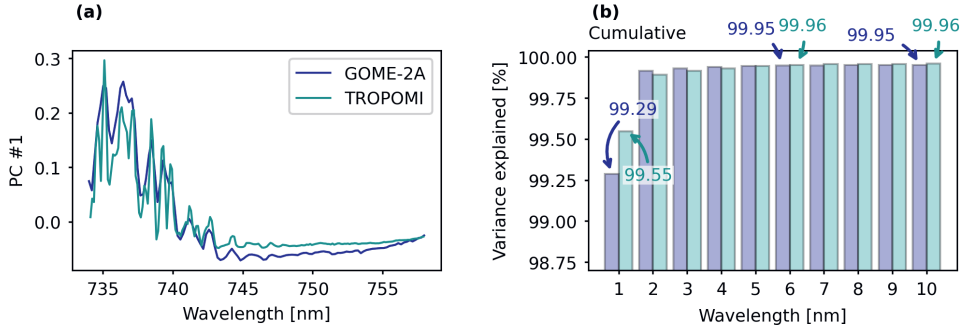


Figure S4.9: Panel (a) shows the leading principal component, PC #1, obtained from GOME-2A (in navy) and ground pixel 100 of TROPOMI (in cyan). Panel (b) shows the cumulative variance of PCs 1 to 10 for both instruments.

Table S4.1: RMSE fit residuals for subsets and the entire retrieval window (734–758 nm) from TROPOMI SIF using four to 10 PCs. Data selection and filtering follow the details described in the captions of Figure 5.4. The shown data represents the average of all 448 ground pixels.

RMSE fit residual	Number of PCs used						
	4	5	6	7	8	9	10
734–745 nm	0.114 %	0.105 %	0.094 %	0.090 %	0.085 %	0.082 %	0.079 %
746–758 nm	0.074 %	0.071 %	0.067 %	0.064 %	0.062 %	0.061 %	0.061 %
734–758 nm	0.095 %	0.089 %	0.081 %	0.078 %	0.074 %	0.072 %	0.070 %

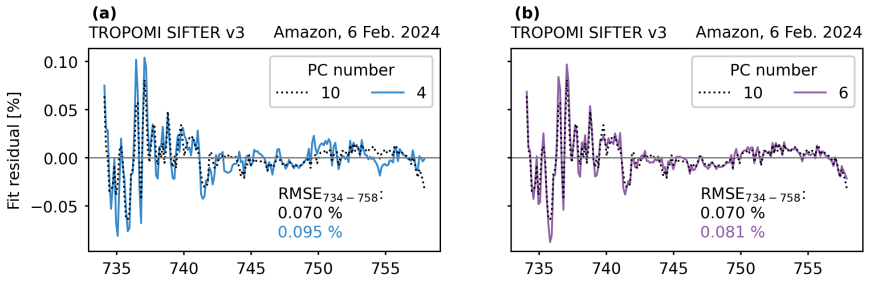


Figure S4.10: Fit residual of the reflectance model used for TROPOMI SIF retrievals. Subplot (a) compares the residuals of $PC_{n=10}$ (dotted black) against $PC_{n=4}$ (in blue), and (b) compares $PC_{n=10}$ against $PC_{n=6}$. Data selection and filtering follow the description in the caption of Figure 5.4.

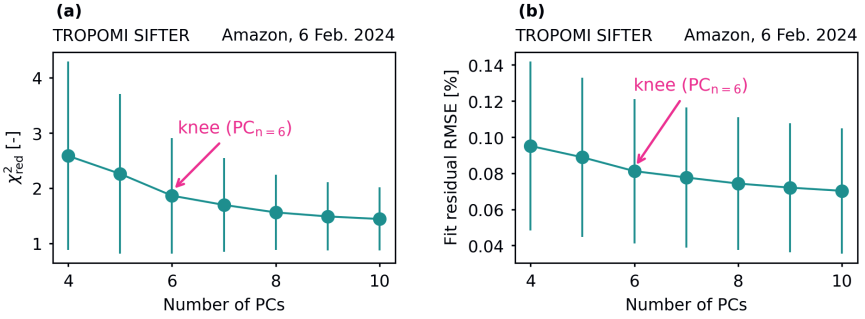


Figure S4.11: Distribution of fit metrics (a) χ^2_{red} and (b) fit residual RMSE (734–758 nm) from TROPOMI SIFTER retrievals using four to 10 PCs. Data selection and filtering follow the description in the caption of Figure 5.4. In both plots, the value of $PC_{n=6}$, the point where the reduction in retrieval fit begins to slow down, is indicated in pink and referred to as the "knee".

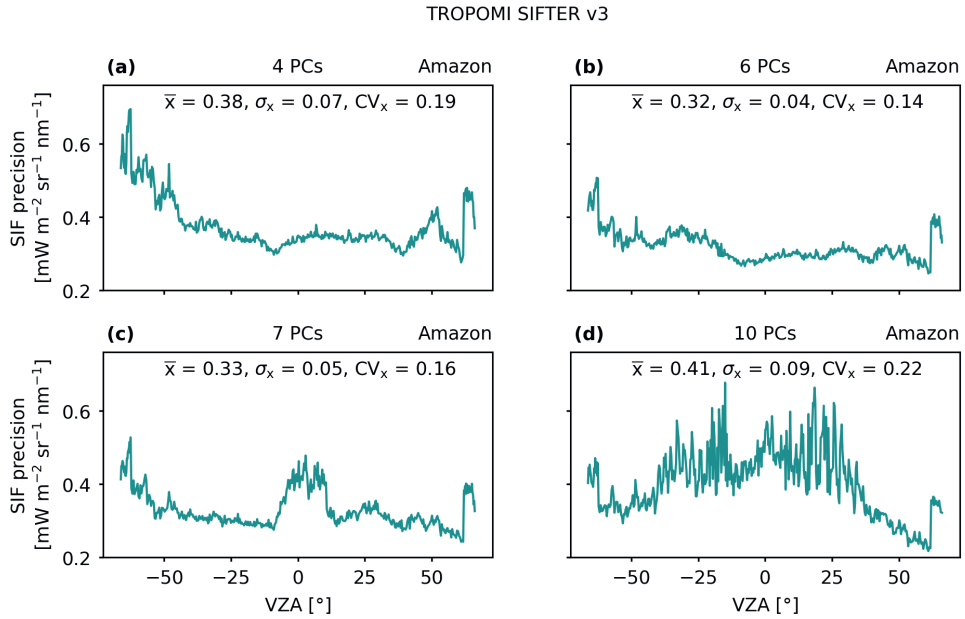


Figure S4.12: Precision in SIF retrieved from TROPOMI using the SIFTER v3 algorithm using (a) $PC_{n=4}$, (b) $PC_{n=6}$, (c) $PC_{n=7}$, and (d) $PC_{n=10}$, averaged per ground pixel (plotted over VZA). Data selection and filtering follow the description in the caption of Figure 5.4.

Comparison between SIFTER v3 and TROPOSIF

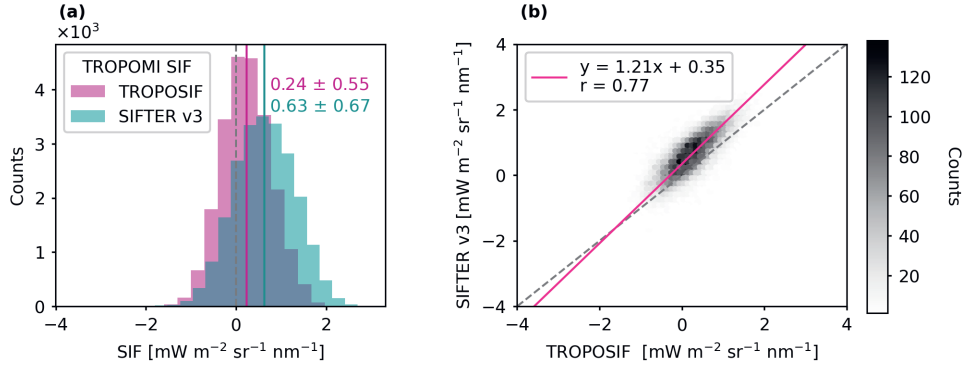


Figure S4.13: Comparison of TROPOMI SIF retrieved from SIFTER v3 and TROPOSIF as described in the caption of Figure 5.6. Subplot (a) shows the histogram of both products with the mean and standard deviation shown in the form $\bar{x} \pm \sigma_x$.

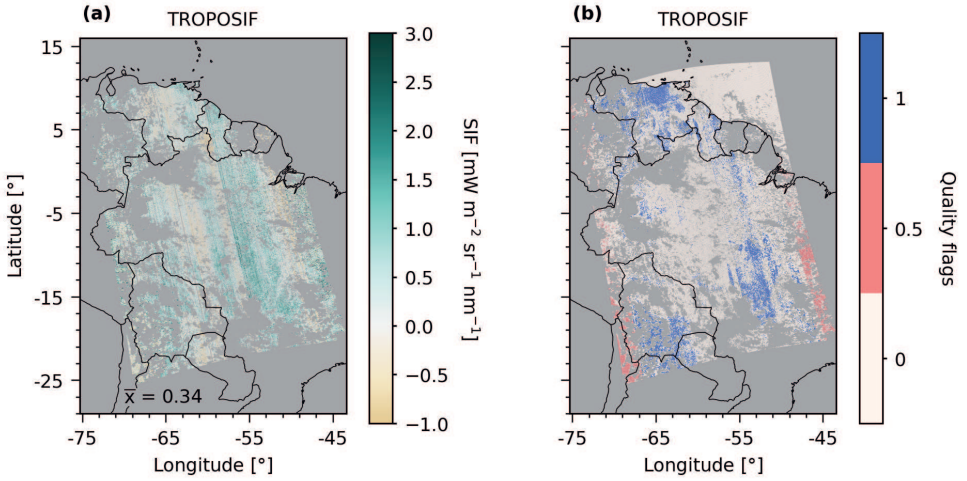


Figure S4.14: Spatial distribution of (a) SIF retrievals from TROPOSIF and (b) the respective quality flags. According to Guanter et al. (2021), quality flags < 1 should be discarded. The data is plotted for all co-sampled pixels that are valid in the TROPOMI SIFTER product. The data represent retrievals on 6 February 2024.

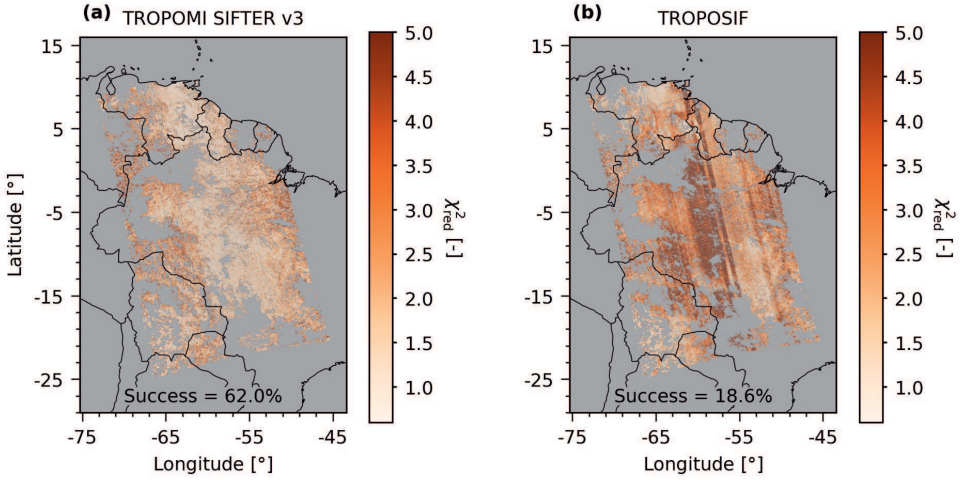


Figure S4.15: Spatial distribution of χ^2_{red} for (a) TROPOMI SIFTER and (b) TROPOSIF. Data were filtered according to the TOA radiation, SZA, VZA, and SIF value requirements defined by the TROPOSIF quality filtering described in Guanter et al. (2021). Moreover, according to the TROPOSIF filtering, χ^2_{red} should range between 0.8 and 2.0. The percentage of data meeting this threshold is shown in text for each product.

Retrieval settings and results of GOME-2B

Table S4.2: RMSE fit residuals for subsets and the entire retrieval window (734–758 nm) from GOME-2B SIFTER v3 using four to 10 PCs. Data selection and filtering follow the details described in the captions of Figure 5.7.

RMSE fit residual	Number of PCs used						
	4	5	6	7	8	9	10
734–745 nm	0.099 %	0.094 %	0.092 %	0.087 %	0.087 %	0.085 %	0.084 %
746–758 nm	0.078 %	0.077 %	0.076 %	0.075 %	0.074 %	0.073 %	0.073 %
734–758 nm	0.088 %	0.086 %	0.084 %	0.081 %	0.080 %	0.079 %	0.078 %

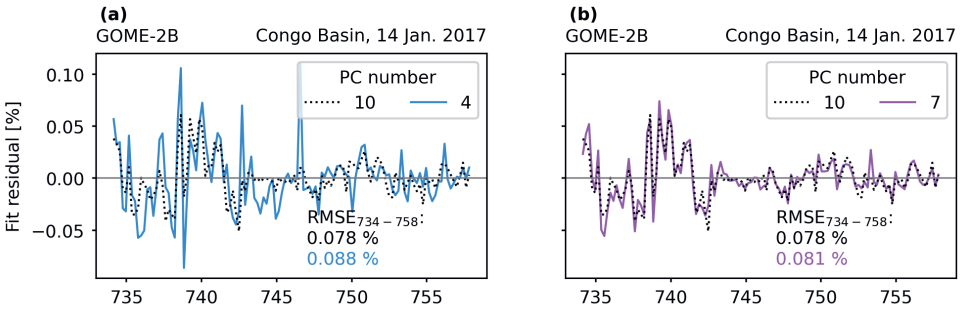


Figure S4.16: Fit residual of the reflectance model used for GOME-2B SIF retrievals. Subplot (a) compares the residuals of $PC_{n=10}$ (dotted black) against $PC_{n=4}$ (in blue), and (b) compares $PC_{n=10}$ against $PC_{n=6}$. Data selection and filtering follow the description in the caption of Figure 5.7.

S4.4 Australian wildfire case study

(a)

Severity	Area affected
Burnt unclassified	11.9 %
Burnt canopy	8.7 %
High canopy scorch	44.9 %
Medium canopy scorch	20.3 %
Low canopy scorch	9.5 %

(b)

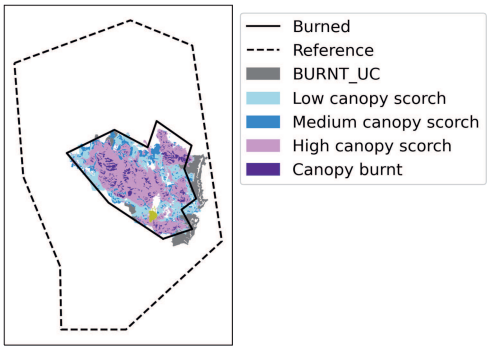


Figure S4.17: Fire severity data of the 2019 eucalyptus forest fire in Australia. (a) Proportion of the burned area classified into five levels of fire severity. (b) Spatial distribution of the different severity classes across the burned area (indicated by solid line) and the reference area (indicated by dashed line). Data from Department of Energy, Environment and Climate Action (2023).

References

Ač, A., Malenovský, Z., Olejníčková, J., Gallé, A., Rascher, U., and Mohammed, G. (2015). Meta-analysis assessing potential of steady-state chlorophyll fluorescence for remote sensing detection of plant water, temperature and nitrogen stress. *Remote Sensing of Environment*, 168:420–436.

Amalo, L. F., Ma'rufah, U., and Permatasari, P. A. (2018). Monitoring 2015 drought in West Java using Normalized Difference Water Index (NDWI). *IOP Conference Series: Earth and Environmental Science*, 149:012007.

Anderegg, W. R. L., Trugman, A. T., Badgley, G., Anderson, C. M., Bartuska, A., Ciais, P., Cullenward, D., Field, C. B., Freeman, J., Goetz, S. J., Hicke, J. A., Huntzinger, D., Jackson, R. B., Nickerson, J., Pacala, S., and Randerson, J. T. (2020). Climate-driven risks to the climate mitigation potential of forests. *Science*, 368(6497).

Anema, J. C. S., Boersma, K. F., Stammes, P., Koren, G., Woodgate, W., Köhler, P., Frankenberg, C., and Stol, J. (2024). Monitoring the impact of forest changes on carbon uptake with solar-induced fluorescence measurements from GOME-2A and TROPOMI for an Australian and Chinese case study. *Biogeosciences*, 21(9):2297–2311.

Anema, J. C. S., Boersma, K. F., Tilstra, L. G., and Tuinder, O. N. E. (2025a). SIFTER solar-induced vegetation fluorescence data from GOME-2A (Version 3.0) [Data set].

Anema, J. C. S., Boersma, K. F., Tilstra, L. G., Tuinder, O. N. E., and Verstraeten, W. W. (2025b). Improved consistency in solar-induced fluorescence retrievals from GOME-2A with the SIFTER v3 algorithm. *Atmospheric Measurement Techniques*, 18(8):1961–1979.

Anema, J. C. S., Boersma, K. F., Tilstra, L. G., van 't Loo, R., and Tuinder, O. N. E. (2025c). Long-term solar-induced fluorescence data record from GOME-2A and GOME-2B (2007–2023) using the SIFTER v3 algorithm.

Ashok, A., Rani, H. P., and Jayakumar, K. (2021). Monitoring of dynamic wetland changes using NDVI and NDWI based landsat imagery. *Remote Sensing Applications: Society and Environment*, 23:100547.

Aubinet, M., Grelle, A., Ibrom, A., Rannik, Ü., Moncrieff, J., Foken, T., Kowalski, A., Martin, P., Berbigier, P., Bernhofer, Ch., Clement, R., Elbers, J., Granier, A., Grünwald, T., Morgenstern, K., Pilegaard, K., Rebmann, C., Snijders, W., Valentini, R., and Vesala, T. (1999). Estimates of the Annual Net Carbon and Water Exchange of Forests: The EUROFLUX Methodology. In *Advances in Ecological Research*, volume 30, pages 113–175. Elsevier.

Bacour, C., Maignan, F., MacBean, N., Porcar-Castell, A., Flexas, J., Frankenberg, C., Peylin, P., Chevallier, F., Vuichard, N., and Bastrikov, V. (2019). Improving Estimates of Gross Primary Productivity by Assimilating Solar-Induced Fluorescence Satellite Retrievals in a Terrestrial Biosphere Model Using a Process-Based SIF Model. *Journal of Geophysical Research: Biogeosciences*, 124(11):3281–3306.

Badgley, G., Anderegg, L. D. L., Berry, J. A., and Field, C. B. (2019). Terrestrial gross primary production: Using NIR_V to scale from site to globe. *Global Change Biology*, 25(11):3731–3740.

Badgley, G., Field, C. B., and Berry, J. A. (2017). Canopy near-infrared reflectance and terrestrial photosynthesis. *Science Advances*, 3(3):e1602244.

Baldocchi, D., Falge, E., Gu, L., Olson, R., Hollinger, D., Running, S., Anthoni, P., Bernhofer, C., Davis, K., Evans, R., Fuentes, J., Goldstein, A., Katul, G., Law, B., Lee, X., Malhi, Y., Meyers, T., Munger, W., Oechel, W.,

Paw, K. T., Pilegaard, K., Schmid, H. P., Valentini, R., Verma, S., Vesala, T., Wilson, K., and Wofsy, S. (2001). FLUXNET: A New Tool to Study the Temporal and Spatial Variability of Ecosystem–Scale Carbon Dioxide, Water Vapor, and Energy Flux Densities. *Bulletin of the American Meteorological Society*, 82(11):2415–2434.

Bandopadhyay, S., Rastogi, A., Rascher, U., Rademske, P., Schickling, A., Cogliati, S., Julitta, T., Mac Arthur, A., Hueni, A., Tomelleri, E., Celesti, M., Burkart, A., Stróżecki, M., Sakowska, K., Gąbka, M., Rosadziński, S., Sojka, M., Iordache, M.-D., Reusen, I., Van Der Tol, C., Damm, A., Schuettemeyer, D., and Juszczak, R. (2019). Hyplant-Derived Sun-Induced Fluorescence—A New Opportunity to Disentangle Complex Vegetation Signals from Diverse Vegetation Types. *Remote Sensing*, 11(14):1691.

Beerling, D. J. (2007). *The Emerald Planet: How Plants Changed Earth's History*. Oxford University Press.

Beringer, J., Hutley, L. B., McHugh, I., Arndt, S. K., Campbell, D., Cleugh, H. A., Cleverly, J., Resco De Dios, V., Eamus, D., Evans, B., Ewenz, C., Grace, P., Griebel, A., Haverd, V., Hinko-Najera, N., Huete, A., Isaac, P., Kanniah, K., Leuning, R., Liddell, M. J., Macfarlane, C., Meyer, W., Moore, C., Pendall, E., Phillips, A., Phillips, R. L., Prober, S. M., Restrepo-Coupe, N., Rutledge, S., Schroder, I., Silberstein, R., Southall, P., Yee, M. S., Tapper, N. J., Van Gorsel, E., Vote, C., Walker, J., and Wardlaw, T. (2016). An introduction to the Australian and New Zealand flux tower network –OzFlux. *Biogeosciences*, 13(21):5895–5916.

Berry, J. A., Beerling, D. J., and Franks, P. J. (2010). Stomata: Key players in the earth system, past and present. *Current Opinion in Plant Biology*, 13(3):232–239.

Biederman, J. A., Scott, R. L., Bell, T. W., Bowling, D. R., Dore, S., Garatuza-Payan, J., Kolb, T. E., Krishnan, P., Krofcheck, D. J., Litvak, M. E., Maurer, G. E., Meyers, T. P., Oechel, W. C., Papuga, S. A., Ponce-Campos, G. E., Rodriguez, J. C., Smith, W. K., Vargas, R., Watts, C. J., Yepez, E. A., and Goulden, M. L. (2017). CO_2 exchange and evapotranspiration across dryland ecosystems of southwestern North America. *Global Change Biology*, 23(10):4204–4221.

Bittner, T., Irrgang, K.-D., Renger, G., and Wasielewski, M. R. (1994). Ultrafast Excitation Energy Transfer and Exciton-Exciton Annihilation Processes in Isolated Light Harvesting Complexes of Photosystem II (LHC II) from Spinach. *The Journal of Physical Chemistry*, 98(46):11821–11826.

Bosman, P. J. M., Van Heerwaarden, C. C., and Teuling, A. J. (2019). Sensible heating as a potential mechanism for enhanced cloud formation over temperate forest. *Quarterly Journal of the Royal Meteorological Society*, 145(719):450–468.

Bowman, D. M., Williamson, G. J., Price, O. F., Ndalila, M. N., and Bradstock, R. A. (2021). Australian forests, megafires and the risk of dwindling carbon stocks. *Plant, Cell & Environment*, 44(2):347–355.

Brandt, M., Verger, A., Diouf, A., Baret, F., and Samimi, C. (2014). Local Vegetation Trends in the Sahel of Mali and Senegal Using Long Time Series FAPAR Satellite Products and Field Measurement (1982–2010). *Remote Sensing*, 6(3):2408–2434.

Brienen, R. J. W., Phillips, O. L., Feldpausch, T. R., Gloor, E., Baker, T. R., Lloyd, J., Lopez-Gonzalez, G., Monteagudo-Mendoza, A., Malhi, Y., Lewis, S. L., Vásquez Martinez, R., Alexiades, M., Álvarez Dávila, E., Alvarez-Loayza, P., Andrade, A., Aragão, L. E. O. C., Araujo-Murakami, A., Arets, E. J. M. M., Arroyo, L., Aymard C., G. A., Bánki, O. S., Baraloto, C., Barroso, J., Bonal, D., Boot, R. G. A., Camargo, J. L. C., Castilho, C. V., Chama, V., Chao, K. J., Chave, J., Comiskey, J. A., Cornejo Valverde, F., Da Costa, L., De Oliveira, E. A., Di Fiore, A., Erwin, T. L., Fauset, S., Forsthofer, M., Galbraith, D. R., Grahame, E. S., Groot, N., Hérault, B., Higuchi, N., Honorio Coronado, E. N., Keeling, H., Killeen, T. J., Laurance, W. F., Laurance, S., Licona, J., Magnussen, W. E., Marimon, B. S., Marimon-Junior, B. H., Mendoza, C., Neill, D. A., Nogueira, E. M., Núñez, P., Pallqui Camacho, N. C., Parada, A., Pardo-Molina, G., Peacock, J., Peña-Claros, M., Pickavance, G. C., Pitman, N. C. A., Poorter, L., Prieto, A., Quesada, C. A., Ramírez, F., Ramírez-Angulo, H., Restrepo, Z., Roopsind, A., Rudas, A., Salomão, R. P., Schwarz, M., Silva, N., Silva-Espejo, J. E., Silveira, M., Stropp, J., Talbot, J., Ter Steege, H., Teran-Aguilar, J., Terborgh, J., Thomas-Caesar, R., Toledo, M., Torello-Raventos, M., Umetsu, R. K., Van Der Heijden, G. M. F., Van Der Hout, P., Guimarães Vieira, I. C., Vieira, S. A., Vilanova, E., Vos, V. A., and Zagt, R. J. (2015). Long-term decline of the Amazon carbon sink. *Nature*, 519(7543):344–348.

Brook, B. W., Ellis, E. C., Perring, M. P., Mackay, A. W., and Blomqvist, L. (2013). Does the terrestrial biosphere have planetary tipping points? *Trends in Ecology & Evolution*, 28(7):396–401.

Byrne, B., Liu, J., Lee, M., Yin, Y., Bowman, K. W., Miyazaki, K., Norton, A. J., Joiner, J., Pollard, D. F., Griffith, D. W. T., Velazco, V. A., Deutscher, N. M., Jones, N. B., and Paton-Walsh, C. (2021). The Carbon Cycle of Southeast Australia During 2019–2020: Drought, Fires, and Subsequent Recovery. *AGU Advances*, 2(4):e2021AV000469.

Cai, Z., Liu, Y., Liu, X., Chance, K., Nowlan, C. R., Lang, R., Munro, R., and Suleiman, R. (2012). Characterization and correction of Global Ozone Monitoring Experiment 2 ultraviolet measurements and application to ozone profile retrievals. *Journal of Geophysical Research: Atmospheres*, 117(D7).

Calvin, K., Dasgupta, D., Krinner, G., Mukherji, A., Thorne, P. W., Trisos, C., Romero, J., Aldunce, P., Barrett, K., Blanco, G., Cheung, W. W., Connors, S., Denton, F., Diongue-Niang, A., Dodman, D., Garschagen, M., Geden, O., Hayward, B., Jones, C., Jotzo, F., Krug, T., Lasco, R., Lee, Y.-Y., Masson-Delmotte, V., Meinshausen, M., Mintenbeck, K., Mokssit, A., Otto, F. E., Pathak, M., Pirani, A., Poloczanska, E., Pörtner, H.-O., Revi, A., Roberts, D. C., Roy, J., Ruane, A. C., Skea, J., Shukla, P. R., Slade, R., Slangen, A., Sokona, Y., Sörensson, A. A., Tignor, M., Van Vuuren, D., Wei, Y.-M., Winkler, H., Zhai, P., Zommers, Z., Hourcade, J.-C., Johnson, F. X., Pachauri, S., Simpson, N. P., Singh, C., Thomas, A., Totin, E., Arias, P., Bustamante, M., Elgizouli, I., Flato, G., Howden, M., Méndez-Vallejo, C., Pereira, J. J., Pichs-Madruga, R., Rose, S. K., Saheb, Y., Sánchez Rodríguez, R., Ürge-Vorsatz, D., Xiao, C., Yassaa, N., Alegría, A., Armour, K., Bednar-Friedl, B., Blok, K., Cissé, G., Dentener, F., Eriksen, S., Fischer, E., Garner, G., Guivarch, C., Haasnoot, M., Hansen, G., Hauser, M., Hawkins, E., Hermans, T., Kopp, R., Leprince-Ringuet, N., Lewis, J., Ley, D., Ludden, C., Niamir, L., Nicholls, Z., Some, S., Szopa, S., Trewin, B., Van Der Wijst, K.-I., Winter, G., Witting, M., Birt, A., Ha, M., Romero, J., Kim, J., Haites, E. F., Jung, Y., Stavins, R., Birt, A., Ha, M., Orendain, D. J. A., Ignon, L., Park, S., Park, Y., Reisinger, A., Cammaramo, D., Fischlin, A., Fuglestvedt, J. S., Hansen, G., Ludden, C., Masson-Delmotte, V., Matthews, J. R., Mintenbeck, K., Pirani, A., Poloczanska, E., Leprince-Ringuet, N., and Péan, C. (2023). IPCC, 2023: Climate Change 2023: Synthesis Report. Contribution of Working Groups I, II and III to the Sixth Assessment Report of the Intergovernmental Panel on Climate Change [Core Writing Team, H. Lee and J. Romero (eds.)]. IPCC, Geneva, Switzerland. Technical report, Intergovernmental Panel on Climate Change (IPCC).

Cao, S., Chen, L., and Yu, X. (2009). Impact of China's Grain for Green Project on the landscape of vulnerable arid and semi-arid agricultural regions: A case study in northern Shaanxi Province. *Journal of Applied Ecology*, 46(3):536–543.

Chance, K. and Kurucz, R. L. (2010). An improved high-resolution solar reference spectrum for earth's atmosphere measurements in the ultraviolet, visible, and near infrared. *Journal of Quantitative Spectroscopy and Radiative Transfer*, 111(9):1289–1295.

Chen, S., Huang, Y., and Wang, G. (2021a). Detecting drought-induced GPP spatiotemporal variabilities with sun-induced chlorophyll fluorescence during the 2009/2010 droughts in China. *Ecological Indicators*, 121:107092.

Chen, S., Huang, Y., and Wang, G. (2021b). Detecting drought-induced GPP spatiotemporal variabilities with sun-induced chlorophyll fluorescence during the 2009/2010 droughts in China. *Ecological Indicators*, 121:107092.

Chu, X., Zhan, J., Li, Z., Zhang, F., and Qi, W. (2019). Assessment on forest carbon sequestration in the Three-North Shelterbelt Program region, China. *Journal of Cleaner Production*, 215:382–389.

Chungu, D., Ng'andwe, P., Mubanga, H., and Chileshe, F. (2020). Fire alters the availability of soil nutrients and accelerates growth of Eucalyptus grandis in Zambia. *Journal of Forestry Research*, 31(5):1637–1645.

Clarke, B., Otto, F., Stuart-Smith, R., and Harrington, L. (2022). Extreme weather impacts of climate change: An attribution perspective. *Environmental Research: Climate*, 1(1):012001.

Coldewey-Egbers, M., Slijkhuis, S., Aberle, B., and Loyola, D. (2008). Long-term analysis of GOME in-flight calibration parameters and instrument degradation. *Applied Optics*, 47(26):4749.

Colombo, R., Celesti, M., Bianchi, R., Campbell, P. K. E., Cogliati, S., Cook, B. D., Corp, L. A., Damm, A., Domec, J.-C., Guanter, L., Julitta, T., Middleton, E. M., Noormets, A., Panigada, C., Pinto, F., Rascher, U., Rossini, M., and Schickling, A. (2018). Variability of sun-induced chlorophyll fluorescence according to stand age-related processes in a managed loblolly pine forest. *Global Change Biology*, 24(7):2980–2996.

Copernicus Climate Change Service (2019). ERA5-Land hourly data from 1950 to present.

Dahl, T. W. and Arens, S. K. (2020). The impacts of land plant evolution on Earth's climate and oxygenation

state – An interdisciplinary review. *Chemical Geology*, 547:119665.

Damm, A., Guanter, L., Paul-Limoges, E., Van Der Tol, C., Hueni, A., Buchmann, N., Eugster, W., Ammann, C., and Schaepman, M. (2015). Far-red sun-induced chlorophyll fluorescence shows ecosystem-specific relationships to gross primary production: An assessment based on observational and modeling approaches. *Remote Sensing of Environment*, 166:91–105.

Davidson, M., Berger, M., Moya, I., Moreno, J., Laurila, T., Stoll, M.-P., and Miller, J. (2003). Photosynthesis from Space. *Earth Observation*.

Dechant, B., Ryu, Y., Badgley, G., Zeng, Y., Berry, J. A., Zhang, Y., Goulas, Y., Li, Z., Zhang, Q., Kang, M., Li, J., and Moya, I. (2020). Canopy structure explains the relationship between photosynthesis and sun- T induced chlorophyll fluorescence in crops. *Remote Sensing of Environment*.

Delang, C. O. and Yuan, Z. (2015). *China's Grain for Green Program: A Review of the Largest Ecological Restoration and Rural Development Program in the World*. Springer International Publishing, Cham.

Department of Energy, Environment and Climate Action (2023). Aggregated Fire Severity Classes from 1998 onward.

Dikty, S. and Richter, A. (2011). GOME-2 on MetOp-A Support for Analysis of GOME-2 In-Orbit Degradation and Impacts on Level 2 Data Products. *ITT 09/10000262*, Final Report(Version 2.0).

Dolman, A., Moors, E., and Elbers, J. (2002). The carbon uptake of a mid latitude pine forest growing on sandy soil. *Agricultural and Forest Meteorology*, 111(3):157–170.

Dorigo, W., Preimesberger, W., Reimer, C., {van der Schalie}, R., Pasik, A., {De Jeu}, R., and Paulik (2019). Soil moisture gridded data from 1978 to present, v201912.0.0.

Doughty, R., Köhler, P., Frankenberg, C., Magney, T. S., Xiao, X., Qin, Y., Wu, X., and Moore, B. (2019). TROPOMI reveals dry-season increase of solar-induced chlorophyll fluorescence in the Amazon forest. *Proceedings of the National Academy of Sciences*, 116(44):22393–22398.

Doughty, R., Kurosu, T. P., Parazoo, N., Köhler, P., Wang, Y., Sun, Y., and Frankenberg, C. (2022). Global GOSAT, OCO-2, and OCO-3 solar-induced chlorophyll fluorescence datasets. *Earth System Science Data*, 14(4):1513–1529.

Drusch, M., Moreno, J., Del Bello, U., Franco, R., Goulas, Y., Huth, A., Kraft, S., Middleton, E. M., Miglietta, F., Mohammed, G., Nedbal, L., Rascher, U., Schuttemeyer, D., and Verhoef, W. (2016). The FLuorescence EXplorer Mission Concept—ESA's Earth Explorer 8. *IEEE Transactions on Geoscience and Remote Sensing*, 55(3):1273–1284.

Duffy, K. A., Schwalm, C. R., Arcus, V. L., Koch, G. W., Liang, L. L., and Schipper, L. A. (2021). How close are we to the temperature tipping point of the terrestrial biosphere? *Science Advances*, 7(3):eaay1052.

Duveiller, G., López-Lozano, R., and Baruth, B. (2013). Enhanced Processing of 1-km Spatial Resolution fAPAR Time Series for Sugarcane Yield Forecasting and Monitoring. *Remote Sensing*, 5(3):1091–1116.

Ebi, K. L. and McGregor, G. (2008). Climate Change, Tropospheric Ozone and Particulate Matter, and Health Impacts. *Environmental Health Perspectives*, 116(11):1449–1455.

Esbensen, K. H., Guyot, D., Westad, F., and Houmoller, L. P. (2002). *Multivariate Data Analysis: In Practice : An Introduction to Multivariate Data Analysis and Experimental Design*. Multivariate Data Analysis.

EUMETSAT (2009). GOME-2 FM3 Long-Term In-Orbit Degradation - Status After 2nd Throughput Test EUMETSAT. *EUM/OPS-EPS/TEN/09/0318*, v2.

EUMETSAT (2022). GOME-2 Metop-A and -B FDR Product Validation Report Reprocessing R3. *EUM/OPS/DOC/21/1237264*, (v4 e-signed).

Fancourt, M., Ziv, G., Boersma, K. F., Tavares, J., Wang, Y., and Galbraith, D. (2022). Background climate conditions regulated the photosynthetic response of Amazon forests to the 2015/2016 El Nino-Southern Oscillation event. *Communications Earth & Environment*, 3(1):209.

Fleming, G. R., Schlau-Cohen, G. S., Amarnath, K., and Zaks, J. (2012). Design principles of photosynthetic light-harvesting. *Faraday Discuss.*, 155:27–41.

Fournier, A., Daumard, F., Champagne, S., Ounis, A., Goulas, Y., and Moya, I. (2012). Effect of canopy structure on sun-induced chlorophyll fluorescence. *ISPRS Journal of Photogrammetry and Remote Sensing*, 68:112–120.

Frankenberg, C. and Berry, J. (2018). Solar Induced Chlorophyll Fluorescence: Origins, Relation to Photosynthesis and Retrieval. In *Comprehensive Remote Sensing*, pages 143–162. Elsevier.

Frankenberg, C., Butz, A., and Toon, G. C. (2011a). Disentangling chlorophyll fluorescence from atmospheric scattering effects in O2 A-band spectra of reflected sun-light. *Geophysical Research Letters*, 38(3).

Frankenberg, C., Fisher, J. B., Worden, J., Badgley, G., Saatchi, S. S., Lee, J.-E., Toon, G. C., Butz, A., Jung, M., Kuze, A., and Yokota, T. (2011b). New global observations of the terrestrial carbon cycle from GOSAT: Patterns of plant fluorescence with gross primary productivity. *Geophysical Research Letters*, 38(17).

Frankenberg, C., Köhler, P., Magney, T. S., Geier, S., Lawson, P., Schwochert, M., McDuffie, J., Drewry, D. T., Pavlick, R., and Kuhnert, A. (2018). The Chlorophyll Fluorescence Imaging Spectrometer (CFIS), mapping far red fluorescence from aircraft. *Remote Sensing of Environment*, 217:523–536.

Frankenberg, C., O'Dell, C., Berry, J., Guanter, L., Joiner, J., Köhler, P., Pollock, R., and Taylor, T. E. (2014). Prospects for chlorophyll fluorescence remote sensing from the Orbiting Carbon Observatory-2. *Remote Sensing of Environment*, 147:1–12.

Frankenberg, C., O'Dell, C., Guanter, L., and McDuffie, J. (2012). Remote sensing of near-infrared chlorophyll fluorescence from space in scattering atmospheres: Implications for its retrieval and interferences with atmospheric CO_2 retrievals. *Atmospheric Measurement Techniques*, 5(8):2081–2094.

Friedlingstein, P., O'Sullivan, M., Jones, M. W., Andrew, R. M., Hauck, J., Landschützer, P., Le Quéré, C., Li, H., Luijkx, I. T., Olsen, A., Peters, G. P., Peters, W., Pongratz, J., Schwingshackl, C., Sitch, S., Canadell, J. G., Ciais, P., Jackson, R. B., Alin, S. R., Arneth, A., Arora, V., Bates, N. R., Becker, M., Bellouin, N., Berghoff, C. F., Bittig, H. C., Bopp, L., Cadule, P., Campbell, K., Chamberlain, M. A., Chandra, N., Chevallier, F., Chini, L. P., Colligan, T., Decayeux, J., Djeutchouang, L. M., Dou, X., Duran Rojas, C., Enyo, K., Evans, W., Fay, A. R., Feely, R. A., Ford, D. J., Foster, A., Gasser, T., Gehlen, M., Gkritzalis, T., Grassi, G., Gregor, L., Gruber, N., Gürses, Ö., Harris, I., Hefner, M., Heinke, J., Hurtt, G. C., Iida, Y., Ilyina, T., Jacobson, A. R., Jain, A. K., Jarníková, T., Jersild, A., Jiang, F., Jin, Z., Kato, E., Keeling, R. F., Klein Goldewijk, K., Knauer, J., Korsbakken, J. I., Lan, X., Lauvset, S. K., Lefèvre, N., Liu, Z., Liu, J., Ma, L., Maksyutov, S., Marland, G., Mayot, N., McGuire, P. C., Metzl, N., Monacci, N. M., Morgan, E. J., Nakaoka, S.-I., Neill, C., Niwa, Y., Nützel, T., Olivier, L., Ono, T., Palmer, P. I., Pierrot, D., Qin, Z., Resplandy, L., Roobaert, A., Rosan, T. M., Rödenbeck, C., Schwinger, J., Smallman, T. L., Smith, S. M., Sospedra-Alfonso, R., Steinhoff, T., Sun, Q., Sutton, A. J., Séférian, R., Takao, S., Tatebe, H., Tian, H., Tilbrook, B., Torres, O., Tourigny, E., Tsujino, H., Tubiello, F., Van Der Werf, G., Wanninkhof, R., Wang, X., Yang, D., Yang, X., Yu, Z., Yuan, W., Yue, X., Zaehle, S., Zeng, N., and Zeng, J. (2025). Global Carbon Budget 2024. *Earth System Science Data*, 17(3):965–1039.

Friedlingstein, P., O'Sullivan, M., Jones, M. W., Andrew, R. M., Hauck, J., Olsen, A., Peters, G. P., Peters, W., Pongratz, J., Sitch, S., Le Quéré, C., Canadell, J. G., Ciais, P., Jackson, R. B., Alin, S., Aragão, L. E. O. C., Arneth, A., Arora, V., Bates, N. R., Becker, M., Benoit-Cattin, A., Bittig, H. C., Bopp, L., Bultan, S., Chandra, N., Chevallier, F., Chini, L. P., Evans, W., Florentie, L., Forster, P. M., Gasser, T., Gehlen, M., Gilfillan, D., Gkritzalis, T., Gregor, L., Gruber, N., Harris, I., Hartung, K., Haverd, V., Houghton, R. A., Ilyina, T., Jain, A. K., Joetzjer, E., Kadono, K., Kato, E., Kitidis, V., Korsbakken, J. I., Landschützer, P., Lefèvre, N., Lenton, A., Lienert, S., Liu, Z., Lombardozzi, D., Marland, G., Metzl, N., Munro, D. R., Nabel, J. E. M. S., Nakaoka, S.-I., Niwa, Y., O'Brien, K., Ono, T., Palmer, P. I., Pierrot, D., Poulter, B., Resplandy, L., Robertson, E., Rödenbeck, C., Schwinger, J., Séférian, R., Skjelvan, I., Smith, A. J. P., Sutton, A. J., Tanhua, T., Tans, P. P., Tian, H., Tilbrook, B., Van Der Werf, G., Vuichard, N., Walker, A. P., Wanninkhof, R., Watson, A. J., Willis, D., Wiltshire, A. J., Yuan, W., Yue, X., and Zaehle, S. (2020). Global Carbon Budget 2020. *Earth System Science Data*, 12(4):3269–3340.

Gamon, J. A., Field, C. B., Bilger, W., Björkman, O., Fredeen, A. L., and Peñuelas, J. (1990). Remote sensing of the xanthophyll cycle and chlorophyll fluorescence in sunflower leaves and canopies. *Oecologia*, 85(1):1–7.

Gao, B.-c. (1996). NDWI—A normalized difference water index for remote sensing of vegetation liquid water from space. *Remote Sensing of Environment*, 58(3):257–266.

Gao, J., Jiao, K., and Wu, S. (2019). Investigating the spatially heterogeneous relationships between climate factors and NDVI in China during 1982 to 2013. *Journal of Geographical Sciences*, 29(10):1597–1609.

Garrigues, S., De Rosnay, P., Pinnington, E., Weston, P., Agusti-Panareda, A., Boussetta, S., Calvet, J.-C., Fairbairn, D., Bacour, C., Engelen, R., and English, S. (2024). Machine Learning-Based Observation Operators to Assimilate Microwave and SIF Satellite Observations into the ECMWF Integrated Forecast System. In *IGARSS 2024 - 2024 IEEE International Geoscience and Remote Sensing Symposium*, pages 4285–4288, Athens, Greece. IEEE.

Gatti, L. V., Basso, L. S., Miller, J. B., Gloor, M., Gatti Domingues, L., Cassol, H. L. G., Tejada, G., Aragão, L. E. O. C., Nobre, C., Peters, W., Marani, L., Arai, E., Sanches, A. H., Corrêa, S. M., Anderson, L., Von Randow, C., Correia, C. S. C., Crispim, S. P., and Neves, R. A. L. (2021). Amazonia as a carbon source linked to deforestation and climate change. *Nature*, 595(7867):388–393.

GCOS (2016). The Global Observing System for Climate: Implementation Needs. Technical Report GCOS-200.

Gerlein-Safdi, C., Keppel-Aleks, G., Wang, F., Frolking, S., and Mauzerall, D. L. (2020). Satellite Monitoring of Natural Reforestation Efforts in China's Drylands. *One Earth*, 2(1):98–108.

Giering, R., Quast, R., Mittaz, J. P. D., Hunt, S. E., Harris, P. M., Woolliams, E. R., and Merchant, C. J. (2019). A Novel Framework to Harmonise Satellite Data Series for Climate Applications. *Remote Sensing*, 11(9):1002.

Giglio, L., Justice, C., Boschetti, L., and Roy, D. (2015). MCD64A1 MODIS/Terra+Aqua Burned Area Monthly L3 Global 500m SIN Grid V006.

Glissenaar, I., Boersma, K. F., Anglou, I., Rijsdijk, P., Verhoelst, T., Compernolle, S., Pinardi, G., Lambert, J.-C., Van Roozendael, M., and Eskes, H. (2025). TROPOMI Level 3 tropospheric NO_2 Dataset with Advanced Uncertainty Analysis from the ESA CCI+ ECV Precursor Project.

Goudar, M., Anema, J. C. S., Kumar, R., Borsdorff, T., and Landgraf, J. (2023). Plume detection and emission estimate for biomass burning plumes from TROPOMI carbon monoxide observations using APE v1.1. *Geoscientific Model Development*, 16(16):4835–4852.

Govender, M., Chetty, K., and Bulcock, H. (2009). A review of hyperspectral remote sensing and its application in vegetation and water resource studies. *Water SA*, 33(2).

Green, J. K., Seneviratne, S. I., Berg, A. M., Findell, K. L., Hagemann, S., Lawrence, D. M., and Gentine, P. (2019). Large influence of soil moisture on long-term terrestrial carbon uptake. *Nature*, 565(7740):476–479.

Grossi, M., Valks, P., Loyola, D., Aberle, B., Slijkhuis, S., Wagner, T., Beirle, S., and Lang, R. (2015). Total column water vapour measurements from GOME-2 MetOp-A and MetOp-B. *Atmospheric Measurement Techniques*, 8(3):1111–1133.

Grossmann, K., Frankenberg, C., Magney, T. S., Hurlock, S. C., Seibt, U., and Stutz, J. (2018). PhotoSpec: A new instrument to measure spatially distributed red and far-red Solar-Induced Chlorophyll Fluorescence. *Remote Sensing of Environment*, 216:311–327.

Gu, Y., Brown, J. F., Verdin, J. P., and Wardlow, B. (2007). A five-year analysis of MODIS NDVI and NDWI for grassland drought assessment over the central Great Plains of the United States. *Geophysical Research Letters*, 34(6):2006GL029127.

Guan, K., Berry, J. A., Zhang, Y., Joiner, J., Guanter, L., Badgley, G., and Lobell, D. B. (2016). Improving the monitoring of crop productivity using spaceborne solar-induced fluorescence. *Global Change Biology*, 22(2):716–726.

Guanter, L., Aben, I., Tol, P., Krijger, J. M., Hollstein, A., Köhler, P., Damm, A., Joiner, J., Frankenberg, C., and Landgraf, J. (2015). Potential of the TROPOspheric Monitoring Instrument (TROPOMI) onboard the Sentinel-5 Precursor for the monitoring of terrestrial chlorophyll fluorescence. *Atmospheric Measurement Techniques*, 8(3):1337–1352.

Guanter, L., Bacour, C., Schneider, A., Aben, I., van Kempen, T. A., Maignan, F., Retscher, C., Köhler, P., Frankenberg, C., Joiner, J., and Zhang, Y. (2021). The TROPOSIF global sun-induced fluorescence dataset from the Sentinel-5P TROPOMI mission.

Guanter, L., Frankenberg, C., Dudhia, A., Lewis, P. E., Gómez-Dans, J., Kuze, A., Suto, H., and Grainger, R. G.

(2012). Retrieval and global assessment of terrestrial chlorophyll fluorescence from GOSAT space measurements. *Remote Sensing of Environment*, 121:236–251.

Guanter, L., Zhang, Y., Jung, M., Joiner, J., Voigt, M., Berry, J. A., Frankenberg, C., Huete, A. R., Zarco-Tejada, P., Lee, J.-E., Moran, M. S., Ponce-Campos, G., Beer, C., Camps-Valls, G., Buchmann, N., Gianelle, D., Klumpp, K., Cescatti, A., Baker, J. M., and Griffis, T. J. (2014). Global and time-resolved monitoring of crop photosynthesis with chlorophyll fluorescence. *Proceedings of the National Academy of Sciences*, 111(14):E1327–E1333.

Guo, M., Li, J., Yu, F., Yin, S., Huang, S., and Wen, L. (2021a). Estimation of post-fire vegetation recovery in boreal forests using solar-induced chlorophyll fluorescence (SIF) data. *International Journal of Wildland Fire*, 30(5):365–377.

Guo, Q., Su, Y., Hu, T., Guan, H., Jin, S., Zhang, J., Zhao, X., Xu, K., Wei, D., Kelly, M., and Coops, N. C. (2021b). Lidar Boosts 3D Ecological Observations and Modelings: A Review and Perspective. *IEEE Geoscience and Remote Sensing Magazine*, 9(1):232–257.

Hajaldaw, M. (2025). SIFTER in action: A workflow for far-red Sun-Induced Fluorescence retrieval from TROPOMI observations. Internship report, Wageningen University and Research, Wageningen.

Han, J., Chang, C. Y.-Y., Gu, L., Zhang, Y., Meeker, E. W., Magney, T. S., Walker, A. P., Wen, J., Kira, O., McNaull, S., and Sun, Y. (2022). The physiological basis for estimating photosynthesis from Chl *a* fluorescence. *New Phytologist*, 234(4):1206–1219.

Hao, D., Zeng, Y., Qiu, H., Biriukova, K., Celesti, M., Migliavacca, M., Rossini, M., Asrar, G. R., and Chen, M. (2021). Practical approaches for normalizing directional solar-induced fluorescence to a standard viewing geometry. *Remote Sensing of Environment*, 255:112171.

Hao, D., Zeng, Y., Zhang, Z., Zhang, Y., Qiu, H., Biriukova, K., Celesti, M., Rossini, M., Zhu, P., Asrar, G. R., and Chen, M. (2022). Adjusting solar-induced fluorescence to nadir-viewing provides a better proxy for GPP. *ISPRS Journal of Photogrammetry and Remote Sensing*, 186:157–169.

Harper, A. B., Powell, T., Cox, P. M., House, J., Huntingford, C., Lenton, T. M., Sitch, S., Burke, E., Chadburn, S. E., Collins, W. J., Comyn-Platt, E., Daioglou, V., Doelman, J. C., Hayman, G., Robertson, E., Van Vuuren, D., Wiltshire, A., Webber, C. P., Bastos, A., Boysen, L., Ciais, P., Devaraju, N., Jain, A. K., Krause, A., Poulter, B., and Shu, S. (2018). Land-use emissions play a critical role in land-based mitigation for Paris climate targets. *Nature Communications*, 9(1):2938.

Hassinen, S., Balis, D., Bauer, H., Begoin, M., Delcloo, A., Eleftheratos, K., Gimeno Garcia, S., Granville, J., Grossi, M., Hao, N., Hedelt, P., Hendrick, F., Hess, M., Heue, K.-P., Hovila, J., Jønch-Sørensen, H., Kalakoski, N., Kauppi, A., Kiemle, S., Kins, L., Koukouli, M. E., Kujanpää, J., Lambert, J.-C., Lang, R., Lerot, C., Loyola, D., Pedergnana, M., Pinardi, G., Romahn, F., Van Roozendael, M., Lutz, R., De Smedt, I., Stammes, P., Steinbrecht, W., Tamminen, J., Theys, N., Tilstra, L. G., Tuinder, O. N. E., Valks, P., Zerefos, C., Zimmer, W., and Zyrichidou, I. (2016). Overview of the O3M SAF GOME-2 operational atmospheric composition and UV radiation data products and data availability. *Atmospheric Measurement Techniques*, 9(2):383–407.

Heimann, M. and Reichstein, M. (2008). Terrestrial ecosystem carbon dynamics and climate feedbacks. *Nature*, 451(7176):289–292.

Hu, X., Li, L., Huang, J., Zeng, Y., Zhang, S., Su, Y., Hong, Y., and Hong, Z. (2024). Radar vegetation indices for monitoring surface vegetation: Developments, challenges, and trends. *Science of The Total Environment*, 945:173974.

Huang, J., Wang, H., Dai, Q., and Han, D. (2014). Analysis of NDVI Data for Crop Identification and Yield Estimation. *IEEE Journal of Selected Topics in Applied Earth Observations and Remote Sensing*, 7(11):4374–4384.

Huang, S., Tang, L., Hupy, J. P., Wang, Y., and Shao, G. (2021). A commentary review on the use of normalized difference vegetation index (NDVI) in the era of popular remote sensing. *Journal of Forestry Research*, 32(1):1–6.

Huete, A., Didan, K., Miura, T., Rodriguez, E., Gao, X., and Ferreira, L. (2002). Overview of the radiometric and biophysical performance of the MODIS vegetation indices. *Remote Sensing of Environment*, 83(1-2):195–213.

Huntzinger, D. N., Michalak, A. M., Schwalm, C., Ciais, P., King, A. W., Fang, Y., Schaefer, K., Wei, Y., Cook, R. B., Fisher, J. B., Hayes, D., Huang, M., Ito, A., Jain, A. K., Lei, H., Lu, C., Maignan, F., Mao, J., Parazoo, N., Peng, S., Poulter, B., Ricciuto, D., Shi, X., Tian, H., Wang, W., Zeng, N., and Zhao, F. (2017). Uncertainty in the response of terrestrial carbon sink to environmental drivers undermines carbon-climate feedback predictions. *Scientific Reports*, 7(1):4765.

Isaac, P., Cleverly, J., McHugh, I., Van Gorsel, E., Ewenz, C., and Beringer, J. (2017). OzFlux data: Network integration from collection to curation. *Biogeosciences*, 14(12):2903–2928.

Jacob, D. J., Turner, A. J., Maasakkers, J. D., Sheng, J., Sun, K., Liu, X., Chance, K., Aben, I., McKeever, J., and Frankenberg, C. (2016). Satellite observations of atmospheric methane and their value for quantifying methane emissions. *Atmospheric Chemistry and Physics*, 16(22):14371–14396.

Jiang, M., Liu, L., Liu, X., and Zou, C. (2025). Stronger response of vegetation photosynthesis to climate change than greenness in pan-Arctic region: First evidence from SIF satellite observations. *Ecological Informatics*, 90:103312.

Joiner, J., Guanter, L., Lindstrot, R., Voigt, M., Vasilkov, A. P., Middleton, E. M., Huemmrich, K. F., Yoshida, Y., and Frankenberg, C. (2013). Global monitoring of terrestrial chlorophyll fluorescence from moderate-spectral-resolution near-infrared satellite measurements: Methodology, simulations, and application to GOME-2. *Atmospheric Measurement Techniques*, 6(10):2803–2823.

Joiner, J., Yoshida, Y., Guanter, L., and Middleton, E. M. (2016). New methods for the retrieval of chlorophyll red fluorescence from hyperspectral satellite instruments: Simulations and application to GOME-2 and SCIAMACHY. *Atmospheric Measurement Techniques*, 9(8):3939–3967.

Joiner, J., Yoshida, Y., Köehler, P., Campbell, P., Frankenberg, C., van der Tol, C., Yang, P., Parazoo, N., Guanter, L., and Sun, Y. (2020). Systematic Orbital Geometry-Dependent Variations in Satellite Solar-Induced Fluorescence (SIF) Retrievals. *Remote Sensing*, 12(15):2346.

Joiner, J., Yoshida, Y., Koehler, P., Frankenberg, C., and Parazoo, N. (2023). SIF-ESDRL2 Daily Solar-Induced Fluorescence (SIF) from MetOp-A GOME-2, 2007-2018, V2.

Joiner, J., Yoshida, Y., Vasilkov, A., Schaefer, K., Jung, M., Guanter, L., Zhang, Y., Garrity, S., Middleton, E., Huemmrich, K., Gu, L., and Belelli Marchesini, L. (2014). The seasonal cycle of satellite chlorophyll fluorescence observations and its relationship to vegetation phenology and ecosystem atmosphere carbon exchange. *Remote Sensing of Environment*, 152:375–391.

Joiner, J., Yoshida, Y., Vasilkov, A. P., Middleton, E. M., Campbell, P. K. E., Yoshida, Y., Kuze, A., and Corp, L. A. (2012). Filling-in of near-infrared solar lines by terrestrial fluorescence and other geophysical effects: Simulations and space-based observations from SCIAMACHY and GOSAT. *Atmospheric Measurement Techniques*, 5(4):809–829.

Joiner, J., Yoshida, Y., Vasilkov, A. P., Yoshida, Y., Corp, L. A., and Middleton, E. M. (2011). First observations of global and seasonal terrestrial chlorophyll fluorescence from space. *Biogeosciences*, 8(3):637–651.

Joiner, J., Yoshida, Y., Zhang, Y., Duveiller, G., Jung, M., Lyapustin, A., Wang, Y., and Tucker, C. J. (2018). Estimation of Terrestrial Global Gross Primary Production (GPP) with Satellite Data-Driven Models and Eddy Covariance Flux Data. *Remote Sensing*, 10(9):1346.

Jonard, F., De Cannière, S., Brüggemann, N., Gentine, P., Short Gianotti, D., Lobet, G., Miralles, D., Montzka, C., Pagán, B., Rascher, U., and Vereecken, H. (2020). Value of sun-induced chlorophyll fluorescence for quantifying hydrological states and fluxes: Current status and challenges. *Agricultural and Forest Meteorology*, 291:108088.

Joshi, N., Mitchard, E. T., Woo, N., Torres, J., Moll-Rocek, J., Ehammer, A., Collins, M., Jepsen, M. R., and Fensholt, R. (2015). Mapping dynamics of deforestation and forest degradation in tropical forests using radar satellite data. *Environmental Research Letters*, 10(3):034014.

Jung, M., Koirala, S., Weber, U., Ichii, K., Gans, F., Camps-Valls, G., Papale, D., Schwalm, C., Tramontana, G., and Reichstein, M. (2019). The FLUXCOM ensemble of global land-atmosphere energy fluxes. *Scientific Data*, 6(1):74.

Kalaji, H. M., Schansker, G., Brestic, M., Bussotti, F., Calatayud, A., Ferroni, L., Goltsev, V., Guidi, L., Jajoo, A., Li, P., Losciale, P., Mishra, V. K., Misra, A. N., Nebauer, S. G., Pancaldi, S., Penella, C., Pollastrini, M.,

Suresh, K., Tambussi, E., Yanniccari, M., Zivcak, M., Cetner, M. D., Samborska, I. A., Stirbet, A., Olsovska, K., Kunderlikova, K., Shelonzek, H., Rusinowski, S., and Bąba, W. (2017). Frequently asked questions about chlorophyll fluorescence, the sequel. *Photosynthesis Research*, 132(1):13–66.

Karki, L., Lieu, J., Xylia, M., Laub, M., Ismangil, D., Virla, L., Rahn, E., Bilbao, B. A., Indriani, S. N., Martin Gallego, P., Suleiman, A. K. A., Schaldch, R., Takama, T., Marques Da Silva, J. R., and Johnson, F. X. (2023). Potentials and barriers to land-based mitigation technologies and practices (LMTs)—a review. *Environmental Research Letters*, 18(9):093003.

Khosravi, N., Vountas, M., Rozanov, V. V., Bracher, A., Wolanin, A., and Burrows, J. P. (2015). Retrieval of Terrestrial Plant Fluorescence Based on the In-Filling of Far-Red Fraunhofer Lines Using SCIAMACHY Observations. *Frontiers in Environmental Science*, 3.

Klaes, K. D., Schlussel, P., Munro, R., Luntama, J.-P., Engeln, A. V., Ackermann, J., and Schmetz, J. (2007). An Introduction to the EUMETSAT Polar system. *Bulletin of the American Meteorological Society*, pages 1085–1096.

Köhler, P., Behrenfeld, M. J., Landgraf, J., Joiner, J., Magney, T. S., and Frankenberg, C. (2020). Global Retrievals of Solar-Induced Chlorophyll Fluorescence at Red Wavelengths With TROPOMI. *Geophysical Research Letters*, 47(15):e2020GL087541.

Köhler, P., Frankenberg, C., Magney, T. S., Guanter, L., Joiner, J., and Landgraf, J. (2018). Global Retrievals of Solar-Induced Chlorophyll Fluorescence With TROPOMI: First Results and Intersensor Comparison to OCO-2. *Geophysical Research Letters*, 45(19):10,456–10,463.

Köhler, P., Guanter, L., and Joiner, J. (2015). A linear method for the retrieval of sun-induced chlorophyll fluorescence from GOME-2 and SCIAMACHY data. *Atmospheric Measurement Techniques*, 8(6):2589–2608.

Kong, Z.-H., Stringer, L., Paavola, J., and Lu, Q. (2021). Situating China in the Global Effort to Combat Desertification. *Land*, 10(7):702.

Kooreman, M., Boersma, K., van Schaik, E., van Versendaal, R., Cacciari, A., and Tuinder, O. (2020). SIFTER sun-induced vegetation fluorescence data from GOME-2A (Version 2.0).

Koren, G., Van Schaik, E., Araújo, A. C., Boersma, K. F., Gärtner, A., Killaars, L., Kooreman, M. L., Kruijt, B., Van Der Laan-Luijkx, I. T., Von Randow, C., Smith, N. E., and Peters, W. (2018). Widespread reduction in sun-induced fluorescence from the Amazon during the 2015/2016 El Niño. *Philosophical Transactions of the Royal Society B: Biological Sciences*, 373(1760):20170408.

Krijger, J. M., Snel, R., Van Harten, G., Rietjens, J. H. H., and Aben, I. (2014). Mirror contamination in space I: Mirror modelling. *Atmospheric Measurement Techniques*, 7(10):3387–3398.

Lara, C., Saldías, G., Paredes, A., Cazelles, B., and Broitman, B. (2018). Temporal Variability of MODIS Phenological Indices in the Temperate Rainforest of Northern Patagonia. *Remote Sensing*, 10(6):956.

Lasslop, G., Reichstein, M., Papale, D., Richardson, A. D., Arneth, A., Barr, A., Stoy, P., and Wohlfahrt, G. (2010). Separation of net ecosystem exchange into assimilation and respiration using a light response curve approach: Critical issues and global evaluation. *Global Change Biology*, 16(1):187–208.

Leite-Filho, A. T., Soares-Filho, B. S., Davis, J. L., Abrahão, G. M., and Börner, J. (2021). Deforestation reduces rainfall and agricultural revenues in the Brazilian Amazon. *Nature Communications*, 12(1):2591.

Lemma, B., Williams, S., and Paustian, K. (2021). Long term soil carbon sequestration potential of smallholder croplands in southern Ethiopia with DAYCENT model. *Journal of Environmental Management*, 294:112893.

Li, S., Yang, S., Liu, X., Liu, Y., and Shi, M. (2015). NDVI-Based Analysis on the Influence of Climate Change and Human Activities on Vegetation Restoration in the Shaanxi-Gansu-Ningxia Region, Central China. *Remote Sensing*, 7(9):11163–11182.

Li, W., Pacheco-Labrador, J., Migliavacca, M., Miralles, D., Hoek Van Dijke, A., Reichstein, M., Forkel, M., Zhang, W., Frankenberg, C., Panwar, A., Zhang, Q., Weber, U., Gentine, P., and Orth, R. (2023). Widespread and complex drought effects on vegetation physiology inferred from space. *Nature Communications*, 14(1):4640.

Li, X. and Xiao, J. (2020). Global climatic controls on interannual variability of ecosystem productivity: Similarities and differences inferred from solar-induced chlorophyll fluorescence and enhanced vegetation index.

Agricultural and Forest Meteorology, 288–289:108018.

Li, X. and Xiao, J. (2022). TROPOMI observations allow for robust exploration of the relationship between solar-induced chlorophyll fluorescence and terrestrial gross primary production. *Remote Sensing of Environment*, 268:112748.

Liang, S. and Wang, J. (2020). Estimate of vegetation production of terrestrial ecosystem. In *Advanced Remote Sensing*, pages 581–620. Elsevier.

Lin, X., Niu, J., Berndtsson, R., Yu, X., Zhang, L., and Chen, X. (2020). NDVI Dynamics and Its Response to Climate Change and Reforestation in Northern China. *Remote Sensing*, 12(24):4138.

Lindenmayer, D. B. and Taylor, C. (2020). New spatial analyses of Australian wildfires highlight the need for new fire, resource, and conservation policies. *Proceedings of the National Academy of Sciences*, 117(22):12481–12485.

Liu, L., Guan, L., and Liu, X. (2017). Directly estimating diurnal changes in GPP for C3 and C4 crops using far-red sun-induced chlorophyll fluorescence. *Agricultural and Forest Meteorology*, 232:1–9.

Liu, L., Liu, X., Wang, Z., and Zhang, B. (2016). Measurement and Analysis of Bidirectional SIF Emissions in Wheat Canopies. *IEEE Transactions on Geoscience and Remote Sensing*, 54(5):2640–2651.

Liu, Y., Li, Z., Chen, Y., Jin, L., Li, F., Wang, X., Long, Y., Liu, C., and Kayumba, P. M. (2025). Global greening drives significant soil moisture loss. *Communications Earth & Environment*, 6(1):600.

Liu, Y., You, C., Zhang, Y., Chen, S., Zhang, Z., Li, J., and Wu, Y. (2021). Resistance and resilience of grasslands to drought detected by SIF in inner Mongolia, China. *Agricultural and Forest Meteorology*, 308–309:108567.

Ludewig, A., Kleipool, Q., Bartstra, R., Landzaat, R., Leloux, J., Loots, E., Meijering, P., Van Der Plas, E., Rozemeijer, N., Vonk, F., and Veefkind, P. (2020). In-flight calibration results of the TROPOMI payload on board the Sentinel-5 Precursor satellite. *Atmospheric Measurement Techniques*, 13(7):3561–3580.

Lv, Y., Liu, J., He, W., Zhou, Y., Tu Nguyen, N., Bi, W., Wei, X., and Chen, H. (2023). How well do light-use efficiency models capture large-scale drought impacts on vegetation productivity compared with data-driven estimates? *Ecological Indicators*, 146:109739.

Lymburner, L., Tan, P., McIntyre, A., Tankapann, M., and Sixsmith, J. (2015). Dynamic Land Cover Dataset Version 2.1.

MacBean, N., Maignan, F., Bacour, C., Lewis, P., Peylin, P., Guanter, L., Köhler, P., Gómez-Dans, J., and Disney, M. (2018). Strong constraint on modelled global carbon uptake using solar-induced chlorophyll fluorescence data. *Scientific Reports*, 8(1):1973.

Madani, N., Parazoo, N. C., Kimball, J. S., Reichle, R. H., Chatterjee, A., Watts, J. D., Saatchi, S., Liu, Z., Endsley, A., Tagesson, T., Rogers, B. M., Xu, L., Wang, J. A., Magney, T., and Miller, C. E. (2021). The Impacts of Climate and Wildfire on Ecosystem Gross Primary Productivity in Alaska. *Journal of Geophysical Research: Biogeosciences*, 126(6):e2020JG006078.

Magney, T. S., Barnes, M. L., and Yang, X. (2020). On the Covariation of Chlorophyll Fluorescence and Photosynthesis Across Scales. *Geophysical Research Letters*, 47(23):e2020GL091098.

Magney, T. S., Bowling, D. R., Logan, B. A., Grossmann, K., Stutz, J., Blanken, P. D., Burns, S. P., Cheng, R., Garcia, M. A., Köhler, P., Lopez, S., Parazoo, N. C., Raczka, B., Schimel, D., and Frankenberg, C. (2019). Mechanistic evidence for tracking the seasonality of photosynthesis with solar-induced fluorescence. *Proceedings of the National Academy of Sciences*, 116(24):11640–11645.

Marrs, J. K., Reblin, J. S., Logan, B. A., Allen, D. W., Reinmann, A. B., Bombard, D. M., Tabachnik, D., and Hutyra, L. R. (2020). Solar-Induced Fluorescence Does Not Track Photosynthetic Carbon Assimilation Following Induced Stomatal Closure. *Geophysical Research Letters*, 47(15):e2020GL087956.

Martini, D., Sakowska, K., Wohlfahrt, G., Pacheco-Labrador, J., Van Der Tol, C., Porcar-Castell, A., Magney, T. S., Carrara, A., Colombo, R., El-Madany, T. S., Gonzalez-Cascon, R., Martín, M. P., Julitta, T., Moreno, G., Rascher, U., Reichstein, M., Rossini, M., and Migliavacca, M. (2022). Heatwave breaks down the linearity between sun-induced fluorescence and gross primary production. *New Phytologist*, 233(6):2415–2428.

Meier, R., Schwaab, J., Seneviratne, S. I., Sprenger, M., Lewis, E., and Davin, E. L. (2021). Empirical estimate of forestation-induced precipitation changes in Europe. *Nature Geoscience*, 14(7):473–478.

Mengistu, A. G., Mengistu Tsidu, G., Koren, G., Kooreman, M. L., Boersma, K. F., Tagesson, T., Ardö, J., Nouvellon, Y., and Peters, W. (2021). Sun-induced fluorescence and near-infrared reflectance of vegetation track the seasonal dynamics of gross primary production over Africa. *Biogeosciences*, 18(9):2843–2857.

Meroni, M., Rossini, M., Guanter, L., Alonso, L., Rascher, U., Colombo, R., and Moreno, J. (2009). Remote sensing of solar-induced chlorophyll fluorescence: Review of methods and applications. *Remote Sensing of Environment*, 113(10):2037–2051.

Moene, A. F. and van Dam, J. C. (2014). *Transport in the Atmosphere-Vegetation-Soil Continuum*. Cambridge University Press, Cambridge.

Mohammed, G. H., Colombo, R., Middleton, E. M., Rascher, U., Van Der Tol, C., Nedbal, L., Goulas, Y., Pérez-Priego, O., Damm, A., Meroni, M., Joiner, J., Cogliati, S., Verhoef, W., Malenovský, Z., Gastellu-Etchegorry, J.-P., Miller, J. R., Guanter, L., Moreno, J., Moya, I., Berry, J. A., Frankenberg, C., and Zarco-Tejada, P. J. (2019). Remote sensing of solar-induced chlorophyll fluorescence (SIF) in vegetation: 50 years of progress. *Remote Sensing of Environment*, 231:111177.

Monteith, J. L. (1972). Solar Radiation and Productivity in Tropical Ecosystems. *The Journal of Applied Ecology*, 9(3):747.

Morata, M., Siegmann, B., García-Soria, J. L., Rivera-Caicedo, J. P., and Verrelst, J. (2025). On the potential of principal component analysis for the reconstruction of full-spectrum SIF emission and emulated airborne-to-satellite upscaling. *Remote Sensing of Environment*, 328:114865.

Moreno, J. F., Goulas, Y., Huth, A., Middleton, E., Miglietta, F., Mohammed, G., Nedbal, L., Rascher, U., Verhoef, W., and Drusch, M. (2016). Very high spectral resolution imaging spectroscopy: The Fluorescence Explorer (FLEX) mission. In *2016 IEEE International Geoscience and Remote Sensing Symposium (IGARSS)*, pages 264–267, Beijing, China. IEEE.

Mota, B., Gobron, N., Morgan, O., Cappucci, F., Lanconelli, C., and Robustelli, M. (2021). Cross-ECV consistency at global scale: LAI and FAPAR changes. *Remote Sensing of Environment*, 263:112561.

Munro, R., Eisinger, M., Anderson, C., Callies, J., Carpaccioli, E., Lang, R., Lefebvre, A., Livschitz, Y., and Albinana, A. P. (2006). *GOME-2 on MetOp*. Proc. of The 2006 EUMETSAT Meteorological Satellite Conference, Helsinki, Finland.

Munro, R., Lang, R., Klaes, D., Poli, G., Retscher, C., Lindstrot, R., Huckle, R., Lacan, A., Grzegorski, M., Holdak, A., Kokhanovsky, A., Livschitz, J., and Eisinger, M. (2016). The GOME-2 instrument on the Metop series of satellites: Instrument design, calibration, and level 1 data processing – an overview. *Atmospheric Measurement Techniques*, 9(3):1279–1301.

Myneni, R. B., Hall, F. G., Sellers, P. J., and Marshak, A. L. (1995). The interpretation of spectral vegetation indexes. *IEEE Transactions on Geoscience and Remote Sensing*, 33(2):481–486.

Nanzad, L., Zhang, J., Tuvdendorj, B., Nabil, M., Zhang, S., and Bai, Y. (2019). NDVI anomaly for drought monitoring and its correlation with climate factors over Mongolia from 2000 to 2016. *Journal of Arid Environments*, 164:69–77.

Nelson, J. A., Walther, S., Gans, F., Kraft, B., Weber, U., Novick, K., Buchmann, N., Migliavacca, M., Wohlfahrt, G., Šigut, L., Ibrom, A., Papale, D., Göckede, M., Duveiller, G., Knohl, A., Hörtnagl, L., Scott, R. L., Zhang, W., Hamdi, Z. M., Reichstein, M., Aranda-Barranco, S., Ardö, J., Op De Beeck, M., Billdesbach, D., Bowling, D., Bracho, R., Brümmer, C., Camps-Valls, G., Chen, S., Cleverly, J. R., Desai, A., Dong, G., El-Madany, T. S., Euskirchen, E. S., Feigenwinter, I., Galvagno, M., Gerosa, G., Gielen, B., Goded, I., Goslee, S., Gough, C. M., Heinesch, B., Ichii, K., Jackowicz-Korczynski, M. A., Klosterhalfen, A., Knox, S., Kobayashi, H., Kohonen, K.-M., Korkiakoski, M., Mammarella, I., Mana, G., Marzuoli, R., Matamala, R., Metzger, S., Montagnani, L., Nicolini, G., O'Halloran, T., Ourcival, J.-M., Peichl, M., Pendall, E., Ruiz Reverter, B., Roland, M., Sabbatini, S., Sachs, T., Schmidt, M., Schwalm, C. R., Shekhar, A., Silberstein, R., Silveira, M. L., Spano, D., Tagesson, T., Tramontana, G., Trotta, C., Turco, F., Vesala, T., Vincke, C., Vitale, D., Vivoni, E. R., Wang, Y., Woodgate, W., Yepez, E. A., Zhang, J., Zona, D., and Jung, M. (2024). X-BASE: The first terrestrial carbon and water flux products from an extended data-driven scaling framework, FLUXCOM-X.

Noël, S., Buchwitz, M., Hilker, M., Reuter, M., Weimer, M., Bovensmann, H., Burrows, J. P., Bösch, H., and Lang, R. (2024). Greenhouse gas retrievals for the CO2M mission using the FOCAL method: First performance

estimates. *Atmospheric Measurement Techniques*, 17(8):2317–2334.

Ollinger, S. V. (2011). Sources of variability in canopy reflectance and the convergent properties of plants. *New Phytologist*, 189(2):375–394.

Omari, K., White, H. P., Staenz, K., and King (2013). Retrieval of Forest Canopy Parameters by Inversion of the PROFLAIR Leaf-Canopy Reflectance Model Using the LUT Approach. *IEEE Journal of Selected Topics in Applied Earth Observations and Remote Sensing*, 6(2):715–723.

Oshio, H., Yoshida, Y., and Matsunaga, T. (2019). On the zero-level offset in the GOSAT TANSO-FTS O_2 A band and the quality of solar-induced chlorophyll fluorescence (SIF): Comparison of SIF between GOSAT and OCO-2. *Atmospheric Measurement Techniques*, 12(12):6721–6735.

Pacheco-Labrador, J., Hueni, A., Mihai, L., Sakowska, K., Julitta, T., Kuusk, J., Sporea, D., Alonso, L., Burkart, A., Cendrero-Mateo, M. P., Aasen, H., Goulas, Y., and Mac Arthur, A. (2019). Sun-Induced Chlorophyll Fluorescence I: Instrumental Considerations for Proximal Spectroradiometers. *Remote Sensing*, 11(8):960.

Pan, Z., Huang, J., Zhou, Q., Wang, L., Cheng, Y., Zhang, H., Blackburn, G. A., Yan, J., and Liu, J. (2015). Mapping crop phenology using NDVI time-series derived from HJ-1 A/B data. *International Journal of Applied Earth Observation and Geoinformation*, 34:188–197.

Pang, G., Wang, X., and Yang, M. (2017). Using the NDVI to identify variations in, and responses of, vegetation to climate change on the Tibetan Plateau from 1982 to 2012. *Quaternary International*, 444:87–96.

Parazoo, N. C., Frankenberg, C., Köhler, P., Joiner, J., Yoshida, Y., Magney, T., Sun, Y., and Yadav, V. (2019). Towards a Harmonized Long-Term Spaceborne Record of Far-Red Solar-Induced Fluorescence. *Journal of Geophysical Research: Biogeosciences*, 124(8):2518–2539.

Pato, M., Alonso, K., Buffat, J., Auer, S., Carmona, E., Maier, S., Müller, R., Rademske, P., Rascher, U., and Scharr, H. (2025). Simulation framework for solar-induced fluorescence retrieval and application to DESIS and HyPlant. *Remote Sensing of Environment*, 330:114944.

Peltoniemi, J. I., Kaasalainen, S., Näränen, J., Rautiainen, M., Stenberg, P., Smolander, H., Smolander, S., and Voipio, P. (2005). BRDF measurement of understory vegetation in pine forests: Dwarf shrubs, lichen, and moss. *Remote Sensing of Environment*, 94(3):343–354.

Peng, B., Guan, K., Zhou, W., Jiang, C., Frankenberg, C., Sun, Y., He, L., and Köhler, P. (2020). Assessing the benefit of satellite-based Solar-Induced Chlorophyll Fluorescence in crop yield prediction. *International Journal of Applied Earth Observation and Geoinformation*, 90:102126.

Petäjä, T., Tabakova, K., Manninen, A., Ezhova, E., O'Connor, E., Moisseev, D., Sinclair, V. A., Backman, J., Levula, J., Luoma, K., Virkkula, A., Paramonov, M., Räty, M., Äijälä, M., Heikkinen, L., Ehn, M., Sipilä, M., Yli-Juuti, T., Virtanen, A., Ritsche, M., Hickmon, N., Pulik, G., Rosenfeld, D., Worsnop, D. R., Bäck, J., Kulmala, M., and Kerminen, V.-M. (2022). Influence of biogenic emissions from boreal forests on aerosol–cloud interactions. *Nature Geoscience*, 15(1):42–47.

Piao, S., Liu, Q., Chen, A., Janssens, I. A., Fu, Y., Dai, J., Liu, L., Lian, X., Shen, M., and Zhu, X. (2019). Plant phenology and global climate change: Current progresses and challenges. *Global Change Biology*, 25(6):1922–1940.

Pierrat, Z., Magney, T., Parazoo, N. C., Grossmann, K., Bowling, D. R., Seibt, U., Johnson, B., Helgason, W., Barr, A., Bortnik, J., Norton, A., Maguire, A., Frankenberg, C., and Stutz, J. (2022). Diurnal and Seasonal Dynamics of Solar-Induced Chlorophyll Fluorescence, Vegetation Indices, and Gross Primary Productivity in the Boreal Forest. *Journal of Geophysical Research: Biogeosciences*, 127(2):e2021JG006588.

Porcar-Castell, A., Malenovský, Z., Magney, T., Van Wittenberghe, S., Fernández-Marín, B., Maignan, F., Zhang, Y., Maseyk, K., Atherton, J., Albert, L. P., Robson, T. M., Zhao, F., Garcia-Plazaola, J.-I., Ensminger, I., Rajewicz, P. A., Grebe, S., Tikkanen, M., Kellner, J. R., Ihalainen, J. A., Rascher, U., and Logan, B. (2021). Chlorophyll a fluorescence illuminates a path connecting plant molecular biology to Earth-system science. *Nature Plants*, 7(8):998–1009.

Porcar-Castell, A., Tyystjärvi, E., Atherton, J., Van Der Tol, C., Flexas, J., Pfündel, E. E., Moreno, J., Frankenberg, C., and Berry, J. A. (2014). Linking chlorophyll a fluorescence to photosynthesis for remote sensing applications: Mechanisms and challenges. *Journal of Experimental Botany*, 65(15):4065–4095.

Qiu, R., Li, X., Han, G., Xiao, J., Ma, X., and Gong, W. (2022). Monitoring drought impacts on crop productivity of the U.S. Midwest with solar-induced fluorescence: GOSIF outperforms GOME-2 SIF and MODIS NDVI, EVI, and NIRv. *Agricultural and Forest Meteorology*, 323:109038.

Qu, S., Wang, L., Lin, A., Yu, D., Yuan, M., and Li, C. (2020). Distinguishing the impacts of climate change and anthropogenic factors on vegetation dynamics in the Yangtze River Basin, China. *Ecological Indicators*, 108:105724.

Randerson, J. T., Li, Y., Fu, W., Primeau, F., Kim, J. E., Mu, M., Hoffman, F. M., Trugman, A. T., Yang, L., Wu, C., Wang, J. A., Anderegg, W. R. L., Baccini, A., Friedl, M. A., Saatchi, S. S., Denning, A. S., and Goulden, M. L. (2025). The weak land carbon sink hypothesis. *Science Advances*.

Rascher, U., Agati, G., Alonso, L., Cecchi, G., Champagne, S., Colombo, R., Damm, A., Daumard, F., de Miguel, E., Fernandez, G., Franch, B., Franke, J., Gerbig, C., Gioli, B., Gomez, J. A., Goulas, Y., Guanter, L., Gutierrez-de-la-Camara, O., Hamdi, K., Hostert, P., Jimenez, M., Kosvancova, M., Lognoli, D., Meroni, M., Miglietta, F., Moersch, A., Moreno, J., Moya, I., Neininger, B., Okujeni, A., Ounis, A., Palombi, L., Raimondi, V., Schickling, A., Sobrino, J. A., Stellmes, M., Toci, G., Toscano, P., Udelhoven, T., and Zaldei, A. (2009). CEFLES2: The remote sensing component to quantify photosynthetic efficiency from the leaf to the region by measuring sun-induced fluorescence in the oxygen absorption bands.

Rascher, U., Alonso, L., Burkart, A., Cilia, C., Cogliati, S., Colombo, R., Damm, A., Drusch, M., Guanter, L., Hanus, J., Hyvärinen, T., Julitta, T., Jussila, J., Kataja, K., Kokkalis, P., Kraft, S., Kraska, T., Matveeva, M., Moreno, J., Muller, O., Panigada, C., Pikl, M., Pinto, F., Prey, L., Pude, R., Rossini, M., Schickling, A., Schurr, U., Schüttemeyer, D., Verrelst, J., and Zemek, F. (2015). Sun-induced fluorescence – a new probe of photosynthesis: First maps from the imaging spectrometer *HyPlant*. *Global Change Biology*, 21(12):4673–4684.

Robinson, N., Allred, B., Jones, M., Moreno, A., Kimball, J., Naugle, D., Erickson, T., and Richardson, A. (2017). A Dynamic Landsat Derived Normalized Difference Vegetation Index (NDVI) Product for the Conterminous United States. *Remote Sensing*, 9(8):863.

Rogelj, J., Shindell, D., Jiang, K., Fifita, S., Forster, P., Ginzburg, V., Handa, C., Kheshgi, H., Kobayashi, S., Kriegler, E., et al. (2018). Mitigation pathways compatible with 1.5 C in the context of sustainable development. In *Global Warming of 1.5 C*, pages 93–174. Intergovernmental Panel on Climate Change.

Rouse, J. W., Haas, R. H., Deering, D. W., Schell, J. A., and Harlan, J. C. (1974). ROUSE JR, John W., et al. Monitoring the vernal advancement and retrogradation (green wave effect) of natural vegetation. Technical Report E75-10354.

Ruddiman, W. F. (2014). *Earth's Climate: Past and Future*. W. H. Freeman and Company, New York, third edition edition.

Sabater, N., Kolmonen, P., Van Wittenberghe, S., Arola, A., and Moreno, J. (2021). Challenges in the atmospheric characterization for the retrieval of spectrally resolved fluorescence and PRI region dynamics from space. *Remote Sensing of Environment*, 254:112226.

Sabater, N., Vicent, J., Alonso, L., Verrelst, J., Middleton, E. M., Porcar-Castell, A., and Moreno, J. (2018). Compensation of Oxygen Transmittance Effects for Proximal Sensing Retrieval of Canopy–Leaving Sun–Induced Chlorophyll Fluorescence. *Remote Sensing*, 10(10):1551.

Sanders, A. F. J., Verstraeten, W. W., Kooreman, M. L., Van Leth, T. C., Beringer, J., and Joiner, J. (2016). Spaceborne Sun-Induced Vegetation Fluorescence Time Series from 2007 to 2015 Evaluated with Australian Flux Tower Measurements. *Remote Sensing*, 8(11):895.

Sanghavi, S., Frankenberg, C., Nelson, R. R., O'Dell, C. W., Rosenberg, R., and Joiner, J. (2025). Impact of Raman Scattering on SIF Retrievals From Hyperspectral Satellite Observations. *Geophysical Research Letters*, 52(15):e2024GL112777.

Schimel, D., Schneider, F. D., and JPL Carbon and Ecosystem Participants (2019). Flux towers in the sky: Global ecology from space. *New Phytologist*, 224(2):570–584.

Schimel, D., Stephens, B. B., and Fisher, J. B. (2015). Effect of increasing CO $_2$ on the terrestrial carbon cycle. *Proceedings of the National Academy of Sciences*, 112(2):436–441.

Schneider, U., Finger, P., Meyer-Christoffer, A., Rustemeier, E., Ziese, M., and Becker, A. (2017). Evaluat-

ing the Hydrological Cycle over Land Using the Newly-Corrected Precipitation Climatology from the Global Precipitation Climatology Centre (GPCC). *Atmosphere*, 8(3):52.

Schreiber, M., Rensing, S. A., and Gould, S. B. (2022). The greening ashore. *Trends in Plant Science*, 27(9):847–857.

Schurgers, G., Ahlström, A., Arneth, A., Pugh, T. A. M., and Smith, B. (2018). Climate Sensitivity Controls Uncertainty in Future Terrestrial Carbon Sink. *Geophysical Research Letters*, 45(9):4329–4336.

Seidl, R., Thom, D., Kautz, M., Martin-Benito, D., Peltoniemi, M., Vacchiano, G., Wild, J., Ascoli, D., Petr, M., Honkaniemi, J., Lexer, M. J., Trotsiuk, V., Mairota, P., Svoboda, M., Fabrika, M., Nagel, T. A., and Reyer, C. P. O. (2017). Forest disturbances under climate change. *Nature Climate Change*, 7(6):395–402.

Seneviratne, S., Zhang, X., Adnan, M., Badi, W., Dereczynski, C., Luca, A., Ghosh, S., Iskandar, I., Kossin, J., Lewis, S., Otto, F., Pinto, I., Satoh, M., Vicente-Serrano, S., Wehner, M., Zhou, B., and Allan, R. (2023). Weather and Climate Extreme Events in a Changing Climate. In *Climate Change 2021 – The Physical Science Basis*, pages 1513–1766. Cambridge University Press, 1 edition.

Seo, B., Lee, J., Lee, K.-D., Hong, S., and Kang, S. (2019). Improving remotely-sensed crop monitoring by NDVI-based crop phenology estimators for corn and soybeans in Iowa and Illinois, USA. *Field Crops Research*, 238:113–128.

Shi, S., Shi, Z., Qu, F., Gong, W., Xu, L., and Liu, C. (2025). Analyzing canopy structure effects based on LiDAR for GPP-SIF relationship and GPP estimation. *Frontiers in Plant Science*, 16:1561826.

Siddans, R., Latter, B., Kerridge, B., Latter, B., Smeets, J., and Otter, G. (2012). Analysis of gome-2 slit function measurements algorithm theoretical basis document. Technical Report version 3.0.

Siegmann, B., Alonso, L., Celesti, M., Cogliati, S., Colombo, R., Damm, A., Douglas, S., Guanter, L., Hanuš, J., Kataja, K., Kraska, T., Matveeva, M., Moreno, J., Muller, O., Pikl, M., Pinto, F., Quirós Vargas, J., Rademske, P., Rodriguez-Morene, F., Sabater, N., Schickling, A., Schüttemeyer, D., Zemek, F., and Rascher, U. (2019). The High-Performance Airborne Imaging Spectrometer HyPlant—From Raw Images to Top-of-Canopy Reflectance and Fluorescence Products: Introduction of an Automatized Processing Chain. *Remote Sensing*, 11(23):2760.

Sillman, S. (1999). The relation between ozone, NOx and hydrocarbons in urban and polluted rural environments. *Atmospheric Environment*, 33(12):1821–1845.

Sloat, L. L., Lin, M., Butler, E. E., Johnson, D., Holbrook, N. M., Huybers, P. J., Lee, J.-E., and Mueller, N. D. (2021). Evaluating the benefits of chlorophyll fluorescence for in-season crop productivity forecasting. *Remote Sensing of Environment*, 260:112478.

Smith, W. K., Biederman, J. A., Scott, R. L., Moore, D. J. P., He, M., Kimball, J. S., Yan, D., Hudson, A., Barnes, M. L., MacBean, N., Fox, A. M., and Litvak, M. E. (2018a). Chlorophyll Fluorescence Better Captures Seasonal and Interannual Gross Primary Productivity Dynamics Across Dryland Ecosystems of Southwestern North America. *Geophysical Research Letters*, 45(2):748–757.

Smith, W. K., Biederman, J. A., Scott, R. L., Moore, D. J. P., He, M., Kimball, J. S., Yan, D., Hudson, A., Barnes, M. L., MacBean, N., Fox, A. M., and Litvak, M. E. (2018b). Chlorophyll Fluorescence Better Captures Seasonal and Interannual Gross Primary Productivity Dynamics Across Dryland Ecosystems of Southwestern North America. *Geophysical Research Letters*, 45(2):748–757.

Smith, W. K., Dannenberg, M. P., Yan, D., Herrmann, S., Barnes, M. L., Barron-Gafford, G. A., Biederman, J. A., Ferrenberg, S., Fox, A. M., Hudson, A., Knowles, J. F., MacBean, N., Moore, D. J., Nagler, P. L., Reed, S. C., Rutherford, W. A., Scott, R. L., Wang, X., and Yang, J. (2019). Remote sensing of dryland ecosystem structure and function: Progress, challenges, and opportunities. *Remote Sensing of Environment*, 233:111401.

Smith, W. K., Fox, A. M., MacBean, N., Moore, D. J. P., and Parazoo, N. C. (2020). Constraining estimates of terrestrial carbon uptake: New opportunities using long-term satellite observations and data assimilation. *New Phytologist*, 225(1):105–112.

Song, L., Guanter, L., Guan, K., You, L., Huete, A., Ju, W., and Zhang, Y. (2018). Satellite sun-induced chlorophyll fluorescence detects early response of winter wheat to heat stress in the Indian Indo-Gangetic Plains. *Global Change Biology*, 24(9):4023–4037.

Song, Y., Wang, J., Yu, Q., and Huang, J. (2020). Using MODIS LAI Data to Monitor Spatio-Temporal Changes

of Winter Wheat Phenology in Response to Climate Warming. *Remote Sensing*, 12(5):786.

Stol, J. and Kitchen, M. (2022). Tumbarumba Flux Data Release 2022{_}v1 (Version 1.0) [Dataset].

Sun, H., Wang, J., Xiong, J., Bian, J., Jin, H., Cheng, W., and Li, A. (2021). Vegetation Change and Its Response to Climate Change in Yunnan Province, China. *Advances in Meteorology*, 2021:1–20.

Sun, W., Song, X., Mu, X., Gao, P., Wang, F., and Zhao, G. (2015). Spatiotemporal vegetation cover variations associated with climate change and ecological restoration in the Loess Plateau. *Agricultural and Forest Meteorology*, 209–210:87–99.

Sun, Y., Frankenberg, C., Jung, M., Joiner, J., Guanter, L., Köhler, P., and Magney, T. (2018). Overview of Solar-Induced chlorophyll Fluorescence (SIF) from the Orbiting Carbon Observatory-2: Retrieval, cross-mission comparison, and global monitoring for GPP. *Remote Sensing of Environment*, 209:808–823.

Sun, Y., Frankenberg, C., Wood, J. D., Schimel, D. S., Jung, M., Guanter, L., Drewry, D. T., Verma, M., Porcar-Castell, A., Griffis, T. J., Gu, L., Magney, T. S., Köhler, P., Evans, B., and Yuen, K. (2017). OCO-2 advances photosynthesis observation from space via solar-induced chlorophyll fluorescence. *Science*, 358(6360):eaam5747.

Sun, Y., Gu, L., Wen, J., van der Tol, C., Porcar-Castell, A., Joiner, J., Chang, C. Y., Magney, T., Wang, L., Hu, L., Rascher, U., Zarco-Tejada, P., Barrett, C. B., Lai, J., Han, J., and Luo, Z. (2023). From remotely sensed solar-induced chlorophyll fluorescence to ecosystem structure, function, and service: Part I—Harnessing theory. *Global Change Biology*, 29(11):2926–2952.

Sutanto, S. J., Blyth, E. M., Wenninger, J., and Hoffmann, G. (2014). HESS Opinions "A perspective on isotope versus non-isotope approaches to determine the contribution of transpiration to total evaporation". *Hydrol. Earth Syst. Sci.*

Tang, H., Armston, J., Hancock, S., Marselis, S., Goetz, S., and Dubayah, R. (2019). Characterizing global forest canopy cover distribution using spaceborne lidar. *Remote Sensing of Environment*, 231:111262.

Tao, X., Liang, S., He, T., and Jin, H. (2016). Estimation of fraction of absorbed photosynthetically active radiation from multiple satellite data: Model development and validation. *Remote Sensing of Environment*, 184:539–557.

Teuling, A. J., Taylor, C. M., Meirink, J. F., Melsen, L. A., Miralles, D. G., Van Heerwaarden, C. C., Vautard, R., Stegehuis, A. I., Nabuurs, G.-J., and De Arellano, J. V.-G. (2017). Observational evidence for cloud cover enhancement over western European forests. *Nature Communications*, 8(1):14065.

Tilstra, L. G., de Graaf, M., Aben, I., and Stammes, P. (2012a). In-flight degradation correction of SCIAMACHY UV reflectances and Absorbing Aerosol Index. *Journal of Geophysical Research: Atmospheres*, 117(D6).

Tilstra, L. G., Tuinder, O. N. E., and Stammes, P. (2012b). A new method for in-flight degradation correction of GOME-2 Earth reflectance measurements, with application to the Absorbing Aerosol Index. *Proceedings of the 2012 EUMETSAT Meteorological Satellite Conference*.

Tilstra, L. G., Tuinder, O. N. E., Wang, P., and Stammes, P. (2021). Directionally dependent Lambertian-equivalent reflectivity (DLER) of the Earth's surface measured by the GOME-2 satellite instruments. *Atmospheric Measurement Techniques*, 14(6):4219–4238.

Tramontana, G., Jung, M., Schwalm, C. R., Ichii, K., Camps-Valls, G., Ráduly, B., Reichstein, M., Arain, M. A., Cescatti, A., Kiely, G., Merbold, L., Serrano-Ortiz, P., Sickert, S., Wolf, S., and Papale, D. (2016). Predicting carbon dioxide and energy fluxes across global FLUXNET sites with regression algorithms. *Biogeosciences*, 13(14):4291–4313.

Turner, A. J., Köhler, P., Magney, T. S., Frankenberg, C., Fung, I., and Cohen, R. C. (2020). A double peak in the seasonality of California's photosynthesis as observed from space. *Biogeosciences*, 17(2):405–422.

Turner, A. J., Köhler, P., Magney, T. S., Frankenberg, C., Fung, I., and Cohen, R. C. (2021). Extreme events driving year-to-year differences in gross primary productivity across the US. *Biogeosciences*, 18(24):6579–6588.

United Nations (2016). Conference of the Parties Twenty - second session Marrakech, 7 – 18 November 2016 Item X of the provisional agenda. *Aggregate effect of the intended nationally determined contributions: an update*, pages 16–7126.

United Nations Environment Programme, Olhoff, A., Bataille, C., Christensen, J., Den Elzen, M., Fransen, T.,

Grant, N., Blok, K., Kejun, J., Soubeyran, E., Lamb, W., Levin, K., Portugal-Pereira, J., Pathak, M., Kuramochi, T., Strinati, C., Roe, S., and Rogelj, J. (2024). *Emissions Gap Report 2024: No More Hot Air ... Please! With a Massive Gap between Rhetoric and Reality, Countries Draft New Climate Commitments*. United Nations Environment Programme.

Usman, M., Liedl, R., Shahid, M. A., and Abbas, A. (2015). Land use/land cover classification and its change detection using multi-temporal MODIS NDVI data. *Journal of Geographical Sciences*, 25(12):1479–1506.

van den Berg, R. A., Hoefsloot, H. C., Westerhuis, J. A., Smilde, A. K., and Van Der Werf, M. J. (2006). Centering, scaling, and transformations: Improving the biological information content of metabolomics data. *BMC Genomics*, 7(1):142.

van der A, R. J., Peters, D. H. M. U., Eskes, H., Boersma, K. F., van Roozendael, M., De Smedt, I., and Kelder, H. M. (2006). Detection of the trend and seasonal variation in tropospheric NO_2 over China. *Journal of Geophysical Research: Atmospheres*, 111(D12):2005JD006594.

van der Meer, F., Bakker, W., Scholte, K., Skidmore, A., De Jong, S., Clevers, J., Addink, E., and Epema, G. (2001). Spatial scale variations in vegetation indices and above-ground biomass estimates: Implications for MERIS. *International Journal of Remote Sensing*, 22(17):3381–3396.

van der Tol, C., Berry, J. A., Campbell, P. K. E., and Rascher, U. (2014). Models of fluorescence and photosynthesis for interpreting measurements of solar-induced chlorophyll fluorescence. *Journal of Geophysical Research: Biogeosciences*, 119(12):2312–2327.

van der Tol, C., Julitta, T., Yang, P., Sabater, N., Reiter, I., Tudoroiu, M., Schuettemeyer, D., and Drusch, M. (2023). Retrieval of chlorophyll fluorescence from a large distance using oxygen absorption bands. *Remote Sensing of Environment*, 284:113304.

van Schaik, E., Kooreman, M. L., Stammes, P., Tilstra, L. G., Tuinder, O. N. E., Sanders, A. F. J., Verstraeten, W. W., Lang, R., Cacciari, A., Joiner, J., Peters, W., and Boersma, K. F. (2020). Improved SIFTER v2 algorithm for long-term GOME-2A satellite retrievals of fluorescence with a correction for instrument degradation. *Atmospheric Measurement Techniques*, 13(8):4295–4315.

van 't Loo, R. (2024). Using Level 2 Solar-Induced Fluorescence: Understanding the angle dependency of GOME-2 SIF. Internship report, Wageningen University and Research, Wageningen.

van Wittenberghe, S., Alonso, L., Verrelst, J., Moreno, J., and Samson, R. (2015). Bidirectional sun-induced chlorophyll fluorescence emission is influenced by leaf structure and light scattering properties — A bottom-up approach. *Remote Sensing of Environment*, 158:169–179.

Veefkind, J., Aben, I., McMullan, K., Förster, H., De Vries, J., Otter, G., Claas, J., Eskes, H., De Haan, J., Kleipool, Q., Van Weele, M., Hasekamp, O., Hoogeveen, R., Landgraf, J., Snel, R., Tol, P., Ingmann, P., Voors, R., Kruizinga, B., Vink, R., Visser, H., and Levelt, P. (2012). TROPOMI on the ESA Sentinel-5 Precursor: A GMES mission for global observations of the atmospheric composition for climate, air quality and ozone layer applications. *Remote Sensing of Environment*, 120:70–83.

Verma, M., Schimel, D., Evans, B., Frankenberg, C., Beringer, J., Drewry, D. T., Magney, T., Marang, I., Hutley, L., Moore, C., and Eldering, A. (2017). Effect of environmental conditions on the relationship between solar-induced fluorescence and gross primary productivity at an OzFlux grassland site. *Journal of Geophysical Research: Biogeosciences*, 122(3):716–733.

Vicent, J., Sabater, N., Tenjo, C., Acarreta, J. R., Manzano, M., Rivera, J. P., Jurado, P., Franco, R., Alonso, L., Verrelst, J., and Moreno, J. (2016). FLEX End-to-End Mission Performance Simulator. *IEEE Transactions on Geoscience and Remote Sensing*, 54(7):4215–4223.

Von Buttlar, J., Zscheischler, J., Rammig, A., Sippel, S., Reichstein, M., Knohl, A., Jung, M., Menzer, O., Arain, M. A., Buchmann, N., Cescatti, A., Gianelle, D., Kiely, G., Law, B. E., Magliulo, V., Margolis, H., McCaughey, H., Merbold, L., Migliavacca, M., Montagnani, L., Oechel, W., Pavelka, M., Peichl, M., Rambal, S., Raschi, A., Scott, R. L., Vaccari, F. P., Van Gorsel, E., Varlagin, A., Wohlfahrt, G., and Mahecha, M. D. (2018). Impacts of droughts and extreme-temperature events on gross primary production and ecosystem respiration: A systematic assessment across ecosystems and climate zones. *Biogeosciences*, 15(5):1293–1318.

Walther, S., Voigt, M., Thum, T., Gonsamo, A., Zhang, Y., Köhler, P., Jung, M., Varlagin, A., and Guanter,

L. (2016). Satellite chlorophyll fluorescence measurements reveal large-scale decoupling of photosynthesis and greenness dynamics in boreal evergreen forests. *Global Change Biology*, 22(9):2979–2996.

Wang, C., Beringer, J., Hutley, L. B., Cleverly, J., Li, J., Liu, Q., and Sun, Y. (2019a). Phenology Dynamics of Dryland Ecosystems Along the North Australian Tropical Transect Revealed by Satellite Solar-Induced Chlorophyll Fluorescence. *Geophysical Research Letters*, 46(10):5294–5302.

Wang, P. and Stammes, P. (2008). FRESCO+: An improved O2 A-band cloud retrieval algorithm for tropospheric trace gas retrievals. *Atmos. Chem. Phys.*

Wang, S., Li, R., Wu, Y., and Zhao, S. (2022a). Effects of multi-temporal scale drought on vegetation dynamics in Inner Mongolia from 1982 to 2015, China. *Ecological Indicators*, 136:108666.

Wang, S., Zhang, Y., Ju, W., Porcar-Castell, A., Ye, S., Zhang, Z., Brümmer, C., Urbaniak, M., Mammarella, I., Juszczak, R., and Folkert Boersma, K. (2020). Warmer spring alleviated the impacts of 2018 European summer heatwave and drought on vegetation photosynthesis. *Agricultural and Forest Meteorology*, 295:108195.

Wang, S., Zhang, Y., Ju, W., Qiu, B., and Zhang, Z. (2021). Tracking the seasonal and inter-annual variations of global gross primary production during last four decades using satellite near-infrared reflectance data. *Science of The Total Environment*, 755:142569.

Wang, S., Zhang, Y., Ju, W., Wu, M., Liu, L., He, W., and Peñuelas, J. (2022b). Temporally corrected long-term satellite solar-induced fluorescence leads to improved estimation of global trends in vegetation photosynthesis during 1995–2018. *ISPRS Journal of Photogrammetry and Remote Sensing*, 194:222–234.

Wang, W., Wang, W.-j., Li, J.-s., Wu, H., Xu, C., and Liu, T. (2010). The Impact of Sustained Drought on Vegetation Ecosystem in Southwest China Based on Remote Sensing. *Procedia Environmental Sciences*, 2:1679–1691.

Wang, X., Biederman, J. A., Knowles, J. F., Scott, R. L., Turner, A. J., Dannenberg, M. P., Köhler, P., Frankenberg, C., Litvak, M. E., Flerchinger, G. N., Law, B. E., Kwon, H., Reed, S. C., Parton, W. J., Barron-Gafford, G. A., and Smith, W. K. (2022c). Satellite solar-induced chlorophyll fluorescence and near-infrared reflectance capture complementary aspects of dryland vegetation productivity dynamics. *Remote Sensing of Environment*, 270:112858.

Wang, X., Qiu, B., Li, W., and Zhang, Q. (2019b). Impacts of drought and heatwave on the terrestrial ecosystem in China as revealed by satellite solar-induced chlorophyll fluorescence. *Science of The Total Environment*, 693:133627.

Wang, Y., Chen, Y., Wen, J., Wu, C., Zhou, W., Han, L., and Tang, X. (2024). Early warning of drought-induced vegetation stress using multiple satellite-based ecological indicators. *Ecological Indicators*, 169:112857.

Weatherhead, E. C., Reinsel, G. C., Tiao, G. C., Meng, X.-L., Choi, D., Cheang, W.-K., Keller, T., DeLuisi, J., Wuebbles, D. J., Kerr, J. B., Miller, A. J., Oltmans, S. J., and Frederick, J. E. (1998). Factors affecting the detection of trends: Statistical considerations and applications to environmental data. *Journal of Geophysical Research: Atmospheres*, 103(D14):17149–17161.

Wedow, J. M., Ainsworth, E. A., and Li, S. (2021). Plant biochemistry influences tropospheric ozone formation, destruction, deposition, and response. *Trends in Biochemical Sciences*, 46(12):992–1002.

Wen, J., Köhler, P., Duveiller, G., Parazoo, N., Magney, T., Hooker, G., Yu, L., Chang, C., and Sun, Y. (2020). A framework for harmonizing multiple satellite instruments to generate a long-term global high spatial-resolution solar-induced chlorophyll fluorescence (SIF). *Remote Sensing of Environment*, 239:111644.

Wen, J., Tagliabue, G., Rossini, M., Fava, F. P., Panigada, C., Merbold, L., Leitner, S., and Sun, Y. (2025). Detection of fast-changing intra-seasonal vegetation dynamics of drylands using solar-induced chlorophyll fluorescence (SIF). *Biogeosciences*, 22(8):2049–2067.

Wen, L., Mason, T. J., Ryan, S., Ling, J. E., Saintilan, N., and Rodriguez, J. (2023). Monitoring long-term vegetation condition dynamics in persistent semi-arid wetland communities using time series of Landsat data. *Science of The Total Environment*, 905:167212.

WHO (2022). *World Health Statistics 2022: Monitoring Health for the SDGs, Sustainable Development Goals*. World Health Organization, Geneva, 1st ed edition.

Woodgate, W., Phinn, S., Devereux, T., and Aryal, R. R. (2025). Bushfire recovery at a long-term tall eucalypt flux site through the lens of a satellite: Combining multi-scale data for structural-functional insight. *Remote Sensing of Environment*, 317:114530.

Woolliams, E. R., Mittaz, J. P., Merchant, C. J., Hunt, S. E., and Harris, P. M. (2018). Applying Metrological Techniques to Satellite Fundamental Climate Data Records. *Journal of Physics: Conference Series*, 972:012003.

Wu, G., Guan, K., Jiang, C., Peng, B., Kimm, H., Chen, M., Yang, X., Wang, S., Suyker, A. E., Bernacchi, C. J., Moore, C. E., Zeng, Y., Berry, J. A., and Cendrero-Mateo, M. P. (2020). Radiance-based NIR_v as a proxy for GPP of corn and soybean. *Environmental Research Letters*, 15(3):034009.

Xiao, J.-L., Zeng, F., He, Q.-L., Yao, Y.-X., Han, X., and Shi, W.-Y. (2021). Responses of Forest Carbon Cycle to Drought and Elevated CO2. *Atmosphere*, 12(2):212.

Xu, R., Li, Y., Teuling, A. J., Zhao, L., Spracklen, D. V., Garcia-Carreras, L., Meier, R., Chen, L., Zheng, Y., Lin, H., and Fu, B. (2022). Contrasting impacts of forests on cloud cover based on satellite observations. *Nature Communications*, 13(1):670.

Xue, J. and Su, B. (2017). Significant Remote Sensing Vegetation Indices: A Review of Developments and Applications. *Journal of Sensors*, 2017:1–17.

Yang, J. and Huang, X. (2021). The 30 m annual land cover dataset and its dynamics in China from 1990 to 2019. *Earth System Science Data*, 13(8):3907–3925.

Yang, P. and van der Tol, C. (2018). Linking canopy scattering of far-red sun-induced chlorophyll fluorescence with reflectance. *Remote Sensing of Environment*, 209:456–467.

Yang, P., Van Der Tol, C., Campbell, P. K. E., and Middleton, E. M. (2021). Unraveling the physical and physiological basis for the solar- induced chlorophyll fluorescence and photosynthesis relationship using continuous leaf and canopy measurements of a corn crop. *Biogeosciences*, 18(2):441–465.

Yang, X., Tang, J., Mustard, J. F., Lee, J.-E., Rossini, M., Joiner, J., Munger, J. W., Kornfeld, A., and Richardson, A. D. (2015). Solar-induced chlorophyll fluorescence that correlates with canopy photosynthesis on diurnal and seasonal scales in a temperate deciduous forest. *Geophysical Research Letters*, 42(8):2977–2987.

Yin, Y., Byrne, B., Liu, J., Wennberg, P. O., Davis, K. J., Magney, T., Köhler, P., He, L., Jeyaram, R., Humphrey, V., Gerken, T., Feng, S., Digangi, J. P., and Frankenberg, C. (2020). Cropland Carbon Uptake Delayed and Reduced by 2019 Midwest Floods. *AGU Advances*, 1(1):e2019AV000140.

Zhang, J., Gonsamo, A., Tong, X., Xiao, J., Rogers, C. A., Qin, S., Liu, P., Yu, P., and Ma, P. (2023a). Solar-induced chlorophyll fluorescence captures photosynthetic phenology better than traditional vegetation indices. *ISPRS Journal of Photogrammetry and Remote Sensing*, 203:183–198.

Zhang, J., Xiao, J., Tong, X., Zhang, J., Meng, P., Li, J., Liu, P., and Yu, P. (2022a). NIRv and SIF better estimate phenology than NDVI and EVI: Effects of spring and autumn phenology on ecosystem production of planted forests. *Agricultural and Forest Meteorology*, 315:108819.

Zhang, L. and Schwärzel, K. (2017). China's Land Resources Dilemma: Problems, Outcomes, and Options for Sustainable Land Restoration. *Sustainability*, 9(12):2362.

Zhang, M., Yuan, X., Zeng, Z., Pan, M., Wu, P., Xiao, J., and Keenan, T. F. (2025). A pronounced decline in northern vegetation resistance to flash droughts from 2001 to 2022. *Nature Communications*, 16(1):2984.

Zhang, M., Zhang, J., Liu, M., Guo, L., Ma, F., Xie, L., Xu, M., and Yun, A. (2017). Simulation on the Future Change of Soil Organic Carbon from Phaeozems under Different Management Practices in Northeast China. *Sustainability*, 9(7):1129.

Zhang, W., Luo, G., Hamdi, R., Ma, X., Li, Y., Yuan, X., Li, C., Ling, Q., Hellwich, O., Termonia, P., and De Maeyer, P. (2023b). Can Gross Primary Productivity Products be effectively evaluated in regions with few observation data? *GIScience & Remote Sensing*, 60(1):2213489.

Zhang, W., Wei, F., Horion, S., Fensholt, R., Forkel, M., and Brandt, M. (2022b). Global quantification of the bidirectional dependency between soil moisture and vegetation productivity. *Agricultural and Forest Meteorology*, 313:108735.

Zhang, X., Van Der A, R., Ding, J., Eskes, H., Van Geffen, J., Yin, Y., Anema, J., Vagasky, C., L. Lapierre, J.,

and Kuang, X. (2023c). Spaceborne Observations of Lightning NO$_2$ in the Arctic. *Environmental Science & Technology*, 57(6):2322–2332.

Zhang, Y., Fang, J., Smith, W. K., Wang, X., Gentine, P., Scott, R. L., Migliavacca, M., Jeong, S., Litvak, M., and Zhou, S. (2023d). Satellite solar-induced chlorophyll fluorescence tracks physiological drought stress development during 2020 southwest US drought. *Global Change Biology*, 29(12):3395–3408.

Zhang, Y., Gao, J., Liu, L., Wang, Z., Ding, M., and Yang, X. (2013). NDVI-based vegetation changes and their responses to climate change from 1982 to 2011: A case study in the Koshi River Basin in the middle Himalayas. *Global and Planetary Change*, 108:139–148.

Zhang, Y., Joiner, J., Gentine, P., and Zhou, S. (2018a). Reduced solar-induced chlorophyll fluorescence from GOME-2 during Amazon drought caused by dataset artifacts. *Global Change Biology*, 24(6):2229–2230.

Zhang, Y., Xiao, X., Zhang, Y., Wolf, S., Zhou, S., Joiner, J., Guanter, L., Verma, M., Sun, Y., Yang, X., Paul-Limoges, E., Gough, C. M., Wohlfahrt, G., Gioli, B., Van Der Tol, C., Yann, N., Lund, M., and De Grandcourt, A. (2018b). On the relationship between sub-daily instantaneous and daily total gross primary production: Implications for interpreting satellite-based SIF retrievals. *Remote Sensing of Environment*, 205:276–289.

Zhang, Y. and Ye, A. (2021). Quantitatively distinguishing the impact of climate change and human activities on vegetation in mainland China with the improved residual method. *GIScience & Remote Sensing*, 58(2):235–260.

Zhang, Y., Zhang, Q., Liu, L., Zhang, Y., Wang, S., Ju, W., Zhou, G., Zhou, L., Tang, J., Zhu, X., Wang, F., Huang, Y., Zhang, Z., Qiu, B., Zhang, X., Wang, S., Huang, C., Tang, X., and Zhang, J. (2021). ChinaSpec: A Network for Long-Term Ground-Based Measurements of Solar-Induced Fluorescence in China. *Journal of Geophysical Research: Biogeosciences*, 126(3):e2020JG006042.

Zhang, Z. and Zhang, Y. (2023). Solar angle matters: Diurnal pattern of solar-induced chlorophyll fluorescence from OCO-3 and TROPOMI. *Remote Sensing of Environment*, 285:113380.

Zhang, Z., Zhang, Y., Zhang, Q., Chen, J. M., Porcar-Castell, A., Guanter, L., Wu, Y., Zhang, X., Wang, H., Ding, D., and Li, Z. (2020a). Assessing bi-directional effects on the diurnal cycle of measured solar-induced chlorophyll fluorescence in crop canopies. *Agricultural and Forest Meteorology*, 295:108147.

Zhang, Z., Zhang, Y., Zhang, Y., and Chen, J. M. (2020b). Correcting Clear-Sky Bias in Gross Primary Production Modeling From Satellite Solar-Induced Chlorophyll Fluorescence Data. *Journal of Geophysical Research: Biogeosciences*, 125(9):e2020JG005822.

Zhao, D. F., Buchholz, A., Tillmann, R., Kleist, E., Wu, C., Rubach, F., Kiendler-Scharr, A., Rudich, Y., Wildt, J., and Mentel, Th. F. (2017). Environmental conditions regulate the impact of plants on cloud formation. *Nature Communications*, 8(1):14067.

Zou, C., Du, S., Liu, X., and Liu, L. (2024). TCSIF: A temporally consistent global Global Ozone Monitoring Experiment-2A (GOME-2A) solar-induced chlorophyll fluorescence dataset with the correction of sensor degradation. *Earth System Science Data*, 16(6):2789–2809.

Publications

Zhang, X., Van Der A, R., Ding, J., Eskes, H., Van Geffen, J., Yin, Y., Anema, J., Vagasky, C., L. Lapierre, J., and Kuang, X. (2023c). Spaceborne Observations of Lightning NO$_2$ in the Arctic. *Environmental Science & Technology*, 57(6):2322–2332

Goudar, M., Anema, J. C. S., Kumar, R., Borsdorff, T., and Landgraf, J. (2023). Plume detection and emission estimate for biomass burning plumes from TROPOMI carbon monoxide observations using APE v1.1. *Geoscientific Model Development*, 16(16):4835–4852

Anema, J. C. S., Boersma, K. F., Stammes, P., Koren, G., Woodgate, W., Köhler, P., Frankenberg, C., and Stol, J. (2024). Monitoring the impact of forest changes on carbon uptake with solar-induced fluorescence measurements from GOME-2A and TROPOMI for an Australian and Chinese case study. *Biogeosciences*, 21(9):2297–2311

Anema, J. C. S., Boersma, K. F., Tilstra, L. G., Tuinder, O. N. E., and Verstraeten, W. W. (2025b). Improved consistency in solar-induced fluorescence retrievals from GOME-2A with the SIFTER v3 algorithm. *Atmospheric Measurement Techniques*, 18(8):1961–1979

Anema, J. C. S., Boersma, K. F., Tilstra, L. G., van 't Loo, R., and Tuinder, O. N. E. (2025c). Long-term solar-induced fluorescence data record from GOME-2A and GOME-2B (2007–2023) using the SIFTER v3 algorithm (under review for ESSD)

Acknowledgements

First and foremost, I am very grateful to my supervisor and promoter, Folkert, for his support and guidance, for teaching me the importance of clear scientific storytelling, for offering constructive critiques of my work, and most of all for his consistent trust and belief in my progress. Folkert, I am also grateful that you encouraged my enthusiasm for exploring side paths, while teaching me to remain focused on the primary goal. Your repeated reminders of "uitzoomen, uitzoomen, uitzoomen" helped me gain more perspective and efficiency, and significantly improved my work. I will carry these words of advice with me moving forward.

I also want to thank Piet, Olaf, and Gijs, who have all played a key role during my PhD. Piet, thank you for your overall interest, support, guidance, and helpful advice over the past years, as well as your kindness. I appreciated that you were always available to discuss my ideas, share your perspectives, and invest the time in our brainstorming sessions. Olaf, thank you for your support throughout my PhD and your involvement in processing the SIF retrievals from GOME-2. Whenever I had a question, you took the time to answer it thoroughly, which I greatly appreciated. Gijs, your involvement with my work helped me in multiple ways. Your extensive knowledge and detailed memory of previous research seemed endless and proved highly valuable in the development of SIFTER v3. Moreover, your positive words about the research truly helped during the more challenging times. Finally, I really enjoyed all your stories and the conversations we had.

Furthermore, I would like to thank Wouter and Ingrid for welcoming me into the carbon group in Wageningen. Being part of this group deepened my understanding of the carbon cycle. Our discussions during the weekly meetings provided valuable input and feedback, especially during the first part of my PhD. Being involved with both KNMI and Wageningen University helped me to connect satellite-based vegetation monitoring more closely to carbon-cycle processes, which tremendously supported my understanding and research. In addition, I thank all colleagues and partners with whom I worked in the LANDMARC and AC SAF projects for their fruitful discussions.

Overall, my PhD life can be divided into two periods: during and after the COVID-19 pandemic. The first was a period in which my flatmates Céline and Maria doubled as my colleagues, and where my bedroom was also my office, with a decorative curtain hung to separate my personal life from my research. Webex served as the primary medium to connect with my new colleagues. After the pandemic, the RD&SW department at KNMI provided a working environment with open doors, spontaneous discussions, occasional laughter, and a genuinely supportive atmosphere.

The strong contrast between these two settings showed me that science is a more social matter than is often believed. Strong ideas, inspiration, insights, and moments of encouragement often arise from conversations during coffee breaks or lunchtime discussions.

This supportive environment was shaped by my colleagues at KNMI, whom I would all like to thank. Jos vG and Ronald, thank you for helping share the developed GOME-2 SIF products with the world by making them accessible through TEMIS. Robert, thank you for your help reprocessing the GOME-2 SIF products. I thank all my colleagues within the Satellite Retrieval and Validation group for their helpful feedback on my work (and presentations). Tim, thank you for your interest in my work, the advice you have provided along the way, and the nice conversations we had, which I truly valued. Frank, thank you for reminding me of the value of taking time off, an insight that proved very valuable. Jacqueline, your presence and openness greatly contributed to the welcoming environment within the department. Maarten, thank you for your efforts in retrieving TROPOMI SIF, for your PhD advice and encouragement, and for all enjoyable conversations, which often served as a welcome break. I also want to thank many of my colleagues, including, but not limited to Benjamin, Diko, Felipe, Isidora, Job, Kasper, Mengyao, Serena, Victor, and Yutao, for the many fun Friday evenings we shared. Benjamin and Yutao, thank you for all the productive and entertaining moments we shared in "our" office.

Ruben and Mohammed, I enjoyed working with you and supervising you on the topic of SIF during your internships at KNMI. Your work also contributed to the work presented in this thesis, specifically in Chapters 3 and 5. Carlijn, Gerbrand, and Mohammed, I am pleased that your efforts led to the exciting developments in applying the SIFTER v3 algorithm to TROPOMI observations (shown in Chapter 5). Carlijn, I will closely follow your PhD work on SIF and wish you lots of sucess and, most of all, fun in the coming years.

In addition to my work at KNMI, I also spent many Tuesdays at the MAQ department in Wageningen. As mentioned above, I am grateful for the discussions and feedback my colleagues in the carbon group provided. I want to thank Anne-Wil and Marnix for our collaboration in organising the "Monitoring carbon fluxes from land use, land-use change and forestry" symposium. It was a pleasure working with you.

I am fortunate to be surrounded by many supportive people, both family and friends. While I cannot name everyone here, I would like to highlight a few friends who have been especially important to me during this academic journey. Mark, even though we pursued our PhDs in different countries and on slightly different topics (vegetation versus volcano monitoring), we were truly in this together! Isabel, thank you for being such a constant source of encouragement. Manu, over these past years, you have become an important friend to me. Furthermore, your advice and research experience have helped me tremendously: from great tips to improve my Fortran and Python code to offering broader academic guidance. Michelle, thank you for always being there and celebrating even my smallest wins.

Finally, I thank my parents, Tjeerd and Birgitta, my siblings, Charlotte, Leon, Pascal, and Michelle, and my husband Philip for their unlimited love and support. My parents, in particular, taught me to always follow through on what I start (or, "wie 'A' zegt, moet ook 'B' zeggen"), a mindset that has proven to be valuable throughout my studies and PhD.

Netherlands Research School for the
Socio-Economic and Natural Sciences of the Environment

D I P L O M A

for specialised PhD training

The Netherlands research school for the
Socio-Economic and Natural Sciences of the Environment
(SENSE) declares that

Juliëtte Catherine Sophie Anema

born on 11 September 1994 in Alphen aan den Rijn, the Netherlands

has successfully fulfilled all requirements of the
educational PhD programme of SENSE.

Wageningen, 5 June 2026

SENSE coordinator PhD education

Dr Ir Peter Vermeulen

The SENSE Director

Dr Jampel Dell'Angelo

The SENSE Research School declares that **Juliëtte Catherine Sophie Anema** has successfully fulfilled all requirements of the educational PhD programme of SENSE with a workload of 39.1EC, including the following activities:

SENSE PhD Courses

- A1: Environmental Research in Context (2021)
- A2 Research in context activity: 'Co-organised and chaired the Monitoring carbon fluxes from land use, land-use change and forestry Symposium' (2024)

Other PhD and Advanced MSc Courses

- Land use and ecosystem change, Karlsruhe Institute of Technology (2022)
- Scientific Writing, Wageningen Graduate Schools (2022)
- Project and Time Management, Wageningen Graduate Schools (2022)
- Efficient Writing Strategies, Wageningen Graduate Schools (2022)
- Presenting with Impact, Wageningen Graduate Schools (2022)

Management and Didactic Skills Training

- Co-organised and co-hosted the RDSW department weekly lunch seminar series at KNMI (2023)
- Initiated and established a community for Early Career Scientists in Remote Sensing community, including the organization and chairing of a dedicated symposium and several networking activities (2022-2024)
- Hosting and co-organised a 3-day General Assembly meeting of the H2020 LANDMARC project at KNMI (2022)
- Co-supervised two MSc internships at KNMI (2025-2026)

Oral Presentations

- *Addressing degradation and geometry effects to develop consistent global solar-induced fluorescence records from GOME-2A and GOME-2B (2007-2023)*. EGU, 22-24 May 2022, Vienna, Austria
- *Improved consistency of solar-induced fluorescence long records from GOME-2*. EUMETSAT Meteorological Satellite Conference, 30 September-4 October 2024, Würzburg, Germany

This research received funding from the Horizon 2020 research and innovation programme (grant no. 869367) and the European Organisation for the Exploitation of Meteorological Satellites (EUMETSAT) Atmospheric Composition Satellite Application Facility (AC SAF).

Financial support from the Meteorology and Air Quality group at Wageningen University for printing this thesis is grately acknowledged.

Cover design by Juliëtte C.S. Anema.
Printed by ProefschriftMaken.

